JARA|FIT

Annual Report 2010

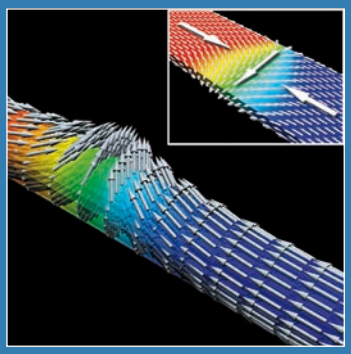

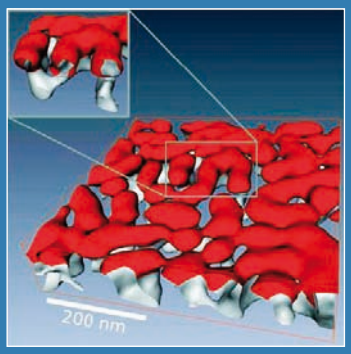

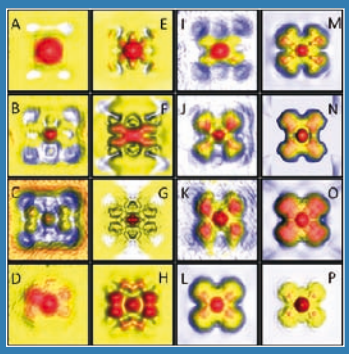

AN INITIATIVE OF

RWTH AACHEN UNIVERSITY

JÜLICH FORSCHUNGSZENTRUM

Publication Details

JARA-FIT
Jülich Aachen Research Alliance
for Fundamentals of Future Information Technologies
Annual Report 2010

Published by:
Forschungszentrum Jülich GmbH, 52425 Jülich
RWTH Aachen University, 52062 Aachen

Editors:
Dr. Wolfgang Speier
Managing Director JARA-FIT
Forschungszentrum Jülich GmbH
52425 Jülich
Germany
Phone: ++49-2461-613107

Prof. Dr. Markus Morgenstern
Scientific Director JARA-FIT
II. Institute of Physics B RWTH Aachen University
52074 Aachen
Germany
Phone: ++49-241-8027075/6

Prof. Dr. Detlev Grützmacher
Scientific Director JARA-FIT and Director JARA
Peter Grünberg Institute – Semiconductor Nanoelectronics
Forschungszentrum Jülich GmbH
52425 Jülich
Germany
Phone: ++49-2461-612340/1

Contact:
Dr. Wolfgang Speier
w.speier@fz-juelich.de

Layout:
Ulrike Adomeit
Thomas Pössinger

Year of publication: 2011

2011

JARA-FIT

Jülich Aachen Research Alliance for

Fundamentals of Future Information Technology

Annual Report 2010

Forschungszentrum Jülich

RWTH Aachen

Dear Reader,

Information technology is increasingly pervading all areas of our society and life. It has assumed a key function in areas as varied as communication and organisation within the professional and private world, industrial production, transport and logistics, energy and environmental technology, health and medical care, and last but not least entertainment. In the next decade, the development of IT systems will be dominated by two major trends - a continuation of the exponential increase in performance and efficiency ("Moore´s law") by further down-scaling, new materials, and novel device concepts - and additional functionalities ("More than Moore") by the emergence of advanced concepts in, e.g., sensors and wireless transmission. Beyond this, new concepts of quantum information processes seem close ahead and are likely to bring new innovations in the field of future information technology.

RWTH Aachen University and Forschungszentrum Jülich have recognized that these scientific grand challenges can only be solved when reaching a critical mass in terms of scientific competence, joint research infrastructure and shared teaching activities. This has lead to the founding of the Jülich Aachen Research Alliance (JARA) and its section ´Fundamentals of Future Information Technology' (JARA-FIT).

Our section JARA-FIT is now in its fourth year and, we are proud to state, has emerged to one of the internationally leading organisations in nanoelectronics and future information technology. Presently, JARA-FIT is composed of 26 senior research groups and 14 junior research groups situated in Aachen and/or Jülich. This concept bears fruit, as either manifested in an increasing number of joint papers, prizes awarded to researchers or successes in project applications. This is now also recognized by internationally renowned scientist, who become attracted by our concept and the unique possibilities offered by us. We are particularly excited to have convinced David DiVincenzo from IBM to join our section. He has received an Alexander von Humboldt Professorship, the most valuable international research award in Germany. This professorship is granted to internationally leading researchers working abroad to enable them to conduct cutting-edge research as Humboldt professors at German universities on a sustainable basis. Together with Barbara Terhal, also from IBM, and Hendrik Bluhm, from Harvard University, he founded the new Institute for Quantum Information with the ultimate goal to establish a solid-state-based quantum-information-processing approach. It is also great news to hear that Hendrik Bluhm will receive the Alfried Krupp-award for young professors this year. Other prominent examples are the starting grant by European Research Council for Christoph Stampfer (one of our newly founded JARA-FIT junior research groups), the prestigious Wolf Prize in Physics from Israel awarded to Knut Urban, the Gay-Lussac-Humboldt Prize awarded to Claus M. Schneider by the French Ministry and the Alexander von Humboldt Foundation, and the World Class University Professorship awarded to Manfred Martin in Korea. We are also thrilled by the fact that the German Research Foundation has accepted our joint application for a Collaborative Research Centre for Nanoswitches based on resistively switchable chalcogenides and has prolonged our research unit on spin relaxation and coherence phenomena. But, already new developments are underway: we will soon establish the Helmholtz Nanoelectronic Facility (HNF) as the first dedicated nanoelectronics user facility in Germany, have initiated a master course for nanoelectronics at Aachen and are asked to submit a proposal for a graduate school for the Fundamentals of Future Information Technology as part of the German excellence initiative. Clearly, we are fit to approach the challenges ahead. We hope that readers will join us in our excitement to set the foundation of future information technology.

Markus Morgenstern
Scientific Director JARA-FIT

Detlev Grützmacher
Scientific Director JARA-FIT and Director JARA

Contents

JARA-FIT in Headlines

Foundation of Peter Grünberg Institute in Jülich

The foundation of the Peter Grünberg Institute was marked by a celebration and a scientific colloquium on 7. and 8. April 2011. The Peter Grünberg Institute (PGI) is formed out of parts of former Institut für Festkörperforschung (IFF) und Institut für Bio- und Nanosysteme (IBN) and will provide the central platform for basic research in the field of nanoelectronics in the Jülich-Aachen region. In the tradition of Peter Grünberg, the PGI researchers set out to develop innovative approaches for information processing and data transmission and are designing new storage architectures, which will form the basis for tomorrow's hardware. In future, PGI will also operate the Helmholtz Nanoelectronic Facility (see below). All Jülicher activities in JARA-FIT are now concentrated in PGI.

Top International Physicist David DiVincenzo teaching and researching for JARA-FIT

David DiVincenzo, international expert in the field of quantum physics, has taken up his position as the first JARA professor. He has taken over the directorship of the newly founded Institute of Theoretical Nanoelectronics and was appointed professor at the Institute for Quantum Information at RWTH Aachen University (details see below). David DiVincenzo was awarded the Alexander von Humboldt Professorship, the most coveted international research prize in Germany: The prize money provided by the Alexander von Humboldt Foundation is invested in setting up the two institutes. Further resources for equipment and infrastructure will be provided by RWTH Aachen University and Forschungszentrum Jülich. In his position as university professor in Aachen and as director of an institute in Jülich, DiVincenzo will have full rights and access to resources at both institutions. The JARA professorship was set up in order to attract highly acclaimed international scientists to the Jülich-Aachen region. The JARA professorship offers institutional affiliation with a combination of full rights, obligations and resources at both locations. His research activities on the topic of quantum physics will be integrated into JARA-FIT. He studied at the University of Pennsylvania, where he completed his B.S.E. in 1979, before going on to complete his master's followed by his PhD in 1983. He has been working at the Physical Sciences Department, IBM T. J. Watson Research Center, in Yorktown Heights, NY, since 1985.

Knut Urban received prestigious Wolf Prize in Physics for Breakthrough in Electron Microscopy

The world-famous Wolf Prize in Physics was jointly awarded to Knut Urban from Forschungszentrum Jülich, Maximilian Haider from CEOS GmbH, Heidelberg and Harald Rose from Technische Universität Darmstadt. On 29. May 2011, the scientists received the award, including prize money of $ 100,000, for their work in advancing electron microscopy. The prize was presented by the President of the State of Israel, Shimon Peres, and the Minister of Education, Gideon Sa'ar, in the Israeli Parliament, the Knesset, in Jerusalem.

Quelle des Fotos: Sasson Tiram

Hendrik Bluhm receives Alfried Krupp-Förderpreis

Hendrik Bluhm, newly appointed Chair for Experimental Physics at the RWTH Aachen, is awarded the Alfried Krupp Prize for Young University Teachers 2011. The Alfried Krupp von Bohlen and Halbach foundation provides 1 million € to support the establishment of his research group in Aachen within the next 5 years. Hendrik Bluhm's research fields are semiconductor spin qubits and high-sensitivity magnetic scanning experiments. He joined RWTH Aachen and JARA in March 2011 (see below). The award ceremony will take place in October.

JARA-FIT Juniorprofessor Christoph Stampfer receives ERC Starting Grant

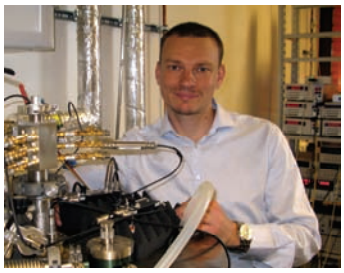

Christoph Stampfer, JARA-FIT Juniorprofessor for „Experimental Nanoelectronics“ receives an „ERC Starting Grant“ of the European Research Council (ERC). He was successful with his proposal on „Graphene Quantum Electromechanical Systems“. The aim of his project is to develop a new class of mechanically tunable quantum devices based on graphene for gaining control over the mechanical and electromechanical properties of graphene nano-membranes and suspended graphene nanostructures. The ERC has granted more than 1.79 million € for 5 years in the recognition of his excellentwork and the possibility to explore new regimes of quantum physics with potentially important technological applications.

Manfred Martin nominated for the Korean World Class University Programme

Within the Korean World Class University Programme (WCU) JARA-FIT scientist Manfred Martin from RWTH Aachen University was appointed WCU Professor at Seoul National University (SNU). He is one of 13 German professors from various disciplines being awarded with such a position at Korean universities. In SNU's Department of Materials Science and Engineering Manfred Martin is involved in teaching and research on the long term stability of functional oxides. At RWTH Aachen University Manfred Martin is holding the Chair of Physical Chemistry I since 2000. His research activities cover the field of Physical Chemistry of Solids with a special emphasis on defects, diffusion and reactivity of solids. In the past few years, he has also worked on chemically induced insulator-metal transitions.

Claus M. Schneider received Gay-Lussac-Humboldt prize

JARA-FIT Scientist Claus M. Schneider from Forschungszentrum Jülich received the Gay-Lussac-Humboldt prize on Tuesday, 6 April 2010, in Paris in recognition of his scientific achievements and his work in promoting French-German scientific cooperation. The award, which includes prize money of € 25,000, is conferred annually by the French Ministry of Education and Research and the Alexander von Humboldt Foundation. Claus M. Schneider is director of the Peter Grünberg Institute and holder of the first UAMR professorship, recently created by the University Alliance Metropolis Bochum, Duisburg-Essen and Dortmund (UAMR).

Heiner Müller-Krumbhaar Receives Badge of Honour from German Physics Society

On 12 November 2010, JARA-FIT scientist Heiner Müller-Krumbhaar was presented with the badge of honour of the German Physics Society (DPG) for outstanding contributions to the aims of the Society. Müller-Krumbhaar was honoured for his commitment to physics in schools and his long-standing work as chairman of the Dynamics and Statistical Physics Division. As a co-organizer of the "Year of Physics" in 2000 and a member of the steering committee of the "World of Physics", he was considered to have made a major contribution to raising the profile of the DPG. Heiner Müller-Krumbhaar was director at the former Institut für Festkörper-forschung and has recently retired.

Peter A. Grünberg awarded honorary membership of the German Physics Society

Peter A. Grünberg was awarded honorary membership of the German Physics Society at their Spring Conference in Dresden in March 2011. DPG thus recognizes "his discovery of interlayer exchange coupling and giant magnetoresistance in thin transition metal layers arising from it, for which he received the Nobel Prize for Physics in 2007 (together with Albert Fert, Paris) (...) as well as his publications, which helped to significantly increase the prestige in society at large of physics in Germany".

Helmholtz Professorship for Siegfried Mantl

In recognition of his special scientific achievements, Forschungszentrum Jülich has conferred a Helmholtz Professorship on JARA-FIT scientist Siegfried Mantl, thus retaining his outstanding expertise in the field of application-oriented semiconductor technology. Together with his research group in the new Peter Grünberg Institute at Jülich and in collaboration with leading industrial companies, the physicist intends to use the available resources to advance basic research for the nanoelectronics of the future.

Awards for young scientists of JARA-FIT

Sebastian Feste received the 2010 prize of excellency of the Forschungszentrum Jülich. He worked during his Ph.D. on the preparation and analysis of semiconducting devices at the former Institute for Bio- and Nanosystems. He was honoured with 5.000€ for his outstanding work in the field of silicon-based nanoelectronics. Presently, he is working at the Purdue Universität in Indiana (US).

Dominic Lencer, Graduate student of the I. Institute of Physics (IA) of the RWTH Aachen, received the „Graduate Student Gold Award“of the Materials Research Society in April 2010. The physicist conducted research in his Ph.D. on optimal materials for phase change memories. He succeeded to gain fundamental insights about an important class of materials which can rapidly change between a crystalline and amorphous phase as a result of external stimuli.

Helmholtz Nanoelectronic Facility takes off

The construction of the Helmholtz Nano-electronic Facility (HNF) was commenced this year with a ground-breaking ceremony. In the next 3 years a modern, 1000-square-meter large cleanroom center will be built and a total sum of around 25 million Euro invested. Materials, processes and structures in the nanometer range will be developed in this facility for the next generation of semiconductor chips. The Helmholtz-Association will invest 12 million Euro in the erection of the ultra-modern clean-room center building. An additional 13 million Euro will also be provided for the funding of scientific and technical equipment.

The equipment will complement equipment originating from projects of the Federal Ministry of Education and Research (BMBF). The facility will be compatible to industry standards and will include equipment for cleaning, lithography, inspection of semiconductor wafers, ion beam treatment (implanter and tandetron) as well as for further nanoelectronic process technology. The so-called nano fabrication cluster will combine a large number of components for the fabrication, processing and analysis of very small structures on artificial crystals. It is possible to transport samples within the 6 m x 15 m large chamber without breaking the vacuum and therefore to ensure contamination-free surfaces. The modular construction provides the platform for industry and university partners` use of their own equipment in the new Helmholtz Nano Facility.

Application for a DFG Collaborative Research Centre on Nanoswitches accepted

The German Research Foundation (DFG) has accepted the application for a Collaborative Research Centre by JARA-FIT: „Resistiv schaltende Chalkogenide für zukünftige Elektronikanwendungen: Struktur, Kinetik und Bauelementskalierung – Nanoswitches“ (SFB 917), starting on 1. July 2011. The application has been selected out of 62 draft proposals. In traditional semiconductor-based electronics, structural defects are detrimental to the desired device performance. In contrast, structural defects in oxides and a class of chalcogenides can represent the essential nano-scale functionalities for resistive switching, a phenomena where the resistance of a material can be switched upon an external stimuli between different states. The SFB will focus on the defect-based switching phenomena utilizing changes in the phase and valence of oxides and higher chalcogenides. An understanding of the microscopic mechanisms of the switching processes and a tailoring of the relevant defects on a nanometer scale will enable novel approaches in electronics and may result in a paradigm shift towards a defect-based electronics technology. The Collaborative Research Centre will be established at RWTH Aachen together with Forschungszentrum Jülich and the Institute Access at RWTH. Speaker of the Collaborative Research Centre will be Matthias Wuttig. The Steering Committee comprises Rainer Waser (deputy speaker), Regina Dittmann (PGI-7), Joachim Mayer (GfE & ER-C), Martin Salinga (I. Physikalisches Institut), and Ulrich Simon (Institut für Anorganische Chemie).

Draft proposal for JARA-FIT Graduate School accepted as part of the second phase of the Excellence Initiative

The joint commission of the German Research Foundation and the German Council of Science and Humanities (Wissenschaftsrat) has selected the draft proposal for a JARA-FIT Graduate School “Fundamentals of Future Information Technology” for submission of a detailed funding application as part of the second phase of the Excellence Initiative by the German federal and state governments. A full proposal has to be submitted until September 2011. The final decision will be made in June 2012.

DFG Research Group 912 on Spin Electronis extended

The DFG has approved the extension of the Research Group 912 on Spin Electronis headed by Prof. Markus Morgenstern and Prof. Gernot Güntherodt.

Nanoelectronics Days 2010

JARA-FIT launched the “Nanoelectronics Days 2010”. The conference was held in the main building of the RWTH Aachen University, from 4. to 7. October 2010. 250 Researchers from established research institutions, universities and industry such as IBM, ASML, AIXTRON, LETI, IMEC, K.I.T., EPFL, aixXACCT, Argonne National Lab, TASC, University of Madrid, Nanostructure Consortium Lund, University of Singapore, Tohoku University, Hokkaido University, etc. discussed the recent results and achievements in nanoelectronics. The ND2010 poster award was sponsored by the NRW Cluster NanoMikro&Werkstoffe. Eike Linn was awarded the first prize for the poster on "Solving the sneak path obstacle for crossbar arrays." The second place won Sebastian Kuhlen with the theme "Coherent electrical spin manipulation in indium gallium arsenide and strained." Dieter Weber won the third prize with his poster "Three-terminal memory device based on channel doping by electric field-driven oxygen intercalation". The winners received cash prizes worth a total of 1700 €.

41. IFF Spring School: Oxides with Exotic Properties and Great Scope for Application

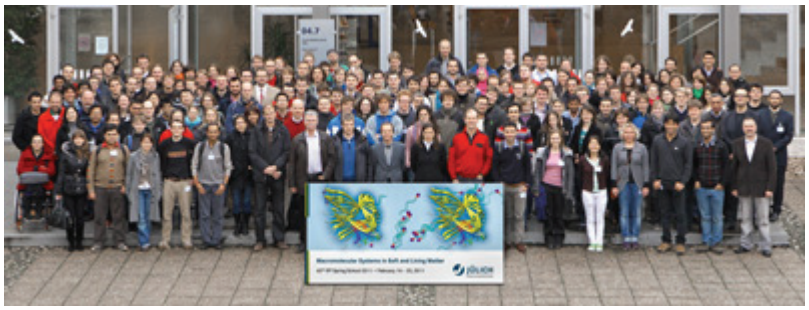

The "IFF Spring School" opened its doors for the 41st course lasting from 8 March until 19 March 2010. The motto of the Spring School run by the former Institute for Solid State Research was "Electronic Oxides: Correlation Phenomena, Exotic Phases, and Novel Functionalities". Within the framework of this course, scientists from JARA-FIT together with other institutions give students and young scientists from all over the world a comprehensive overview of a current topic - which changes each year - in the field of solid state physics. 208 undergraduate and postgraduate students and young scientists from 104 universities and institutions world-wide, including US, Nigeria and China, attended the spring school.

New Appointments

Qubit physicist Hendrik Bluhm

Hendrik Bluhm joined the faculty of physics at the RWTH Aachen University in March 2011. He heads the institute of physics IIC and works on Spin Qubits and Mesoscopic Scanning Measurements. He studied in Freiburg and left after the Vordiplom to the US to continue his studies at Stanford University (US), where he graduated in physics beginning of 2008. Afterwards, he went to Harvard University (US) to work as a postdoctoral researcher in the group of Amir Yacoby. He will be affiliated with the institute for quantum information founded by David DiVincenzo.

Theoretician Barbara Terhal

Barabara Terhal joined the faculty of physics at the RWTH Aachen University end of 2010. She was born in the Netherlands and studied physics in Amsterdam, where she received her MSc in 1995 and Ph.D in 1999. She then went to the US and worked at Caltech and IBM Watson Research Center (US), where she has been Research Staff Member since 2002. She is interested in quantum physics and the theory of quantum entanglement. She came together with David DiVincenzo to Aachen and joined his institute for quantum information.

Electron microscopist Rafal Dunin-Borkowski

Rafal E. Dunin-Borkowski was appointed Director of the Institute for Microstructure Research of the newly formed Peter Grünberg Institute and the Ernst Ruska-Centre for Microscopy and Spectroscopy with Electrons (ER-C) in Forschungszentrum Jülich end of 2010. He is Professor of Experimental Physics at RWTH Aachen University and Adjunct Professor in the Technical University of Denmark. He studied at the University of Cambridge and received his Ph.D. in 1994. He worked as a scientist at the Department of Materials Science and Metallurgy in the University of Cambridge (UK), the Center for Solid State Science at Arizona State University (US) and the Department of Materials in the University of Oxford (UK). Before coming to Aachen, he was also founding director of the Center for Electron Nanoscopy in the Technical University of Denmark in Lyngby.

Junior Professor Riccardo Mazzarello

Riccardo Mazzarello joined the faculty of physics beginning of 2010 as a Junior professor for Theoretical Nanoelectronics in the department of physics of the RWTH Aachen University. He studied phyics at the University of Genua (Italy) and received his Ph.D at the University of Hamburg. His interest is in computer-based material science and solid state physics and he worked at SISSA and ICTP in Triest (Italy) and ETH Zürich (CH).

Semiconductor physicist Joachim Knoch

Joachim Knoch was appointed head of the Institute of Semiconductor Electronics (IHT) at the Faculty of Electrical Engineering and Information Technology in April 2011. He studied physics at RWTH Aachen University, Germany and Queen Mary, University of London (UK). He received the MS and PhD degrees from RWTH Aachen University and has worked as a scientist at Massachusetts Institute of Technology (US), Forschungszentrum Jülich and IBM Zurich Research Laboratory (CH). Since 2008 he was professor of electrical engineering at TU Dortmund University, where he was mainly working on electronic transport in nanowire/tube transistors.

New Management of JARA and JARA-FIT

Detlev Grützmacher (PGI, Forschungszentrum Jülich) is the Managing Director of the Jülich Aachen Research Alliance since 1. April 2010. Dr. Wolfgang Speier has taken over the position of general management of JARA-FIT, beginning 1. January 2011.

General Information

JARA-FIT Members

Prof. Dr. S. Andergassen, Institut für Theorie der Statistischen Physik, RWTH Aachen

Prof. Dr. H. Bluhm, II. Physikalisches Institut und Institut für Quanteninformation, RWTH Aachen

Prof. Dr. S. Blügel, Peter Grünberg Institut – Quanten-Theorie der Materialien, Forschungszentrum Jülich
Institute for Advanced Simulation, Forschungszentrum Jülich

Prof. Dr. T. Brückel, Peter Grünberg Institut – Streumethoden, Forschungszentrum Jülich
Jülich Centre for Neutron Science

Prof. Dr. A. Böker, Makromolekulare Materialien und Oberflächen, DWI an der RWTH Aachen

Prof. Dr. D. P. DiVincenzo, Institut für Quanteninformation, RWTH Aachen
Peter Grünberg Institut – Theoretische Nanoelektronik, Forschungszentrum Jülich
Institute for Advanced Simulation, Forschungszentrum Jülich

Prof. Dr. R. Dronskowski, Lehrstuhl für Festkörper- und Quantenchemie und Institut für Anorganische Chemie, RWTH Aachen

Prof. Dr. R. Dunin-Borkowski, Peter Grünberg Institut – Microstrukturforschung, Forschungszentrum Jülich
Ernst Ruska-Centrum für Mikroskopie und Spektroskopie mit Elektronen

Prof. Dr. G. Güntherodt, II. Physikalisches Institut A, RWTH Aachen

Prof. Dr. D. Grützmacher, Peter Grünberg Institut – Halbleiter-Nanoelektronik, Forschungszentrum Jülich

Prof. Dr. C. Honerkamp, Institut für Theoretische Festkörperphysik, RWTH Aachen

Prof. Dr. P. Kögerler, Institut für Anorganische Chemie (Molekularer Magnetismus), RWTH Aachen
Peter Grünberg Institut – Elektronische Eigenschaften, Forschungszentrum Jülich

Prof. Dr. U. Klemradt, II. Physikalisches Institut B, RWTH Aachen

Prof. Dr. J. Knoch, Institut für Halbleitertechnik, RWTH Aachen

Prof. Dr. P. Loosen, Lehrstuhl für Technologie Optischer Systeme, RWTH Aachen
Fraunhofer-Institut für Lasertechnik, Aachen

Prof. Dr. S. Mantl, Peter Grünberg Institut – Halbleiter-Nanoelektronik, Forschungszentrum Jülich

Prof. Dr. M. Martin, Institut für Physikalische Chemie, RWTH Aachen

Prof. Dr. J. Mayer, Gemeinschaftslabor für Elektronenmikroskopie
Ernst Ruska-Centrum für Mikroskopie und Spektroskopie mit Elektronen

Prof. Dr. R. Mazzarello, Institut für Theoretische Festkörperphysik, RWTH Aachen

Prof. Dr. V. Meden, Institut für Theorie der Statistischen Physik, RWTH Aachen

Prof. Dr. W. Mokwa, Institut für Werkstoffe der Elektrotechnik 1 – Mikrostrukturintegration, RWTH Aachen

Prof. Dr. M. Morgenstern, II. Physikalisches Institut B, RWTH Aachen

Prof. Dr. A. Offenhäusser, Peter Grünberg Institut – Bioelektronik, Forschungszentrum Jülich

Prof. Dr. E. Pavarini, Peter Grünberg Institut & Institut for Advanced Simulation, Forschungszentrum Jülich

Prof. Dr. R. Poprawe, Fraunhofer-Institut für Lasertechnik, Aachen

Prof. Dr. G. Roth, Institut für Kristallographie, RWTH Aachen

Prof. Dr. H. Schoeller, Institut für Theorie der Statistischen Physik, RWTH Aachen

Prof. Dr. U. Simon, Institut für Anorganische Chemie, RWTH Aachen

Prof. Dr. J. Splettstößer, Institut für Theorie der Statistischen Physik, RWTH Aachen

Prof. Dr. C. Stampfer, II. Physikalisches Institut B, RWTH Aachen
Peter Grünberg Institut – Halbleiter-Nanoelektronik, Forschungszentrum Jülich

Prof. Dr. C. M. Schneider, Peter Grünberg Institut – Elektronische Eigenschaften, Forschungszentrum Jülich

Prof. Dr. T. Taubner, I. Physikalisches Institut A, RWTH Aachen

Prof. Dr. S. Tautz, Peter Grünberg Institut – Funktionale Nanostrukturen auf Oberflächen, Forschungszentrum Jülich

Prof. Dr. B.M. Terhal, Institut für Quanteninformation, RWTH Aachen

Prof. Dr. A. Vescan, Lehr- und Forschungsgebiet GaN-Bauelementtechnologie, RWTH Aachen

Prof. Dr. R. Waser, Institut für Werkstoffe der Elektrotechnik 2, RWTH Aachen
Peter Grünberg Institut – Elektronische Materialien, Forschungszentrum Jülich

Prof. Dr. M. Wegewijs, Peter Grünberg Institut – Theoretische Nanoelektronik, Forschungszentrum Jülich

Prof. Dr. M. Wuttig, I. Physikalisches Institut A, RWTH Aachen

JARA-FIT Institutes

Peter Grünberg Institut/ Institut for Advanced Simulation – Quanten-Theorie der Materialien, Forschungszentrum Jülich

S. Blügel

The analysis and computation of electronic properties of solid-state systems relevant for basic science and practical applications in collaboration with experimentalists is the hallmark of our research. An important asset of our institute is the competence in developing conceptual and computational methods (density functional theory and beyond, wave-packet propagation, diagram techniques). Emphasis is on the investigation of complex magnetism, magnetism in reduced dimensions, spin-dependent electronic transport phenomena, collective excitations and quasi-particles. A second research theme is nano-scale tribology, friction, adhesion, plastic deformation. Computational materials science research is established by combining first-principles results with macroscopic methods (molecular dynamics, Monte Carlo).

Lehrstuhl für Makromolekulare Materialien und Oberflächen, DWI an der RWTH Aachen

A. Böker

The chair of Macromolecular Materials and Surfaces is part of the DWI an der RWTH Aachen. The DWI is an independent research institute affiliated to RWTH Aachen University focused on polymer / soft matter materials development with the mission of novel and active properties. Under the heading “Science for Innovation” we aim at a tailor-made surface functionality of soft materials, especially fibers, films, membranes, textiles, and biomaterials. Beyond knowledge-oriented, basic approaches, work at DWI is dedicated to the translation and implementation of this knowledge into application-oriented concepts for functional films and surfaces, antimicrobial polymers and surfaces, encapsulation and release, functional membranes, and biomedical devices. The major research topics at the chair of Macromolecular Materials and Surfaces include bioconjugate polymer materials, nanoparticle composites and guided self-assembly.

Peter Grünberg Institut - Streumethoden, Forschungszentrum Jülich

Th. Brückel

At the Institute of Scattering Methods, we focus on the investigation of structural and magnetic order, fluctuations and excitations in complex or nanostructured magnetic systems and highly correlated electron systems. Our research is directed at obtaining a microscopic atomic understanding based on fundamental interaction mechanisms. The aim is to relate this microscopic information to macroscopic physical properties. To achieve this ambitious goal, we employ the most advanced synchrotron X-ray and neutron scattering methods and place great emphasis on the complementary use of these two probes. Some of our efforts are devoted to dedicated sample preparation and characterization from thin films and multilayers via nano-patterned structures to single crystals for a wide range of materials from metals to oxides.

Peter Grünberg Institut/ Institut for Advanced Simulation – Theoretische Nanoelektronik, Forschungszentrum Jülich

D. DiVincenzo, group leaders E. Pavarini, M. Wegewijs

The behavior of interacting electrons in nano-scale structures is a primarly focus. The Kondo effect, involving the interaction of an isolated spin impurity with conduction electrons, or the formation and transport of high-spin complexes forming spin quadripoles, are particular areas of expertise. Novel computational techniques permit accurate calculations with thousands of atoms, and in complex multi-functional perovskites.
Correlated electrons also form the basis of the physical creation of qubits, and the coherence and dynamics of such qubits, and mutiqubit systems, is being investigated.

Lehrstuhl für Festkörper- und Quantenchemie und Institut für Anorganische Chemie, RWTH Aachen

R. Dronskowski

The institute is specialized in the fields of synthetic and quantum-theoretical solid-state chemistry, bordering with materials science, solid-state and theoretical physics, crystallography, as well as quantum and computational chemistry. In detail, we synthesize novel, sometimes extremely sensitive, compounds and elucidate their compositions and crystal structures by means of X-ray and neutron diffractional techniques. The characterization of their physical properties, that is electronic transport and magnetism, also plays a very important role.
We regularly perform solid-state quantum-chemical calculations from first principles to yield the electronic (band) structures and, in particular, to extract the important chemical bonding information needed to thoroughly understand the interplay between chemistry and physics. Syntheses are theory-driven and experiments challenge theories.

Peter Grünberg Institut – Mikrostrukturforschung, Forschungszentrum Jülich

R. Dunin-Borkowski

The institute works on topical fields in solid-state physics. Strategically two directions are followed. Firstly, to make key contributions to the development and application of ultra-high resolution transmission electron microscopy, in particular to aberration-corrected electron optics for subangstrom structural and spectroscopic resolution. Secondly, to produce a number of selected material systems and to study their physical properties. Examples are high-temperature superconductors and the novel complex metallic alloys. The former provide the basis of our work on SQUID sensors and on ac-Josephson effect based Hilbert spectroscopy for the THz range.

II. Physikalisches Institut (IIA), RWTH Aachen

G. Güntherodt

Our research activities are focused on i) semiconductor-based spinelectronics, ii) “spin-momentum transfer torque” for magnetization switching in magnetic nanostructures, and on iii) nanomagnetism of magnetic heterointerfaces. These areas are based on our dedicated expertise in i) ultrafast pump-probe experiments of the all-optical or all-electrical type for investigating the electron spin dynamics in semiconductors, ii) patterning of magnetic nanostructures and high-frequency measurements of magnetization dynamics and its excitations and iii) nanomagnetic investigations of exchange-biased ferro-/antiferromagnetic interfaces for magnetization pinning in magnetic multilayers. - While all-optical schemes are applied to III-V semiconductors, the all-electrical methods open the path toward Si- or C-based spintronic devices. Both techniques allow us to inject and detect phase-triggered coherent spin packets, subject to manipulation by electric or magnetic fields, representing a basis for future quantum information processing.

Peter Grünberg Institut – Halbleiter-Nanoelektronik, Forschungszentrum Jülich

D. Grützmacher

The institute’s research activities are based on its competence in semiconductor heterostructure and nanostructure research, both in fundamental and device physics as well as in material and process development. They address three major fields. (1) Si-CMOS technology: novel materials and new device concepts are used to drive CMOS to its limits. (2) III-V and III-nitride semiconductors: high frequency devices are developed up to and into the terahertz range. (3) Nanostructures for quantum electronics: devices based on the tunneling effect and ferromagnetic/semiconductor hybrid structures are investigated, the latter particularly in view of spintronic applications.

Institut für Theoretische Festkörperphysik, RWTH Aachen

C. Honerkamp

The research groups in this institute study many-particle interactions in solids, ranging from quantum effects in magnetic systems over electron correlation effects leading to unconventional superconductivity and magnetism to the dynamics of structural phase transitions. Recent work has focused on interaction effects in graphene systems, topological insulators, pnictide high-temperature superconductors and chalcogenide phase-change materials. The powerful theoretical methods employed and developed here comprise quantum Monte Carlo techniques, the functional renormalization group, density-functional theory and molecular dynamics.

II. Physikalisches Institut (IIB) – Röntgenstreuung und Phasenumwandlungen, RWTH Aachen

U. Klemradt

Our research is centered at the investigation of nanoscale structures and fluctuations, with focus on nanoparticles, polymer-based nanocomposites and ferroic materials. Of particular interest are phase transitions in smart materials like shape memory alloys. The main experimental tools are X-ray scattering and acoustic emission spectroscopy. We use both laboratory tubes and synchrotron facilities for X-ray experiments and operate a 6-circle diffractometer at HASYLAB (DESY, Hamburg), which is especially suited to the analysis of thin films. Core techniques are small angle X-ray scattering (SAXS), grazing incidence scattering (GISAXS and reflectometry), and photon correlation spectroscopy using coherent X-rays (XPCS).

Institut für Anorganische Chemie – Molekularer Magnetismus, RWTH Aachen & Peter Grünberg Institut – Elektronische Eigenschaften (Molekularer Magnetismus), Forschungszentrum Jülich

P. Kögerler

The Molecular Magnetism Group focuses on the chemistry and fundamental physics of discrete and networked magnetically functionalized inorganic molecules. Based on its experience with the control and understanding of magnetic characteristics of purely molecular origin, the group synthesizes magnetic materials based on transition metal clusters that exhibit a complex interplay of charge transport and static/ dynamic magnetic properties such as phase transitions, hysteresis, or quantum tunneling. To functionally combine magnetic state switching and charge transport in systems for FIT spintronic devices, the molecule-surface interface is addressed, in particular employing surface structure-directed coupling reactions to molecular aggregates, single-stranded molecular conductors, or 2D networks.

Lehrstuhl für Technologie Optischer Systeme, RWTH Aachen (RWTH-TOS) & Fraunhofer-Institut für Lasertechnik, Aachen

P. Loosen

Extreme ultraviolet radiation (XUV, 1-50 nm, or EUV at 13.5 nm) enables new optical, analytical and manufacturing technologies because of its characteristic interaction with matter, its short wavelength and recent progress on light sources and optical components (e.g. EUV lithography). XUV tools are already deployed by the semiconductor industry, which significantly pushes the further development of XUV technology. Future applications which will support scientific progress in a variety of fields such as nanoelectronics or biotechnology are also within the scope of our research. Activities include structuring on a nanometer scale using interference lithography, XUV microscopy for imaging of dynamic processes or at-wavelength inspection of multilayer mask-blanks for hidden defects, and characterization of thin film coated surfaces using grazing-incidence reflectometry.

Institut für Physikalische Chemie (IPC), RWTH Aachen

M. Martin

The institute's research activities are based on its competence in the physical chemistry of solids with a special emphasis on defects and diffusion in inorganic solids, in particular oxides. Within JARA-FIT two major fields are addressed. (1) Ionic transport: transport of oxygen ions in the bulk, across and along grain boundaries and in space charge zones is investigated by means of secondary ion mass spectrometry (SIMS). (2) Electronic transport: amorphous and highly non-stoichiometric oxides are investigated concerning correlations between structure, electrical conductivity, and electronic structure. Insulator–metal transitions are studied with a view to applications in data storage.

GFE – Gemeinschaftslabor für Elektronenmikroskopie

J. Mayer

GFE is a central facility of RWTH Aachen University and has state-of-the-art equipment in the fields of transmission electron microscopy, scanning electron microscopy, electron microprobe analysis, focused ion beam instruments and atomic force microscopy. GFE provides services for a large number of institutes from RWTH Aachen University and a broad range of industrial companies. In the field of information technology, GFE participates in research projects on nonvolatile memories and on nanoscale CMOS devices. The head of the GFE is co-director of the Ernst Ruska Centre for Microscopy and Spectroscopy with Electrons and coordinates the RWTH user activities and contribution to the Centre.

Institut für Werkstoffe der Elektrotechnik 1 – Mikrostrukturintegration, RWTH Aachen

W. Mokwa

The institute's research activities are focused on the development of micro systems for medical and life-science applications. In particular different transponder-based systems for measuring intraocular and intravascular pressure were tested successfully. The EPIRET-implant for stimulation the retina of blind patients shows excellent results. For life science applications the focus is on micro fluidic applications for fluidic management and biological cell handling, development of sensors for fermentation processes in micro titer plates, micro electrodes for neuron cell stimulation, and on micro coils for mobile compact nuclear magnetic resonance devices. In 500 m^2 clean room thin-film-, assembly-, and testing processes can be carried out under DIN-ISO-9001:2000 requirements.

II. Physikalisches Institut (IIB) – Rastersondenmethoden, RWTH Aachen

M. Morgenstern

The research group develops scanning probe methods working in particular at low temperatures down to 0.3 K and in high magnetic fields up to 14 T in order to investigate the electronic structure of interacting electron systems and systems relevant for nanoelectronic applications. Thereby, we exploit the advantage of mapping the electronic structure down to the atomic scale at an energy resolution down to 0.1 meV, but also use the scanning probes for the excitement of the systems under study. Current topics of interest are graphene flakes and monolayers, quantum Hall physics in III-V-materials, confined wave functions in quantum dots, artificial spin chains, nanomagnetic systems, and phase change materials.

Peter Grünberg Institut – Bioelektronik, Forschungszentrum Jülich

A. Offenhäusser

Our research aims for the application of micro- and nanoelectronics to brain and life sciences. Research activities focus on two main topics: electromagnetic sensing and bioelectronic hybrid systems. This requires a better understanding of the interactions between biological systems and electronic substrates and the development of new technologies, resulting in new concepts of the interconnection of biological matter to electronic probes, and novel approaches to study cellular functions at the micro- and nanoscale. Here, we aim at a better understanding of the physiological behavior and mechanisms of neuronal information processing and new tools for diagnostics and imaging.

Institut für Kristallographie, RWTH Aachen

G. Roth

The institute's research profile covers the topics synthesis, structure and properties of novel materials. The synthetic activities include the preparation of new or crystal-chemically modified compounds with interesting properties in bulk poly- or single-crystalline form. Crystal and magnetic structures are studied by powder and single crystal X-ray as well as neutron diffraction methods (outstation at FRM-II/Garching) with special emphasis on complex, defect dominated systems such as partially disordered, incommensurately modulated structures and composite crystals. Among the materials recently studied are superconductors (modulated CaAlSi), fullerenes (C_70 high pressure polymer), spin-chain-compounds (vanadates and cuprates) and pyroxene-type multiferroics.

Peter Grünberg Institut – Elektronische Eigenschaften, Forschungszentrum Jülich

C. M. Schneider

The institute is engaged in the study of electronic and magnetic phenomena in novel materials and is one of the birthplaces of magnetoelectronics. Present research concentrates on the fundamental aspects, properties, and control of spin-transfer processes. The activities cover several facets, e.g., the development of new magnetic materials or the engineering of interfaces to improve the spin injection efficiency. Further important research fields comprise nanomagnetism and nanospintronics, which may form a bridge to quantum information processing. To this end new techniques and procedures are being established. Spintronics is also firmly linked to the condensed matter program, providing access to and knowledge about new material classes for use in the spintronics activities of the present program.

Institut für Theorie der Statistischen Physik, RWTH Aachen

S. Andergassen, V. Meden, H. Schoeller, J. Splettstösser, M. Wegewijs

The members of the institute are investigating the spectral and transport properties of low-dimensional quantum systems in contact with heat and particle reservoirs. The research focuses on the development of many-body methods for strongly correlated mesoscopic systems in nonequilibrium (quantum field theory and renormalization group in nonequilibrium) as well as on the application to experimentally realizable physical systems like semiconductor quantum dots, quantum wires (e.g. carbon nanotubes), and molecular systems.

Institut für Anorganische Chemie (IAC), RWTH Aachen

U. Simon

Our research is devoted to the preparation, characterization and assembly of electrically functional molecules as well as ligand stabilized metal- and semiconductor nanoparticles. We focus on fundamental questions related to the size and ligand-dependent properties of the prepared nanoparticles with respect to the uptake mechanism into cells, the impact on relevant biological systems and their use in nanoelectronics. Investigations related to the assembly in one, two and three dimensions and the electrical characterization of the formed nanostructures by means of local probe measuring techniques are performed in this context. A further topic is the formation of anisotropic nanostructures, like nanopillars, of controlled size and shape utilizing nanosphere lithography (NSL) in combination with reactive ion etching.

II. Physikalisches Institut (IIB) – Kohlenstoff-Nanoelektronik, RWTH Aachen & Peter Grünberg Institut – Halbleiter-Nanoelektronik, Forschungszentrum Jülich

C. Stampfer

The research group focus on studying electronic and mechanical properties of carbon-based systems that have critical dimensions on the nanometer scale. Such structures approach the atomic scale and the ultimate limit of solid state miniaturization. In particular we investigate systems based on nanostructured graphene (a monoatomic sheet of graphite) and carbon nanotubes. Current interests include (i) developing advanced processing technologies for fabricating novel nanodevices, (ii) understanding new and interesting transport phenomena that arise in these devices, and (iii) learning how to control and detect the charge, spin and mechanical degrees of freedom in these systems. Potential applications include ultra-fast electronics, new spin-based nanoelectronic device concepts and applied quantum technology.

Peter Grünberg Institut – Funktionale Nanostrukturen auf Oberflächen, Forschungszentrum Jülich

S. Tautz

Our research tackles fundamental issues in the quest towards functional nanostructures at surfaces, with a particular emphasis on nanoelectronics. Since our focus is placed on molecular materials, an important aspect of our work covers the structural investigations and spectroscopy of complex molecular adsorbates on metal, semiconductor and insulator surfaces. Based on these interface studies, the growth of thin films and nanostructures is investigated. Here, our work is directed towards hybrid materials, comprising both organic and inorganic components. Charge transport being the most important function in the context of nanoelectronics, transport experiments on single molecules and nanostructures round off our activities. It is a specific asset of our institute that we combine well-established surface techniques with the development of new experimental methods.

Lehr- und Forschungsgebiet GaN-Bauelementtechnologie, RWTH Aachen

A. Vescan

The research activities of the GaN Device group are focused on the area of group-III nitride device and technology development. The activities include investigation and development of practical technological building blocks for electronic devices, but also address fundamental device issues and limitations. Currently, particular interest is given to high-frequency and high-power device applications, where scaling issues as well as robustness aspects are being investigated. Novel gate dielectric materials are being pursued and their interface properties to GaN are being investigated. Also, alternative heterostructure device concepts are being developed, aimed at enhanced linearity in high-frequency devices as well improved switching behavior in the high-power regime.

Institut für Werkstoffe der Elektrotechnik 2, RWTH Aachen & Peter Grünberg Institut - Elektronische Materialien, Forschungszentrum Jülich

R. Waser

We focus on the physics and chemistry of electronic oxides and organic molecules, which are promising for potential memory, logic, and sensor functions. Our research aims at a fundamental understanding of nanoelectronic functions based on ferroelectricity, piezoelectricity, space charge effects, and electrochemical redox processes and at the elucidation of their potential for future device application. For this purpose, our institute provides a broad spectrum of facilities ranging from dedicated material synthesis, atomically controlled film deposition methods, molecular self-assembly routes, and integration technologies, to the characterization of processes, structures, and electronic properties with atomic resolution.

I. Physikalisches Institut (IA), RWTH Aachen

M. Wuttig

The institute's research activities are focused on the development of novel materials for advanced optoelectronic applications. In particular, materials for optical and electronic data storage have been developed in the last few years. For this class of materials we developed design rules and an atomistic understanding of essential material properties. This work has enabled novel functionalities of phase change materials in applications as non-volatile memories. Organic materials are a second focus, where we work on routes to tailor material properties for optoelectronic applications ranging from displays, to solar cells and electronic devices.

The new Institute for Quantum Information

Hendrik Bluhm[1], David P. DiVincenzo[1,2], and Barbara M. Terhal[1]

[1]RWTH Aachen University
[2]Peter Grünberg Institut (PGI-2)/Institute for Advanced Simulation (IAS-3): Theoretical Nanoelectronics, Forschungszentrum Jülich

At the end of 2010, the new Institute for Quantum Information (IQI) was created within the Theoretical Condensed Matter group at RWTH Aachen. This Institute will be growing in 2011, and will undertake research in a broad range of topics in Quantum Information, going from fundamental theory to the conceptual and experimental problems involved in creating a functioning quantum computer. The work will be in close coordination with the Institute for Theoretical Nanoelectronics at Forschungszentrum Jülich.

The founding of the IQI has been marked by the arrival of three new prominent researchers in the field: Prof. Hendrik Bluhm from Harvard University, and Profs. Barbara Terhal and David DiVincenzo from IBM Research. The startup of the Institute is amply provided for by DiVincenzo's International Award for Research in Germany of the Alexander von Humboldt Foundation, and he is now the first JARA Professor of RWTH Aachen University and Forschungszentrum Juelich.

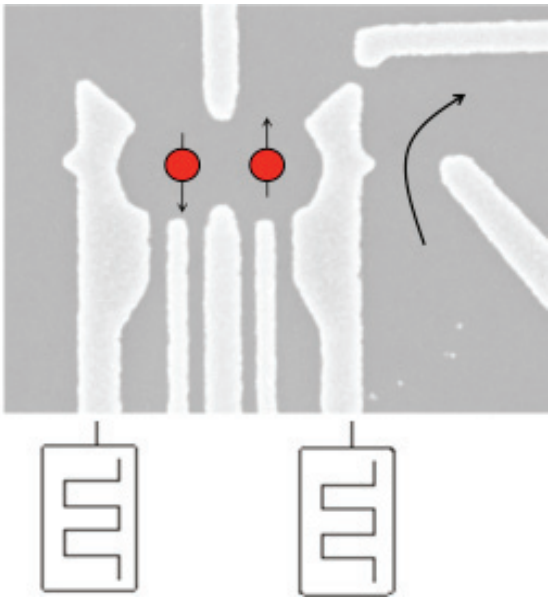

A central interest of this group is the realization of qubits in solid state structures. Bluhm is currently conducting experiments on spin qubits held within quantum dots in a GaAs heterostructure. The dots are defined and manipulated by metallic gates sitting atop the structure (Fig. 1). By exquisite control of the sea of nuclear spins present throughout the quantum dot structure, the electron spins can be maintained coherently for times much longer than their natural relation times, and quantum gates of good fidelity can be achieved.

The theorists of the IQI take inspiration from these experimental advances, and work on plans for new experiments to achieve greater functionality of quantum information processing in these sorts of systems. The possibilities for spin qubits, as envisioned by the theorists, are many: the control of nuclear spins must be further enhanced, possibly by the adoption of new materials techniques from, for example, the silicon/germanium heterostructure community; new couplers are needed to achieve entanglement between far-separated quantum dot structures; and schemes need to be worked out that would permit useful functionalities to emerge at structures with more (e.g., tens) of spin qubits, perhaps for the purpose of quantum simulation.

As more staff are added to the Institute, experimental attention is likely to extend beyond semiconductor qubits. The theoretical agenda already encompasses a much greater range of possibilities. DiVincenzo continues to be active with the group at IBM Research on the investigation of superconducting qubits, and their scaling up to arrays of modest size (8) within the coming years. Many issues of modelling and quantum control will be pursued in this area at the IQI.

It is clear that well controlled quantum measurements are very essential in quantum information processing. Terhal and DiVincenzo are now pursuing a study of the efficacy of weak measurement in quantum computing. Weak measurements do not give much information, but in their ideal form they also do not cause significant disturbance. The repeatability of these measurements gives they potential flexibility in quantum information problems. For example, it appears that measurements can be broken up into separate simpler pieces that can be done sequentially.

Selected Research Reports

Synthesis and Structural Characterization of Ultra-thin Flexible Gold Nanowires

A. Kisner[1], M. Heggen[2], K. Tillmann[2], Y. Mourzina[1], A. Offenhäusser[1]

[1]Peter Grünberg Institut-9, Forschungszentrum Jülich, Germany
[2]Peter Grünberg Institut-5, Forschungszentrum Jülich, Germany

Gold nanowires (AuNWs) were produced by electroless reduction of $HAuCl_4$ in a micellar structure formed by oleylamine and investigated by means of high-resolution transmission electron microscopy (HRTEM). Micrometer long ultra-thin flexible AuNWs with 1-2 nm diameter and AuNWs with about 12 nm diameter and a few hundred nm length were produced. In contradiction with previous work, the bodies of the 12 nm nanowires are defect-free along the axial direction, their extremities, however, show the presence of twin boundaries. Although AuNWs are stable in solution for months, they were found to be quite sensitive to electron beam irradiation during HRTEM experiments, with a tendency to break up into face centered cubic (fcc) Au droplets. It is proposed that the micellar configuration of oleylamine plays a fundamental role in the atomic arrangement of nanowires.

Au nanowires are one of the fundamental building blocks for the fabrication of nanodevices. The atomic structure of these nanowires plays a crucial role regarding their electromechanical properties. The synthesis of stable high aspect ratio ultra-thin Au nanowires with highly oriented structure remains challenging. A promising and pioneer successful wet chemical approach to produce micrometer long ultrathin gold nanowires was recently demonstrated by Halder et al., and subsequently by others in similar attempts [1]. However, a detailed investigation of the atomic structure of those nanowires has not been shown yet. Herein, we show that employing a similar approach, ultra-thin Au nanowires with average diameters of 1-2 nm and 12 nm can be produced by an electroless reduction of $HAuCl_4$ in a micellar structure formed by oleylamine. Using HRTEM we analyzed the structure of Au nanowires and nanoparticles that are produced together during the synthesis of AuNWs and are thought to be the "seeds" for the AuNWs growth. A model based on the micellar configuration of oleylamine to explain the observed atomic structure is proposed.

AuNWs were synthesized by dissolving 0.07 g of $HAuCl_4 \cdot 3H_2O$ in a mixed solution composed of 1 mL of oleylamine and 1 mL of hexane. To speed up the reaction the solution was added to a glass containing 9 mL of oleylamine at room temperature and the mixture was left undisturbed for 24 h. After that period, the solution was heated to 80°C for 5 h. The AuNWs were precipitated out by centrifugation and sequentially washed several times with ethanol and then redispersed in hexane.

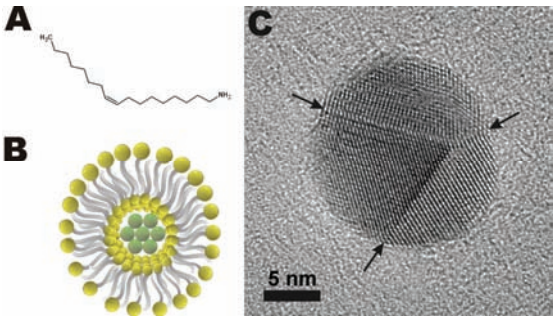

FIG. 1: A. Molecular structure of oleylamine. B. Illustration of the micellar configuration of oleylamine molecules surrounding a Au nuclei (green spheres).Yellow spheres represent the $-NH_2$ group, while the gray tails represent the hydrophobic chain of the molecule. C. HRTEM image of a gold nanoparticle with a spherical shape. Arrows indicate the twin boundaries.

Owing to their molecular structure, which is formed by a polar head group ($-NH_2$) and a hydrophobic tail, oleylamine molecules (Fig. 1A) can form inverted micelles, where the amine groups can coordinate and consequently reduce the gold ions (Fig. 1B) [2]. In the synthesis based on solution-phase, these reduced gold ions form small nuclei. After grown until a certain critical size, these nuclei present well-defined crystallographic facets and form crystalline seeds. The seeds can further grow into nanoparticles with several possible shapes, where the final shape of the particles is mainly defined by a minimization of the surface energy.

Figure 1C shows a HRTEM image of a Au nano-particle produced during the synthesis of AuNWs. The particle has a diameter of 11 nm and a spherical shape which minimizes the surface area and maintains a low surface energy. Twin boundaries are observed. During the synthesis the nanoparticles are capped with the oleylamine molecule, but the defects on their surface make them highly susceptible to localized oxidative etching by O_2/Cl^- [3]. This localized etching means that the etched face of the nanoparticle is activated and can consequently grow in one direction producing nanorods and nanowires. Figure 2 A shows an

electron micrograph of a nanoparticle and AuNWs at low magnification. Thick AuNWs of 10-14 nm in diameter as well as ultra-thin AuNWs with a diameter of 1-2 nm were found. The extremities of the thick nanowires often show a characteristic bulging.

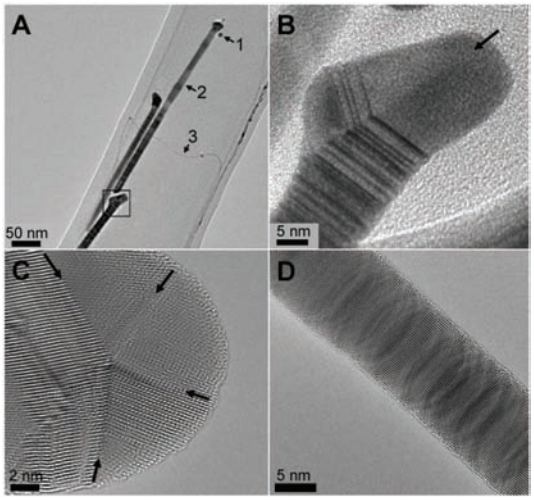

FIG. 2: A. Electron micrograph of AuNWs at low magnification. The arrows indicate a nanoparticle (1), a thick (2) and an ultra-thin AuNW (3). B. shows an enlarged image of an extremity of a thick AuNW which corresponds to the boxed section of A. The arrows point at a twin boundary. C HRTEM image of a AuNW extremity showing twin boundaries (arrows). D. defect-free body a AuNW.

Figure 2B shows an enlarged image of the extremity of the thick AuNW. The arrows point at a twin boundary. Figure 2C displays a HRTEM image of another AuNW extremity showing several twin boundaries. A HRTEM image of the body of a thick AuNW is displayed in Figure 2D which shows wavy contrast features. These are due to a bending of the nanowire along its long axis which causes a fluctuation of the high-resolution imaging conditions. Dislocations, stacking faults, twin boundaries or any other defects were not observed. In general, we have observed that the main bodies of the thick AuNW are defect-free and single crystalline. The observation of defect-free single-crystalline nanowires is in contradiction with investigations by Halder et al. [1], who proposed that AuNWs produced by this micellar approach follows an oriented attachment mechanism of growth. In that case, twin defects were seen along the growth direction of AuNWs. In fact, the experimental conditions used by Halder et al. involved more chemicals and higher temperatures than those used by us, and are likely the main reasons for the differences observed in the atomic structure of the nanowires. Additionally, in comparison with nanowires produced by hard-matter template approaches, the surface of the wires fabricated here is relatively smoother.

Figure 3A displays an electron micrograph showing a high density of ultra-thin AuNWs. The average diameter of such wires is 1-2. The wires are several micrometer long and highly flexible. The extremities of the ultra-thin AuNWs show qualitatively the same bulging like the thick AuNWs. In solution-phase the wires are stable for months, however, upon electron irradiation during HRTEM studies, the ultra-thin AuNWs degrade and break up into fractions. Figure 3B I-V shows a sequence of micrographs of the same ultra-thin AuNW taken at different magnifications during a time interval of about one minute demonstrating the degradation of the wire. Image IV shows a fragment of the nanowire at atomic resolution. The fragment is single crystalline and oriented along a [011] direction of its fcc structure. A spacing of 0.3 nm between atomic columns along the [011] direction was measured, which is in accordance to the [011] lattice spacing of 0.29 nm of the fcc-Au lattice.

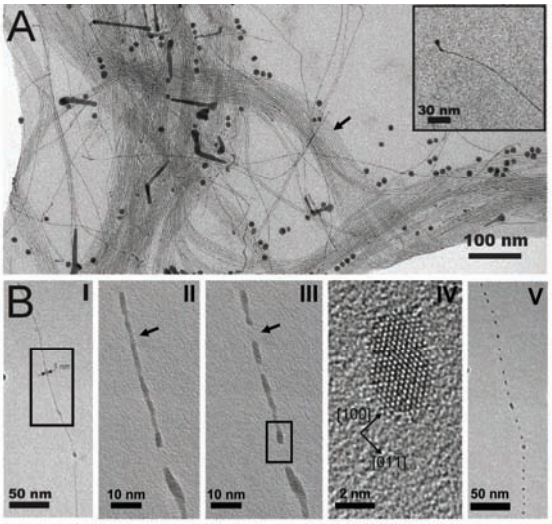

FIG. 3: A. Micrograph of bundles (arrow) of ultra-thin AuNWs. The inset shows the extremity of an ultra-thin AuNW. B. A sequence of HRTEM images with different magnification which shows the breaking (arrows) of a AuNWs under electron beam irradiation. The images II and III were taken from the boxed region of I. Image IV (the boxed region of III) shows a fragment of the nanowire at atomic resolution. The fragment is oriented along a [011] direction of the fcc-Au structure. Image V corresponds to image I after exposing the AuNW to the electron beam for about one minute and shows a chain of drop-like fractions of the wire.

Taking these observations into account, we consider that the oleylamine molecules with their micellar and tubular configuration have a fundamental impact on the atomic arrangement of the nanostructures observed here. That is, once the small nuclei start form, the shape of the subsequent nanocrystal is controlled by the organic molecule, which act as both a capping agent and a stabilizer that thermodynamically reduces the surface energy. Thus, the presence of this capping agent can avoid the formation of defects such as twins, stacking faults or dislocations along the AuNWs.

This work was supported by a research grant provided by Forschungszentrum Jülich.

[1] A. Halder, N. Ravishankar, Adv. Mater. 19, 1854 (2007).

[2] A. Kisner, S. Lenk, D. Mayer, Y. Mourzina, A. Offenhäusser, J Phys. Chem. C, 113, 20143 (2009).

[3] Y. Xiong and Y. Xia, Adv. Mater. 19, 3385 (2007).

Two-dimensional optical control of electron spin orientation by linearly polarized light in InGaAs

K. Schmalbuch[1], S. Göbbels[1], Ph. Schäfers[1], Ch. Rodenbücher[1], P. Schlammes[1],Th. Schäpers[2], M. Lepsa[2], G. Güntherodt[2], B. Beschoten[2]

[1]II. Institute of Physics, RWTH Aachen University, Otto-Blumenthal-Straße, 52074 Aachen, Germany
[2] PGI-8, Institute of Bio- and Nanosystems, Forschungszentrum Jülich, 52425 Jülich, Germany

Optical absorption of circularly polarized light is well known to yield an electron spin polarization in direct band gap semiconductors. We demonstrate that electron spins can even be generated with high efficiency by absorption of linearly polarized light in $In_xGa_{1-x}As$. By changing the incident linear polarization direction we can selectively excite spins in both polar and transverse directions. These directions can be identified by the phase during spin precession using time-resolved Faraday rotation. We find that the spin orientations do not depend on the crystal axes suggesting an extrinsic excitation mechanism.

The generation of spin-polarized charge carriers by optical orientation in non-magnetic semiconductors is well established. In optical orientation the angular momentum of circularly polarized photons will be transferred to electrons and holes during absorption [1]. This can result in a large spin polarization of 50% in bulk III-V semiconductors. Besides static imaging and probing of the spin polarization [2], optical pump-probe measurements using time-resolved Faraday rotation (TRFR) have become a standard method for both triggering and probing of spin coherence in semiconductors [3]. In contrast, optical absorption of linearly polarized photons should not result in net spin polarization as an equal number of spin-up and spin-down electrons and holes will be generated according to the standard theory.

The studies discussed here were performed on a 300 nm thick $In_xGa_{1-x}As$ (x = 4.9%) epilayer grown on semi-insulating (001) GaAs by molecular-beam epitaxy. The room temperature carrier density was set to $n \sim 3 \times 10^{16}$ cm^{-3} by Si doping to allow for long spin dephasing times at low temperatures. Phase triggering of electron spin coherence is achieved by either circularly or linearly polarized picosecond pump pulses. The incident polarization direction of the latter can be changed continuously by an angle φ as defined in Fig. 1(a). Spin precession is probed in a transverse external magnetic field B (oriented along the y direction) by a second time-delayed linearly polarized probe pulse using standard measurements of the TRFR angle Θ_F, which is a measure of the polar spin component s_z. Its time dependent evolution can be described by an exponentially damped cosine function

$$\Theta_F(\Delta t) = \Theta_0 \exp\left(-\frac{\Delta t}{T_2^*}\right)\cos\left(\omega_L \Delta t + \delta\right) \quad (1)$$

with amplitude Θ_0, transverse spin dephasing time T_2^*, Larmor frequency ω_L, time-delay Δt between pump and probe pulses and phase factor δ.

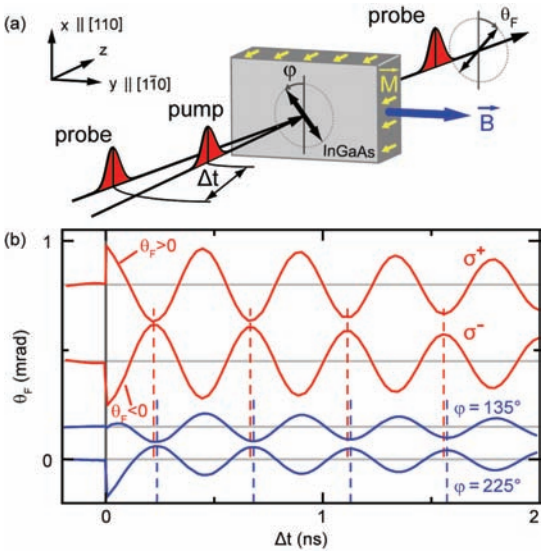

FIG. 1: (a) Setup for all-optical measurements of TRFR using linearly polarized pump pulses. The incident linear polarization direction can continuously be adjusted by the angle Θ_F (b) Comparison of TRFR after excitation by circularly [red curves] and linearly [blue curves] polarized pump pulses. Data are taken at $T = 30$ K in a transverse magnetic field of 0.5 T. The dashed vertical lines indicate a phase shift in the precession between circular and linear excitation. A vertical offset is added for clarity.

Fig. 1(b) depicts TRFR measurements after optical excitation with both circularly and linearly polarized pump pulses using a laser energy near the fundamental band gap of the InGaAs layer. Data were taken at $T = 30$ K and B = 0.5 T. When using circularly polarized light the angular momentum of the photon will be absorbed during interband absorption resulting in spin-polarized electrons and

holes. By changing the light helicity from σ^+ to σ^-, we can control the initial spin orientation between parallel and antiparallel alignment relative to the incident light propagation direction ($\pm$ z direction). The resulting TRFR measurements are depicted in Fig. 1(b) [red curves] for σ^+ and σ^- laser excitation under nearly normal incidence. The change of the initial spin orientation is easily seen by a sign change of Θ_F right after excitation ($\Delta t = 0$ ns). When using linearly polarized pump pulses, no net spin polarization is expected. In Fig. 1(b) we show TRFR data taken for normal incidence at two distinct polarization angles of linearly polarized pump pulses, which differ by 90° [blue curves]. We, however, clearly observe spin precession [4]. Surprisingly, the amplitude is only slightly reduced compared to the curves taken under σ^+ and σ^- excitation demonstrating that optical orientation of electron spins by linearly polarized light is strikingly efficient. Note that spins of opposite directions can be excited when changing the polarization by 90° from 135° to 225° and switches furthermore sign every 90° rotation.

The sign reversal is further described in Fig. 2(a), where the polarization angle resolution is enhanced in a regime of sign reversal. It is clearly seen that spin precession is observed at all angles. The sign reversal of Θ_F between point A (red color code $\Theta_F > 0°$) and point B (blue color code $\Theta_F < 0°$) is accompanied by a continuous change of the phase δ of the precessing spins. The phase can be extracted from fitting all TRFR traces in Fig. 2(a) using Eq. 1. As seen in Fig. 2(b), the phase continuously changes from -180° to almost 0° within a small range of linear polarization angles. We want to emphasize that in our polar configuration we only probe spins, which have a finite projection along the $\pm z$ axis. For $\delta = 0°$, spins are oriented in the polar + z direction at $\Delta t = 0$, which results in a TRFR curve starting in a positive maximum [see also Fig. 2(c)]. On the other hand, spins are oriented in the -z direction for $\delta = -180°$. This explains the sign reversal between points A and B in Fig. 2(a). In contrast, for a phase of $\delta = -90°$ spin precession starts with $\Theta_F = 0°$ at $\Delta t = 0$, which is illustrated in Fig. 2(c). This unambiguously demonstrates that spins will be oriented along the x axis (transverse to both incident light direction and magnetic field direction) at the respective linear polarization angle. It is important to note that the excitation of transverse spins is unique to the optical orientation with linearly polarized light. It cannot be observed for excitation with circularly polarized light. Knowing that we can excite both polar and transverse spins with linearly polarized light, we can now decompose the projections for any polarization angle along the polar and the transverse direction using $\Theta_p = \Theta_0 \cos\delta$ and $\Theta_t = \Theta_0 \sin\delta$, respectively. As shown in Fig. 2(d), polar and transverse spin signals change sign at different pump polarization angles. By carefully adjusting the polarization angle φ we achieve a full two-dimensional control over the initial spin orientation, which cannot be realized by any other electrical or optical technique.

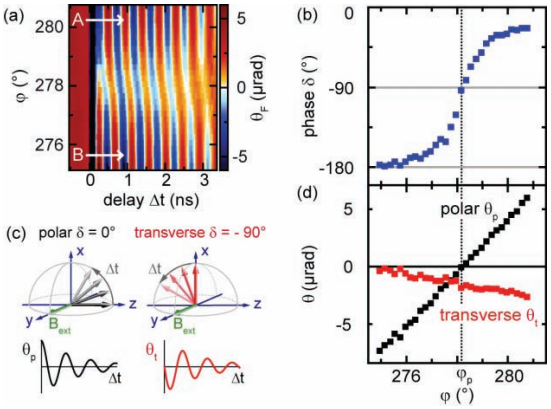

FIG. 2: (a) TRFR for optical excitation with linearly polarized laser pulses measured in n-InGaAs at T = 30 K and B = 0.5 T for φ = 275° – 281°. The sign reversal is accompanied by a continuous phase shift of the precessing spins. (b) Phase of precessing spins at different incident light polarization angles φ near a sign reversal. (c) Illustration of spins oriented in polar and transverse direction and respective TRFR curve as expected in the polar observation direction. According to the measured phase, Θ_F will be decomposed into polar and transverse amplitudes plotted in (d) as a function of incident laser polarization angle.

In conclusion, we have demonstrated that optical orientation of electron spins by linearly polarized light is very effective. By the phase during spin precession we can unambiguously prove that spins can be generated in both polar and transverse directions. Surprisingly, the spin orientation is independent of the in-plane crystallographic directions of the sample [4], pointing to an extrinsic origin of the optically generated spin polarization.

Work supported by DFG through FOR 912.

[1] I. Žutić, J. Fabian, and S. Das Sarma, Rev. Mod. Phys. **76**, 323 (2004).

[2] S.A. Crooker and D.L. Smith, Phys. Rev. Lett. **94**, 236601 (2005).

[3] J.M. Kikkawa and D.D. Awschalom, Nature (London) **397**, 139 (1999).

[4] K. Schmalbuch *et al.*, Phys. Rev. Lett. **105**, 246603 (2010).

Phase-Coherence and Spin-Orbit Coupling in InAs Nanowires

S. Estévez Hernández[1], M. Akabori[1], K. Sladek[1], Ch. Volk[1], S. Alagha[1], H. Hardtdegen[1], M. G. Pala[2], J. Schubert[1], M. Schnee[1], N. Demarina[1], D. Grützmacher[1], Th. Schäpers[1]

[1]Peter Grünberg Institut (PGI-9): Semiconductor Nanoelectronics, Forschungszentrum Jülich, 52425 Jülich, Germany
[2]IMEP-LAHC, UMR 5130, MINATEC, Grenoble INP, 3 Parvis Louis Néel, BP 257, 38016 Grenoble, France

The phase-coherence and spin-orbit coupling in InAs nanowires is investigated by means of interference experiments, i.e. universal conductance fluctuation and weak anti-localization measurements. The InAs nanowires were grown by selective area metal-organic vapor-phase epitaxy. Control of the electron interference is achieved by applying a magnetic field or by using a top- or back-gate electrode. For the phase-coherence length a values of several 100nm was found at temperatures below 1 K, while for the spin-orbit scattering length a value of 70nm was extracted from the comparison with theoretical calculations.

Due to their small dimensions, semiconductor nanowires offer an exciting route to study charge or spin related interference effects in the low-temperature electron transport [1]. By choosing the narrow-band-gap semiconductor InAs as a material for the nanowire, the common problem connected with carrier depletion at the surface can be avoided. In fact, due to the Fermi level pinning within the conduction band at the surface an electron accumulation layer is formed. In addition, the strong electric field, resulting from the modulation of the potential profile at the surface is expected to lead to a pronounced Rashba spin-orbit coupling. The latter effect is interesting for spinelectronic devices, since it would allow the control of the spin orientation by electrical means, i.e. by a gate electrode. Here, we investigated the phase-coherence and spin-orbit coupling in InAs nanowires by means of electron interference experiments.

The InAs nanowires were selectively grown on a patterned GaAs (111)B substrate by low-pressure metal-organic vapor phase epitaxy in an N_2 atmosphere at a temperature of 650 °C. The wires have a diameter *d* of approximately 100nm. For the transport measurements the nanowires were contacted individually by Ti/Au electrodes using electron-beam lithography. Gate control was achieved either by using the highly-doped Si substrate as a back-gate or by using additional top-gate electrodes defined by electron beam lithography. In the latter case, a novel approach was utilized for the gate isolation by employing $GdScO_3$ and $LaLuO_3$ as a high-*k* dielectric [2,3]. The advantage of $GdScO_3$ and $LaLuO_3$ is their high dielectric constant, i.e. k = 22 and 30, respectively, which is expected to allow a gate control at lower gate voltages compared to more common dielectrics, e.g. SiO_2, with comparable layer thickness. For a complete coverage of the nanowire by the high-*k* dielectric, pulsed laser deposition was employed.

In Fig. 1(a) a scanning electron micrograph of an InAs nanowire covered by a 1.6µm long gate is shown. As illustrated in Fig. 1(b) for gate isolation a 10nm thick $LaLuO_3$ layer was used. As can be seen from the output characteristic shown in Fig. 1(c), an efficient gate control of the nanowire conductance is achieved by this approach [3].

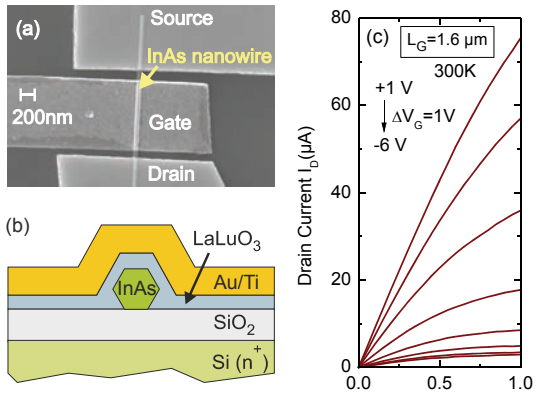

FIG. 1: (a) Scanning electron beam micrograph of an InAs nanowire field-effect transistor with a 1.6µm long gate. (b) Schematics of the transistor cross-section. (c) Output characteristics of the field-effect transistor with a 1.6µm long gate at room temperature.

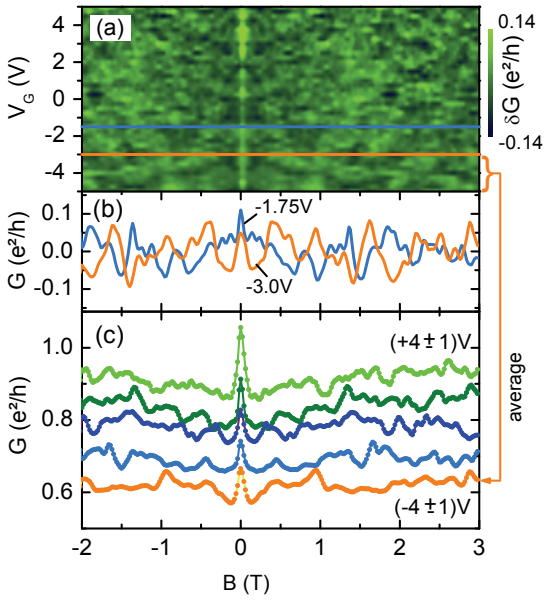

FIG. 2: (a) Color-scaled conductance as a function of magnetic field and gate voltage at 0.5 K. The trace of the conductance fluctuations shown in (b) are indicated by the horizontal lines. (b) Magnetoconductance at 0.5K at V_G=−1.75V (light blue curve) and at −3.0V (orange curve). (c) Averaged magnetoconductance corrections for fluctuation measurements within a 2V wide gate-voltage interval.

On back-gated InAs nanowires the magneto transport was investigate at temperatures as low as 0.5K [4]. As can be seen in Fig. 2(a), the nanowire conductance fluctuates as a function of magnetic field B and gate voltage V_G. From the correlation field B_c at different gate voltages information on the phase-coherence length was obtained. It is found that l_ϕ is relatively large in the order of several 100nm and slightly increases with increasing the gate bias from -5V to +5V. The latter effect can be attributed to the decrease of electron-electron scattering with increasing carrier concentration.

Information on the spin-orbit scattering length l_{so}, which is a measure for the strength of spin-orbit coupling, can be obtained from weak antilocalization measurements. The signature of this effect is a conductance maximum at zero magnetic field. However, as can be seen in Fig. 2(b), the pronounced conductance fluctuations prevent to observe any antilocalization effect. Nevertheless, by averaging the conductance fluctuations over a gate voltage range of 2V, these conductance fluctuations can be suppressed. As can be seen in Fig. 2(c), now a clear conductance peak is resolved at zero magnetic field, indicating the presence of weak antilocalization.

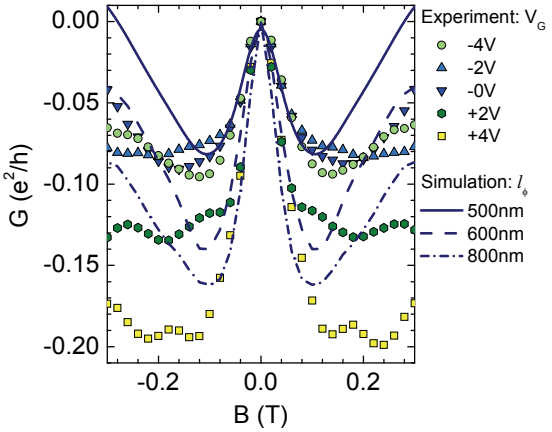

FIG. 3: Averaged magnetoconductance corrections for fluctuation measurements within a 2V wide gate-voltage interval (dots). The center-gate voltages of the intervals are: +4, +2, 0, −2, −4V. The lines represent the corresponding simulations.

So far, no theoretical model is available, which describes the weak antilocalization effect in conductors of circular geometry. In order to obtain information on the phase coherence length l_ϕ and the spin orbit scattering length l_{so}, simulations based on a recursive two-dimensional Green's-function approach were performed. The corresponding simulation results can be seen in Fig. 3. From the comparison with the experimental data one finds that the spin-orbit scattering length is relatively short, i.e. 70nm, indicating a strong spin-orbit coupling.

Our results show that InAs nanowires are interesting candidates for the realization of nano-electronic devices based on electron interference as well as on spin-related effects.

[1] C. Thelander, P. Agarwal, S. Brongersma, J. Eymery, L. Feiner, A. Forchel, M. Scheffler, W. Riess, B. Ohlsson, U. Gösele, and L. Samuelson, Mater. Today **9**, 28 (2006).

[2] C. Volk, J. Schubert, K. Weis, S. Estévez Hernández, M. Akabori, K. Sladek, H. Hardtdegen, and Th. Schäpers, Appl. Phys. A, **100**, 305 (2010)

[3] C. Volk, J. Schubert, M. Schnee, K. Weis, M. Akabori, K. Sladek, H. Hardtdegen, and Th. Schäpers, Semicond. Sci. Technol. **25**, 085001 (2010)

[4] S. Estévez Hernández, M. Akabori, K. Sladek, Ch. Volk,1 S. Alagha, H. Hardtdegen, M. G. Pala, N. Demarina, D. Grützmacher, and Th. Schäpers, Phys. Rev. B **82**, 235303 (2010)

Self-catalyzed Growth of InAs Nanowires for Nano-devices

Th. Grap[1], F. Haas[1], T. Rieger[1],Ch. Blömers[1], K. Sladek[1], A. Winden[1], M. v.d. Ahe[1], Th.E. Weirich[1,2], M. I. Lepsa[1], H. Hardtdegen[1], D. Grützmacher[1]

[1]Peter Grünberg Institute 9: Semiconductor Nanoelectronics, Forschungszentrum Jülich, 52425 Jülich
[2]Central Facility for Electron Microscopy, RWTH Aachen University

The self catalyzed molecular beam epitaxy (MBE) and metalorganic vapor phase epitaxy (MOVPE) of InAs nanowires (NWs) are presented. The preparation conditions and the morphological and structural properties of the NWs grown by the two techniques are compared. For both situations, the growth temperatures are quite similar to those employed for layers. However, the structural and morphological characteristics differ quite strongly indicating different growth mechanisms.

The growth of III-V semiconductor nanowires (NWs) has received attention due to their self-organized, bottom up formation without the surface damage expected in similar structures obtained by etching, in a top down approach. In particular, InAs NWs are of special interest for potential applications due to their electronic and spin-related properties. Usually, gold particles are used to catalyze the InAs NW growth. Their size and location determine the diameter and position of the NWs. However, this implies the risk of gold incorporation into the NWs during growth. For MOVPE, in most of the cases, much lower growth temperatures have been used for NWs compared to those of layers. In these conditions, carbon can be additionally incorporated. Both impurities are detrimental to the transport properties of the wires. Therefore, the investigation of self-catalyzed growth processes is attractive with respect to nano-device applications. Here we report on a comparative study of InAs NWs self-catalyzed MBE and MOVPE growth.

The InAs nanowires were grown on (111)B GaAs substrates which were masked using spin-coated hydrogen silsesquioxane (HSQ). An annealing step converts HSQ to amorphous SiO_x. Before MBE growth, the oxide layer was superficially wet chemically etched in very diluted HF so that pin holes are formed. For MOVPE growth, the SiO_x layer was structured in hole arrays using electron beam lithography and reactive ion etching.

MOVPE In contrast to other groups, N_2 was used as the carrier gas for InAs NW growth [1]. The influence of temperature (T_G) was studied on growth in the range of 550°C to 700°V. The wires grow catalyzed by the substrate in (111) direction. High aspect ratios of 80 are achieved for $T_G \geq 650$°C as presented in Fig.1. The smallest diameters for this aspect ratio are obtained at 650°C. It is demonstrated that the volume of the NWs remains constant for $T_G \geq 600$°C. Here growth is determined by gas phase diffusion of the reactive species. At $T_G \leq 650$°C, the selectivity of growth on different facets becomes less pronounced owing to a lower surface diffusion length. The optimal T_G 650°C is similar to temperatures used for InAs layer growth. The ratio of group V to group III source partial pressure (V/III ratio) was varied from 55 to 220. It has no influence on the morphology. The NWs grow at a rate of about 1.2 µm/min and are depicted in Fig. 2a at two different magnifications. Perfect selectivity and high shape uniformity are found from wire to wire and along the wire. The tips of the wires exhibit faceting (inset). The optimum T_G and V/III ratio for InAs NWs grown using H_2 carrier gas has been reported to be below 600°C and 27 [2], respectively, and is much lower than for our wires. Our growth process should be therefore advantageous with respect to conductivity control.

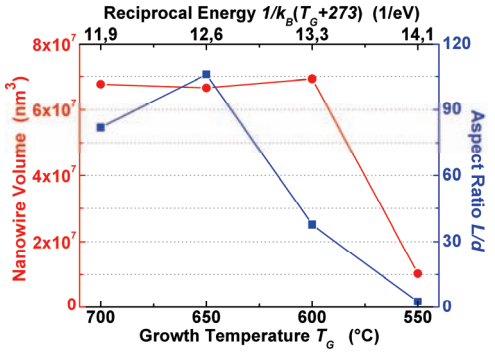

FIG. 1: MOVPE grown InAs nanowire volume (red) and aspect ratio L_{mean}/d_{mean} (blue) as a function of growth temperature.

The NWs exhibit a large amount of stacking faults as demonstrated in Fig. 3a [3]. A rapid succession of zinc blende (ZB) and wurtzite (WZ) regions is observed.

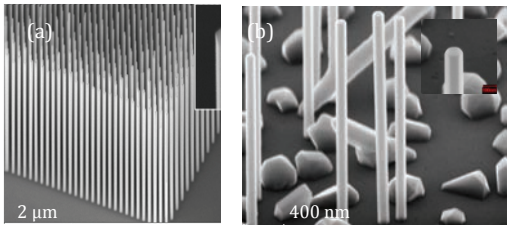

FIG. 2: Scanning electron micrographs presenting the morphology of NWs produced by MOVPE (a) and MBE right at optimized growth conditions. The MOVPE grown wires exhibit faceting at the top whereas a droplet is observed for the MBE grown wires (insets).

MBE Systematic investigations for different growth parameters and time have been carried out for the growth of InAs NWs by MBE [4, 5]. The results demonstrate that growth proceeds via the vapor-liquid-solid (VLS) mechanism from In droplets which develop at the beginning and are situated over the pre-existing pinholes in HSQ (see Fig.2b inset). The density and diameter of the NWs are very sensitive to the surface preparation. They grow perpendicular to the substrate indicating the crystallographic relation to the (111)B surface and preferential growth direction. The NWs have a hexagonal prism morphology, with the facets pertaining to the {110} family and are not tapered (see Fig.2b). A T_G window between 470 °C and 530 °C has been identified [4]. As seen in Fig. 2b, apart from NWs, also crystallites grow on the surface. Outside the T_G range mentioned above, for lower T_G, the number of crystallites increases and they coalesce hindering the NW growth and for higher T_G, In evaporates before the droplets can form. The length and diameter of the NWs increase linearly with time and are influenced evidently by the beam fluxes. As the In beam flux increases, the nanowire length increases at first before it becomes constant, while the diameter increases almost linearly. Concerning the As beam flux influence, two different behaviours can be distinguished. At lower As fluxes, the length increases and the diameter decreases linearly with As flux, as long as the droplet is maintained. At higher As fluxes, these two NW characteristics behave inversely. This may indicate that the In droplet at the NW tip vanishes and that the sink for In adatoms disappears. Then all the atoms impinging on the NW surface contribute to radial growth instead of axial growth. The optimum growth conditions, which result in high aspect ratio NWs, correspond to V/III ratios in the range of 6-8 and a T_G of 530°C (see Fig. 4) [5]. The corresponding growth rate is ~0.8 µm/h. A kinetic model was developed the results of which agree well with the experimental data and confirm the VLS growth mechanism. Regarding axial growth, the model reveals a low diffusion rate of the group III element from the substrate but a significant one from the NW side walls to the top and no As diffusion. The crystallographic structure, determined by transmission electron microscopy (TEM), is ZB with rotational twins (see Fig. 3 b). A comparison was made of InAs NW self-catalyzed growth.

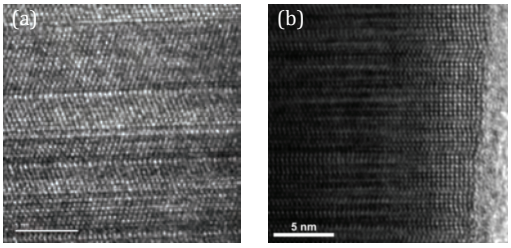

FIG. 3: transmission electron micrographs showing the structure of InAs NWs deposited by MOVPE (a, alteration ZB/WZ) and MBE (b, ZB with twinning).

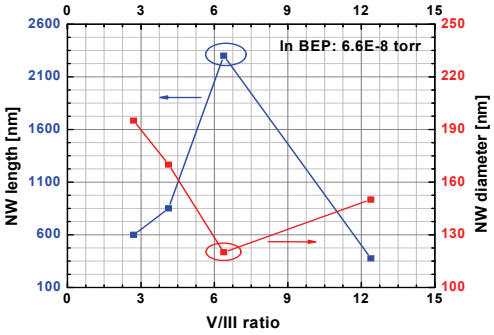

FIG. 4: MBE grown *InAs NW length and diameter as a function of the V/III ratio for constant In beam flux.*

The catalysis of MOVPE NW growth is induced by the substrate surface whereas it is determined by an In-droplet in MBE. The growth rate in MOVPE was higher by approximately two orders of magnitude. The growth of high aspect ratio NWs is determined by gas phase diffusion and surface diffusion along the substrate and the NW sidewalls. In contrast MBE growth could be explained by a surface kinetic model. Different crystallographic structures were observed: a fast alternating sequence of ZB/WZ for MOVPE and only ZB with rotational twins for MBE. How this influences the electrical properties of the NWs still needs to be studied.

[1] M. Akabori, K. Sladek, H. Hardtdegen, Th. Schäpers, D. Grützmacher, Journal of Crystal Growth **311**, 3813 (2009)

[2] K. Tomioka, P. Mohan, J. Noborisaka, S. Hara, J. Noborisaka, S. Hara and T. Fukui, J. Crystal Growth **298**, 644 (2007)

[3] K. Sladek, A. Penz, K. Weis, St. Wirths, C. Volk, S. Alagha, M. Akabori, S. Lenk, M. Luysberg, H. Lüth, H. Hardtdegen, Th. Schäpers and D. Grützmacher, Mater. Res. Soc. Symp. Proc. Vol. 1258-P02-05 (2010)

[4] M. I. Lepsa, C. Blömers, Th. Grap, S. Lenk, Th, Schäpers, H. Lüth, and D. Grützmacher, Proceedings of ISCS 2010, pp. 364

[5] M. I. Lepsa, Ch. Blömers, Th. Grap, S. Lenk, Th, Schäpers, H. Lüth, and D. Grützmacher, Proceedings of MBE 2010 Conf., P1.22 on CD.

Time-dependent transport: Interaction-induced adiabatic current

M.R. Wegewijs[1,2] , F. Reckermann[1], J. Splettstoesser[2]

[1] PGI-2: Peter Grünberg Institute, Forschungszentrum Jülich, 52425 Jülich
[2] Institute for Theory of Statistical Physics, RWTH Aachen University

We calculate the *time-dependent* transport current through a quantum dot *adiabatically driven* by a phase-shifted gate and bias voltage. We show that the additional dc current due to retardation of the quantum dot state is entirely generated by the electron-electron interaction. Lock-in measurement of this adiabatic dc current enables a "time-averaged" extension of non-linear transport spectroscopy which can probe effects of interactions, tunnel asymmetries and even the change in the ground state spin-degeneracy *without a magnetic field*.

Transport through nano-scale devices modulated by time-dependent applied electric fields is an active field of research important for transport spectroscopy and manipulation of the charge and spin degrees of freedom in nano-structures. A particularly gentle way of time-dependently probing a system is through "adiabatic pumping" [1]. Here a finite dc current is generated in the absence of an applied bias by a weak, low frequency periodic modulation of system parameters. Adiabaticity in a transport situation means that many electrons visit the system during one cycle of the driving with frequency Ω and that the modulation is too weak and too slow to excite the device by direct state-to-state transitions. In this report we analyze an interacting quantum dot in the single-electron tunneling (SET) regime, adiabatically driven by out-of-phase gate and bias potentials. In contrast to previous works, the applied bias can be arbitrary, i.e., we modulate the parameters around a *non-equilibrium steady state* supporting a finite dc current. We show that the strong local interaction *generates* an additional adiabatic dc current, which is identically zero without interaction for any value of the applied voltages and magnetic field. This adiabatic dc current can be measured using lock-in techniques and used for a new type of non-linear transport spectroscopy: plotted as function of the time-averaged gate and bias voltage, it gives rise to a new type of "stability diagram", which is a central tool in quantum transport measurements. We consider a quantum dot weakly tunnel coupled to two electrodes and capacitively coupled to a gate in the common situation where a single orbital level with strong Coulomb interaction U is dominating the transport. The gate and bias voltage are modulated with frequency Ω around the working point specified by the voltages $\bar{V}_g$ and $\bar{V}_b$:

$$V_x(t) = \bar{V}_x + \delta V_x \sin(\Omega t + \varphi_x), \qquad x = b, g. \quad (1)$$

with $\varphi_b = 0$ and $\varphi_g = -\pi/2$. We denote the spin-resolved dot number operator by $n_\sigma = d_\sigma^\dagger d_\sigma$, where the spin $\sigma = \uparrow, \downarrow$ is quantized along the external magnetic field (if present). The Hamiltonian of the quantum dot reads $H_{\rm D}(t) = \sum_\sigma \varepsilon_\sigma(t) n_\sigma + U n_\uparrow n_\downarrow$. The energy of an electron created by $d_\sigma^\dagger$ equals $\varepsilon_\sigma(t) = -\alpha V_g(t) + \sigma B/2$ using the shorthand $\sigma = \pm 1$ for spin $\uparrow, \downarrow$. Importantly, the time-dependent gate voltage $V_g(t)$ capacitively modulates this energy with lever arm $\alpha < 1$. Furthermore, B is the Zeeman energy in units $e = \hbar = k_B = 1$. The many-body eigenstates of $H_D(t)$ are $|0\rangle$, $|\sigma\rangle = d_\sigma^\dagger |0\rangle$ with $\sigma = \uparrow, \downarrow$ and $|2\rangle = d_\uparrow^\dagger d_\downarrow^\dagger |0\rangle$ with energies 0, $\varepsilon_\sigma(t)$, $\sum_\sigma \varepsilon_\sigma(t) + U$, respectively. The time-dependent bias $V_b(t)$ enters through the electro-chemical potentials $\mu_r(t) = \pm V_b(t)/2$ of electrodes $r = L, R$, which are described by $H_{\rm E}(t) = \sum_{r,k,\sigma} \big(\varepsilon_k + \mu_r(t)\big) c_{rk\sigma}^\dagger c_{rk\sigma}$. Finally, $H_{\rm T} = \sum_{r,k,\sigma} t_r d_\sigma^\dagger c_{rk\sigma} + H.c.$ describes the tunneling between the dot and the electrodes, with tunnel coupling strength $\Gamma_r = 2\pi\rho_r |t_r|^2$, where t_r is the amplitude and ρ_r the density of states of electrode $r = L, R$. We define $\Gamma = \sum_r \Gamma_r$. We consider here the important case where the transport is affected dominantly through the modulation of the energy level positions $\varepsilon_\sigma(t)$ and the bias energy window $\mu_L(t) - \mu_R(t)$. Since the total Hamiltonian $H(t) = H_{\rm E}(t) + H_{\rm D}(t) + H_{\rm T}$ contains strong interaction on the dot, adiabatic time-dependence and a non-linear bias voltage we calculate the time-dependent occupation probabilities of the many-body dot states, $\mathbf{p}(t) = (p_0(t), p_\downarrow(t), p_\uparrow(t), p_2(t))$ from a master equation

$$\dot{\mathbf{p}}(t) = \int_{-\infty}^{t} dt' \mathbf{W}(t,t') \mathbf{p}(t'). \quad (2)$$

The kernel, $\mathbf{W}(t,t')$, accounts for changes of the dot occupations due to electron tunnel processes to/from the electrodes. Although it explicitly depends on both time arguments t and t' (in contrast to the time-independent case) it can be calculated perturbatively for slowly varying fields [2] and we restrict ourselves to the lowest order contributions in both the tunneling coupling (single-electron tunneling) and in the time-dependent perturbation of external system parameters (adiabatic driving). We consistently solve

the time-dependent kinetic equation by expanding it around the instantaneous reference solution and account to first order for the actual delay suffered by the system due to the finite rate of sweeping the voltages. The time-dependent current flowing from lead $r = L, R$ into the dot is found in a similar way and can be decomposed into two corresponding parts, $I_{t,r}^{(i)}$ and $I_{t,r}^{(a)}$. Averaging the two current contributions over a modulation cycle we obtain $\overline{I}_r^{(i/a)} = \frac{\Omega}{2\pi}\int_0^{\frac{2\pi}{\Omega}} dt\, I_{t,r}^{(i/a)}$. For small modulation amplitudes, $\overline{I}_r^{(i)}$ equals the dc current one would measure for time-independent voltages equal to $\overline{V}_g$ and $\overline{V}_b$. Plotting $d\overline{I}_L^{(i)}/d\overline{V}_b$ as function of these voltages, one obtains the standard Coulomb blockade stability diagram. The adiabatic correction to this current, $I_{t,r}^{(a)}$, vanishes in the limit $\delta V \Omega \to 0$. The quantity of central interest here, $\overline{I}_r^{(a)}$, is the additional dc current component due to the retardation of the quantum dot state. This quantity can be obtained experimentally, e.g., by subtracting from the total measured time-averaged current its low frequency limit. The time-dependent adiabatic current can be expressed in terms of the rates of change of the average instantaneous charge, $\langle n \rangle_t^{(i)}$, and the spin polarization due to the magnetic field, $\langle S_z \rangle_t^{(i)}$:

$$I_{t,r}^{(a)} = \frac{(\Gamma_r + \gamma_r)(\Gamma - \gamma) + \beta_r \beta}{\Gamma^2 - \gamma^2 + \beta^2} \frac{d}{dt}\langle n \rangle_t^{(i)}$$

$$+2\frac{(\Gamma_r + \gamma_r)\beta - \beta_r(\Gamma + \gamma)}{\Gamma^2 - \gamma^2 + \beta^2} \frac{d}{dt}\langle S_z \rangle_t^{(i)} \qquad (3)$$

where the prefactors in Eq. (3) contain

$$\gamma_r(t) = \tfrac{1}{2}\Gamma_r \sum_\sigma \left[f\left(\varepsilon_{\sigma r}(t)\right) - f\left(\varepsilon_{\sigma r}(t) + U\right) \right] \qquad (4)$$

$$\beta_r(t) = \tfrac{1}{2}\Gamma_r \sum_\sigma \sigma \left[f\left(\varepsilon_{\sigma r}(t)\right) - f\left(\varepsilon_{\sigma r}(t) + U\right) \right] \qquad (5)$$

and their sums $\gamma = \Sigma_r \gamma_r$, and $\beta = \Sigma_r \beta_r$, where $\sigma = \pm$ (corresponding to $\uparrow, \downarrow$) and $r = L, R$. All these quantities depend on time through the distance to resonance $\varepsilon_{\sigma r}(t) = \varepsilon_\sigma(t) - \mu_r(t)$ in the arguments of the Fermi-function $f(\omega) = (\exp(\omega/T) + 1)^{-1}$ with temperature T. From Eq. (3) we infer a necessary condition for a non-vanishing time-averaged adiabatic current which also holds for more complex systems: the adiabatic dc current $\overline{I}_L^{(a)}$ can only be non-zero if two resonance conditions for single-electron tunneling are satisfied *simultaneously*. If only a single resonance condition is satisfied (3) is a total time-derivative of a periodic function, resulting in a zero time-average. The resonances in $\overline{I}_L^{(a)}$ are thus located at resonance line *crossings* of the standard $d\overline{I}_L^{(i)}/d\overline{V}_b$ map. The prefactors in Eq. (3) reveal that the adiabatic dc current is *entirely induced by the Coulomb interaction* U: since the tunnel rates Γ_r and $\Gamma = \Sigma_r \Gamma_r$ are time-independent and $\gamma_r = \beta_r = 0$ for $U = 0$ the adiabatic current $I_{t,r}^{(a)}$ is a total time-derivative, which, integrated over a period, yields $\overline{I}_r^{(a)} = 0$. This result can in fact be proven rigorously for any order in the tunnel coupling Γ, i.e., beyond the weak coupling regime considered here.

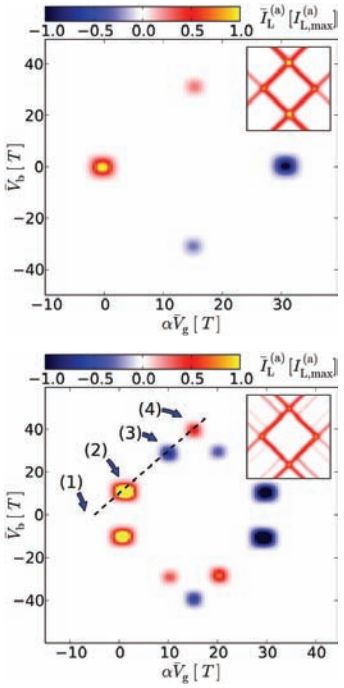

In the experimentally important regime of strong local interaction *U»T»Γ* the dependence on the time-averaged gate and bias voltage for zero magnetic field is plotted in the upper Figure as a *time-averaged* stability diagram. In contrast to the standard ($d\overline{I}_L^{(i)}/d\overline{V}_b$) stability diagram shown in the inset this map of pumped current indeed shows resonant enhancements only at discrete points of size $\propto T$ where two SET resonances meet. The occurrence and sign of adiabatic dc current at a charge degeneracy point can be tied to the change in spin-degeneracy in the ground state: the sign is positive (negative) if the ground state spin-degeneracy increases (decreases) with the quantum dot charge and it vanishes if there is no change. The time-averaged stability diagram thus directly reveals non-degenerate ground states if $\overline{I}_L^{(a)}$ vanishes in the linear response regime. Indeed, in the lower panel for a magnetic field *B»T* the adiabatic dc current is completely suppressed in the linear response regime $\overline{V}_b$*»T* marked by (1). The additional features marked (3-4) sensitively depend both in sign and magnitude on the asymmetry of the coupling Γ_L/Γ_R.

[1] P.W. Brouwer, Phys. Rev. B 58, R10 135 (1998)

[2] J. Splettstoesser et al., Phys. Rev. B 74, 085305 (2006)

Strained (Si/$Si_{1-x}Ge_x$) heterostructure Tunnel-FETs and MOSFETs

M. Schmidt[1], R. A. Minamisawa[1], W. Yu[1], S. Richter[1], B. Zhang[1], S. Lenk[1], M. Luysberg[2] , R. Luptak[1], D. Buca[1], Q. T. Zhao[1], S. Mantl[1]

[1]Peter Grünberg Institute 9 (PGI 9), Forschungszentrum Jülich, 52425 Jülich, Germany
[2]Peter Grünberg Institute 5 (PGI-5), Forschungszentrum Jülich, 52425 Jülich, Germany

Two different field effect devices based on high mobility compressively strained SiGe layers are presented. First, planar band-to-band Tunnel-FETs with different Ge atomic concentrations are compared. Then, quantum well strained Si /strained $Si_{0.5}Ge_{0.5}$ /strained Si *p*-type MOSFETs are investigated. The devices integrate high mobility SiGe channels with novel $GdScO_3$ and $LaLuO_3$ high-k dielectrics.

I. Band-to-band tunneling FETs

Band-to-band tunnel field effect transistor (TFET) have gained a lot of attention due to the potential for extremely low off current, and the possibility to lower the subthreshold swing beyond the 60 mV/dec limit of conventional MOSFETs. Si based TFETs exhibit poor performance with low on-current Ion and high subthreshold swing due to the low tunnel probabilities through the relatively large band gap. Strained SiGe layers with smaller bandgaps than Si can increase the tunneling currents.

Tunnel-FET (TFET) devices were fabricated on a compressive strained Si1-xGex /SOI heterostructure layer using a gate first process. After the HfO2/TiN gate deposition BF2 and As ion implantations were carried out for the source and drain side, respectively.

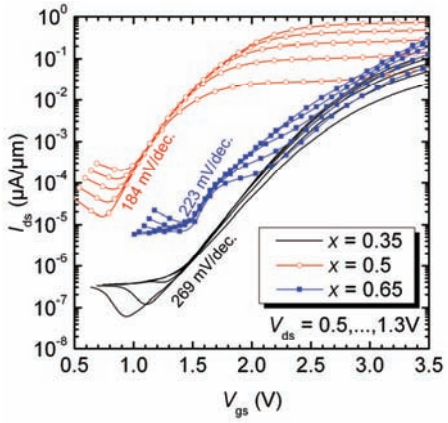

Fig.1 Experimental transfer characteristics of n-TFETs for three different Ge concentrations. The subthreshold slopes presented are the smallest slopes determined for each Ge concentration.

The transfer characteristics of n-TFETs with $Si_{1-x}Ge_x$ are presented in Fig. 1 for different Ge concentrations in the layer and V_{ds} between 0.5 and 1.3 V. The V_{ds} varies on the n-side while the voltage on the p-side was fixed to zero bias during the measurements. Similarly to a conventional n-MOSFET, a gate voltage of $V_{gs} > 0$ (in conjunction with $V_{ds} > 0$) is applied for the on-state. One should note that in this case the tunneling occurs at the p-i-junction.

All devices show reasonable I_{on}/I_{off} ratios of 10^3 and subthreshold slopes below 300 mV/dec. These slopes are substantially better than those measured in GOI devices at room temperature [1]. The highest on-current and the smallest $S = 184$ mV/dec are observed for the transistor using strained $Si_{0.5}Ge_{0.5}$ layer. The on-current enhancement of about one order of magnitude in this transistor compared to the $Si_{0.65}Ge_{0.35}$ device is primarily due to the smaller bandgap of the $Si_{1-x}Ge_x$ layer. These experimental results are in agreement with the simulated tunneling probability for electrons and holes $T^{e,h}(x)$.

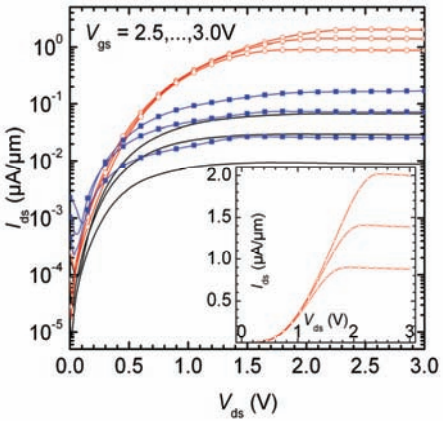

Fig. 2: Output characteristics for SiGe TFETs with Ge atomic concentrations of 35%, 50% and 65%. The inset shows the output curves for Si0.5Ge0.5 TFETs in linear scale with typical S-shape characteristics

For 65 at.% Ge TFETs, both on- current ,I_{on}, (plotted in Fig. 2) and subthreshold slope, S, are improved compared to devices with 35 at%, but they degrade with respect to the 50 at% devices. Since the output current of a TFET is the tunneling current between the source and the channel, determined by the gate voltage, its subthreshold slope depends on several parameters including: the gate oxide thickness, the $Si_{1-x}Ge_x$/SOI heterostructure thickness and the abruptness of the doping profile at the source to channel.

II. High mobility Si0.5Ge0.5 QW p-MOSFETs

p-type MOSFETs were fabricated with quantum well (QW) strained Si/strained $Si_{0.5}Ge_{0.5}$/strained SOI heterostructures. Alternative gate dielectrics of $GdScO_3$ and $LaLuO_3$ with higher-k value than the widely used HfO_2 were integrated in the devices. Our emphasis is focus on the mobility characterization of these new gate/channel stacks.

All devices present good electrical performance. The inverse subthreshold slope degrades from 90 mV/dec to 134 mV/dec by reducing the gate length down to 100 nm due to short channel effects. The relatively low I_{on} is related to a related to high S/D resistances.

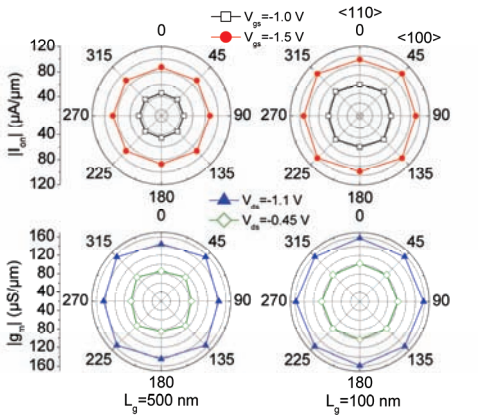

Fig.3: Ion (top) and gm (bottom) as a function of the channel orientation of biaxially compressively strained Si0.5Ge0.5 p-MOSFETs with GdScO3 as a gate dielectric. Lg= 500 nm (left) and 100 nm (right). 0° corresponds to one of the <110> directions..

The corresponding on-current, Ion, and the transconductance, g_m, as a function of the channel orientation averaged over several transistors are plotted in Figure 3 [19]. No significant variations of the electrical transport in <100> and <110> crystal directions is observed. In our device fabrication process, the short channel is defined by gate patterning and not by etching of narrow SiGe mesa. Thus our microscopic mesa structures retain the biaxial strain. As a consequence, the SiGe channels are under a biaxial compressive strain. The hole mobility increases in biaxially strained Si and SiGe due to valence band splitting at the Γ point resulting in reduced carrier scattering, rather than a change of the effective masses. Since the top HH valence band is symmetric around the Γ point, the mobility does not depend on the crystalline direction.

The effective hole mobility in the strained $Si_{0.5}Ge_{0.5}$ QW device was extracted by the use of the split C-V method applied on long-channel devices. At lower gate voltages (V_g < 1.0 V), holes are only confined in the $Si_{0.5}Ge_{0.5}$ QW due to the large valence band offset between the strained $Si_{0.5}Ge_{0.5}$ and strained Si layers, and as the gate voltage increases the top Si cap turns to inversion forming an additional channel.

The effective hole mobility as a function of inversion charge density was investigated for different high-k gate dielectrics (Fig 4). SiGe channel devices showed, with no exception, higher hole mobilities than Si channel devices. A hole mobility of about 200 cm2/V·s was obtained for strong inversion conditions, which is about 2.5 times higher than the Si universal hole mobility. Besides this enhancement, we also see that the mobility extracted from LaLuO3 transistors is very similar to values obtained for HfO2 transistors. These mobility values are in agreement with literature values for strained Si/Si0.54Ge0.46 channel devices with classical SiO2 gate dielectric. This suggests that hole scattering at high-k/strained Si and SiO2/strained Si interfaces is similar and thus no significant mobility degradation due to high-k integration isfound.

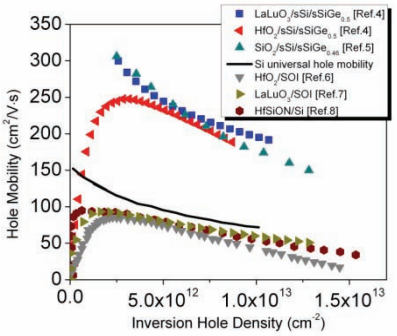

Fig. 4. Benchmarking of hole mobilities for strained Si and strained SiGe channels with different high-k gate oxides.

[1] D. Kazazis, P. Jannaty, A. Zaslavsky, C. Le Royer, C. Tabone, L. Clavelier, and S. Cristoloveanu, Applied Physics Letters, vol. 94, p. 263508, (2009).

[2] E. Durg˘un Özben E, J.M. Lopes, A. Nichau, M.Schnee, S. Lenk, A. Besmehn, K.K. Bourdelle, Q. T. Zhao, J. Schubert, S. Mantl. IEEE Trans Electron Dev, 58, p.617 (2011).

[3] R. A. Minamisawa, J. M. J. Lopes, M. Schmidt, E. Durgun Özben, J.-M. Hartmann, D. Buca, Q. T. Zhao, and S. Mantl, Proceeding of EUROSOI Conference 2011

[4] W. Yu, B. Zhang, Q.T. Zhao, J.-M. Hartmann, D.Buca, A. Nichau, R. Lupták, J.M. Lopes, S. Lenk, M. Luysberg, K. K. Bourdelle, X. Wang and S. Mantl, Solid State Electronics, in press

[5] I. Åberg, C.N. Chléirigh, and J. L. Hoyt, IEEE Trans. Electron Devices 53, 1021 (2006).

[6] O. Bonno, S. Barraud, F. Andrieu, D. Mariolle, F. Rochette, M. Cassé, J. M. Hartmann, F. Bertin, and O. Faynot, 2007 VLSI Symp. Tech. Dig. 2007, 134 (2007).

[7] E. Durğun Özben, J. M. J. Lopes, A. Nichau, M. Schnee S. Lenk, A. Besmehn, K. K. Bourdelle, Q.T. Zhao, J. Schubert and S. Mantl, IEEE Electron Devices Letter 32, 15 (2011).

[8] V. Barral, T. Poiroux, F. Andrieu, C. Buj-Dufournet, O. Faynot, and T. Ernst, 2007 Proc. IEEE Int. Conf. Commun., 61 (2007).

Electron and hole mobilities of Ω-gated Si NW-array MOSFETs

S. Habicht, Q.T. Zhao, D. Buca, S. Mantl

Peter Grünberg Institute 9 (PGI 9): Semiconductor Nanoelectronics, Forschungszentrum Jülich, 52425 Jülich, Germany

Non-planar CMOS concepts such as FinFETs and nanowire (NW) MOSFETs are intensively studied for sub-20nm FETs. These devices can take advantage of mobility enhancement by choosing the optimum crystal orientation for current transport. It is, therefore, interesting to study the integration of novel materials into such multigate devices.

The electrical characteristics of Ω-gated *n*- and *p*-NW array FETs on (001) strained/unstrained silicon-on-insulator (S/SOI) substrates are investigated. NW MOSFETs consisting of 1000 parallel NWs with cross sections of 20x20 nm^2 and 4 nm SiO_2 gate oxide were fabricated along <110> and <100> crystal directions (Fig.1). The devices presented here have a channel length of 2 µm. Electron and hole mobilities were extracted employing the split C-V method to determine the gate capacitance and to eliminate parasitic capacitances. The devices feature excellent I-V characteristics: off-currents (I_{off}) as low as 10^{-14} A, ideal subthreshold swings of 60 mV/dec and maximum I_{on}/I_{off} ratios of 10^{11} for both *n* and *p*-type transistors on SOI and SSOI substrates (Fig.1). The C-V characteristics as well as the ideal inverse subthreshold swings indicate high quality of the gate oxide and low interface state density.

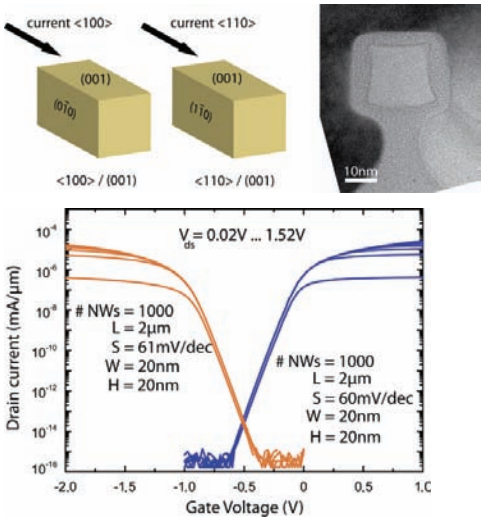

Fig.1 (top) Schematic view of NW devices fabricated on (001)Si. Compared to planar devices three surfaces contribute to carrier transport. TEM image of a Ω-gated 20x20nm2 NW. (bottom) Transfer characteristic of n- and p-NW FETs with <110> channel direction.

P-type NW-array FETs aligned along <110> direction showed 1.4 times larger on-currents and 1.3 times higher transconductances compared to devices oriented along <100> direction. This improvement is explained by the 40% higher hole mobility measured on <110> *p*-FETs compared to <100> devices (Fig.2) [1]. Decreased band splitting between the HH- and LH sub-bands due to the electric quantum confinement degrades mobility of (100) at high gate electric fields (high values of Ninv). Moreover, reduced scattering, originating from surface roughness and interband scattering, results for <110> p-FETs, due to the linear dependence of the scattering rate on the electric field. The hole mobility gain as a function of inversion carrier density Ninv for <110> p-FETs is presented in Fig 2.

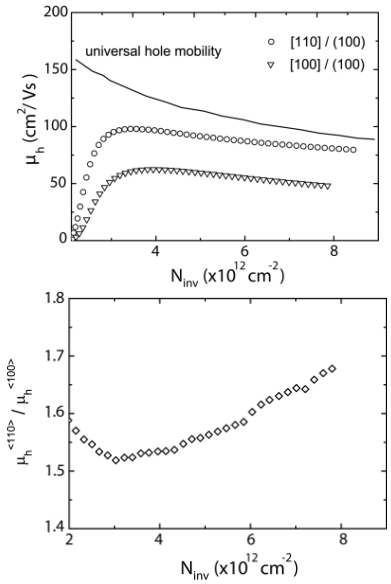

Fig. 2: Hole mobilities of <110> and <100>NW-array p-FETs (top) and the hole mobility gain as a function of inversion carrier density N_{inv} for <110> p-FETs (bottom).

N-FETs NW devices fabricated along <100> crystal direction show 1.3 times enhanced on-currents and 45% increased electron mobility compared to <110> channel direction (Fig.3). These enhancements are ascribed to the anisotropy of electron mobility and to re-population of conduction sub-bands along the Si NW [2]. The mobility gain for *n*-FETs along <100>

saturates with increasing inversion carrier density N_{inv} (Fig.3) as a further increase of the gate voltage does not change the occupancy of the Δ_2 sub-bands.

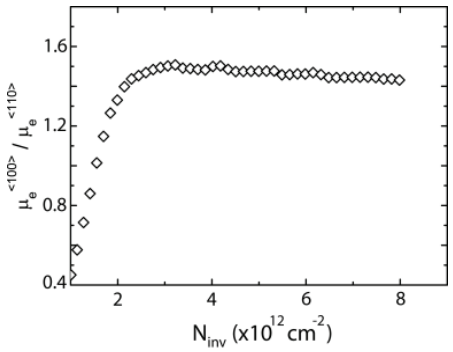

Fig. 3: The mobility gain for <100> n-FETs saturates with increasing inversion carrier density N_{inv}..

Similar NW devices were fabricated using SSOI substrates. It is known that biaxial tensile strain efficiently improves the electron mobility in Si. The initial stress in the SSOI layer was 1.5 GPa. Lateral strain relaxation through patterning is employed to transform biaxial tensile strain into uniaxial tensile strain along the NW [2, 3]. The electrical characteristics of uniaxially tensile strained NW-array FETs with channels oriented along <110> and <100> are compared. Similarly to unstrained Si NW array n-FETs, the on-current of <100> uniaxial tensile strained channels increases by a factor of 1.2 compared to strained <110> channels. (Fig.4). The comparison of strained and unstrained *n*-FETs along <110> and <100> clearly demonstrates improved electron mobilities for strained channels of both, <110> and <100> channel orientations [5].

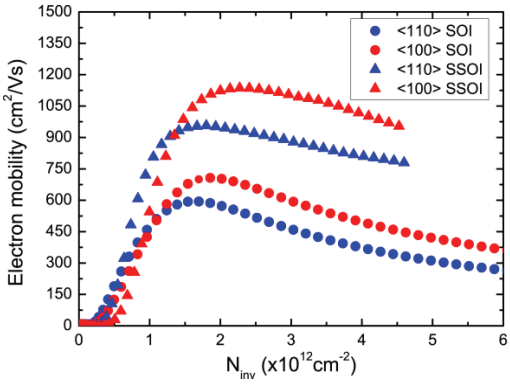

Fig. 4: Electron mobilities for NW-array n-FETs aligned along <110> and <100> for SOI and SSOI substrates.

Low temperature I-V characterization of strained and unstrained NW array *n*-FETs, at temperatures ranging from 4K to 280K, was performed. The inverse subthreshold swing, S(T), follows perfectly the theoretical predicted behavior (Fig.5). An increase of the threshold voltage, $V_{th}(T)$, with decreasing temperature of -0.6 mV/K for strained Si and -0.85 mV/K for unstrained Si devices was measured. The off-currents of the NW array MOSFETs are independent on the channel orientation, the strain within channel, as well as the type of the device (n- or p-type).

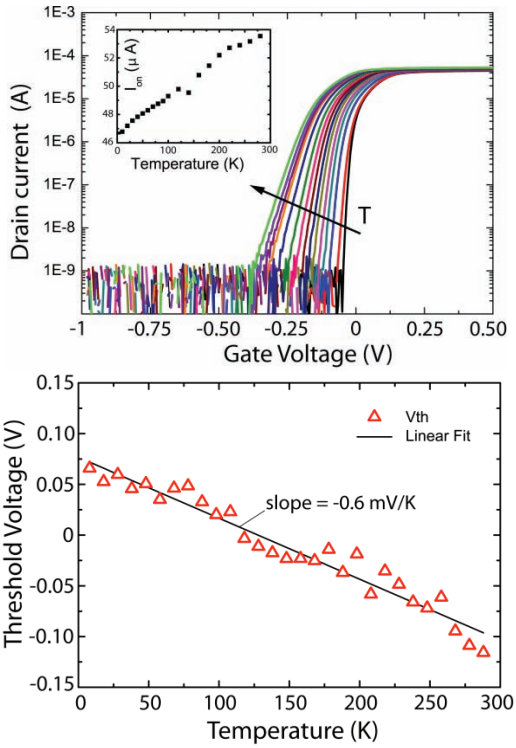

Fig. 5: Transfer characteristics and on current (inset) of <110> strained NW n-FET for T ranging from 4K to 280K (ΔT=20K).The lower graph shows the threshold voltage $V_{th}(T)$-dependence for <110> strained Si device.

In conclusion, 20x20 nm2 NW array transistors with 1000 parallel wires show excellent performance with inverse subthreshold slopes close to 60 mV/dec and very large Ion/Ioff ratios up to 1012. Optimum results were obtained with nanowires oriented along <110> for n-FETs and and <100> for p-FETs on (100) Si.

[1] S. Habicht, S.F. Feste, Q.-T. Zhao and S. Mantl, ESSDERC 2010, Seville, 372 (2010)

[2] J. Chen, T. Saraya, K. Miyaji, K. Shimizu and T. Hiramoto, Jpn. Jour. Appl. Phys., **48**, 011205 (2009)

[3] S.F. Feste, J. Knoch, S. Habicht, D. Buca, Q.-T. Zhao and S. Mantl, Solid State Electron, **53**, 1257 (2009

[4] R.A. Minamisawa, S. Habicht, D. Buca, R. Carius, S. Trellenkamp, K.K. Bourdelle and S.Mantl, J. Appl. Phys., **108**, 124908 (2010).

[5] M. Chu, T. Nishida, X. Lv, N. Mohta and S. E. Thompson, J. Appl. Phys., **103**, 113704 (2008)

Electron-electron interaction in a surface quantum Hall system

S. Becker[1], C. Karrasch[2], T. Mashoff[1], M. Pratzer[1], M. Liebmann[1], V. Meden[2], M. Morgenstern[1]

[1]II. Physikalisches Institut B, RWTH Aachen University
[2]Institut für Theorie der Statistischen Physik, RWTH Aachen University

Using low-temperature scanning tunneling spectroscopy (STS) applied to the Cs-induced two-dimensional electron system (2DES) on *p*-type InSb(110), we probe electron-electron interaction effects in the quantum Hall regime. In quantitative agreement with calculations we find an exchange enhancement of the spin splitting. Moreover, we observe a characteristic Coulomb gap in the density of states at the Fermi level. These results demonstrate that scanning tunneling spectroscopy is able to probe electron-electron interaction down to a resolution below all relevant length scales [1].

Quantum Hall (QH) physics is a paradigm for the study of interacting quantum systems. The most intriguing QH phases are driven by electron-electron (e-e) interaction which, however, is screened by nearby gates and competes with disorder. Thus, a challenge towards a microscopic investigation of e-e interaction is to provide a sufficiently clean and electrically decoupled system probed down to the relevant length scales, most notably the magnetic length $l_B = (\hbar/eB)^{1/2} \approx 10$ nm at 6 T. STS achieves the required resolution, as has been demonstrated on adsorbate induced III-V semiconductor 2DES [2] and on graphene.

We used our home-built scanning tunneling microscope (STM) operating at 5 K in ultrahigh vacuum (UHV) in order to explore the local density of states (LDOS) of a 2DES in the QH regime by measuring the differential conductivity (dI/dV) with respect to the sample bias voltage.

The 2DES was prepared in UHV by cleavage of a *p*-type InSb single crystal (N_A = 1.1 x 10^{21} m^{-3}) and subsequent Cs adsorption of 1.1 % of a monolayer (3.7 x 10^{16} m^{-2}) onto the cooled (110) surface. The single Cs atoms act as surface donors which bend the bands downwards and induce a 2DES ($N_S \approx$ 2.7 x 10^{16} m^{-2}). The band bending reaches deep into the bulk, decoupling the confined states of the 2DES from the bulk valence band (BVB) 600 nm apart (Fig. 1a). Spatially averaged dI/dV curves (Fig. 1b) indeed show only features of the 2DES if it is contacted from the side via a stripe of silver paint. The observed energies (E_0 = -130 meV, E_1 = -50 meV) of the lowest two subbands agree well with calculated values obtained from the Poisson equation. From the spin-split Landau levels (LL) observed in a perpendicular magnetic field, an effective mass $m^* = 0.022m_0$ and g factor $|g^*|$ = 42 can be deduced in accordance with values for the InSb bulk conduction band. The peak widths correspond to a potential disorder of 16 meV, given mainly by the dopants of the bulk.

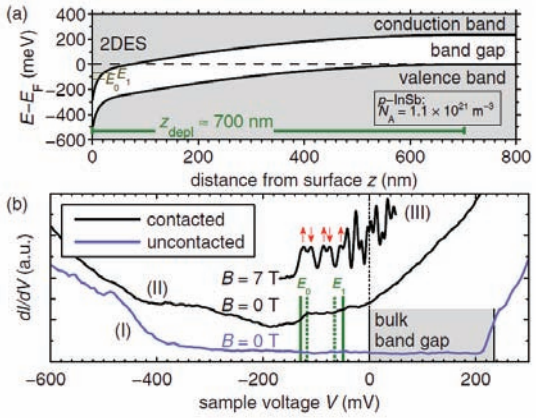

FIG. 1: (a) Calculated band bending using 1D Poisson equation with subband energies E_0, E_1 of the 2DES and the depletion zone. (b) Spatially averaged dI/dV curves without (I) and with (II, III) contacting the 2DES; (II) at 0 T with calculated (broken lines) and measured (solid) subband energies; (III) at 7 T showing spin-split Landau levels (red arrows).

A short-range effect of e-e interaction is the exchange enhancement (EE) of the spin splitting due to the fact that the effective repulsion between electrons with parallel spin is smaller than for antiparallel spins. This eventually leads to an increase of the spin splitting energy E_{SS} at odd filling factors [3]. Figure 2a shows dI/dV spectra taken at a fixed position while ramping the magnetic field B providing the so-called Landau fan. Varying B, the conductance lines are wavy and deviate from $E_{i,n} = E_i + \hbar\omega_c\,(n+½) +/- ½\, g^*\mu_B B$ with subband index i, LL index n, spin index +/-, cyclotron frequency $\omega_c = eB/m^*$, and Bohr magneton μ_B.

One reason for waviness is a shift of E_F with magnetic field taking place once the increasing degeneracy of LLs favors a transition to the next LL. More importantly, g^* is filling factor dependent due to the EE. Analyzing the spin splitting E_{SS} of the lowest LL (Fig. 2b), we find an oscillating deviation $\Delta(B)$ from ordinary Zeeman splitting (straight line)

with amplitude of about 0.75 meV (Fig. 2c) and maxima (minima) around odd (even) filling factors as expected for EE.

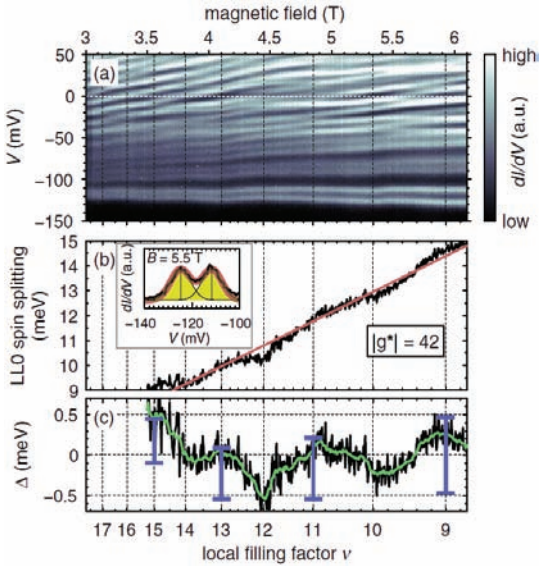

FIG. 2: (a) Landau fan showing dI/dV as grayscale. (b) Spin splitting energy E_{SS} of the lowest LL extracted by Gaussian fits as shown in the inset. (c) Deviation Δ from the linear fit in (b). Inner line: smoothing of raw data (black). Vertical bars: calculated values of EE between neighboring filling factors.

The amplitude is in excellent agreement with theoretical estimates for EE (vertical bars in Fig. 2c) as obtained by treating the Coulomb interaction using a random phase approximation with $m^* = 0.02m_0$ and $g^* = -42$. However, the results barely change if these or other system parameters are varied within reasonable limits (e.g., less than 1% for $g^* = -38$). Thus, magnitude and oscillation phase of $\Delta(B)$ compare favorably with a parameter-free calculation of EE.

For localized electrons interacting via the long-ranged part of the Coulomb interaction, the averaged tunnelling DOS is expected to show a gap at E_F. For a 2DES with unscreened repulsions at $T = 0$ K, a qualitative analysis gives $D_0(E) \sim \varepsilon_r^2|E - E_F|$ [4]. More elaborate analytical and numerical results leave no doubt about the existence of a Coulomb gap while the exact shape remains controversial. A linear Coulomb gap was deduced from various experiments by other groups.

Figure 3a shows the spatially averaged *dI/dV* curve (thick line) at $B = 7$ T. Instead of a peak at E_F, one observes a double peak with a minimum at 0 mV. The sum of two identical Gaussian peaks – representing the two spin levels of this particular LL – matches the measured DOS except for a suppression at E_F. Taking the difference between measured DOS and the sum of the two Gaussians eliminates all single-particle effects leaving only the dip at E_F (blue line). If we modify the Coulomb gap to account for finite temperature and screening effects [5] as well as for the energy resolution of our experiment, we obtain the red, dotted curve in Fig. 3a in excellent agreement with the experiment.

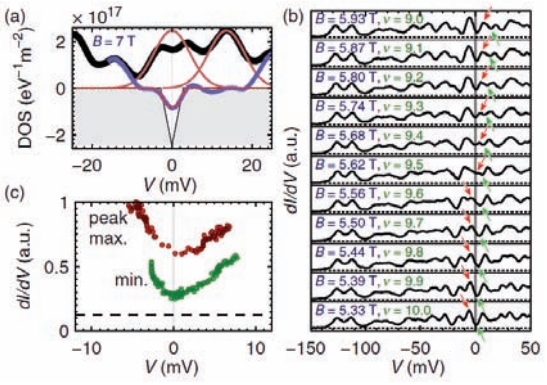

FIG. 3: (a) Thick black line: spatially averaged dI/dV curve at 7 T; brown lines: Gaussian fits for the two LLs around E_F; blue line: difference between these two. Thin black line: bare Coulomb gap; red dotted line: Coulomb gap including finite temperature, screening, and energy resolution. (b) dI/dV spectra at same position in different B fields. Red (green) arrows follow a peak (dip) across E_F. (c) dI/dV value of marked peak (dip) in (b) as function of energy.

The facts that we do not observe the dip at E_F without localization (at $B = 0$ T) and that we can reproduce it by a reasonable, parameter-free calculation strongly suggests that we observe the Coulomb gap. We can rule out inelastic excitations as a cause which would lead to much larger half widths of the gap.

Surprisingly, a Coulomb gap – although typically thought of being a phenomenon related to disorder averaging or spatial averaging – is also observed in the local DOS. The intensity of a particular LDOS peak is suppressed when moved through E_F by increasing B. Figure 3b shows corresponding *dI/dV* curves at a fixed position. The upper arrows follow a single spin level as it crosses E_F and the peak intensity is plotted in Fig. 3c. A *dI/dV* suppression at E_F is also found for fixed B, if different positions are probed within the potential landscape. The finding of Coulomb suppression in the LDOS requires further studies and might be related to Coulomb glass dynamics.

[1] S. Becker, C. Karrasch, T. Mashoff, M. Pratzer, M. Liebmann, V. Meden, and M. Morgenstern, Phys. Rev. Lett. **106**, 156805 (2011).

[2] S. Becker, M. Liebmann, T. Mashoff, M. Pratzer, and M. Morgenstern, Phys. Rev. B **81**, 155308 (2010).

[3] T. Ando *et al.*, J. Phys. Soc. Jpn. **37**, 1044 (1974).

[4] A. L. Efros *et al.*, J. Phys. C **8**, L49 (1975).

[5] F. G. Pikus and A. L. Efros, Phys. Rev. B **51**, 16871 (1995).

Self-organized MBE growth of Ge quantum dots directed by extreme ultraviolet interference lithography

S. Danylyuk[1], G. Mussler [2], S. Brose[1], L. Juschkin[1*], G. Panaitov[2], D. Grützmacher[2], P. Loosen[1]

[1]Chair for Technology of Optical Systems, RWTH Aachen University
[2]Peter Grünberg Institute 9 : Semiconductor Nanoelectronics, Forschungszentrum Jülich, Germany
*on leave at University College Dublin, Ireland

Quantum dot arrays (QDs) based on Si/Ge heterosystem are highly interesting objects with unique electronic and optical properties. Creating a dense and well-ordered array of these structures allows the realisation of a novel type of solid matter - "artificial crystals" - with energy band distributions not existing in nature. In this work we report about realisation of ordered Ge quantum dot arrays fabricated by means of extreme ultraviolet interference lithography (XIL) and molecular–beam epitaxy (MBE).

Quantum dots are quasi-zero dimensional semi-conductor structures on the nanometer scale, which provide a confining potential for charge carriers in all three dimensions. Hence, these artificial atoms have a completely different energy structure compared to bulk material or other semiconductor nanostructures, such as quantum wells or quantum wires. Therefore, novel device applications based on QDs in the field of electronics, optoelectronics, spintronics or even quantum computation are envisioned. Currently, the main method to create large arrays of QD is self-organised growth in Stranski Krastanov mode. Main drawbacks of the self-organised QDs are the strong variation in shape and size as well as the random position of the QDs. For device applications, it is mandatory to control exactly the position of the Ge QDs in order to address individual QDs. In addition, the uniformity of the QDs regarding size and shape is of utter importance to ensure the identical energy structure of all QDs.

One of the most promising methods to create an ordered QD arrays with high resolution is the self-organisation of QDs on substrates, prepatterned by the XUV interference lithography. It is currently the only technique that can realistically achieve the sub-20 nm resolution for large and dense arrays of nanostructures. XIL relies upon soft x-ray / extreme ultraviolet light at wavelengths of 10 – 15 nm, so that highly accurate patterns with a spatial resolution of typically 5 – 10 nm are obtained. In addition, interaction of light with matter maximises in this spectral range (absorption lengths lie in the range of 100 nm), which ensures photochemical sensitivity, very efficient use of photons and independence of substrate material. Further benefits over traditional electron-beam lithography include no charging effect, negligible proximity effect and moderate to high throughput. This method is being used already with synchrotron radiation sources with great success. In this work we demonstrate the possibility to perform the patterning using a laboratory EUV source.

The high-power laboratory sources of short-wavelength radiation based on gas discharge pinch plasmas are actively developed in Aachen for more than 10 years. These thermal sources are not inherently coherent, however, they can be tuned to radiate in a limited bandwidth from a rather small (down to 250 µm) region (pinch), thus providing a required partial coherence. We have shown recently that one can obtain a highly intensive radiation around 11 nm efficiently filtered to $\Delta\lambda/\lambda \sim 3\text{-}4\%$ [1], which is a requirement for achromatic Talbot interference [2].

In this approach a so-called Talbot self-imaging is utilised. Classically, a grating, or any structure with periodic transmission profile will form self-images in certain near-field planes after the grating when illuminated by monochromatic light. Recently it was shown that allowing the light not to be perfectly monochromatic, i.e. with a bandwidth of the order of few percent, one can obtain not only direct images of the grating, but also an image with a half of the period of the grating. Both, monochromatic and achromatic Talbot effects can be used for patterning with XUV light. The benefits, in comparison with other techniques, include a mask error correction, large depth of focus and a relatively simple optical setup. A frequency doubling effect with achromatic Talbot images allows to reduce requirements of the mask fabrication, e.g., to obtain a 20 nm period on a wafer, only a 40 nm period transmission mask is necessary.

In addition, the required spatial coherence length reduces with the period of structures, which makes the Talbot approach suitable for sub-20 nm periods. On the other hand, the contrast of achromatic images does not exceed a quarter of initial contrast of the mask and depends on the spatial coherence of the source. As a result, successful sub-20 nm structuring in this regime require rigorous

simulation of Talbot patterns to determine an optimum coherence length and a suitable transmission mask design. Another challenge is caused by the fact that for short-wavelength radiation and sub-100 nm periods, the distance from the grating to a Talbot plane is between 1 and 100 micrometer. This means that illuminated wafers needs to be in the proximity of the mask, and the distance should be controlled with sub-micrometer precision.

Taking into account these considerations, we have realised a laboratory-scale setup for XUV interference patterning with transmission masks for structuring on a sub-100 nm scale. The system is designed to accept up to 2" substrates with single illumination fields exceeding 100 µm x 100 µm. Three capacitive sensors are used to control not only the distance between mask and wafers, but also a relative tilt. Double polished Si wafers with a total thickness variation (TTV) below 1 µm are used to guarantee sub-1 µm distance precision in all illuminated area. A special type of transmission mask was developed together with FZJ to provide us necessary flexibility with wavelength choice. Our masks use niobium membranes that are known for their mechanical stability [3] and have a high transmission at 11 nm. The transmission grating design is shown in Fig. 5. As an absorbing material, chromium or nickel is used, which allow us not only to match the efficiency of standard 13.5 nm SiNx-based gratings but also to exceed it in a wavelength range between 8 and 15 nm. We have achieved membranes with areas up to 1000 µm x 1000 µm and with sub-100 nm e-beam patterned structures. The masks demonstrate excellent contrast (>1:20) and in addition also act as a spectral filter, effectively blocking all radiation above 15 nm.

a)

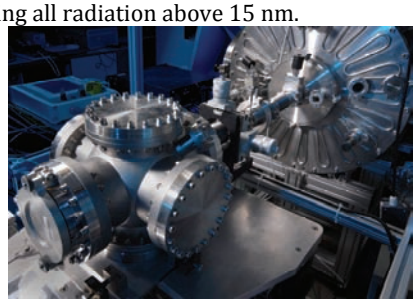

b)

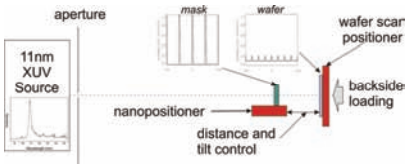

FIG. 1: XUV-IL illumination set-up realised at TOS with a wafer loading chamber and a source behind (a). The principal scheme of the XUV-IL nano-patterning system (b).

High-resolution e-beam resists, such as HSQ, PMMA and ZEP are used with typical exposure times between 2 and 10 min, depending on thickness and type of the resist.

To demonstrate the feasibility of the achromatic Talbot interference method, we have modelled and manufactured a mask with a series of line and space (L/S) patterns with periods down to 200 nm. The results of the exposure of the positive ZEP520A resists are shown in Fig. 2.

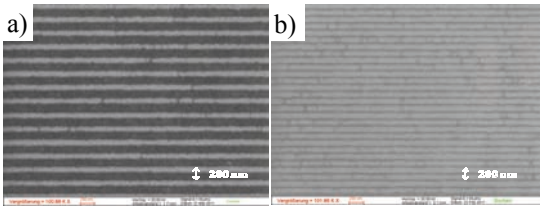

FIG. 2: SEM images of lines/space pattern produced by proximity printing (a) and achromatic Talbot interference lithography (b) with the same mask. The period reduction is demonstrated.

The predicted frequency doubling is clearly visible, allowing us to create patterns with 100 nm period with 200 nm period on the mask.

Subsequently, the same mask has also allowed us to create a dot patterns with a crossed double exposure of lines/spaces array. By a careful optimization of the exposure, development and etching parameters, we have obtained high-quality templated Si substrates. Using these templated substrates, we succeeded in growing Ge QD arrays with a good degree of ordering over a large spatial extend (300 µm * 300 µm), as shown in Fig. 3. In this case the hole diameter was 100 nm, that led to nucleation of 4 Ge QDs in each patterned hole.

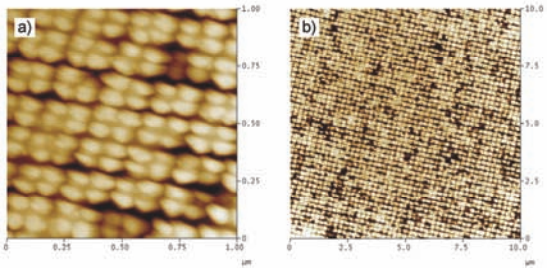

FIG. 3: AFM images of a Ge QD array realized on a Si substrate, templated by means of XIL at RWTH-TOS. The hole period amounts to 200 nm. Each hole is filled with 4 Ge QDs that nucleate at the corners.

Further work on optimisation of the quality of the masks, improving of vibration isolation and quality of the pattern transfer should allow to decrease the periodicity of the patterns to the target size of 20 nm, enabling lateral coupling of QDs.

[1] K. Bergmann, S. V. Danylyuk, L. Juschkin, Optimization of a gas discharge plasma source for extreme ultraviolet interference lithography at a wavelength of 11 nm, J. Appl. Phys. 106, 073309 (2009)

[2] H. H. Solak, Y. Ekinci, Achromatic spatial frequency multiplication: A method for production of nanometer-scale periodic structures, J. Vac. Sci. Technol. B 23 (6), 2705 (2005).

[3] S.V. Danylyuk, R. Ott, G. Panaitov, G. Pickartz, E. Hollmann, S.A. Vitusevich, A.E. Belyaev and N. Klein, Aluminium nitride-niobium multilayers and free-standing structures for MEMS, Thin Solid Films 515, 489 (2006)

Solid state reactions in the system Ga-O-N

J. Brendt, D. Röhrens, M. Martin

Institute of Physical Chemistry, RWTH Aachen University

Gallium nitride as well as gallium oxide are interesting base materials for (opto-) electronic components such as light emitting diodes or sensors [1,2]. Recently, we found that highly non-stoichiometric, amorphous gallium oxide, undoped and doped with nitrogen, exhibits an insulator–metal transition upon heating with a conductivity jump up to 7 orders of magnitude [3]. This novel mechanism is driven by crystallization of β-Ga_2O_3 within the amorphous gallium oxide matrix, i.e. a heterogeneous solid state reaction, and opens up a potential route for applications in resistive switching [3,4]. To get a deeper understanding of the solid state reactions in the system Ga-O-N we investigated them by means of *in situ* X-ray absorption spectroscopy and neutron diffraction [5,6].

A common way of synthesising α-GaN is the ammonolysis of β-Ga_2O_3:

$$Ga_2O_3 + 2\ NH_3 \rightarrow 2\ GaN + 3\ H_2O \qquad (I)$$

The reaction is accomplished by flowing ammonia over a β-Ga_2O_3 powder in a temperature range between 600 and 1100 °C. The backward reaction from α-GaN to β-Ga_2O_3 can be performed by oxidation of GaN with oxygen gas:

$$GaN + 3/2\ O_2 \rightarrow Ga_2O_3 + N_2 \qquad (II)$$

Although the ammonolysis of β-Ga_2O_3 is of such enormous importance, systematic and quantitative studies of the reaction mechanism and the reaction kinetics were rare. It was therefore our first aim to investigate the kinetics of the ammonolysis of β-Ga_2O_3 powders according to reaction (I) under *in situ* conditions and to understand the underlying reaction mechanism. The second aim of our studies was to investigate the kinetics of the oxidation of α-GaN powders according to reaction (II) also under *in situ* conditions and to describe the kinetics quantitatively. In both cases, we used X-ray absorption spectroscopy (XAS) at the Ga *K*-edge under *in situ* conditions, i.e. in the temperature range between 600 and 900 °C and in flowing, reactive gases (ammonia and oxygen, respectively).

At all investigated temperatures, the EXAFS spectra, $\mu(E,t)$, recorded during the ammonolysis of β-Ga_2O_3 show complete conversion to the product phase, α-GaN, *i.e.* the last spectrum during the ammonolysis equals the α-GaN standard. From the measured, time-dependent EXAFS, $\chi(E,t)$, the distribution functions (RDF) can be obtained which are shown as function of time in Fig. 1. The first coordination shell in the RDF shows only slight changes, while the second peak in the RDF increases rapidly with time. This behavior is due to the nature of the second coordination shell around Ga atoms in α-GaN and β-Ga_2O_3. In the nitride, there is a clearly defined second coordination shell with 12 gallium neighbors in a distance of 0.318 nm, whereas in the oxide the second shell is very diffuse, with 20 gallium neighbors in a distance range from 0.304 to 0.344 nm. Hence, the partially destructive interference in *k*-space leads to smaller amplitude in *R*-space.

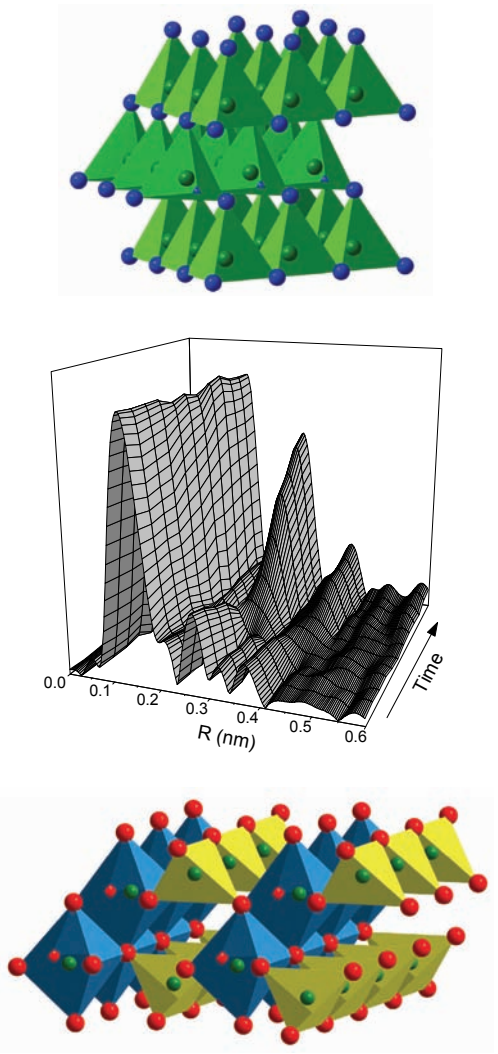

FIG. 1: Changes in the k^3-weighted radial EXAFS distribution function (middle) during the ammonolysis of β-Ga_2O_3 (bottom) to α-GaN (top) at 780 °C [5].

For a quantitative analysis of the reaction kinetics the normalized, time-dependent *in situ* spectra, $\mu(E,t)$, and the extracted time-dependent $\chi(k,t)$ are fitted with linear combinations of α-GaN and β-Ga_2O_3 reference spectra.

$$\mu(E,t) = a_\mu(t)\cdot\mu(E)_{Ga_2O_3} + b_\mu(t)\cdot\mu(E)_{GaN} \quad (1)$$

$$\chi(k,t) = a_\chi(t)\cdot\chi(k)_{Ga_2O_3} + b_\chi(t)\cdot\chi(k)_{GaN} \quad (2)$$

Here $\mu(E)_i$ and $\chi(k)_i$ (i = Ga_2O_3, GaN) are the normalized spectra (in *E*- and *k*-space) of pure β-Ga_2O_3 and α-GaN. The weighting factors $a_\mu(t)$, $b_\mu(t)$, $a_\chi(t)$, and $b_\chi(t)$ are time-dependent and describe the reaction kinetics. We fitted $\mu(E,t)$ and $\chi(k,t)$ separately for the following reason. For $\mu(E,t)$, the fitting range in energy space is from 20 eV before the edge to 50 eV behind the edge. This presents a fit of the XANES region which is sensitive to changes in the electronic structure of the samples. For $\chi(k,t)$, the fits in *k*-space were performed in a fitting range from 25 to 90 nm^{-1}. This presents an EXAFS fit, which is sensitive to structural changes during the reaction.

The fitting results show that throughout the ammonolysis both the XANES-region, reflecting the electronic structure, and the EXAFS-region, reflecting the local structure around gallium atoms, can be described very well by a linear combination of α-GaN and β-Ga_2O_3 spectra only. In addition the phase fractions $a_i(t)$ and $b_i(t)$ that we obtained from Eqs. (1) and (2) are identical. We may thus conclude: (i) No other phases than α-GaN and β-Ga_2O_3 are present during the ammonolysis reaction. This result is confirmed by neutron scattering and Rietveld refinement [5] of samples quenched after different times of ammonolysis. (ii) The changes in the electronic structure and in the short range order around Ga proceed with the same rate.

The phase fraction $b(t)$ relating to the growth of GaN can be described well by an Avrami kinetics, $b(t) = 1 - \exp(-(k(t-t_o))^n)$ where k is the rate constant, n the Avrami exponent, and t_0 an incubation time. The obtained Avrami exponents scatter around n = 3. This value corresponds to a reaction mechanism with fast nucleation at the beginning of the reaction and subsequent three-dimensional growth of nuclei with a constant growth rate. During the latter part of the reaction the formation of the new phase at the interface between the matrix and the nucleus is rate determining. Thus, our experimental data show that the ammonolysis of Ga_2O_3 starts with a fast nucleation of GaN nuclei, and then the reaction is determined by further growth of GaN at the interface between Ga_2O_3 and GaN. These results are confirmed by TEM investigations after ammonolysis showing a small GaN nucleus of about 40 nm diameter within a β-Ga_2O_3 grain.

The oxidation of GaN powder to β-Ga_2O_3 shows a completely different behavior that can be modeled using a layer growth model as applied earlier by Wolter *et al.* [7] to explain the oxidation of GaN epilayers.

A schematic comparison of the different reaction mechanisms for the ammonolysis of β-Ga_2O_3 and the oxidation of GaN is shown in Fig. 2. The ammonolysis of β-Ga_2O_3 is characterized by nucleation and growth of α-GaN nuclei resulting in destruction of the original grain morphology. In contrast, the oxidation of α-GaN is characterized by growth of a β-Ga_2O_3 layer covering the complete GaN grain and preserving the original grain morphology. In both cases, transport of nitrogen and oxygen is assumed to take place along fast diffusion pathways, such as grain boundaries or dislocations as indicated schematically in Fig. 2.

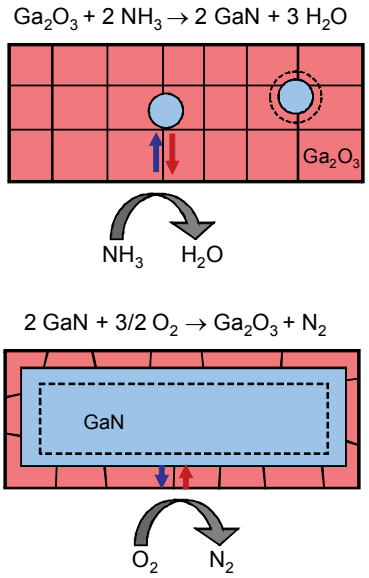

FIG. 2: Schematics of the ammonolysis of β-Ga_2O_3 with nucleation and growth of α-GaN (top) and the oxidation of α-GaN with growth of a β-Ga_2O_3 layer (bottom). In both cases the black lines indicate fast diffusion pathways for oxygen (red arrow) and nitrogen (blue arrow) which could be cracks, grain boundaries or dislocations.

[1] S. J. Pearton, F. Ren, Adv. Mater. 12, 1571 (2000)

[2] S. Cho, J. Lee, I. Park, S. Kim, Mat. Lett. 57, 1004 (2002)

[3] L. Nagarajan, R. A. De Souza, D. Samuelis, I. Valov, A. Börger, J. Janek, K. D. Becker, P. C. Schmidt, M. Martin, Nature Materials **7**, 391 (2008)

[4] R. Waser, M. Aono, Nature Materials **6**, 833 (2007).

[5] J. Brendt, D. Samuelis, T.E. Weirich, M. Martin, Phys. Chem. Chem. Phys. **11**, 3127 (2009)

[6] D. Roehrens, J. Brendt, D. Samuelis, M. Martin, Journal of Solid State Chemistry **183**, 532 (2010)

[7] S. D. Wolter, S. E. Mohney, H. Venugopalan, A. E. Wickenden, D. D. Koleske, J. Electrochem. Soc. **145**, 629 (1998)

Dephasing time of GaAs electron spin qubits coupled to a nuclear bath exceeding 200 μs

Hendrik Bluhm[1], Sandra Foletti[1], Izhar Neder[1], Mark Rudner[1], Diana Mahalu[2,3], Vladimir Umansky[2,3] & Amir Yacoby[1]

[1] Department of Physics, Harvard University, Cambridge, Massachusetts 02138, USA
[2] Braun Center for Submicron Research, Department of Condensed Matter Physics, Weizmann Institute of Science, Rehovot 76100, Israel
[3] 2nd Institute of Physics C, RWTH Aachen University, Germany

Qubits, the quantum mechanical bits required for quantum computing, must retain their fragile quantum states for a long time. In many types of electron spin qubits, the primary source of decoherence is the interaction between the electron spins and nuclear spins of the host lattice. For electrons in gate defined GaAs quantum dots, previous spin echo measure-ments have revealed coherence times of about 1 μs at magnetic fields below 100 mT [1,2]. Here, we show that coherence in such devices can survive to much longer times. At fields above a few hundred millitesla, the coherence time measured using a single-pulse spin echo is 30 μs. At lower magnetic fields, the echo first collapses, but then revives at times determined by the relative Larmor precession of different nuclear species. Using a multiple-pulse Carr-Purcell-Meiboom-Gill echo sequence, the decoherence time can be extended to more than 200 μs, which represents an improvement by two orders of magnitude compared to previous measurements [1,2].

The promise of quantum dot spin qubits as a solid state approach to quantum computing is demonstrated by the successful realization of initialization, control and single shot readout of electron spin qubits in GaAs quantum dots [3,4,5]. To further advance spin based quantum computing, it is vital to mitigate decoherence due to the interaction of the electron spin with the spins of nuclei of the host material. Through the hyperfine interaction, an electron spin in a GaAs quantum dot is subjected to a fluctuating effective magnetic field produced by the nuclear spins. One can partially eliminate its effect by flipping the electron spin halfway though an experiment, a procedure known as Hahn-echo.

The spin qubit studied in this work consists of two isolated electrons confined in a double quantum dot, created by applying negative voltages to metallic gates that locally deplete a two dimensional electron gas (2DEG) (see Fig. 1a). The Hilbert space of our logical qubit is spanned by the states $|\uparrow\downarrow\rangle$ and $|\downarrow\uparrow\rangle$, i.e. the m=0 subspace of two separated spins. The exchange interaction between the two electrons is controlled via rapid changes of the voltages in order to control of the qubit (see Fig. 1).

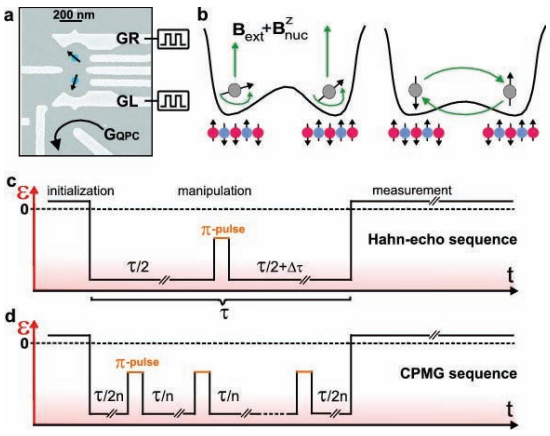

Fig. 1. Qubit control. a, SEM micrograph of a device similar to the one used. b, Left: an initially prepared singlet state oscillates between S and T_0 with frequency $g^*\mu_B\Delta B^z_{nuc}/\hbar$, which changes over time due to slow fluctuations of the hyperfine field gradient ΔB^z_{nuc}. Right: switching on the tunnel coupling between the two dots leads to the coherent exchange of the electron spins. c, Hahn-echo sequence: after evolving for a time τ/2, the two electrons are exchanged with a π-pulse. d, Carr-Purcell-Meiboom-Gill sequence.

The experimental procedures follow those of [1]. We initialize the system with both electrons residing in a single dot, where the ground state is a spin singlet. As the electrons are separated into different dots, they experience a difference $\Delta B^z_{\mathrm{nuc}}$ between the z-components of the hyperfine fields in the two dots. This field gradient causes precession between the singlet S and the triplet $T_0 \equiv (|\uparrow\downarrow\rangle + |\downarrow\uparrow\rangle)/\sqrt{2}$, and its fluctuations lead to dephasing of the qubit. We implement echo π-pulses by pulsing gates such that inter-dot tunneling leads to an exchange of the two electron spins. The pulse profiles for the Hahn-echo and CPMG sequence are shown in Fig. 1c,d. Readout of the final qubit state is accomplished by spin-to-charge conversion and a quantum point contact (QPC).

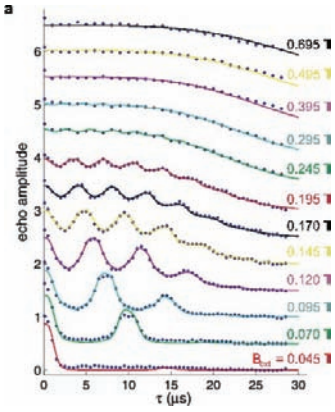

Fig. 2. Echo amplitude. a, Echo signal as a function of the total evolution time, τ, for different values of magnetic field. The fits to the data are obtained by extending the model of ref [6]. Curves are offset for clarity.

Fig. 2 shows the Hahn-echo signals for different magnetic fields B_{ext}. The echo amplitudes are normalized such that they are unity at short times (no decoherence) and eventually drop to zero for a fully randomized state. At high fields we find a decay of the Hahn-echo signal approximately as $\exp(-(\tau/30\mu s)^4)$. As the magnetic field is reduced, the echo signal develops oscillations with a time scale of microseconds, which evolve into full collapses of the signal with revivals at later times on a ten microsecond time scale. Using a model discussed elsewhere, we have fit all the data in Fig. 2 with a single set of field-independent parameters which were chosen to obtain a good match with all datasets, including the number of nuclei in each of the two dots, *N*. In addition, the scale factor for each dataset was allowed to vary to account for the imperfect normalization of the data. The fit parameters are in good agreement with independent estimates.

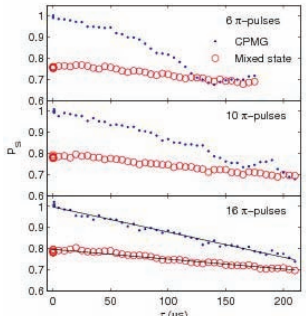

Fig. 3. CPMG decoupling experiments with 6, 10 and 16 π-pulses at Bext = 0.4 T. The blue dots show the readout signal of the CPMG pulses, the red circles represent reference measure-ments which produce a completely dephased state. PS is the sensor signal normalized so that a singlet corresponds to PS=1. Visibility loss increases PS compared to the actual singlet probability P(S), so that the value for the mixed state exceeds the ideal value of 0.5. The linear fits to the 16-pulse data (black lines) intersect at τ = 276 μs, which can be taken as a rough estimate or lower bound of the coherence time.

Substantially longer coherence times are expected for more elaborate decoupling sequences [7]. We implemented the CPMG sequence with n·π-pulses, as shown in Fig. 1d. Fig. 3 shows data for n = 6, 10 and 16. For n = 16, the echo signal clearly persists for more than 200 μs, two orders of magnitude larger than previously shown. The duration of each of the π-pulses could easily be reduced below the 6 ns used here. One may hope to achieve millisecond scale coherence times with improved decoupling sequences [7] without adding complexity. Thus, 10^5-10^6 operations could be carried out on one qubit while maintaining the state of another. The excellent agreement with a model for the field and time dependence of the Hahn-echo revivals shows that many aspects of the dephasing of electron spins due to the nuclear hyperfine interaction are now well understood.

We thank D. J. Reilly for advice on implementing the RF readout system and J. R. Maze for discussions. We acknowledge funding from ARO/IARPA, the Department of Defense and the National Science Foundation under award number 0653336. I.N. and M.R. were supported by NSF grant DMR-0906475. This work was performed in part at the Center for Nanoscale Systems (CNS), a member of the National Nanotechnology Infrastructure Network (NNIN), which is supported by the National Science Foundation under NSF award no. ECS-0335765.

1. Petta, J. R. et al. Coherent manipulation of coupled electron spins in semiconductor quantum dots. Science 309, 2180 (2005).

2. Koppens, F. H. L., Nowack, K. C. & Vandersypen, L. M. K. Spin echo of a single spin in a quantum dot. Phys. Rev. Lett. 100, 236802 (2008).

3. Koppens, F. H. L. et al. Control and detection of singlet-triplet mixing in a random nuclear field. Science 309, 1346 (2005).

4. Foletti, S., Bluhm, H., Mahalu, D., Umansky, V. & Yacoby, A. Universal quantum control in two-electron spin quantum bits using dynamic nuclear polarization. Nature Physics 5, 903 (2009).

5. Nowack, K. C., Koppens, F. H. L., Nazarov, Y. V. & Vandersypen, L. M. K. Coherent control of a single electron spin with electric fields. Science 318, 1430 (2007).

6. Cywinski, L., Witzel, W. M. & Das Sarma, S. Pure quantum dephasing of a solid-state electron spin qubit in a large nuclear spin bath coupled by long-range hyperfine mediated interactions. Phys. Rev. B 79, 245314 (2009).

7. Lee, B., Witzel, W. M. & Das Sarma, S. Universal pulse sequence to minimize spin dephasing in the central spin decoherence problem. Phys. Rev. Lett. 100, 160505 (2008).

Spin-orbit interaction and asymmetry effects on Kondo ridges at finite magnetic field

S. Grap[1], S. Andergassen[1], J. Paaske[2], V. Meden[1]

[1] Institut für Theorie der Statistischen Physik, RWTH Aachen University
[2] Nano-Science Center, Niels Bohr Institute Copenhagen, Denmark

We study electron transport through a serial double quantum dot with Rashba spin-orbit interaction (SOI) and Zeeman field *B* in presence of local Coulomb repulsion. The linear conductance as a function of a gate voltage V_g shifting the levels shows two *B=0* robust Kondo ridges against SOI as time-reversal symmetry is preserved. Resulting from the crossing of a spin-up and a spin-down level at vanishing SOI two additional Kondo plateaus appear at finite *B*. They are not protected by symmetry and rapidly vanish if the SOI is turned on. Left-right asymmetric level-lead couplings and detuned on-site energies lead to a simultaneous breaking of left-right and bonding-anti-bonding state symmetry. In this case the finite-*B* Kondo ridges in the V_g-*B* plane are bent with respect to the V_g-axis. For the Kondo ridge to develop different level renormalizations must be compensated by adjusting *B*.

In linear response transport through quantum dots the spin Kondo effect shows up as a plateau in the conductance G when varying the level positions by an external gate voltage V_g, often referred to as a *Kondo ridge* [1]. Its width is set by the local Coulomb interaction U on the dot, which, in the Kondo regime, exceeds width r of the Lorentzian resonance in $G(V_g)$ at U=0. Breaking the two-fold Kramers-degeneracy by a local Zeeman field of amplitude B destroys the Kondo ridge; along the V_g-axis the conductance plateau is split up into two Lorentzian resonances. In contrast, although breaking spin-rotational symmetry by designating a certain (spin) direction, the SOI does not destroy the Kondo effect [2]. In the presence of SOI spin is no longer a good quantum number but a Kramers doublet remains as time-reversal symmetry is conserved. In multi-level dots increasing B might lead to energetically degenerate states (level crossings) resulting from different orbitals. For a spin-up and -down state and a gate voltage tuned such that an electron fluctuates between these states one might expect the emergence of a spin Kondo effect at *finite B* [3]. Here we consider a setup where the orbital quantum number does not arise in the leads and thus disregard orbital Kondo effects. In contrast to the standard B=0 Kondo effect the one appearing at finite B is not protected by time-reversal symmetry and we show that it is destroyed in the presence of a finite SOI.

We here study a serial double quantum dot, each having a single spin-degenerate level (at B=0) described by a tight-binding model with two lattice sites coupled by electron hopping t and connected to two semi-infinite noninteracting leads via tunnel couplings $\Gamma_{L/R}=\pi t_{L,R}^2 \rho_{\text{leads}}$, see Fig. 1. The on-site energies of the two levels are given by $\varepsilon_{1/2}=V_g\pm\delta$. The Rashba SOI α is modeled as an imaginary electron hopping with spin-dependent sign between the two lattice sites [4]. We here exclusively consider the coupling of B to the spin degree of freedom (Zeeman term) and neglect its effect on the orbital motion. B can be tilted by an angle θ with respect to the SOI, the relevant component being the perpendicular one. The local Coulomb repulsion is modeled as an on-site U as well as a nearest-neighbor U' repulsion and treated within an approximate static functional-renormalization group approach [5].

The single-particle spectrum of the noninteracting isolated double dot is easily determined [5]. For θ=0 corresponding to B parallel to the SOI α can be absorbed into an effective hopping $t_{\text{eff}}=\sqrt{t^2+\delta^2+\alpha^2}$ and $\lambda=V_g\pm(t_{\text{eff}}\pm B)$. For the appearance of a spin Kondo effect (after turning on $\Gamma_{L/R}$ as well as U and U') it is necessary that two degenerate levels of opposite spin are located at zero energy (the chemical potential). Zero energy spin-degenerate levels are obtained at B=0 and $V_g=\pm t_{\text{eff}}$ (bonding and anti-bonding states). This will lead to the standard spin Kondo effect related to the presence of a Kramers doublet when U and U' are switched on. Increasing B the spin-up level of the bonding state and the spin-down level of the anti-bonding one approach each other. For either α=0 or θ=0 they become degenerate and cross at zero energy for $B_c=\pm t_{\text{eff}}$ and V_g=0. Besides the two B=0 Kondo ridges developing for all dot parameters, for α=0 or θ=0 one might expect the appearance of two finite-B Kondo ridges. In the basis of the many-body energies of the isolated interacting double dot this corresponds to a singlet-triplet Kondo effect.

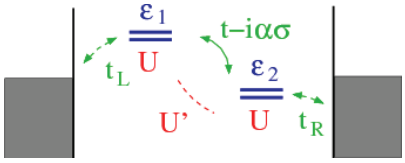

Fig.1 Model

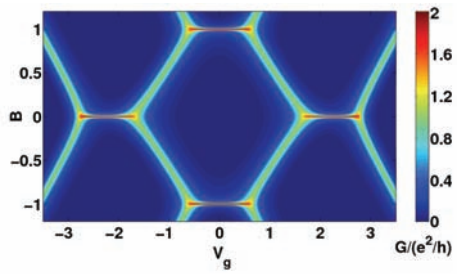

FIG. 2: Conductance $G(V_g;B)$ for $t = 1$, $U = U' = 1$, $t_{L/R} = 0.3$, and $\delta = 0$ in the absence of SOI ($\alpha = 0$).

For the linear conductance $G(V_g,B)$ we first focus on the case of vanishing SOI (α=0) or Θ=0, the SOI being absorbed into t_{eff}. Figure 1 displays the expected two pairs of B=0 and V_g=0 Kondo ridges for a L/R-symmetric setup. Due to the renormalization of the inter-dot hopping the B=0 plateaus are not centered around $V_g=\pm t_{eff}$ but renormalized gate voltages. For the present parameters the renormalization of the inter-dot hopping and B (almost) cancel each other such that the finite B ridges are located at $B_c\approx\pm t_{eff}$. Transforming the dot-lead coupling into the basis of bonding (b) and anti-bonding ($\bar{b}$) states of the non-interacting isolated dot, the couplings are $\Gamma_{b,L/R}=\frac{\sqrt{t^2+\delta^2}\mp\delta}{2\sqrt{t^2+\delta^2}}\Gamma_{L/R}$, and $\Gamma_{\bar{b},L/R}=\Gamma_{b,R/L}\,t^2_{L/R}/t^2_{R/L}$. For the considered case the bonding and anti-bonding states have the same total coupling $\Gamma_{b/\bar{b}}=\Gamma_{b/\bar{b},L}+\Gamma_{b/\bar{b},R}$ and are L/R-symmetric implying unitary conductance. Increasing $|B|$ from B=0 the Kondo ridges are suppressed on the exponential Kondo scale and resonance peaks of height e^2/h and width r develop. Eventually the peaks corresponding to the spin-up level of the bonding state and the spin-down level of the anti-bonding one merge with the finite-B Kondo ridges. We note that $G(V_g,B)$ is symmetric with respect to $B\rightarrow -B$ and $V_g\rightarrow -V_g$. While the former symmetry is given by the Hamiltonian and holds for all parameter sets, the latter is specific to the parameters chosen here ($t_L=t_R$ and δ=0). The conductance remains symmetric under $V_g\rightarrow -V_g$ if at least either δ=0 or $t_L=t_R$. holds leading to equally reduced conductance plateaus with respect to the unitary value.

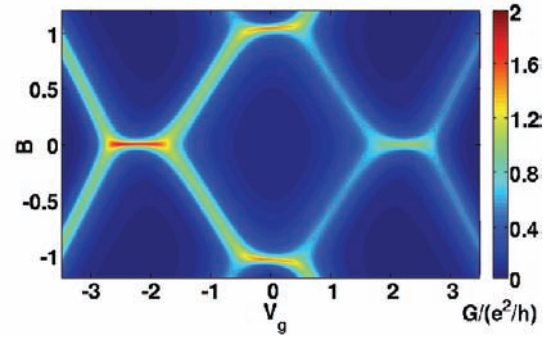

FIG. 3: Conductance $G(Vg;B)$ for $t = 1$, $U = U' = 1$, $\alpha = 0$ with $t_L = 0.3$, $t_R = 0.5$ and $\delta = -0.3$.

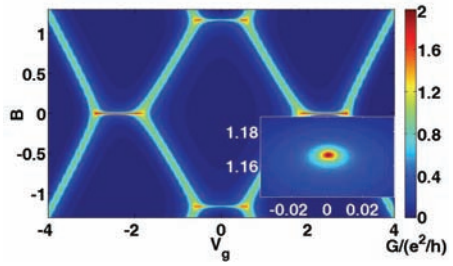

FIG. 4: Conductance $G(V_g;B)$ for $t = 1$, $U = U' = 1$, $t_{L/R} = 0.3$, and $\delta = 0$ with $\Theta = 0.01$ and finite SOI $\alpha = 0.6$. Inset: Conductance $G(\Theta;B)$ at V_g=0.

The most interesting situation arises if the L/R-symmetry and the bonding-anti-bonding state symmetries are simultaneously broken for $t_L\neq t_R$ and $\delta\neq$0 leading to a broken $V_g\rightarrow -V_g$ symmetry (see Fig. 2). At B=0 the pronounced difference in the L/R coupling asymmetry of the bonding and anti-bonding states is reflected in the distinct conductance values of the Kondo ridges. With the breaking of the $V_g\rightarrow -V_g$ symmetry the finite-B Kondo ridges are no longer necessarily parallel to the V_g-axis but *bent*. It turns out that the bending direction is always away from the state with stronger total level-lead coupling. For our model this is the state with larger L/R asymmetry. This bending cannot be predicted considering the isolated double-dot as it results from a level renormalization associated with the dot-lead couplings. In experiments on multi-level quantum the states at different energies will have generally different level-lead couplings and finite-B spin Kondo ridges are expected to be bent with respect to the B=0 ones.

The effect of the SOI is shown in Fig. 3 for the symmetric case with a small effective SOI. For the noninteracting single-particle levels of the isolated double dot this implies a small minimal distance between the levels avoiding the crossing at finite B. Therefore remnants of the finite-B Kondo ridges are still observable. Increasing the SOI component perpendicular to the direction of B field by deviating from Θ=0 obviously destroys the finite-B Kondo effect as expected (see inset). This provides a way to probe the presence of SOI in multi-level dots: after observing finite-B spin Kondo ridges one can probe their robustness by changing the direction of B. From the angular dependence of the gap opening in the single-particle energy spectrum the strength of the SOI can be extracted by spectroscopic measurements.

(1) Hewson A.C., The Kondo Problem to Heavy Fermions, (Cambridge University Press, Cambridge, UK, 1993); D. Goldhaber-Gordon et al., Nature 391, 156 (1998).
(2) Meir Y. and N.S. Wingreen, Phys. Rev. B 50, 4947 (1994).
(3) Pustilnik M. et al., Phys. Rev. Lett. 84, 1756 (2000); J. Nygård et al., Nature 408, 342 (2000); W. Izumida et al., Phys. Rev. Lett. 87, 216803 (2001).
(4) Winkler R., Spin-Orbit Coupling Effects in Two-Dimensional Electron and Hole Systems, Springer, Berlin (2003).
(5) Grap S., Andergassen S.; Paaske J., Meden V., Phys. Rev. B 93, 115115 (2011).

Short-range Spin Correlations in Molecular Magnet $\{Mo_{72}Fe_{30}\}$

Z. Fu[1], P. Kögerler[2], U. Rücker[1], Y. Su[3], R. Mittal[3], Th. Brückel[1]

[1]Jülich Centre for Neutron Science JCNS-2 and Peter Grünberg Institut PGI-4, Forschungszentrum Jülich
[2]Institute für Anorganische Chemie, RWTH Aachen University
[3]Jülich Centre for Neutron Science JCNS, Outstation at FRM II

The spin-frustrated molecular magnets have attracted intense interest. As a molecular analogue of the kagome lattice, $\{Mo_{72}Fe_{30}\}$ is one of the largest molecular magnets synthesized to date and represents a highly frustrated spin structure. We investigated the magnetic ground state of $\{Mo_{72}Fe_{30}\}$ by means of diffuse neutron scattering with polarization analysis. We explain the obtained magnetic diffuse scattering successfully within a three-sublattice spin model, which therefore proves to be a good approach to the magnetic ground state of $\{Mo_{72}Fe_{30}\}$.

As the smallest well-defined quantum magnets, molecular magnetic materials have attracted intense interest owning to their fascinating magnetic properties and potential applications in future quantum computing and massive data storage [1]. In molecular magnets, each molecule contains a relatively small number of paramagnetic ions, i.e. spins, interacting via superexchange interactions. The magnetic molecules are well isolated by ligands, so that intermolecular magnetic interactions can be neglected as compared to the dominating intra-molecular interactions. Some of the molecular magnets are ideal systems to observe quantum magnetic phenomena, such as quantum tunneling and quantum coherence. Though most efforts in the field of molecular magnetism have been dedicated to synthesize magnets with high-spin ground states, molecular magnetism is branching out into new areas to explore new types of low-dimensional molecular-based magnets possessing attractive physical properties. In this context, the spin-frustrated molecular magnets allow exotic magnetic ground states and provide valuable test beds for the understanding to geometrical spin frustration from both experimental and theoretical points of view.

As one of the largest molecular magnets ever synthesized, the polyoxomolybdate $\{Mo_{72}Fe_{30}\}$ represents a highly frustrated spin structure with negligible intermolecular interactions. The $\{Mo_{72}Fe_{30}\}$ molecule is shown as the insert of FIG. 3. 30 Fe^{3+} (S = 5/2, L = 0) ions serve as magnetic centers and occupy the vertices of an icosidodecahedron, forming twenty corner-sharing triangles. The 30 spins are antiferromagnetically coupled among nearest neighbors [2]. Despite the difficulty in solving the complete Hamiltonian of this system, an approximate, diagonalizable effective Hamiltonian was adopted to explain the major low-temperature properties of $\{Mo_{72}Fe_{30}\}$ [3]. The classical version of this effective Hamiltonian represents a frustrated ground state spin configuration called the three-sublattice model, where the 30 spins can be divided into three coplanar sublattices with angular spacing of 120° (see the insert of FIG. 3). In order to understand the magnetic ground state of $\{Mo_{72}Fe_{30}\}$, the spin correlations of $\{Mo_{72}Fe_{30}\}$ are investigated quantitatively by means of diffuse neutron scattering with polarization analysis.

The polarized neutron scattering measurements were carried out on deuterated $\{Mo_{72}Fe_{30}\}$ poly-crystals at diffuse neutron spectrometer DNS, FRM II. The incident wavelength is 4.74 Å. Within the quasistatic approximation, the nuclear coherent, spin-incoherent and magnetic scattering cross sections are separated simultaneously with the full *xyz*-polarization method. The absolute scattering intensity from the sample is obtained by the calibration against the spin incoherent scattering from a Vanadium standard.

FIG. 1 shows the nuclear coherent, spin-incoherent and paramagnetic components separated from the total scattering by means of *xyz*-polarization method. The spin-incoherent scattering intensity is nearly constant, suggesting a successful separation of different scattering contributions. The nuclear coherent scattering shows a broad hump at high Q around 1.80 $Å^{-1}$, which can be attributed to the scattering from amorphous crystal water. Several nuclear Bragg peaks are located within the Q range 0.25-1.00 $Å^{-1}$, which are consistent with the simulation of the powder diffraction pattern (marked as the blue line at the bottom of FIG. 1) of $\{Mo_{72}Fe_{30}\}$. The magnetic scattering obtained is almost 40 times smaller than the total scattering intensity, leading to long counting time to acquire reasonable statistics.

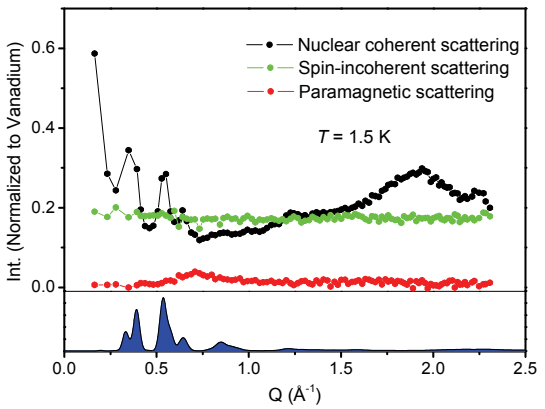

FIG. 1: Nuclear coherent (black circles), spin-incoherent (green circles) and paramagnetic (red circles) contributions to the total scattering of {Mo72Fe30} at 1.5 K from xyz-polarization analysis on DNS. The blue area is the powder diffraction simulation convoluted with experimental resolution.

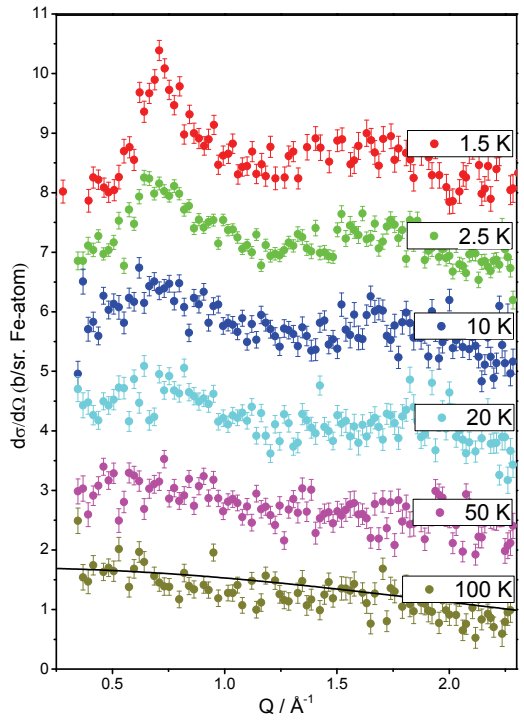

FIG. 2: Temperature evaluation of the differential magnetic scattering cross section $d\sigma/d\Omega$ obtained from DNS measurements on deuterated {Mo72Fe30} polycrystals. The data at different temperatures are displaced vertically by 1.5 b sr^{-1} per Fe atom each for clarity. The solid line is the pure paramagnetic form factor of Fe^{3+} (S = 5/2).

FIG. 2 presents the differential magnetic cross section, $d\sigma/d\Omega$, extracted from the total scattering cross section at 1.5, 2.5, 10, 20, 50, and 100 K from DNS measurements. The magnetic scattering above 50 K agrees with the pure paramagnetic form factor of Fe^{3+} ions (black line in FIG. 2). Below 20 K, a diffuse peak at $Q \approx 0.70$ Å^{-1} is seen to evolve and sharpen upon cooling, indicating the presence of short-range antiferromagnetic spin correlations. No long-range magnetic ordering can be detected even down to 1.5 K owning to the strong geometrical spin frustration of the individual molecules and the lack of intermolecular magnetic interactions.

In order to determine the nature of the short-range magnetic order for the magnetic ground state of {Mo72Fe30}, we compare our experimental data with a simulation based on a rigid three-sublattice spin model consisting of classical $S = 5/2$ Fe^{3+} spins. The analysis of the data starts with the equation given by I. A. Blech and B. L. Averbach in Ref [4] for the differential magnetic scattering cross section of spin pairs, which, already in powder average, can be written as,

$$\frac{d\sigma_{mag}}{d\Omega} = \frac{2}{3}S(S+1)\left(\frac{\gamma e^2}{mc^2}\right)^2 f^2(Q) + \left(\frac{\gamma e^2}{mc^2}\right)^2 \times \sum_n \left[a_n \frac{\sin Qr_n}{Qr_n} + b_n \left(\frac{\sin Qr_n}{Q^3 r_n^3} - \frac{\cos Qr_n}{Q^2 r_n^2} \right) \right],$$

where $(\gamma e^2/mc^2) = -0.54\times10^{-12}$ cm is the magnetic scattering length, S is the spin quantum number of the scattering ion, $f(Q)$ is the magnetic scattering form factor, r_n is the distance from an atom at an arbitrary origin to the nth atom in the same molecule, and a_n and b_n are related to the probability of finding spin pairs with parallel components.

Only the spin correlations within individual molecules are considered in the simulation because the inter-molecular magnetic correlations are negligible. It should be noticed that actually every molecule in the sample could possess a specific ground state within the three-sublattice spin model, because the three spin sublattices can rotate as long as the 120° angle among their unit vectors is fulfilled. Therefore the final simulation should take a numerical average over all versions of the three-sublattice spin model, as shown by the blue line in FIG. 3. The simulation agrees well with the measured profile of the magnetic diffuse scattering.

[1] D. Gatteschi, R. Sessoli and J. Villain, *Molecular Nanomagnets* (Oxford University Press, Oxford, 2006).

[2] A. Müller, *et al.*, *ChemPhysChem* **2**, 517 (2001).

[3] J. Schnack, M. Luban and R. Modler, *Europhys. Lett.* **56**, 863 (2001).

[4] I. A. Blech and B. L. Averbach, *Physics (N. Y.)* **1**, 31 (1964).

Frequency domain studies of current-induced magnetization dynamics in single magnetic-layer nanopillars

N. Müsgens[1,2], S. Fahrendorf[1,2], B. Özyilmaz[1,2], A. Heiss[2], J. Mayer[2], G. Güntherodt[1,2], B. Beschoten[1,2]

[1]II. Institute of Physics, RWTH Aachen University, Otto-Blumenthal-Straße, 52074 Aachen, Germany
[2]Central Facility for Electron Microscopy, RWTH Aachen University, Aachen, Germany

We demonstrate by direct frequency domain measurements that a sufficiently large but unpolarized d.c. current flowing perpendicular to a single thin nanoscale ferromagnetic layer can drive highly coherent GHz oscillations in this layer. We discuss two types of observed spin-wave modes as a function of magnetic field and an unexpected asymmetry with respect to the field polarity. The surprising small mode linewidth down to 4 MHz for Co at room temperature (RT) suggests a high coherence due to nonlocal spin transfer effects. Our results confirm recent predictions of current-induced spin-wave excitations in single magnetic layers.

Recent studies suggest that an unpolarized current passing perpendicular to a single thin ferromagnetic (FM) layer can induce spin-transfer torque effects in this FM layer [1, 2]. Due to spin-filtering effects a current flow through a single ferromagnetic layer embedded into nonmagnetic (NM) leads (NM/FM/NM trilayer) creates a spin accumulation of opposite sign on both sides of the ferromagnet. Spin diffusion in the normal-metal electrodes perpendicular to the current-flow direction, not included in the Slonczweski model [3], along with a nonuniform magnetization, results in a spin torque at each side of the ferromagnet. The direction of the torque is to align the magnetization with the direction of the accumulated spins. For symmetric systems both torques are equal in magnitude and hence cancel each other. Asymmetric leads break the symmetry of the trilayer and generate a net torque on the magnetization. Additional inhomogeneities of the magnetization normal to the thin film plane enhance the asymmetry of the system thus increasing the acting torque. This mechanism allows a single ferromagnetic layer with inhomogeneous magnetization to exert a spin transfer torque on itself and thus to excite spin wave excitations for one current polarity only [1].

The studies discussed here were performed on single magnetic-layer asymmetric nanopillars [4] consisting of 10 nm Cu/15 nm Co/150 nm Cu layer stack with either circular (diameter ~ 40 nm) or elliptical (30 × 90 nm2) cross-section.

The device is connected to microwave probes and a dc current flows through a bias-tee, along with a 100 µA ac current. The high frequency components of the resistance changes due to magnetization dynamics are analyzed using a spectrum analyzer with a bandwidth of the circuit of $0.1 \le f \le 20$ GHz. The electron flow from the thick to the thin Cu layer lead, known to cause a destabilizing torque, is defined as the negative current polarity. All measurements are performed at room temperature and for each power spectrum $\Delta P(I, H)$ presented the current independent background noise has been subtracted.

Typical changes in the differential resistance dV/dI as a function of current bias are shown in Fig. 1 (a). To better visualize the current and field

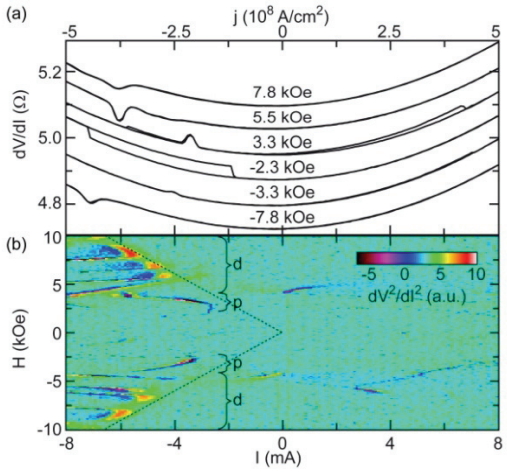

FIG. 1: Differential resistance of a circular shaped single Co-layer Cu/Co/Cu nanopillar (d ~ 40 nm) as function of magnetic field aligned in the out-of-plane direction. (a) Differential resistance dV/dI vs. I for representative magnetic field values. (b) False color plot of d^2V/dI^2 vs. I and H varying between ±10 kOe. The black dashed line indicates the boundary of the resistance features; p and d denote the peak and dip regimes in dV/dI in (a), respectively.

dependence of these resistance changes and for a better distinction from the parabolic background we plot in Fig. 1(b) the second derivative (d^2V/dI^2) color coded as a function of current and applied magnetic field. For increasing field values we first observe peaks in the differential resistance, which represent an increase in junction resistance. These features shift with increasing fields to higher negative current values. The opposite dependence is observed for the dips, appearing at slightly higher magnetic fields, which indicate a decrease in junction resistance. Such resistance changes have been theoretically attributed to spin-wave excitations.

For microwave emission analysis we first consider the microwave spectrum of the circular sample for H = −3.3 kOe and currents from −4 mA to −8 mA (Fig. 2(a)). At I = −4.8 mA, slightly beyond the peak observed in the differential resistance (Fig. 2(b), bottom), we begin to resolve a microwave signal at ~ 2.23 GHz. As the current is increased in magnitude the initial signal grows in amplitude and shifts to smaller frequencies until I ~ −6.8 mA, beyond which the excitation frequency increases again. The very narrow linewidth of down to 4 MHz for Co at RT (Fig. 2(a) inset) demonstrates the unexpected high coherence of the observed magnetization dynamics. As can be seen in Fig. 2(b) the above described "low" frequency dynamics is representative for the peak regime (compare Fig. 1(b)). The onset of microwave emission shifts to higher negative current values for increasing absolute fields consistent with the shift of the peak position in d2V/dI2.

Besides the "low-f" mode an additional high frequency mode is observed (Fig. 3(a)). The onset of the "high-f" mode is related to a decrease in dV/dI vs. I near −4 mA (bottom panel of Fig. 3(a)) and does not correspond to a higher harmonics of the "low-f" mode. The frequency of this high-f mode with a typical linewidth of ~ 10 MHz near I = −5 mA

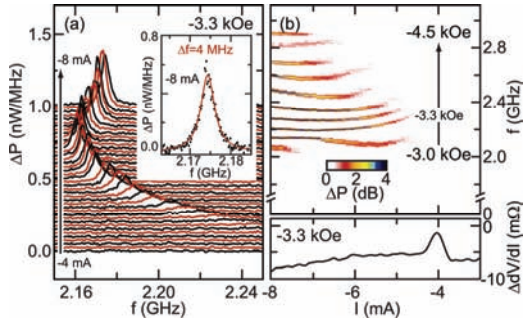

FIG. 2: Spectra of emitted microwave power ΔP(I,H,f) for a circular nanopillar at room temperature. (a) ΔP(f) for H = −3.3 kOe and −8 mA < I < −4 mA (curves are shifted for clarity); inset: Lorentzian fit to the spectra taken at I = −8 mA. (b) Current dependence of the microwave power density in logarithmic scale of selected mode frequencies at different field values; bottom: ΔdV/dI (parabolic background subtracted) vs. I at H = −3.3 kOe.

increases linearly with increasing negative current. The microwave signal exhibits a frequency jump near −6 mA linked to a strong dip in the differential resistance. The jump is attributed to transitions between different excited spin-wave modes as theoretically predicted [1], and the high-f mode vanishes for further increasing fields. In comparison to single mode excitations the modes in the bistability regime have broader linewidths of 10 MHz and 90 MHz for the low-f and high-f mode, respectively, at I = −8 mA and H = 5.5 kOe. This indicates a decrease in temporal coherence

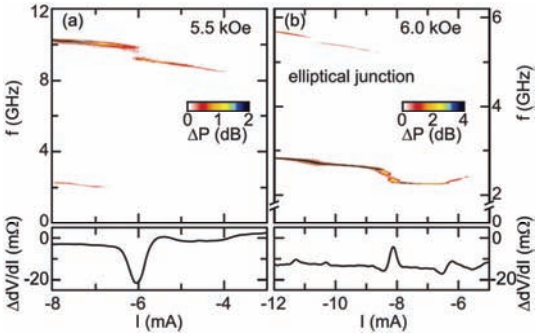

FIG. 3: Spectra of emitted microwave power ΔP(I,H,f) for a circular (a) and elliptical (b) nanopillar at room temperature. (a) Emitted microwave power density of mode frequencies at H = 5.5 kOe as function of current; bottom: ΔdV/dI vs. I at H = 5.5 kOe. (b) Microwave peaks power density vs. I of mode frequencies at H = 6.0 kOe; bottom: ΔdV/dI vs. I at 6 kOe.

In conclusion, we have demonstrated the excitation of highly coherent spin waves in single FM layer nanopillars by an unpolarized current for out-of-plane magnetic fields. Consistent with theoretical predictions the excitation takes place for one current polarity only. Dynamical modes at different frequencies are found for circular and elliptical cross sections of the nanopillars.

Work supported by DFG through SPP 1133.

[1] M. Stiles *et al.*, Phys. Rev. B **69**, 054408 (2004); M.L. Polianki *et al.*, Phys. Rev. Lett. **92**, 26602 (2004).

[2] B. Özyilmaz *et al.*, Phys. Rev. Lett. **93**, 76604 (2004).

[3] J.C. Slonczewsi, J. Magn. Magn. Mater. **195**, L1(1996); L. Berger, Phys. Rev. B **54**, 9353 (1996).

[4] B. Özyilmaz *et al.*, J. Appl. Phys. **101**, 063920 (2007), N. Müsgens *et al.*, J. Phys. D: Appl. Phys. **41**, 164011 (2008).

Ab Initio Design of Magnetic Properties at Hybrid Organic-Ferromagnetic Interfaces

N. Atodiresei[1], V. Caciuc[1], P. Lazic[2], S. Blügel[1,3]

[1]IAS-1/PGI-1: Institute for Advanced Simulation and Peter Grünberg Institut Quantum Theory of Materials, Forschungszentrum Jülich, 52425 Jülich
[2]Massachusetts Institute of Technology, Cambridge, 02139 Massachusetts, USA
[3]JARA-HPC

Conceptual theoretical studies have been performed in order to understand how to precisely manipulate the local spin-polarization present at the interface formed between organic molecules and a ferromagnetic surface. Although adsorbed molecules might be nonmagnetic, due to an energy dependent spin-polarization, in a given energy interval the molecules have a net magnetic moment delocalized over the molecular plane. As a consequence, near the Fermi level, at the molecular site an inversion of the spin-polarization with respect to the ferromagnetic surface might occur. As a key result, we demonstrate the possibility to selectively and efficiently inject spin-up and spin-down electrons from a ferromagnetic-organic interface, an effect that can be exploited in future spintronic devices.

Merging the concepts of molecular electronics with spintronics opens a very exciting avenue in designing and building future nanoelectronic devices. In this context, the design of nanoscale spintronic elements in multifunctional devices relies on a clear theoretical understanding of the physics at the electrode molecule interfaces and in particular, the functionality of specific molecules in a given organic-metal surface environment. The density functional theory (DFT) provides a framework where a realistic understanding of these systems with predictive power can be expected.

In a first step, we performed *ab initio* calculations of prototype conjugated organic molecules adsorbed on a ferromagnetic 2 ML Fe/W(110) surface, a well established system in spin-polarized scanning tunneling microscopy (SP-STM) experiments. We selected organic molecules containing $\pi(p_z)$-electron systems like benzene (Bz), cyclopentadienyl radical (Cp), and cyclooctatetraene (Cot) because they are representative of classes of organic molecules with significantly different reactivities. As a general feature of the adsorption geometry, we note that all adsorbed molecules have a nonplanar structure in which the H atoms are situated above C atoms (0.35 up to 0.45 Å). The shortest C-Fe bond is about 2.1 Å and corresponds to the C atoms sitting directly on top of Fe while the C atoms situated in bridge positions are 2.3 up to 2.5 Å away from Fe atoms. Furthermore, each of the molecules is nonmagnetic upon adsorption on the ferromagnetic surface.

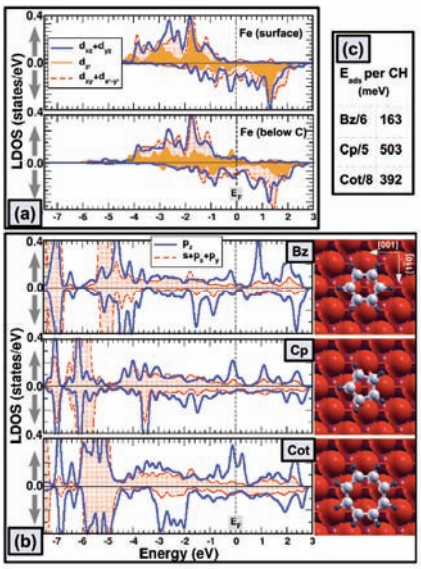

FIG. 1 (a) Spin-resolved local density of states of an Fe atom at the pristine surface (upper panel) and an Fe atom below the C atom of the Cot molecule (lower panel); (b) adsorption geometries and the spin-resolved local density of states of the Bz, Cp and Cot molecules adsorbed on the 2ML Fe/W(110); (c) the adsorption energies of the Bz (C6H6), Cp (C5H5) and Cot (C8H8) molecules.

A general picture of the binding mechanism between Bz, Cp, and Cot molecules and the ferromagnetic surface can be extracted from the analysis of the spin-resolved local density-of-states (LDOS) of the calculated molecule surface systems shown in Fig. 1. In the spin-up channel, the p_z atomic type orbitals, which originally form the π-molecular orbitals hybridize with the majority d states of the Fe atoms forming molecule-metal hybrid combinations with bonding and antibonding character. The bonding states are situated at low energies while the antibonding combinations appear at much higher energies, more precisely in an energy window situated around the Fermi level. The spin-polarized LDOS of the adsorbed Bz, Cp, and Cot molecules show a very intriguing feature: the energy dependent spin polarization.

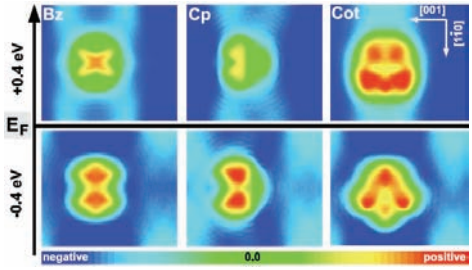

FIG. 2: The spin polarization above the Bz, Cp and Cot molecules adsorbed on the 2ML Fe/W(110) surface plotted for occupied ([-0.4, 0.0] eV) and unoccupied ([0.0, 0.4] eV) energy intervals around the Fermi level. All the organic molecules show a high, locally varying spin polarization ranging from attenuation to inversion with respect to the ferromagnetic Fe film.

As clearly visible in Fig. 1(b), for a given energy interval the number of spin-up and spin-down states is unbalanced. For that specific interval the molecule has a net magnetic moment delocalized over the molecular plane since it is carried mostly by the p_z states. Even more interesting, as depicted in the LDOS, around the Fermi level the states with large weight are in the spin-up channel at the molecular site, while on the clean Fe surface these states are in the spin down channel. As a consequence, at the molecular site an inversion of the spin polarization occurs with respect to the ferromagnetic surface. This effect is clearly seen in Fig. 2 which illustrates the spin polarization at 2.5 Å above the molecule in the energy intervals below [-0.4, 0.0] eV and above [0:0, 0.4] eV the Fermi level. A common characteristic for all the molecule-ferromagnetic surface systems is the high and locally varying spin polarization ranging from attenuation to inversion with respect to the ferromagnetic surface [1].

To demonstrate here the universal applicability of the theory driven concept, we apply in a second step spin polarized scanning tunneling microscopy (SP-STM) [2] to directly observe with site sensitivity the spin polarization above a cobalt-phthalocyanine molecule (CoPc), adsorbed on out-of-plane magnetized 2 ML Fe/W(110).

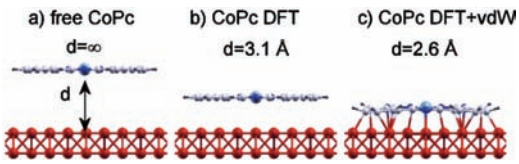

FIG. 3: The geometry and electronic structure for an isolated CoPc (a) and adsorbed on an Fe surface (b) without and (c) with vdW forces included during the relaxation.

Optimized molecule-surface geometries for the first-principles calculations were obtained by including long-range van der Waals interactions during the relaxation, leading to an excellent agreement of theoretical and experimental data. The role of van der Waals forces is crucial as it brings the molecule 0.5 Å closer to the surface and distorts the molecular geometry (see Fig. 3). This new adsorption geometry has a drastically different electronic structure due to the overall changes of hybridization between molecule and substrate. The newly formed molecule-surface hybrid states have, within a given energy interval, an unbalanced, locally varying electronic charge in the up and down channels which is mapped in SP-STM. For a direct comparison of the first-principles calculations with constant-current SP-STM images, isocharge surfaces above the CoPc are extracted from the spatial variation of the energy integrated spin polarized local density of states (SP-LDOS). This approach mimics the experimental situation of a local and spin-sensitive tip probing the charge density above the surface at constant current and thereby, accounts for the variation of decay lengths of the different states into vacuum (see Fig. 4). Only when the van der Waals relaxed adsorption geometry is used we find an excellent agreement of experimental findings and DFT calculations. Remarkably, not only reduction of but also inversion and amplification of the local spin polarization can equally be observed.

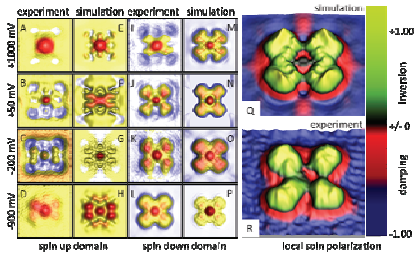

FIG. 4: Experimental and simulated SP-STM images at different bias voltages for both spin directions (A-P) and local spin polarization maps (Q,R).

To summarize, the spin polarization of a ferromagnetic surface can be locally tailored by flat adsorbing organic molecules containing $\pi(p_z)$-electron onto it. Although adsorbed molecules are nonmagnetic, due to an energy dependent spin polarization, in a given energy interval the molecules have a net magnetic moment delocalized over the molecular plane. Therefore, the local spin polarization is identified as a unique property of the molecule-substrate hybrid states. Our *ab initio* study demonstrates that electrons of different spin [i.e., up and down] can selectively be injected from the same ferromagnetic surface by locally controlling the inversion of the spin polarization close to the Fermi level. Ultimately, this allows us to precisely engineer the magnetic properties of hybrid organic-ferromagnetic interfaces that can be further exploited to design more efficient spintronic devices based on organic molecules.

The theoretical calculations have been performed on JUROPA and JUGENE supercomputers at the Jülich Supercomputing Center, Forschungszentrum Jülich.

[1] N. Atodiresei, J. Brede, P. Lazic, V. Caciuc, G. Hoffmann, R. Wiesendanger, S. Blügel, Phys. Rev. Lett. 105, 066601 (2010).

[2] J. Brede, N. Atodiresei, S. Kuck, P. Lazic, V. Caciuc, Y. Morikawa, G. Hoffmann, S. Blügel, R. Wiesendanger, Phys. Rev. Lett. 105, 047204 (2010).

[3] P. Lazic, N. Atodiresei, M. Alaei, V. Caciuc, R. Brako, S. Blügel, Comp. Phys. Comm. 2010, 181, 371.

Injection locking of the gyrotropic vortex motion in a nanopillar

R. Lehndorff[1], D. E. Bürgler[1], P. Grünberg[1], C. M. Schneider[1], Z. Celinski[2]

[1]PGI-6: Electronic Properties, Forschungszentrum Jülich, 52425 Jülich
[2]Center for Magnetism and Magnetic Nanostructures, University of Colorado at Colorado Springs, USA

Spin-torque oscillators (STO) are a promising application for the spin-transfer torque effect. The major challenge is to increase the microwave output power by synchronizing an array of STOs. We study the effect of external high-frequency signals on the current-driven vortex dynamics and demonstrate injection locking of the gyrotropic mode as a prerequisite for STO synchronization.

The action of spin-polarized currents on a magnetic system – the spin-transfer torque – offers a novel handle on magnetization dynamics. One of the potential applications is seen in spin-torque oscillators (STO). These are pillar-shaped structures with a "fixed" magnetic layer acting as a polarizer for the electric current and a second "free" magnetic layer the magnetization of which oscillates under the impact of the spin-polarized current. The magnetoresistive response due to giant or tunnelling magnetoresistance (GMR, TMR) in the magnetic layered structure turns the nanometre-scaled STO structures into sources for high-frequency (HF) signals in the GHz range. The HF is tunable via the direct current (DC) and the external magnetic field. However, the HF output power of an STO is presently far too low for applications. Ongoing research aims at strategies to significantly increase the output power. The excitation of an array of STOs in a synchronized, phase-locked manner is believed to deliver a significant power increase, as N coherently coupled STOs emit up to the N^2-fold power. The required STO-STO coupling can be achieved in two ways. The first mechanism involves spin waves in a common ferromagnetic layer. However, this interaction is short-range due to the fast decay of spin waves and requires a STO-STO separation clearly below 1 µm. The second coupling mechanism via microwaves propagating in common electrodes permits a larger STO separation, because electrical microwave signals propagate with negligible losses over long distances. Experimentally, this situation can be addressed by injection locking experiments [1], which study the interaction of a STO with an externally applied HF signal. Here we demonstrate phase-locking of the DC current-driven gyrotropic vortex motion in a vortex STO to external HF signals, and derive from the HF amplitude dependence of the locking criteria for the required STO output power for synchronization [2].

We fabricate cylindrical pillars of 230nm diameter by optical and e-beam lithography from multilayers of Ag 150 nm/Fe 2 nm/Ag 6 nm/Fe 20 nm/Au 50nm grown by molecular beam epitaxy. The upper Fe layer and the Au cap form the pillar, while the remaining Ag/Fe/Ag layers constitute the bottom electrode (inset of Fig. 1). The electrode layout allows for contacting by two microwave probes via coplanar waveguides. One is used to inject a DC current and an HF current (f_{ext}) from a network analyzer. The second probe is connected to a 30 dB amplifier and a spectrum analyzer (see Fig. 2). In Fig. 1 we compare GMR measurements with corresponding micromagnetic simulations. The quasi-uniform onion state occurs when the field is reduced after saturation and the vortex state nucleates at low fields after field reversal. The magnetization of the extended layer is saturated along an easy axis for fields larger than 20 mT [3]. Thus, we are able to prepare a vortex state in the nanodisk while the magnetization of the extended layer is saturated along a magnetic easy axis of bcc Fe, e.g. by applying +25 mT after negative saturation. Positive DC currents (i.e. electron flow from the nanomagnet to the extended layer) excite the vortex state by spin-transfer torque into the gyrotropic mode that shows up as an HF voltage signal of about 1 GHz due to the GMR response of the Fe/Ag/Fe trilayer. By adding a HF component to the driving current we are able to demonstrate phase-locking of the DC current-induced gyrotropic motion to electric HF signals even if they are slightly out of tune. Figure 2 shows a measurement, where the vortex was excited by a current of 32 mA to a frequency of f_{osc}=1.518 GHz, while an external signal of -17 dBm or 20 µW was swept from f_{ext}=1.35 to 1.7 GHz. This leads to a clear shift of the vortex frequency f_{osc} between 1.42 and 1.61 GHz. From 1.46 to 1.57GHz f_{osc} is completely locked to the external signal f_{ext} and is thus masked by it. In order to evaluate the synchronization behaviour we fit the frequency variation f_{osc} of the forced vortex motion with the frequency f_{ext} of the

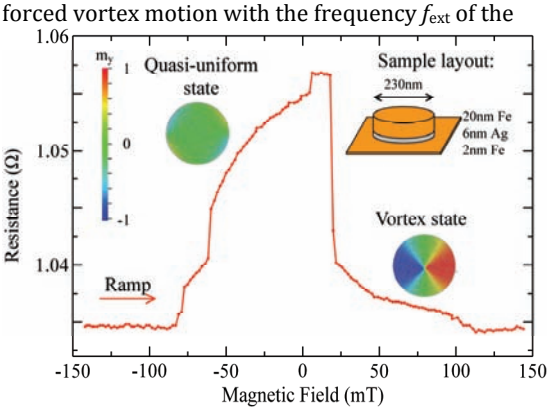

FIG. 1: *CPP-GMR in comparison with micromagnetic calculations of the magnetization structure in the nanodisk. Inset: Sample layout.*

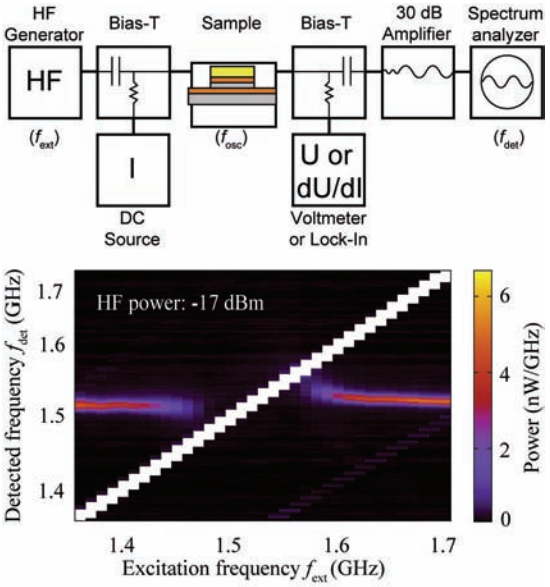

FIG. 2: *Setup for injection locking and power spectra (f_{det}, vertical axis) of the current-induced gyrotropic mode as a function of HF excitation frequency (f_{ext}, horizontal axis). The power at f_{ext} exceeds the colour scale and appears as a diagonal white line.*

injected HF signal to a formula derived by Slavin and Tiberkevich for nonlinear oscillators [Eq. (48b) of Ref. [4]]:

$$f_{osc} = f_{ext} + \mathrm{sign}(f_0 - f_{ext})\sqrt{(f_0 - f_{ext})^2 - \Delta^2}, \quad (1)$$

where $f_0=f_{osc}(I_{HF}=0)$ is the frequency of the free-running vortex STO and Δ is the phase-locking range. An example of a fit is shown in the inset of Fig. 3. The main figure shows an increase of Δ with increasing amplitude of the external signal in accordance with the linear dependence predicted by Slavin and Tiberkevich [4]. However, the linear extrapolation to zero excitation amplitude (dashed line in Fig. 3) yields a non-vanishing locking range of about 18 MHz. This inconsistency may arise from the assumption of weak excitation in the theoretical model. Figure 4 shows the locking behaviour of the vortex STO when excited by a fixed DC current of 32 mA and an external 1.55 GHz signal of variable amplitude. For weak excitation the STO is not

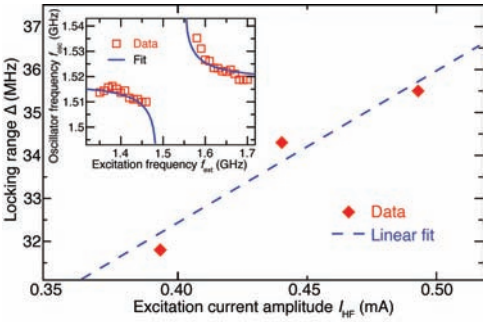

FIG. 3: Locking range Δ as a function of the external HF excitation amplitude. Inset: Fit of Eq. (1) to the locking behaviour for IDC=32mA and -16 dBm

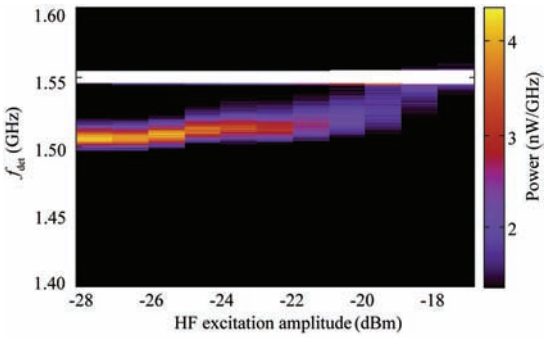

FIG. 4: *Locking behaviour of a vortex STO as a function of the HF excitation amplitude at f_{ext}=1.55 GHz and I_{DC}=32 mA. Locking occurs at about -18 dBm..*

influenced and emits at its free-running frequency f_0≈1.52 GHz. With increasing HF amplitude the STO tends to adjust to the external frequency and phase-locks for excitation amplitudes exceeding -18 dBm. We estimate the external HF power at -18 dBm reaching the pillar to be of the order of 1.3 μW and the microwave power generated by the vortex STO to roughly 0.4 nW. This low value is related to the low absolute resistance and GMR ratio, which result in small resistance changes induced by the magnetization dynamics. Consequently, the output power of our GMR-based vortex STO is about 3 orders of magnitude too small to phase-lock another vortex STO. Under these conditions synchronization of an array of vortex STOs seems unlikely, unless the output power of each single STO is significantly increased, e.g. by employing highly spin-polarized ferromagnetic electrode materials (Heusler alloys) or TMR structures with much larger MR ratios.

In conclusion, we demonstrated phase-locking of the current-driven vortex motion in an STO to an external HF signal, being a prerequisite for the synchronization of vortex STOs. The relative locking range $2\Delta/f_0$≈5% allows for a distribution of free-running frequencies in a STO array, which seems compatible with present fabrication technology. The power requirements for synchronization, however, call for STOs with much higher output power.

[1] W. H. Rippard, M. R. Pufall, S. Kaka, T. J. Silva, S. E. Russek, and J. A. Katine, Phys. Rev. Lett. **95**, 067203 (2005).

[2] R. Lehndorff, D. E. Bürgler, C. M. Schneider, and Z. Celinski, Appl. Phys. Lett. **97**, 142503 (2010).

[3] R. Lehndorff, D. E. Bürgler, S. Gliga, R. Hertel, P. Grünberg, and C. M. Schneider, Phys. Rev. B **80**, 054412 (2009).

[4] A. Slavin and V. Tiberkevich, IEEE Trans. Magn. **45**, 1875 (2009).

Anisotropic anomalous and spin Hall effects from first principles

Y. Mokrousov

IAS-1: Institute for Advanced Simulation – Quantum Theory of Materials and JARA-HPC , Forschungszentrum Jülich, 52425 Jülich

The importance of various types of the Hall effects for technology and spintronics applications is constantly rising. However, it was noticed just recently that one of the intrinsic and fundamental properties of the transverse conductivity tensor is its extremely large anisotropy. Such an anisotropy was first explained by us from the first principles for the anomalous Hall effect in uniaxial hcp Co, and was also demonstrated for ordered FePt alloy. Recently, we also predicted the occurrence of such anisotropy for the spin Hall conductivity tensor in any non-cubic metal or antiferromagnet, owing to its broken symmetry by magnetization. In a situation of a profoundly anisotropic conductivity tensor, a number of interesting phenomena can arise, and new technological functionalities can be achieved.

The energy scale of the spin-orbit interaction (SOI) in solids is normally considered small, however, it gives rise to many phenomena of technological importance and general interest – the well-known examples are the magnetocrystalline anisotropy energy and anisotropic magnetoresistance. The anomalous part of the Hall effect (AHE) results from the spin-dependent transverse velocities that charge careers acquire in the presence of a longitudinal electric field due to SOI [1]. In paramagnets the spin-dependent transverse velocities of spin-up and spin-down electrons are exactly opposite generating a transverse pure spin current, which is known as the spin Hall effect (SHE). And while the anomalous Hall effect, besides wide applications in magnetism, is famous for its topological origin owing to the relation between the Berry curvature of electrons in a solid and the anomalous velocity [1], the SHE allows to access the spin degree of electron without making use of magnetism and is believed to play an important role in future generation of spintronic devices.

In 2009 [2] we demonstrated that the intrinsic, Berry curvature driven anomalous Hall conductivity (AHC) exhibits a very large anisotropy as function of the magnetization direction in the crystal of uniaxial ferromagnets, appearing already in the first order with respect to directional cosines. Taking as an example elemental hcp Co, we demonstrated from *ab initio* that the ratio of the AHCs for the out-of-plane and in-plane directions of the magnetization constitutes a large value of 4, in accordance to available experimental measurements for this when acting on it, while the former preserves its spin thus keeping spin as a good quantum number.

material. Such strong angular dependence of the AHC is necessary to take into account when comparing to measurements performed on polycrystalline samples, as shown for Co [2]. Moreover, we also showed how the anisotropic AHC can be directly related to the temperature dependence of the AHC. When analyzing the energy distribution of the AHC calculated via the linear response Kubo formula, it was also possible to relate the AHC anisotropy to the low-energy interband electronic transitions [2].

Recently, we undertook a study of the intrinsic AHE in ordered L10 FePt alloy. In a combined experimental and theoretical work, we showed that in samples of FePt with a small degree of disorder the intrinsic Berry curvature contribution is dominant, and accounts to as much as 70% of the experimentally measured Hall signal [3]. This makes this material promising from a technological point of view due to its high magnetic anisotropy energy and high Kerr rotation, and a playground for testing different ideas in the field of Berry phase related phenomena. In particular, we analyzed the AHC anisotropy in this compound, and found it to be very large, with the values of the AHC for the out-of-plane and in-plane magnetization of 818 and 409 S/cm, respectively, which can be traced back to the uniaxiality of this alloy [4]. Additionally, we decomposed the SOI in FePt into spin-conserving and spin-flip parts, of which the latter flips the spin of the electronic wavefunction

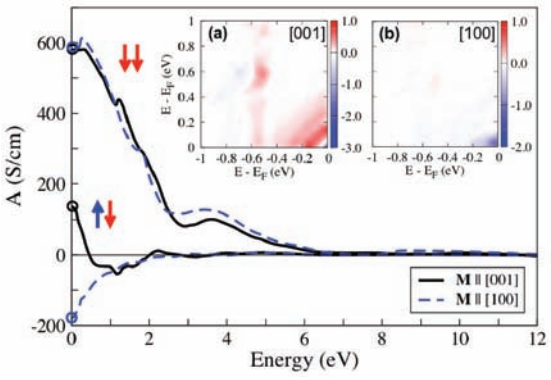

*FIG. 1: Cumulative contribution to the anomalous Hall conductivity of FePt from spin-flip (up-down arrows) and spin-conserving (down-down arrows) dichroic spectra above energy ω. The two insets display the energy-energy density of contributions to the spin-flip conductivity for **M** along [001] and [110] directions (in 10^5 a.u./eV²).*

The magnitude of the spin-flip SOI determines the "spin-purity" of the spin and charge currents arising in the AHE and SHE.

For FePt we found that the spin-flip part of SOI solely determines the magnitude of the AHC anisotropy in this alloy. Moreover, we also found that the structure of the spin-flip AHC is quite different from the spin-conserving AHC. By analyzing the contributions to the AHC from states separated by an energy larger than ω, the so-called cumulative AHC $A(\omega)$, we demonstrated that while the spin-conserving transitions are "smeared" over a region of energy of several eV, the spin-flip transitions are localized much closer to the Fermi energy on the scale of the SOI strength of the system, c.f. Fig. 1. By referring to the density of transitions between states of certain occupied and unoccupied states (inset of Fig. 1), it also became possible to track down the so-called "ladder" transitions to the spin-flip AHC between the bands of similar dispersion crossing the Fermi energy. Such transitions, unaccounted for previously, can provide a source of the effective magnetic field in reciprocal space, complementary to well-known "monopole" degeneracies at the Fermi level. When scaling the spin-orbit strength of Pt atoms, we also understood that the pronounced role of the spin-flip transitions in FePt stems from the large SOI of Pt, which led us to the general conclusion that in materials containing heavy ions, the spin-flip transitions cannot be neglected [4].

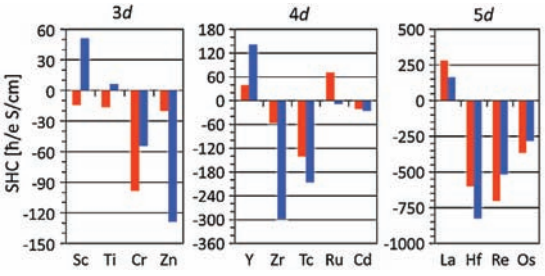

FIG. 2: For hcp metals Sc, Ti, Zn, Y, Zr, Tc, Ru, Cd, La, Hf, Re, Os and antiferromagnetic Cr the spin Hall conductivities σ_{xyz} and σ_{zxy} are shown as red and blue bars, respectively. The change of sign in the values of the conductivities can be observed for Sc, Ti and Ru. For these metals the collinearity of the spin polarization with the electric field or with the direction of the measurement can be achieved.

One of the most interesting manifestations of the anisotropy of the transverse conductivity was predicted by us theoretically from the first principles for the intrinsic spin Hall effect [5]. Within the AHE, changing the magnetization direction in the crystal changes the electronic structure of the crystal itself, resulting in a strong anisotropy of transport, discussed previously. In the SHE of paramagnets, there is no magnetization to control, however, the spin-polarization of the induced spin current depends on the direction along which this current is measured. The SHE is called to be anisotropic if the magnitude of the spin current depends on the direction of the spin polarization of this current [5].

By performing first principles linear response calculations we found that the anisotropy of the SHE, although completely absent in cubic metals, can be very large in non-cubic materials, as can be clearly seen from Fig. 2, in which two different transverse components of the spin conductivity tensor are shown in red and blue (for the in-plane and out-of-plane spin-polarization of the spin current). We can clearly see from this figure that almost all non-cubic 3*d*, 4*d* and 5*d* transition metals exhibit a large anisotropy of the SHE. In this respect it seems particularly fruitful to underline that in antiferromagnets of any crystal structure and given direction of the local magnetization, the SHE is always anisotropic (c.f. case of Cr in Fig. 2) [5].

From Fig. 2, the change of sign of the conductivity when the spin polarization of the current is rotated from the out-of-plane to in-plane direction can be seen for Sc, Ti and Ru. This marks the occurrence of the so-called anti-ordinary spin Hall effect [5]. In the anti-ordinary spin Hall effect, when rotating the electric field (the direction along which the spin current is measured), a complete collinearity between the spin polarization of the current and the electric field (direction of the spin current) can be achieved for a certain "magic" angle in the crystal, which is determined only by the values of the two conductivities. Additionally, for Ru, one can see that in complex transition metals it is possible to achieve the effect of the *colossal* anisotropy of the SHE, when upon rotation of the spin polarization of the current, a complete (or an order of magnitude) quenching of the spin current is possible.

At the end, we can conclude, that the anisotropic nature of the transverse transport of various kind, such as anomalous, spin, ordinary Hall effects etc., is a general phenomenon which stems from a intrinsically anisotropic structure of the off-diagonal conductivity in systems with symmetry broken by geometry, magnetization, etc. [5] Practically, the anisotropy of the Hall effects gives us an additional degree of control over spin-polarized transport properties of complex materials.

[1] N. Nagaosa, J. Sinova, S. Onoda, A. H. MacDonald and N. P. Ong, Reviews of Modern Physics **82**, 1539 (2010)

[2] E. Roman, Y. Mokrousov and I. Souza, Physical Review Letters **103**, 097203 (2009)

[3] K. M. Seemann, Y. Mokrousov, A. Aziz, J. Miguel, F. Kronast, W. Kuch, M. G. Blamire, A. T. Hindmarch, B. J. Hickey, I. Souza and C. H. Marrows, Physical Review Letters **104**, 076402 (2010)

[4] H. Zhang, F. Freimuth, S. Blügel, Y. Mokrousov and I. Souza, Physical Review Letters **106**, 117202 (2011)

[5] F. Freimuth, S. Blügel and Y. Mokrousov, Physical Review Letters **105**, 246602 (2010)

Synthesis and Theory of Correlated Transition-Metal Carbodiimides

X. Tang[1], A. L. Tchougréeff[1,2], R. Dronskowski[1]

[1]Institute of Inorganic Chemistry, RWTH Aachen University
[2]Poncelét Laboratory, Independent University of Moscow, Moscow Center for Continuous Mathematical Education, Russia

Recent synthetic studies targeted at the carbodiimides of the di- and trivalent transition metals have succeeded in the novel antiferromagnetic *M*NCN (*M* = Mn, Fe, Co, Ni) and ferromagnetic $Cr_2(NCN)_3$ phases, a major breakthrough in exploratory solid-state chemistry. Although $Cr_2(NCN)_3$ adopts the same crystal structure as its antiferromagnetic oxide counterpart Cr_2O_3, both experiment and GGA+*U* electronic-structure theory show that $Cr_2(NCN)_3$ is ferromagnetic. Its saturation magnetization is larger than the one of the most prominent oxide ferromagnet, maghemite. By contrast, the *M*NCN case is less simple in terms of theory. While GGA+*U* theory reproduces the experimentally observed insulating behavior for *M* = Mn, Co, and Ni, a (semi)metallic state is falsely predicted for FeNCN. Upon employing the local many-particle effective Hamiltonian crystal field method, the ground states, the excitation spectra and the insulating behavior have been successfully predicted for the entire *M*NCN series.

Extended pseudochalcogenides such as the solid-state carbodiimides incorporating NCN^{2-} units have been extensively investigated within the recent years, and new routes for synthesizing the entire *M*NCN series of the divalent 3*d* metals have been found. For an overview, see Ref. 1 and the references within. In a nutshell, the antiferromagnetic properties of these *M*(II) carbodiimides are similar to those of the corresponding oxides, simply because the carbodiimide anion replaces the oxide anion in the spirit of a "divalent nitride" ion. Fortunately enough, the very existence of the 3*d* transition-metal carbodiimides and their metastable thermochemical character had been predicted on the basis of approximate density-functional calculations prior to their syntheses.

Within the last year, the first transition-metal(III) carbodiimide has now been synthesized [2]. Once again, the difficulty lies in chosing the right preparative conditions: green $Cr_2(NCN)_3$ results from a metathesis between $CrCl_3$ and ZnNCN at 300 ºC under dynamic vacuum for 12 h, followed by another heat treatment at 550 ºC for additional two days. The crystal-structural determination on the basis of high-resolution powder X-ray diffraction yields isotypism with chromium(III) oxide and the corundum type. Surprisingly enough, $Cr_2(NCN)_3$ exhibits ferromagnetic properties, in contrast to all other transition-metal carbodiimides and, also, the isotypical oxide.

The hexagonal crystal structure of chromium(III) carbodiimide corresponds to a formally layered structure with each layer consisting of alternating Cr(III) and carbodiimide ions along the *c* axis, similar to the transition-metal(II) carbodiimides. Figure 1 (left) shows the octahedral coordination of the trivalent chromium cation, corresponding to a distorted N_6 octahedron with practically identical Cr—N bond lengths of about 2.09 Å. The 2:3 stoichiometry ensures that each N atom, on the other side, bonds only to two Cr. The practically linear NCN^{2-} ion experiences a distorted tetrahedral coordination by the Cr(III) ions and adopts the symmetrical carbodiimide shape with C—N = 1.21 Å (Figure 1, right).

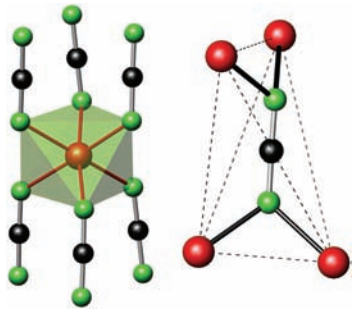

FIG. 1: The octahedral coordination environments of the red Cr^{3+} cation (left) and distorted tetrahedral coordination of the carbodiimide anion (right) with nitrogen atoms in green and carbon atoms in black.

The magnetic susceptibility data of $Cr_2(NCN)_3$ were determined at magnetic fields up to 0.5 T between 2 and 400 K (Figure 2). Chromium(III) carbodiimide is characterized by a hysteretic magnetization with a coercivity H_c of ca. 0.01 T (100 Oe) and a saturation magnetization of close to 3.5 μ_B. The small coercivity of the new compound is quite typical for a magnetically soft material. In addition, the inverse susceptibility versus temperature plot in the temperature range beyond 200 K manifests a positive paramagnetic Curie temperature, and a linear fit to the Curie–Weiss law in that region arrives at a θ value of 178 K (Figure 2). The experimentally derived paramagnetic moment arrives at 3.6 μ_B which is quite close to an ideal octahedral $3d^3$ high-spin system. Note that 3.87 μ_B is expected for a $^4A_2$ ground state with three unpaired electrons. We also note that at low temperatures, the

novel phase shows a slightly larger specific magnetization than maghemite, the world's most important ferromagnetic oxide.

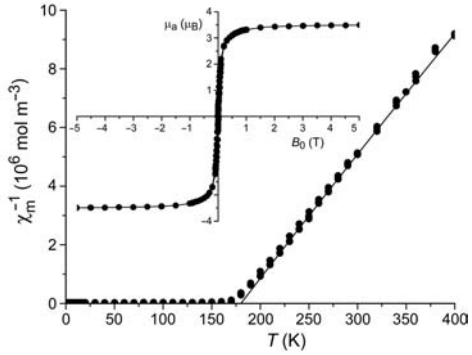

FIG. 2: Reciprocal magnetic susceptibility as a function of the temperature and hysteretic loop (insert) of chromium carbodiimide.

To theoretically model the here found ferromagnetism of $Cr_2(NCN)_3$, density-functional theory both using GGA and GGA+*U* functionals was applied in order to reveal more magnetic and electronic details. Indeed, the calculated spin saturation moments are in good agreement with the experimental moment. Also, the electronic structure of $Cr_2(NCN)_3$ both seen from GGA and GGA+*U* are similar to the one of Cr_2O_3, although the ferromagnetic state lies lower for the carbodiimide. We conclude that $Cr_2(NCN)_3$ is a ferromagnetic intermediate between a charge-transfer and Mott–Hubbard insulator, in good accord with the macroscopic appearance of a green ferromagnetic material.

Despite the density-functional predictions of the *M*NCN phases and the successful treatment of the ferromagnetic ground state of chromium carbodiimide, applying this method in its GGA+*U* version for the entire *M*NCN series in order to describe more subtle features of their electronic structure, however, turns out to be problematic [3]. To do so, a thorough study of these materials was based on a popular plane-wave-pseudopotential code (VASP) and the generalized-gradient approximation (GGA-PBE) for the exchange-correlation functional. The projector-augmented wave method was used, with a large cutoff energy (400 eV) and a very fine *k*-point mesh to sample the complete Brillouin zone and to calculate the densities of states. As alluded to already, electron-electron Coulomb interactions in combination with the self-interaction correction were considered in the rotationally invariant way (GGA+*U*) with a single effective Hubbard parameter *U*. The resulting densities of states are shown in Figure 3, both encouraging and discouraging at the same time: as seen from the central and right panels, CoNCN and NiNCN are correctly predicted to be insulators and thus optically transparent while FeNCN (left panel) is falsely predicted to be (semi)metallic as obvious from the significant density of states at the Fermi energy. FeNCN is a red insulator, however, a true disaster for (correlated) density-functional theory. This is not an isolated example because DFT-based methods often fail to reproduce the correct optical behavior of such materials containing transition-metal ions.

In order to arrive at a better theoretical description, the ground states and the *d* excitations of these compounds must be addressed with a wave-function technique such as the local many-electron effective Hamiltonian crystal field method. It proceeds by assuming an electronic wave function of the system which is the product between the full configuration-interaction function of the *d* electrons and another ligand wave function covering the remaining *sp* electrons; the latter is taken in a semiempirical single-determinant approximation. The product wave function is antisymmetric, that is, it changes its sign when the coordinates of each *d*/*sp* pair of electrons are interchanged.

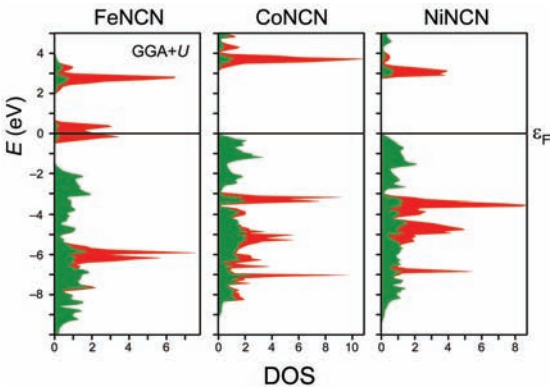

*FIG. 3: Density of states of MNCN family of materials as coming from density-functional GGA+*U *calculations. The* d*-orbital projected DOS is given in red, the nitrogen-projected DOS in green.*

This approach immediately predicts the insulating nature of FeNCN and, also, correctly reproduces the spin-magnetic moments of the ground state, in good agreement with the measured magnetic moments of FeNCN (and also CoNCN and NiNCN) [4]. In addition, the true many-body nature of the method allows to predict the *d*-*d* excitation spectra of such materials. The latter will be checked against experimental data in the near future.

It is a pleasure to thank DFG for continuous support.

[1] X. Liu, L. Stork, M. Speldrich, H. Lueken, R. Dronskowski, *Chem. Eur. J.* **2009**, *15*, 1558–1561.

[2] X. Tang, H. Xiang, X. Liu, M. Speldrich, R. Dronskowski, *Angew. Chem. Int. Ed.* **2010**, *49*, 4738–4742.

[3] H. Xiang, R. Dronskowski, B. Eck, A. L. Tchougréeff. *J. Phys. Chem. A* **2010**, *114*, 12345–12352.

[4] A. L. Tchougréeff, R. Dronskowski. *J. Phys. Chem. A* **2011**, *115*, 4547—4552.

Beating the Walker limit with massless domain walls in cylindrical nanowires

Ming Yan[1], Attila Kakay[1], Sebastian Gliga[2] and Riccardo Hertel[3]

[1] Peter Grünberg Institut (PGI-6), Forschungszentrum Jülich, Germany
[2] Center for Nanoscale Materials, Argonne National Laboratory, Argonne, IL, USA
[3] Institut de Physique et Chimie des Materiaux de Strasbourg, Universite de Strasbourg

We present a micromagnetic study on the current-induced propagation of transverse domain walls (DWs) in thin soft-magnetic cylindrical nanowires. Due to the axial symmetry of the wire, these DWs are found to be effectively zero-mass micromagnetic objects. Consequently, they are able to travel arbitrarily fast without encountering the Walker limit, which all the massive DWs are subject to. The propagation of the DW is characterized by a spiraling motion around the wire. Our simulation data are confirmed by an analytical model.

A precisely controlled displacement of magnetic DWs by means of electric currents [1] is essential for the realization of the "race track memory" [2], a promising concept for future magnetic data storage devices. To achieve this, however, there exists a major obstacle, namely, the well-known Walker breakdown[3], which occurs when DWs are driven strongly enough to reach a critical velocity. The DW structure then collapses and undergoes a series of complex cyclic transformations. The Walker limit is thus the maximum velocity at which DWs can propagate without changing their structure. In a broader physical context, the Walker limit is connected to the mass of moving DWs [4]. This concept is based on theanalogy between the energy increase of a moving DW, arising from the distortion of its structure, to kinetic energy of a moving object. Moving DWs in thin magnetic strips in fact display particle-like behaviour, including momentum and inertia. As the DW velocity increases, the energy continues to increase until it reaches a limit where Walker breakdown takes place. A DW would be massless if its structure did not change during its motion. We show that such massless DWs indeed exist, namely, transverse walls in thin cylindrical nanowires [5]. The vanishing DW mass leads to astounding dynamic properties, such as the absence of Walker limit and intrinsic pinning.

A transverse DW formed in a 10 nm diameter cylindrical Py wire compared to a transverse wall in a 100 nm wide strip of 10 nm thickness (up-right).

Using a finite-element method, we perform micromagnetic study on the dynamic properties of such DWs by numerically solving the Gilbert equation with additional spin transfer torque terms:

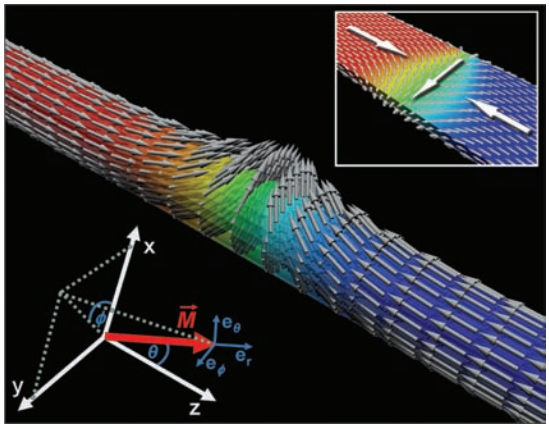

FIG. 1: A transverse DW formed in a 10 nm diameter cylindrical Py wire compared to a transverse wall in a 100 nm wide strip of 10 nm thickness (up-right).

$$\frac{d\vec{m}}{dt} = \gamma \vec{H}_{\text{eff}} \times \vec{m} + \frac{\alpha}{M_s}\left[\vec{m} \times \frac{d\vec{m}}{dt}\right]$$

$$-\left(\vec{u}\cdot\vec{\nabla}\right)\vec{m} + \frac{\beta}{M_s}\vec{m} \times \left[\left(\vec{u}\cdot\vec{\nabla}\right)\vec{m}\right], (1)$$

where $\vec{m}$ is the normalized local magnetization, M_S the saturation magnetization, γ the gyromagnetic ratio, $\vec{H}_{\text{eff}}$ the effective field, α the Gilbert damping factor, ß the non-adiabatic spin transfer parameter. The vector $\vec{u}$ is defined as $\vec{u} = -\frac{g\mu_B P}{2eM_s}\vec{j}$, where $\vec{j}$ is the current density, g is the Landé factor, μB the Bohr magneton, e the electron charge and P the polarization rate of the current. Typical material parameters of Permalloy (Py) are used in the simulation. Figure 1 shows the simulated configuration of a transverse wall in a 4 μm cylindrical wire with 10 nm diameter. Due to the axial symmetry, the structure of the wall and its energy are invariant with respect to rotations of the magnetization in the xy plane.

An electrical current along +z displaces the DW towards the –z direction, i.e., in the electron flow direction. In addition to the linear motion the DW rotates about the axis of the wire, as illustrated schematically in Fig. 2.

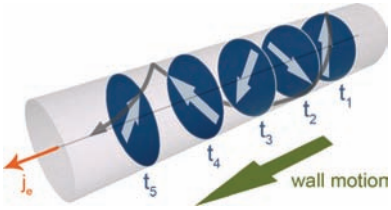

2. Schematic illustration of the current-driven DW motion. The blue cross-sections indicate the position of the wall plane at successive moments in time, while the arrows represent the orientation of the transverse magnetization.

In the simulations, α is set to 0.02 while the value of P varies. The DW velocity as a function of the current density J is plotted in Fig. 3a in a 10 nm diameter cylindrical wire for different values of ß. The inset a_2 of Fig. 3 displays the lower range of J, as typically used in experiments. The results show that the velocity depends linearly on J and is independent of ß. For comparison, we simulated the DW motion in a thin strip using the same parameters (inset a_1 of Fig. 3). The cylindrical wire displays several fundamental differences. First, there is no intrinsic pinning when ß=0, while in the case of the strip a minimum (critical) current density must be injected to initiate the DW motion.

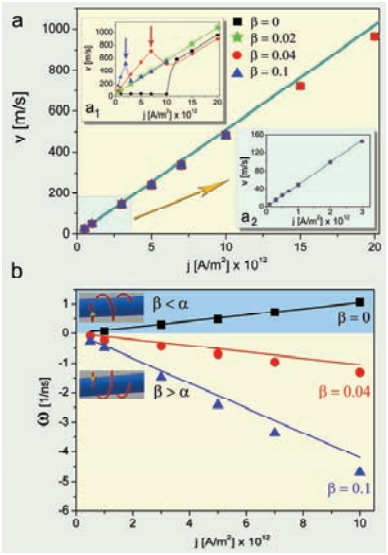

Fig. 3. Simulated DW linear velocity (a) and angular velocity (b) as a function of the current density j with α = 0.02 and different values of ß in the case of a 10 nm round Py wire. Inset (a1): Simulated DW dynamics in a 100 nm wide and 10 nm thick strip. Inset (a2): closeup of the data for lower values of j The lines display analytic values.

Secondly, the DWs in the round wire behave like massless objects, i.e., their profile does not change during the motion. Correspondingly, there is no Walker breakdown in the case of the cylindrical wire. In the strip, however, the Walker limit occurs when ß>a, as indicated by the arrows in the inset a_1 of Fig. 3. Thirdly, the DW velocity does not depend o ß in the cylindrical wire. The DW reaches a constant velocity immediately after the application of the current and stops immediately after the current stops, which is consistent with the absence of mass and inertia. The characteristics of the angular dynamics are summarized in Fig. 3b. The angular velocity shows a linear dependence on J and is found to be proportional to (ß-a).We also adopt an analytical model to study the DW dynamics for this particular geometry. A spherical coordinate system is used as shown in Fig. 1. by the good agreement between the analytical model and simulations. For simplicity, we first consider the field-driven motion In the case of the cylindrical wires, the demagnetizing field effect, which plays a significant role in DW dynamics in flat strips, vanishes due to the axial symmetry. The DW motion therefore can be easily solved, in the current-driven case yielding with

$$\dot{\theta} = -\frac{(1+\alpha\beta)u_z}{1+\alpha^2}\frac{\partial\theta}{\partial z}\Big|_{wc} \quad (2)$$

$$\dot{\phi} = \frac{(\beta-\alpha)u_z}{1+\alpha^2}\frac{\partial\theta}{\partial z}\Big|_{wc}, \quad (3)$$

where the subscript WC denotes the DW center. The linear velocity of the DW, given by $v = \dot{\theta}\cdot\partial z/\partial\theta$, is basically equal to u [plotted as a line in Fig. 3a] and independent on ß. The angular velocity of the DW, given by $\dot{\phi}$, is proportional to (ß-α). Clearly, the non-adiabatic term only affects the rotational motion of the DW. Given the symmetry of the wire, the DW is free to rotate without any deformation, resulting the massless behaviour of the DW. The dependence of the frequency of the DW rotation on the difference between α and ß provides a possibility for the measurement of the non-adiabatic spin transfer torque term ß, which is generally difficult to determine. Also, the polarization rate P can be determined from the current-driven DW velocity, which in this case is almost exactly equal to u (cf. Fig. 3).

In conclusion, transverse DWs in cylindrical nanowires has a unique dynamic property, namely, being effectively massless. Such inertia-free DWs show particular dynamic properties which should allow one to precisely and efficiently control their position with electric currents and to extract important physical parameters.

[1] L. Berger, Phys. Rev. B , 1572 (1986).

[2] S.S.P. Parkin, M. Hayashi, and L. Thomas, Science , 190 (2008).

[3] N.L. Schryer, and L.R. Walker, J. Appl. Phys. , 5406 (1974).

[4] W. Döring, Z. Naturforschg. a, 373 (1948).

[5] M. Yan, A. Kákay, S. Gliga, and R. Hertel, Phys. Rev. Lett. 057201 (2010).

KKRnano: A Program for Large Scale Density Functional Calculations

R. Zeller[1] , A. Thiess[2,3] , S. Blügel[3,4]

[1]IAS-3: Institute for Advanced Simulation, Forschungszentrum Jülich, 52425 Jülich
[2]GRS: German Research School for Simulation Sciences
[3]PGI-1: Quantum Theory of Materials, Forschungszentrum Jülich, 52425 Jülich
[4]IAS-1: Institute for Advanced Simulation, Forschungszentrum Jülich, 52425 Jülich

KKRnano is a newly developed electronic structure code applicable to large insulating, semiconducting and metallic systems. It is massively parallelized for the efficient use of up to a hundred thousand processors and works with computing times which increase only linearly with the number of atoms in the systems. This opens the way to extend the limit for routine density functional electronic structure studies from a few hundred to many thousand atoms.

In the last three years we have developed a computer program for density-functional electronic-structure calculations for systems with many thousand atoms. This program is based on multiple-scattering theory within the Korringa-Kohn-Rostoker (KKR) formulation and can deal with systems extending over several nanometers. Consequently, we name it KKRnano.

KKRnano was designed from the outset to run efficiently on massively parallel supercomputers like the IBM Blue Gene/P available in Jülich. The second design aim was to avoid the unfavourable increase of the computing time proportional to the third power of the number of atoms which occurs if standard methods are used to solve the density-functional equations. In KKRnano the computing time increases linearly with the number of atoms if total energy changes of the order of meV per atom are tolerated compared to the standard full-potential KKR Green function (GF) method [1].

We obtain linear scaling of the computational effort as function of system size by an algorithm [2] based on the screened KKR method [3] which avoids wavefunctions and directly calculates the Kohn-Sham Green function by solving sparse systems of complex linear equations of dimension $N\ (l + 1)^2$. Here N is the number of atoms and l depends on the angular spatial resolution around the atoms, usually $l = 3$ is sufficient. We solve these equations iteratively by the quasi-minimal residual (QMR) method and calculate the electron density from the Green function by a contour integral in the complex energy plane using a few tenths of energy mesh points. Linear scaling for the computational effort is achieved by exploiting the concept of nearsightedness of electronic matter as it was called by Nobel Prize winner Walter Kohn. The concept means that in systems without long range electric fields the electronic density at a point in space insignificantly depends on potential changes far away. In KKRnano the nearsightedness is exploited by choosing a truncation region around each atom and neglecting Green function contributions arising from the outside of the truncation region.

The increase of the computing time as function of system size and the effect of the truncation on the total energy accuracy are shown in FIG. 1 and FIG. 2 for two chosen example systems, Pd substitutionally doped with 3% Ni atoms and MgO with 5% of the oxygen atoms replaced by nitrogen atoms.

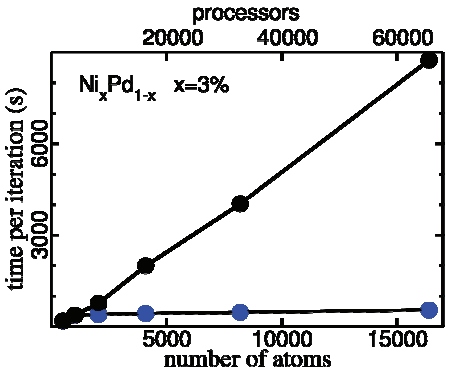

FIG. 1: Scaling behaviour of the wall clock time in one self-consistency step for dilute NiPd systems as function of system size using a truncation region of 959 atoms and no truncation (lower and upper curves). Four processors per atom are used.

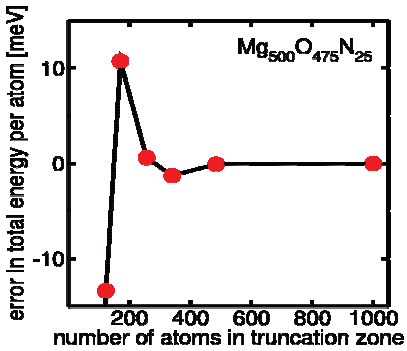

FIG. 2: Total energy error per atom as function of the number of atoms in the truncation region for a MgO system of 1000 atoms with 5% oxygen atoms replaced by nitrogen atoms.

Both example systems are of considerable physical interest, PdNi shows a quantum phase transition at about 2.5% Ni concentration and MgO doped with nitrogen is discussed as a transition metal free, room

temperature ferromagnet with resistive switching properties useful for the next generation of nonvolatile memory. The electronic structure of these systems depends critically on defect distribution and interaction effects between defect atoms. The well established standard method for disordered systems, the KKR-CPA with its single-site mean-field description fails here because neither short range order effects nor, in particular, the long range giant magnetic polarization clouds around Ni atoms in Pd can be described reasonably. In KKRnano such effects are accessible because large supercells can be treated with prescribed defect distribution.

FIG. 1 shows the wall clock time used in one density functional self-consistency step as function of the number of atoms in the system with and without spatial truncation of the Green function. Without truncation the time increases almost linearly if the number of processors is increased proportionally to the number of atoms. This means that the quadratically scaling total computational work is almost perfectly distributed over the increasing number of processors. If errors of the order of meV per atom are tolerated, the calculations can be speeded up by truncating the Green function, because then, the linear equations must be solved only in the truncation region. FIG. 1 shows for a truncation region of 959 atoms that the wall clock time only slightly increases with system size. This means that with truncation the total work increases only linearly and is again well distributed over the processors.

The good scaling behaviour can be explained from the multiple-scattering point of view of the KKRGF method [1]. In this method, space is divided into nonoverlapping cells around the atomic sites. For each cell, first a single-site scattering problem is solved using an angular momentum expansion of density, potential and wavefunctions. This part of KKRnano is straightforwardly parallelized using a simple matching between cells and processors. The complete multiple scattering is then obtained by solution of large systems of linear equations. Due to the iterative technique chosen in KKRnano the solution of the linear equations is also easily and efficiently parallelized because during the iterations no coupling between different cells occurs.

Because the linear scaling property of KKRnano is connected with total energy errors, it is important to know how large these errors are. Typical truncation errors are shown in FIG. 2 for the MgO:N system. The total energy error rapidly decreases with increasing size of the truncation region and is small enough if the truncation region contains more than a few hundred atoms. Similar accuracy for large metallic systems was found in a model study using periodic Cu and Pd supercells containing 131072 atoms [2].

For routine applications of KKRnano and for applications to even larger systems it is desirable to find ways to further reduce both wall clock time and computing time. Here we made considerable progress in the last year by developing a preconditioner for the linear equations and by using parallelization not only over the atoms, but also over the energy points, the two spin directions in magnetic systems and over the $L = (l + 1)^2 = 16$ angular momentum components.

The energy parallelization is dynamically load balanced by putting the energy points into two or three groups to deal with the considerably different number of iterations at different energy points. The L parallelization, which is implemented presently only for the linear equation solver, but not for the rest of the program, is normally used with MPI message passing. Alternatively, for memory bound applications we use OPENMP to utilize the shared memory available in multicore CPUs. During the Blue Gene/P Extreme Scaling Workshop 2010 we were able to run a NiPd test system of 3072 atoms using from 3072 to 294912 processors, which means that KKRnano can use the entire Blue Gene/P. Increasing the number of processors from 147456 to 294912 gave a speedup of 1.6 for the wall clock time in the L parallelized part of KKRnano, whereas the time became larger for the remaining part. This part was fastest with 147456 processors.

It is well known that solving linear equations by iterative matrix multiplications can be accelerated by preconditioning. The preconditioner is a matrix which approximates the inverse of the original matrix as well as possible. Unfortunately, traditional preconditioners like ILU cannot be computed with the high degree of parallelization used in KKRnano. To overcome this difficulty, we developed a new preconditioner [4] that exploits the block structure of the original screened KKR matrix. In this matrix all blocks except for the ones on the diagonal only depend on the geometry of the system which is periodic or nearly periodic if relaxations of the atoms into their equilibrium positions are taken into account. As preconditioner we use a multilevel block-circulant matrix that is easy to compute and parallelize and leads to speedup factors between three and ten in applications of KKRnano for the systems we have studied so far. Another factor of two we gain by starting the QMR iterations with results from the previous self-consistency step.

With these recent improvements we anticipate that KKRnano, a full-potential all-electron program for large arbitrarily shaped supercells, can be widely applied to density functional electronic structure calculations for systems containing many thousand atoms.

[1] N. Papanikolaou, R. Zeller and P. H. Dederichs, J. Phys.: Condens. Matter 14, 2799 (2002)

[2] R. Zeller, J. Phys.: Condens. Matter 20, 294215 (2008)

[3] R. Zeller, P. H. Dederichs, B. Újfalussy, L. Szunyogh, and P. Weinberger, Phys. Rev. B 52, 8807 (1995)

[4] M. Bolten, A. Thiess, I. Yavneh and R. Zeller, submitted to Lin. Alg. Appl.

Magnetization distribution in the tetragonal phase of $BaFe_2As_2$

Y. Xiao[1], Y. Su[2], P. J. Brown[3], T. Chatterji[2,3], Th. Wolf[4], Th. Brückel[1, 2]

[1]Jülich Centre for Neutron Science JCNS-2 and Peter Grünberg Institute PGI-4: Scattering Methods, Forschungszentrum Jülich, Germany
[2]Jülich Centre for Neutron Science JCNS at FRM II
[3]Institut Laue-Langevin, Grenoble, France
[4]Karlsruhe Institute of Technology, Karlsruhe, Germany

The pnictide superconductors and their parent compounds have drawn extensive attention because they provide a new opportunity to investigate the mechanism of non-BCS exotic superconductivity [1,2]. Similar to high-T_c cuprates, superconductivity in iron pnictides is in proximity to magnetism. Scattering methods in particular neutron scattering have been playing an important role in the understanding of the interplay between superconductivity and magnetism. By using conventional neutron diffraction method, we have determined the magnetic structure of few representative parent compounds, such as $BaFe_2As_2$[3], $EuFe_2As_2$[4] and SrFeAsF[5]. Furthermore, investigation on the magnetization density distribution via polarized single-crystal neutron diffraction has been undertaken very recently on $BaFe_2As_2$. The experimental results provide strong evidence that besides the spin and the lattice degrees of freedom, the orbital degree of freedom might also play an important role in iron pnictides[6].

All iron pnictides are found to be of layered structure in nature. For undoped iron pnictides, the chains of parallel Fe spins within the FeAs layers couple antiferromagnetically in the *ab* plane of the orthorhombic lattice with an antiparallel arrangement along the *c* axis. This antiferromagnetic order in the parent compounds is likely due to a spin-density-wave instability caused by Fermi-surface nesting. The undoped iron pnictides are not superconducting under ambient pressure, while the magnetic order is suppressed and superconductivity emerges concomitantly upon carrier doping.

The nature of magnetism and possible orbital order in iron pnictide compounds are still very controversial and therefore additional experimental information on these degrees of freedom for the parent compounds can be helpful in understanding the nature of superconductivity in these compounds. In order to get direct information about the electronic structure of the parent compound we have undertaken a polarized neutron-diffraction experiment on $BaFe_2As_2$ to determine the field-induced magnetization distribution. The structural parameters were determined from unpolarized neutron integrated intensity measurements made using the four-circle diffractometer D9 and flipping ratios were measured using the polarized neutron diffractometer D3. Both instruments are installed on the hot neutron source of the high-flux reactor of the Institute Laue-Langevin in Grenoble. The sample was held at constant temperature in a closed-cycle refrigerator on D9 whereas on D3 it was oriented with a $[1\,\bar{1}\,0]$ axis parallel to the vertical field direction of a 9 T cryomagnet. The polarized neutron flipping ratios from the crystal were measured in the paramagnetic tetragonal phase at T = 200 K using a neutron wavelength 0.825 Å.

The flipping ratios measured for equivalent reflections and for repeated measurements of the same reflection were averaged together to give a mean value of *R* and used to calculate the magnetic structure factors FM using the relationship

$$F_M = \frac{(R-1)F_N}{2(P^+ + P^-)},$$

Where P^+ and P^- are the efficiencies of neutron polarization parallel and antiparallel to the applied field; F_N is the nuclear structure factor.

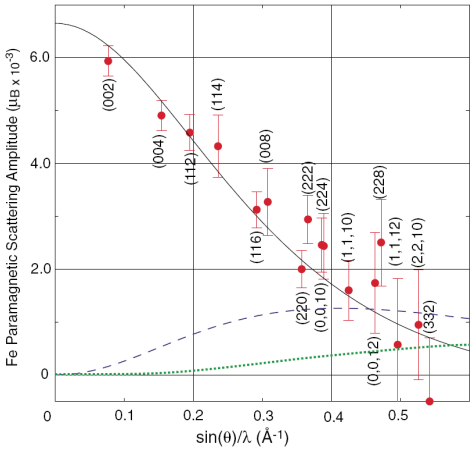

FIG. 1: Paramagnetic scattering amplitudes measured for Fe in $BaFe_2As_2$ at 200 K. The solid curve shows the $\langle J_0 \rangle$ form factor for neutral Fe, scaled to the paramagnetic magnetization of 6.65×10^{-3} μ_B/Fe. The dashed and the dotted curves show $\langle j_2 \rangle$ and $\langle j_4 \rangle$ form factors, which multiply the anisotropic terms in the magnetic scattering on the same scale.

The magnetization induced in a crystal by a field of 9 T applied the (001) plane at 200 K was measured as 0.01 μ_B/f.u. It is the sum of a paramagnetic part due

to magnetic excitation of electrons near the Fermi surface and a diamagnetic part to which all electrons contribute. The diamagnetic volume susceptibility is given by the Langevin equation. The diamagnetic contribution to the magnetic structure factor is

$$F_{dia} = \frac{HC}{|k|}\sum_i \frac{df_i(k)}{dk}\exp ik\cdot r_i,$$

where $f_i(k)$ is the atomic form factor. The constant C has the value 1.52×10-5 μBT-1Å2. The diamagnetic contribution to the magnetization calculated using the atomic form factors for Ba, Fe, As is -0.0033 μB/f.u., the paramagnetic part of the magnetization is therefore 0.01-(-0.0033)= 0.0133μB/f.u.. The diamagnetic contributions to the magnetic structure factors were calculated and values of Fdia were subtracted from the magnetic structure factor FM obtained from the flipping ratios to give the paramagnetic structure factors Fpara.

An effective form factor for the Fe atom, obtained by dividing each Fpara by the geometric structure factor of Fe for that reflection is shown in Fig. 1 where it is compared with the Fe 3d free atom curve scaled to 6.65×10-3μB. The low-angle reflections fall on the curve with experimental error but at higher angles, at which the higher order form factors <j2> and <j4> become appreciable, significant scatter is apparent which may characterize an aspherical magnetization distribution.

The method of maximum entropy provides a model free method for reconstructing an image from sparse and noisy data. We have used this method to clarify the shape of the distribution. The maximization procedure coded was used to make the maximum entropy reconstruction of the magnetization distribution projected down $[1\bar{1}0]$, from the measured magnetic structure factors. The result of the reconstruction is shown in Fig. 2. The reconstruction shows clearly that the magnetization is confined to the region around the iron atoms and that there is no significant magnetization associated with either As or Ba atoms. The magnetization around the Fe atom is significantly nonspherical with a shape that appears to extend in the [111] directions of the projection. Further clarification of the shape of the iron-atom magnetization was obtained by fitting the magnetic structure factors to a multipole model in which they are expressed as

$$F_M(k) = a_0\langle j_0(|k|)\rangle + \sum_{l=2,4}\langle j_l(|k|)\rangle \sum_{m=-l}^{m=l} a_{lm}Y_{\hat{k}}(lm\pm),$$

where the $\langle j_l(|k|)\rangle$ are the form factor integrals for a neutral Fe atom and the $Y_{\hat{k}}(lm\pm)$ are the real combinations of spherical harmonic functions

$$Y_{\hat{k}}(lm\pm) = \frac{1}{\sqrt{2}}\left[Y_l^{-m}(\hat{k}) \pm (-1)^m Y_l^m(\hat{k})\right]$$

In a site with fourfold symmetry the d-electron orbitals split into three singlet states: $d_{3z^2-r^2}$, $d_{x^2-y^2}$, and d_{xy} and a doublet combination of d_{xz} and d_{yz}. The first two singlet states are derived from the cubic e_g functions and the third singlet and the doublet form the t_{2g} ones. The occupancies of these four nondegenerate orbitals can be derived directly from the coefficients a_{lm}. However the parameters obtained from the unconstrained fit lead to unphysical, negative occupancies for the two e_g-type orbitals but with large estimated standard deviations. A constrained fit in which the ratio between the a_{lm} was fixed to correspond to occupancy of the t_{2g}-type orbitals only, gave equally good agreement.

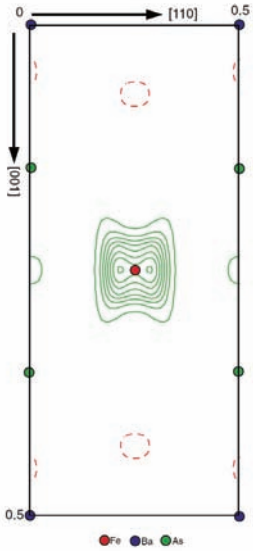

FIG. 2: Maximum-entropy reconstruction of the magnetization distribution in tetragonal BaFe2As2 at 200 K projected down $[1\bar{1}0]$. Contours are drawn at intervals of 10^{-2} μB Å^{-2}.

The results of the present experiment show that at least 96% of the electrons in $BaFe_2As_2$, which give rise to the paramagnetic susceptibility, are localized on the Fe atoms with a radial distribution similar to that of a neutral Fe atom. Their angular distribution shows that they occupy the t_{2g}-type orbitals with a strong preference for the singly degenerate *xy* type which has its maxima in the <110> directions which are not those of any ligand atoms rather than the doubly degenerate *xz* and *yz* types which maximize in a cone containing directions nearly parallel to the Fe-As bond directions. If, as might be expected, there is strong hybridization between Fe and As atoms these hybridized bonding and antibonding states must lie well below and well above the Fermi level leaving narrow 3*d* nonbonding bands at the Fermi surface.

[1] Y. Kamihara et al., J. Am. Chem. Soc. **130**, 3296 (2008).

[2] D. C. Johnston., Advances in Physics **59**, 803(2010).

[3] Y. Su et al., Phys. Rev. B **79**, 064504(2008).

[4] Y. Xiao et al., Phys. Rev. B **81**, 220406(R)(2010).

[5] Y. Xiao et al., Phys. Rev. B **81**, 094523(2010).

[6] P. J. Brown et al., Phys. Rev. B **82**, 024421(2010).

Wave function mapping in graphene quantum dots

M. Pratzer[1], D. Subramaniam[1], C. Pauly[1], V. Geringer[1], M. Liebmann[1], R. Reiter[2], F. Libisch[2], J. Burgdörfer[2], C. Busse[3], T. Michely[3], M. Morgenstern[1]

[1]II. Physikalisches Institut B, RWTH Aachen University, Germany
[2]Institute for Theoretical Physics, Vienna University of Technology, Austria
[3]II. Institute of Physics, University of Cologne, Germany

Using low-temperature scanning tunneling spectroscopy, we map the local density of states (LDOS) of graphene nanodots prepared on Ir(111) at various energies. Due to the Ir band gap appearing within the valence band around the K_g-point, graphene properties are maintained and the observed experimental results could be reproduced by a third nearest neighbour tight-binding calculation neglecting the substrate, at least, for low energy states. From analysis of the peak widths as a function of energy, we deduce that the inverse electron lifetime increases linearly with energy up to about 1.1 eV. This can be explained by electron tunnelling from graphene into an Ir surface state.

The preparation and measurements have been performed in an ultrahigh vacuum system (base pressure p=2·10^{-10} mbar) equipped with a high resolution scanning tunneling microscope (STM) operating at 5 K [1]. After cleaning the Ir(111) single crystal by cycles of sputtering and annealing, graphene quantum dots (QD) were grown using chemical vapour deposition (CVD). Details of the CVD process are described elsewhere [2]. We prepared monolayer graphene QDs with diameters in the range of 5 nm to 40 nm. Atomically resolved STM images reveal that the boundary of the QDs only consists of zigzag edges. Fig. 1a represents spectra of differential conductivity average over the hexagonal QD shown in the inset. Three maxima caused by confined electron states are visible as peaks in the *dI/dU* signal. Fig. 1b-d show the corresponding *dI/dU* maps (left) in comparison with calculated maps of the local density of states (LDOS, right). The first confined state at -0.26 eV reveals one maximum of the LDOS in the centre of the QD. At -0.38 eV the maximum turns into a minimum forming a ring shaped structure. The state at -0.6 eV (Fig. 1d) shows a maximum-minimum-maximum sequence from the centre towards the rim of the island, but is already influenced by the Moiré potential caused by the lattice mismatch of graphene and Ir. For calculation of the LDOS we used the third nearest neighbour tight binding approximation including the Moiré potential, which is determined from photoemission data [3], and an absorbing edge, i.e. an additional imaginary potential at the edge. The latter mimics the known strong binding of graphene edges to the Ir substrate [4].

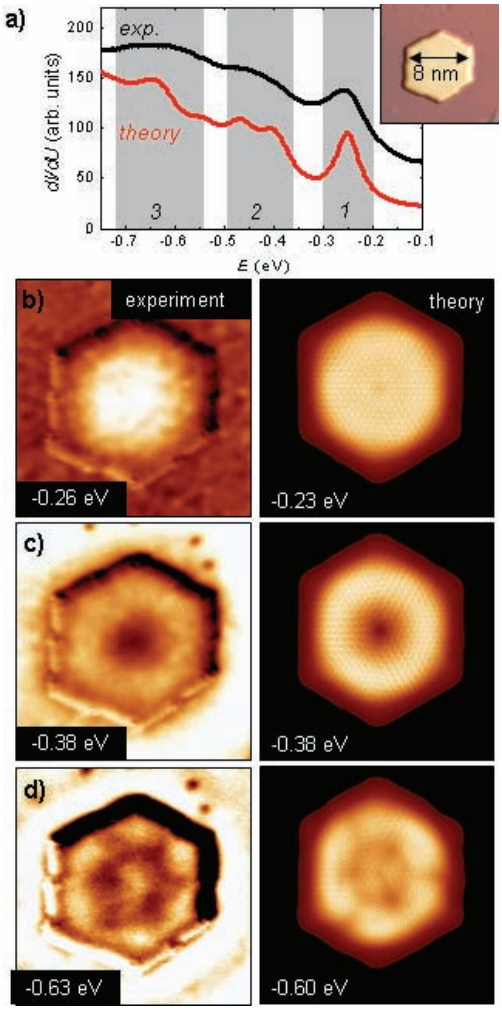

FIG. 1: a) Spectra of differential conductivity (black curve) averaged over the graphene QD shown in the inset. The three maxima correspond to confined electronic states. Tight binding calculation (red curve) with boundary state suppression nicely reproduces the experiment. b)-d) dI/dU images at energies corresponding to the maxima in a) compared to calculated images of local density of states.

For small QDs as shown in Fig. 1 the LDOS can be nicely reproduced. The LDOS of larger QDs, instead, is dominated by a standing wave pattern which could not be explained by the graphene states only. Fig. 2d shows the calculated LDOS of a QD with a length of 20 nm and a width of 12 nm for an energy of 0.36 eV. A characteristic minimum along the short axis is visible. In contrast the corresponding *dI/dU* map (Fig.2e) reveals a maximum along the long axis of the dot and a second maximum along the boundary. Increasing energy leads to shorter wave length of the standing wave pattern scattered at the QD boundary outside as well as inside the island. At 0.66 eV the LDOS inside the QD is again dominated by the Moiré potential (see Fig. 2g). By measuring the distance between adjacent maxima of these LDOS pattern we determined the dispersion relation of this state for the uncovered Ir(111) surface as well as for the graphene areas. The result is presented in Fig. 2a. The two dispersions reveal the same slope, i.e., a Fermi velocity of $5 \cdot 10^5$ m/s. This is exactly the same velocity as for the Ir-S_2 surface state, which was determined by photoemission spectroscopy [3]. Thus, the standing wave pattern observed on the graphene dot must also be induced by the S_2 state of Ir. The energy offset of 141 meV compared to the dispersion of pure Ir maybe explained by hybridization or a charging effect of the graphene dot.

Further, we determined the peak width of the electron states, i. e., the inverse lifetime, with respect to energy. Therefore we fitted the data using a lorentzian curve with a linear offset (inset of Fig. 2c). A linear behaviour of the peak width with respect to energy is found (Fig 2c). Regarding electron-electron [5-7] or electron-phonon interaction [8] within graphene, a linear behaviour is expected, but the large value of ΔE=400 meV at 1.1 eV cannot be explained by these processes, but requires an additional graphene substrate interaction. Therefore, we considered electron tunnelling from the graphene cone into the Ir-S_2 surface state. In Fig 2b the band structure of graphene (blue) and Ir (red) is sketched according to photoemission spectroscopy [3]. The graphene cone is located in a band gap appearing within the valence band of Ir around the K_g-point. Due to the linear dispersion of graphene and the Ir-S_2 state the tunnelling probability decreases linearly for energies closer to the Fermi energy due to the increase of *k* required for the tunnelling process as indicated by the arrows in Fig. 2b. This leads to longer electron lifetimes of the states closer to the Fermi energy, i.e., sharper energy peaks.

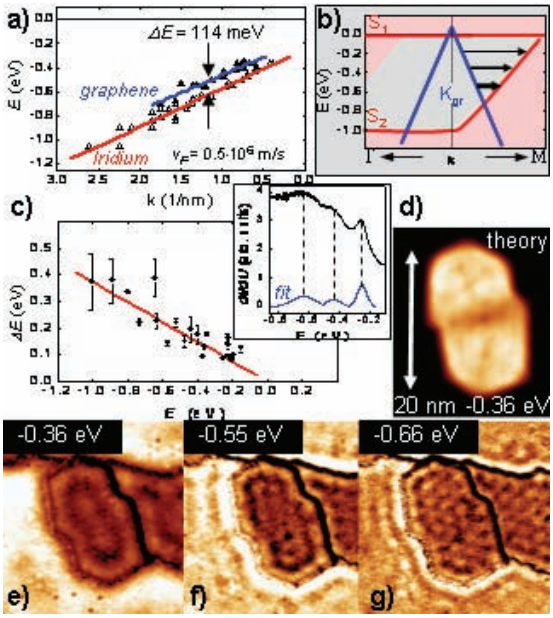

FIG. 2: a) Dispersion relations determined by analyzing the standing wave patterns inside (closed triangles) and outside (open triangles) the graphene dots. The linear fits (red and blue line) correspond to the Ir surface state S_2. b) Sketch of the band structure of Ir (red) and graphene (blue) [3]. c) Data points: energetic width of the states with respect to energy as deduced from lorentzian fits as shown in the inset. Red line: linear fit. d) Calculated map of the LDOS of a graphene dot for -0.36 eV. e)-g) dI/dU maps of the same graphene dot at different energies.

[1] T. Mashoff, M. Pratzer, and M. Morgenstern, Rev. Sci. Instrum. **80**, 053702 (2009).

[2] J. Coraux, A. T. N'Diaye, M. Engeler, C. Busse, D. Wall, N. Buckanie, F.-J. Meyer zu Heringdorf, R. van Gastel, B. Poelsema, and T. Michely, New J. Phys. **11**, 023006 (2009).

[3] I. Pletikosić, M. Kralj, P. Pervan, R. Brako, J. Coraux, A. T. N'Diaye, C. Busse, and T. Michely, Phys. Rev. Lett. **102**, 056808 (2009).

[4] P. Lacovig, M. Pozzo, D. Alfe, P. Vilmercati, A. Baraldi, and S. Lizzit, Phys. Rev. Lett. **103**, 166101 (2009).

[5] C. H. Park, F. Giustino, M. L. Cohen, and S. G. Louie, Phys. Rev. Lett. **99**, 086804 (2007).

[6] M. Calandra, and F. Mauri, Phys. Rev. B **76**, 205411 (2007).

[7] J. P. Carbote, E. J. Nichol, and S. G. Sharapov, Phys. Rev. B **81**, 045419 (2010).

[8] K. M. Borysneko, J. T. Mullen, E. A. Barry, S. Paul, Y. G. Semenov, J. M. Zavada, M. Buongiorno Nardelli, and K. W. Kim, Phys. Rev. B. **81**, 121412 (2010).

Observation of long spin relaxation times in bilayer graphene at room temperature

T.-Y. Yang[1], J. Balakrishnan[2], F. Volmer[1], A. Avsar[2], J. Samm[1], S. R. Ali[1], M. Zeng[2,3], J. Setiawan[2], M. Popinciuc[1], G. Güntherodt[1], B. Özyilmaz[2,3,4], B. Beschoten[1]

[1]II. Institute of Physics, RWTH Aachen University, Otto-Blumenthal-Straße, 52074 Aachen, Germany
[2]Department of Physics, 2 Science Drive 3, National University of Singapore, Singapore 117542, Singapore
[3]Nanocore, 4 Engineering Drive 3, National University of Singapore, Singapore 117576, Singapore
[4]NUS Graduate School for Integrative Sciences and Engineering (NGS), Centre for Life Sciences (CeLS), #05-01,28 Medical Drive, Singapore 117456, Singapore.

We report on a systematic study of spin transport in bilayer graphene(BLG). The spin relaxation time τ_s scales inversely with the mobility μ of BLG samples at room temperature. This indicates the importance of D'yakonov - Perel' spin scattering in BLG. Spin relaxation times of up to 2 ns are observed in samples with the lowest mobility. These times are an order of magnitude longer than any values previously reported for single layer graphene.

The demonstration of micrometer long spin relaxation length in graphene [1], by the pioneering work of Tombros *et al.* [2], has made this two-dimensional material an extremely promising candidate for spintronics applications. So far most spin transport studies have focused on single layer graphene (SLG), while the equally important bilayer graphene (BLG) has not yet received much attention. This is surprising, as the electric field tunable bandgap together with the predicted larger spin orbit (SO) coupling in BLG could pave the way towards true gate control of spin currents. Furthermore, the larger SO coupling makes BLG an ideal test system to unveil the relevant spin dephasing mechanisms in graphene. In initial SLG studies at room temperature (RT) electron momentum scattering by impurities and phonons has been identified as the limiting factor for spin relaxation (Elliott-Yafet (EY) mechanism). Here, we report on a systematic study on spin transport in BLG identifying the relevant spin scattering mechanisms and compare it to SLG. We show that in BLG, even at RT, the dominant spin scattering mechanism is DP-like such that the longest spin relaxation time (τ_s) is observed in samples with the lowest charge carrier mobility (μ). We observe spin relaxation times of up to 2 ns, which are an order of magnitude longer than any values previously reported for SLG studies.

We performed spin transport studies in BLG at room temperature using MgO barriers. Spin valve devices in the non-local geometry are fabricated on MgO covered exfoliated graphene samples using standard e-beam lithography techniques. This is followed by the evaporation of the ferromagnetic contacts (Co). The SEM image after the device fabrication for one of the BLG samples is shown in Fig.1. In order to investigate the nature of spin scattering in BLG, we have evaluated the spin relaxation time τ_s as a function of the field-effect mobility μ and the charge carrier density n at room temperature. The mobility dependence of τ_s provides the most direct way to deduce the dominant scattering mechanism: a linear dependence of τ_s on μ (or the momentum relaxation time τ_p) is a priori suggestive of an Elliott-Yafet (EY) spin scattering mechanism, while the inverse relation ($\tau_s \propto 1/\mu \propto 1/\tau_p$) will indicate the dominance of D'yakonov-Perel' (DP) like spin scattering mechanisms. In general, both mechanisms could simultaneously be relevant.

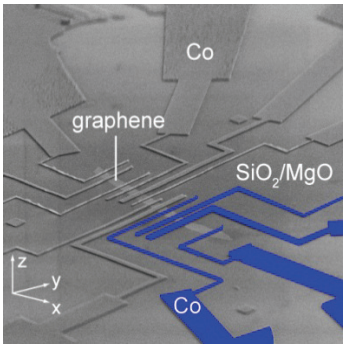

FIG. 1: SEM image of a BLG sample with multiple non-local spin valves.

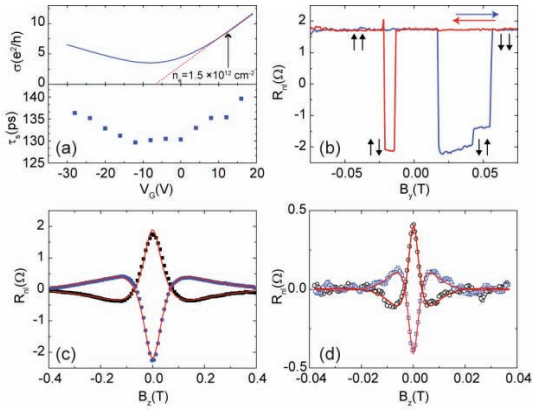

FIG. 2: RT data: (a) □ vs. VG and □s vs. VG for BLG. (b) Non-local resistance measurement as a function of the in-plane magnetic field By(T). The blue and red arrows show the field sweep direction while the black arrows show the relative magnetization orientations of the injector and detector electrodes. Hanle precession measurement for a perpendicular magnetic field Bz(T) sweep for (c) the same sample with □ ~ 2000 cm2/Vs and (d) for a sample with □ ~ 300 cm2/Vs.

For this study, we have selected 17 representative devices on 6 BLG samples whose field effect mobilities vary by more than one order of magnitude, from $\mu \sim 200$ cm²/Vs to 7000 cm²/Vs. The second parameter chosen is the charge carrier density: the density dependence of τ_s and τ_p is used to identify the spin scattering mechanism in SLG (EY). In BLG, the τ_p is often taken to be a constant under the assumption of charge scattering from weak short-range scatterers and charged impurities. This is consistent with the linear dependence of σ on the back gate voltage (Fig. 2a), i.e. on the charge carrier density, which we observe in most of our samples.

The non-local spin signal is measured by sweeping the in-plane magnetic field in a loop from negative (-80 mT) to positive (80 mT) and then back to negative values (-80 mT). A clear bipolar spin transport signal is observed at RT (see Fig. 2b), with a positive value of the non-local resistance for parallel alignment of the electrodes' magnetization and a negative resistance for their anti-parallel alignment ($\Delta R = 4\ \Omega$). To confirm the observed spin signals, conventional Hanle spin precession measurements are performed (Figs. 2c and 2d) at the same electron density of $n = 1.5 \times 10^{12}$/cm² above which the conductance is linear (Fig. 2a, upper panel) and the mobility is well defined within the Boltzmann approximation. The spin relaxation time τ_s can be extracted from the width of the Hanle curve. At $n = 1.5 \times 10^{12}$/cm² we get $\tau_s = 135$ ps for a sample with $\mu = \Delta\sigma/e\Delta n = 2000$ cm²/Vs (Fig. 2c). These values give a spin relaxation length of 0.7 μm.

The spin relaxation time τ_s as a function of gate voltage (doping) is plotted in Fig. 2a (lower panel) showing an increase (< 10%) of τ_s with doping, away from

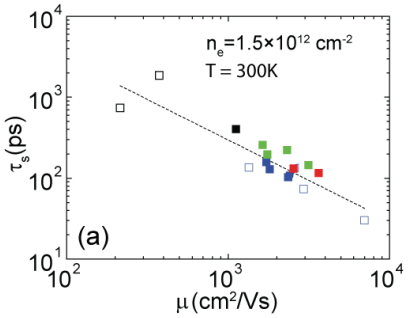

FIG. 3: Results of Hanle precession measurements for BLG at RT with mobilities varying from 200 – 7000 cm2/Vs. □s vs. □ plotted on a log-log scale.

the charge neutrality point (CNP). This is qualitatively similar to the gate tunability of τ_s in SLG.

The dependence of τ_s on μ in the Boltzmann regime is shown in Fig. 3. on a log-log plot. We observe a clear inverse dependence of τ_s on the mobility. Note that all data are taken at an electron density of $n = 1.5 \times 10^{12}$/cm². In samples with the highest mobility τ_s is only 30 ps. On the other hand, we observe a spin relaxation time τ_s of up to 2 ns for samples with the lowest mobilities (see corresponding Hanle curve in Fig. 2d). Such values of τ_s are one order of magnitude longer compared to values reported so far in any SLG experiment. Furthermore, this strong variation of τ_s with μ offers the most direct evidence of the correlation between spin and charge transport. Since higher mobilty samples will typically involve higher momentum relaxation time τ_p, assuming $\mu \propto \tau_p$ in the Boltzmann regime, the inverse dependence of τ_s on μ clearly demonstrates that the DP mechanism is the dominant spin scattering mechanism in BLG at RT [3].

The long spin relaxation time observed in BLG along with the prediction of larger SO coupling make BLG a potential candidate for future spintronic applications. Moreover, these observations take us a step closer for the realization of graphene spinFETs which is of prime importance for any practical application of graphene spintronics.

Work supported by DFG through FOR 912 and by JARA-FIT.

[1] K.S. Novosolev *et al.*, Science **306**, 666 (2004).

[2] N. Tombros *et al.*, Nature **448**, 571 (2007).

[3] T. Y. Yang et al., Phys. Rev. Lett. 107, 047206 (2011)

Electronic excited states in bilayer graphene double quantum dots

C. Volk[1,2], S. Fringes[1], B. Terrés[1,2], J. Dauber[1], S. Engels[1], S. Trellenkamp[2], U. Wichmann[1], and C. Stampfer[1,2]

[1]II. Institute of Physics B, RWTH Aachen University, 52074 Aachen
[2]Peter Grünberg Institute (PGI-8/9), Forschungszentrum Jülich , 52425 Jülich

We report tunneling spectroscopy experiments on a bilayer graphene double quantum dot device which can be tuned by all-graphene lateral gates. The double quantum dot features addition energies on the order of 20 meV. Charge stability diagrams allow to study the tunable inter-dot coupling energy as well as the spectrum of the electronic excited states on a number of individual triple points over a large energy range. The obtained constant level spacing of 1.75±0.27 meV is in good agreement with the expected single-particle energy spacing in bilayer graphene quantum dots. Finally, we investigate the evolution of the electronic excited states in a parallel magnetic field.

Graphene quantum dots (QDs) are interesting candidates for spin qubits with long coherence times since the hyperfine interaction and the spin-orbit coupling are predicted to be very small. A "paper-cutting" technique enables the fabrication of graphene nanoribbons [1], quantum dots, and double quantum dot devices [2,3], where a disorder-induced energy gap allows confining individual carriers in graphene. Most research has been performed on single-layer graphene devices so far. Bilayer graphene allows to open a band gap by an out-of-plane electric field, which may enable a soft confinement potential and may reduce the influence of localized edge states. Moreover, it is expected that ripples and substrate-induced disorder are reduced, which may also increase the mechanical stability suppressing unwanted vibrational modes.

The studied double quantum dot (DQD) device is fabricated based on bilayer graphene obtained from mechanical exfoliation of bulk graphite. Raman spectroscopy measurements are used to unambiguously identify bilayer graphene. Electron beam lithography and reactive ion etching is used to pattern the graphene flake. Metallic contacts are fabricated by electron beam lithography and lift-off.

Figure 1a shows a scanning force micrograph of the device. The diameter of the etched quantum dots (QDs) measures roughly 50 nm and 60 nm, respectively while the width of the roughly 100 nm long constrictions leading to the dots measure 30 nm. In this study we used the left and right gate (LG and RG) to change the number of carriers in the left and right QD (LQD and RQD), respectively, while the central gate (CG) is used to tune the coupling between the dots. Additionally, the back gate (BG) is used to adjust the overall Fermi level.

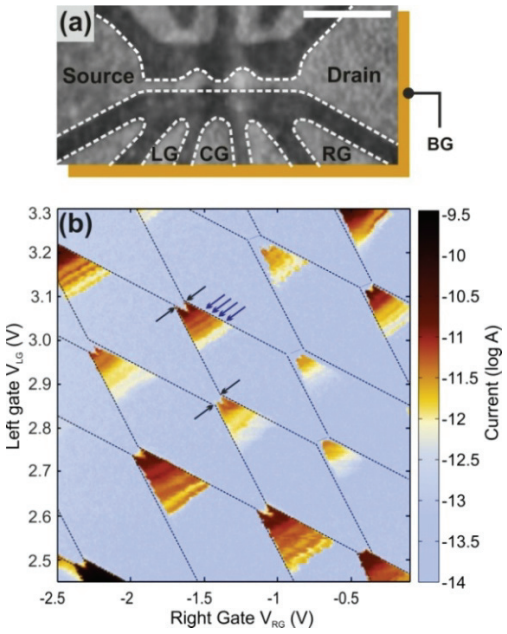

FIG. 1: (a) Scanning force microscope image of the investigated double quantum dot device (the scale bar is 200 nm). (b) Charge stability diagram at finite bias (V_b = 10 mV).

The measurements have been performed in a pumped ^{4}He system with a base temperature of 1.3 K and in a dilution refrigerator with an electron temperature around 100 mK. We have measured the two-terminal conductance by applying a symmetric dc bias voltage V_b while measuring the current with a resolution better than 50 fA.

We tune the back gate and side gate voltages such that the Fermi level crosses all three effective energy gaps created by the thin constrictions. The device is in the DQD regime where the QDs are defined between three energy gaps.

We performed charge stability measurements by varying the left and right gate voltages independently while keeping the bias and central gate voltage constant. A honeycomb pattern characteristic for the charge stability diagram of a DQD is shown in Figure 1b (V_b = 10 mV, T = 100 mK). Electrical transport through the DQD is only possible in the case where the energy levels in both dots are aligned within the source-drain bias window. The triangular-shaped regions (so-called triple points) allow the determination of the addition energies for the left (E_L = 18 meV) and right (E_L = 21 meV) dot respectively. Interestingly, the extracted addition energies are in reasonable agreement with values from single-layer graphene quantum dots with a similar size [2]. The mutual capacitive coupling energy (E_m) between the two QDs can be extracted quantitatively from the splitting of the triple points (see black arrows). By changing the central gate voltage we are able to tune the mutual coupling energy between the QDs from 2.5 to 5 meV.

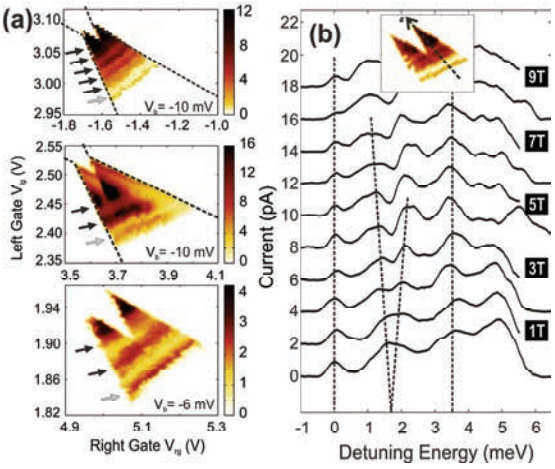

FIG. 2: (a) Individual triple points featuring similar excited state spectra. (b) Current as a function of the detuning energy (measured along the dashed line indicated in the inset) for different B-fields. Traces are offset for clarity.

Additional fine structure inside the triple points is visible (see blue arrows in Figure 1b). Figure 2a shows close-ups of individual triple points highlighting sets of electronic excited state resonances parallel to the triple points base line (see arrows). Along such a parallel line the inter-dot detuning energy, ε, is constant and the current is increased due to transport through an excited state. The electronic nature of these excited states can be proven by the magnetic field dependence as shown below. The detuning energies of the 5 visible excited state resonances in Figure 2a are found to be ε = 1.7, 3.3, 4.9, 6.5, 8.1 meV, respectively. In total we analyzed more than 50 excited states in a range corresponding to roughly 80 different charge configurations on the individual QDs. The electronic excited state energy spacing has been found to be constant over the entire range and a value of Δ = 1.75 ± 0.27 meV has been extracted. Interestingly, this value is in good agreement with the single-particle confinement energy in bilayer graphene QDs, which can be estimated by using the density of states for bilayer graphene. Consequently the single-particle level spacing is given by,

$$\Delta = \frac{4\hbar^2 v_F^2}{\gamma_1}\frac{1}{d^2},$$

where v_F is the Fermi velocity and γ_1 = 0.39 meV is the interlayer hopping energy. Assuming a QD diameter of d = 50 nm, which is in agreement with the lithographically defined QD we obtain a constant (carrier number independent) level spacing of Δ = 1.71 meV. This result is in contrast to single-layer graphene QDs where it has been shown that the single-particle level spacing, $\Delta(N) = h v_F /(d\ N^{1/2})$, depends on the number of charge carriers, N.

We studied the evolution of excited states as function of the magnetic field oriented parallel to the bilayer graphene plane proving the electronic nature of these states. In Figure 2b we show current line cuts along the detuning energy axis (see dashed line) recorded for different parallel magnetic fields. The 1st excited state splits in two peaks, where the characteristic linear peak splitting is 0.2 meV/T (see diverging dashed lines in Figure 2b). A similar effect can also be observed on different triple points. We assume that these splittings are originating from Zeeman spin splitting which is motivated by the linear B-field dependence and their characteristic energy scale.

In summary, we have characterized a tunable bilayer graphene double quantum dot based on a width-modulated graphene nanostructure with lateral graphene gates [4]. We have shown that - in contrast to single layer graphene - the single-particle level spacing is independent on the number of charge carriers on the bilayer quantum dots. By applying a B-field we observed inter-dot transition energy splittings on the order of Zeeman splittings. These results give insights into tunable bilayer graphene double quantum dot devices and open the way to study individual spin states and spin coherence times in future experiments.

[1] B. Terrés, J. Dauber, C. Volk, S. Trellenkamp, U.Wichmann, and C. Stampfer, Appl. Phys. Lett. **98**, 032109 (2011).

[2] F. Molitor, H. Knowles, S. Dröscher, U. Gasser, T. Choi, P. Roulleau, J. Güttinger, A. Jacobson, C. Stampfer, K. Ensslin, and T. Ihn, EPL, **89**, 67005 (2010).

[3] X. L. Liu, D. Hug, L. Vandersypen, Nano Lett., **10**, 1623 (2010).

[4] C. Volk, S. Fringes, B. Terrés, J. Dauber, S. Engels, S. Trellenkamp, U. Wichmann, and C. Stampfer, submitted, (2011).

Low-Noise Biocompatible High-Stable Carbon Nanotube Transistors

V. Sydoruk[1], M. Petrychuk[1,2], A.Ural[3], G.Bosman[3], A.Offenhäusser[1], S.Vitusevich[1]

[1]PGI-8: Bioelectronics, Forschungszentrum Jülich, 52425 Jülich, Germany
[2]Taras Shevchenko National University, Kiev, Ukraine
[3] Department of Electrical and Computing Engineering, University of Florida, USA

We report results of noise spectroscopy of field-effect transistors (FETs) fabricated based on individual carbon nanotube (CNT) using back-gate topography. Lorentzian-shape noise components were analyzed in wide temperature range. The registered noise spectra allow us to estimate the numbers of carriers and to find the energy, position and concentration of traps in the CNT-FET structures. The structures demonstrate high stability and reliability. The results are very promising for development of low-noise biosensors.

Carbon nanotube (CNT) field-effect transistors (FETs) are unique devices that are promising for the development of advanced electronic systems due to the high degree of ordering of carbon atoms on the surface of the 1D tube, which represents a very uniform channel for electron high-speed transport [1]. Because of their huge surface-to-volume ratio, the FETs based on CNT are very promising for biosensor applications. Despite the progress made in CNT-FET technology, transport phenomena are still under debate. We have already reported an investigation of noise properties in back-gate FETs based on the large value of parallel-connected nanotubes [2, 3]. The influence of the SiO_2 layer on current formation in CNT channels and decreasing leakage current after gamma irradiation treatment were recorded. In this work, we report the results obtained on FETs based on individual carbon nanotubes using back-gate topography and noise spectroscopy as a powerful method for studying transport properties. The analysis of flicker and Lorentzian noise components allowed us to estimate carrier concentration and energies traps in the CNT-FETs.

The FET structures under study were fabricated on the base of individual single wall CNTs grown using the chemical vapor deposition (CVD) method on a Si/SiO_2 substrate. The single wall CNT was contacted by two molybdenum electrodes operating as source and drain of the transistor. The width of the electrodes is ~100μm and the distance between them ~6μm. Typical CNT-FET structures are shown in Fig. 1 with total length of (6±1) μm. The heavily doped Si substrate was used as the back gate of the FETs.

In order to study the transport mechanisms in the transistors, current voltage and noise characteristics were measured at different temperatures and applied gate voltages. The relatively high ratio of the current in the off and on states was observed for every sample. The maximum transconductance, g_m, measured at a drain-source bias of 30 mV is found to be as high as 0.1μS. The effective mobility, μ, of the CNT can be estimated using the following equation for long-channel FETs at low drain-source voltage:

$$\mu = \frac{L_{DS}^2 g_m}{C_G V_{DS}} \qquad (1)$$

with $C_G = 2\pi L_{DS}\, \varepsilon_r\, \varepsilon_0 / \ln(2t / r)$, where L_{DS} is the transistor channel length, V_{DS} is the drain voltage, ε_r is the dielectric constant of SiO_2, t is the thickness of the SiO_2 layer, and r is the radius of a CNT. Using ε_r = 3.9, t = 500 nm, V_{DS} = 30 mV, L_{DS} = 6μm, and r = 1.5nm, we obtain μ = 6000 $cm^2\ V^{-1}\ s^{-1}$. Such a mobility value is characteristic of good-quality CNTs.

To investigate the noise properties of the samples we used small gate voltages to decrease the influence of the gate charging effects on the analysis of traps in our structures. The typical noise characteristics of the samples have flicker *(1/f)*, Lorentzian-shape, and thermal components. Current noise power spectral densities as a function of the excess gate voltage, $V_G - V_{th}$, measured in the temperature interval from 70K to 300K are shown in Fig. 2.

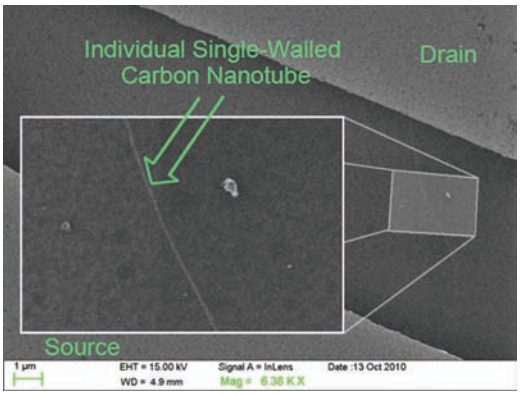

FIG. 1: SEM image of typical a CNT-FET under study

The results demonstrate two different regions separated by a resistance approximately equal to R ~ 1MΩ, which corresponds to the maximum value of the transconductance.

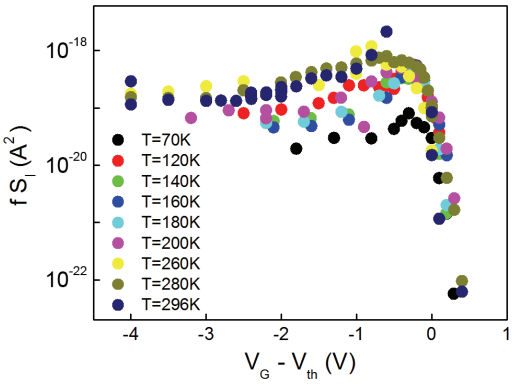

FIG. 2: Normalized noise power spectral density of flicker noise component vs gate voltage measured at V_{DS} = 30 mV, f=1Hz and different temperatures, T(K): 70,120,140,160,180, 200, 260,280,296.

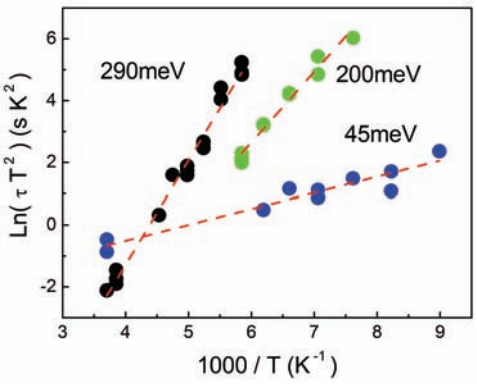

FIG. 3: Arrhenius plot shown for sample 1. Dashed lines correspond to linear fitting, which allows us to calculate the energy levels of the traps.

The dependence on temperature of the flicker noise components was measured in the working point corresponding to maximum transconductance. The analysis of these dependences together with the electrical behavior allows us to conclude that carbon nanotubes have temperature-stable properties.

In addition to the flicker noise, Lorentzian-shaped noise components were observed for all samples. They were clearly resolved in the temperature range investigated. Using an Arrhenius plot (Fig.3), we estimated the energy level of the traps, *Et* , with respect to the conducting band [4]. The energies are found to be 290±10 meV, 200±10 meV and 45±5 meV. From analysis of the results obtained it is follows, that these traps are located near the interface between CNT and SiO_2.

Additional information about trap density can obtained from the plateau of Lorentzian-shaped noise. Usually this component of noise spectra is described by [4]:

$$\frac{f_0 S_I^{LS}}{I^2} = \frac{1}{\pi \cdot N} \frac{\overline{\Delta n^2}}{n} \frac{2}{1+(f/f_0)^2} \qquad (2)$$

where N, n – the total number and concentration of carriers, f_0 and $S_I{}^{LS}$ – characteristic frequency and current noise spectral density of the Lorentzian-shaped process, respectively. Here

$$\overline{\Delta n^2} = (n^{-1} + n_t^{-1} + p_t^{-1})^{-1} \qquad (3)$$

n_t and p_t – concentrations of the electrons and holes on the *t* levels, respectively.

Estimating the number of carriers from the formula $N = L_{DS}^2 / e\mu R_N$ (at R_N = 1.2×10⁶ Ω, μ = 6000 cm² V⁻¹ s⁻¹), and using the maximum of $f_0 S_{I0}^{LS} / I^2$, we can calculate that $\overline{\Delta n^2} / n \sim 1$.

This fact demonstrates that *n* is smaller than n_t and p_t , taking into account Eq. (3). Therefore the concentration of the traps is much higher than the concentration of free carriers. On the other hand, if the relation $\overline{\Delta n^2} / n \sim 1$ holds, the concentration of the carriers can be determined using Eq.(2). The later allows us to unambiguously find the value of carrier mobility in the channel. The obtained results should be used to optimize FETs fabricated on the basis of carbon nanotubes.

In summary, we analyzed transport and noise properties of the FETs based on individual semiconductor CNTs. It was demonstrated that the main source of flicker noise is located near the interface between the carbon nanotube and the SiO_2 layer. The FETs demonstrate stable properties at various temperatures. The recorded Lorenzian-shaped noise components allow us to find the energy of traps near an interface between CNT and SiO_2 as follows: 290±10 meV, 200±10 meV and 45±5 meV. Their concentration was found to be higher than the concentration of carriers in the CNT channel. The number of carriers in the working point of FETs with maximum transconductance was found to be no more than 320. The high values of mobility obtained are characteristic of high-speed transport in the channel of CNT-FETs.

[1] P. J. Burke, Nanotubes and nanowires. World Scientific, Singapore (2007).

[2] S. A. Vitusevich et al., J. Appl. Phys. 107, 063701 (2010).

[3] V. A. Sydoruk et al., Proc. of International conference MSMW'2010, 5546043 (2010).

[4] N. B. Lukyanchikova, Noise Research in Semiconductor Physics, edited by B. K. Jones. Gordon & Breach, Amsterdam, (1996).

Breathing-like modes in an individual multi-walled carbon nanotube

C. Spudat[1], M. Müller[2], L. Houben[3,4], J. Maultzsch[2], K. Goß[1], C. Thomsen[2], C. M. Schneider[1], C. Meyer[1]

[1]PGI-6: Electronic Properties, Forschungszentrum Jülich, 52425 Jülich
[2]Institut für Festkörperphysik, Technische Universität Berlin
[3]PGI-5: Microstructure Research, Forschungszentrum Jülich, 52425 Jülich
[4]ER-C: Ernst Ruska-Centre for Microscopy and Spectroscopy with Electrons

We studied collective vibrational breathing modes in the Raman spectrum of a multi-walled carbon nanotube. Correlating the results obtained by spectroscopy with high-resolution transmission-electron microscopy, we found that these modes have energies differing by more than 23% from the radial breathing modes of the corresponding single-walled nanotubes. This shift in energy can be explained with inter-shell interactions using a model of coupled harmonic oscillators. The strength of this interaction can be related to the coupling strength expected for few-layer graphene.

Multiwalled carbon nanotubes (MWCNTs) can be imagined as multiple graphene sheets rolled up in tubes, which are embedded into one another (inset FIG. 1). This material is interesting for application in nanoelectromechanical devices [1]. It is crucial for this purpose, however, to understand and measure the coupling between the nanotube shells. This coupling is caused by inter-shell interactions, and Raman spectroscopy is a versatile tool to study the nature of this coupling. Its strength shows up in the movement of the layers and shells against each other. Unfortunately, the corresponding inter-layer mode in graphite, the B_{2g} mode, is silent in infrared as well as in Raman spectroscopy. In multi-walled carbon nanotubes (MWCNTs), however, the corresponding vibrational motion has its origin in the radial breathing modes (RBMs) of the nanotube walls, which can be observed with Raman spectroscopy. Thus, carbon nanotubes can be seen as a model system for few-layer graphene.

Raman spectroscopy provides only indirect information of the atomic structure of CNTs. A correlation of aberration-corrected high-resolution electron-transmission microscopy (HR-TEM) and spectroscopy measurements on the same CNT significantly helps to interpret the low-frequency Raman spectrum experimentally observed [2].

MWCNTs were synthesized by chemical vapor deposition on a grid suitable for HR-TEM. The grid was prepared with a marker structure in order to identify individual tubes for the spectroscopic and microscopic measurements.

The HR-TEM image (inset FIG. 1) reveals that this MWCNT is composed of six walls. The shell diameters of the tubes range from d = 0.84 nm for the innermost tube to d = 4.34 nm for the outermost tube. The distance between two shells is constant within the error of the measurements and Δr = 0.35 nm. We compare the diameters obtained in the HR-TEM measurement to the energy of the resonant Raman modes in the low-frequency spectrum. Usually, these resemble the RBMs of single walled carbon nanotubes and depend on the diameter of the tubes.

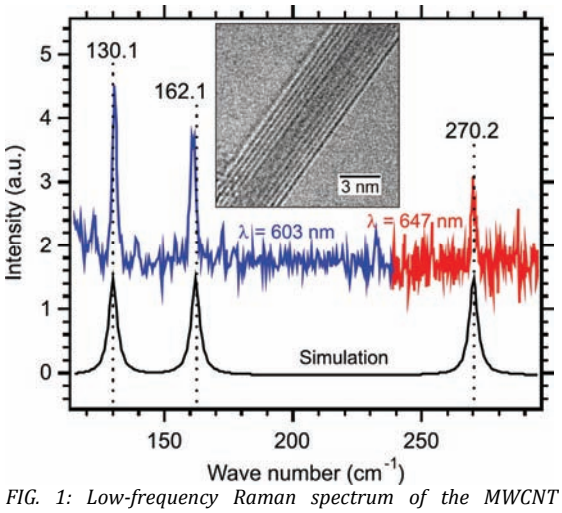

FIG. 1: Low-frequency Raman spectrum of the MWCNT measured at two different wavelengths (blue and red line) and its simulation. Inset: HR-TEM micrograph of the same MWCNT. The nanotube shells appear bright.

Frequency dependent Raman measurements of the same MWCNT are shown in FIG. 1. They were performed prior to the HR-TEM imaging in order to avoid any influence of defects that might be induced by electron irradiation. We observe three modes, which exhibit a strong resonance effect as expected for RBMs. Furthermore, their line width is 3 - 4 cm^{-1}, a typical value for RBMs of SWCNTs. Therefore, we assume that these peaks have their origin in the breathing modes of the tubes, which form the MWCNT.

The Raman shifts ω_{Raman} of the modes observed can be compared with the diameters obtained in the HR-TEM measurements using the relation

$$\omega_{\mathrm{RBM}} = \frac{A}{d_{\mathrm{T}} + B}$$

to convert the tube diameters d_{T} into Raman shifts ω_{RBM} as they would be expected for individual single-walled carbon nanotubes. A and B are sample-dependent constants, which are chosen to be A = 223.75 cm^{-1} and B = 0 for tubes without any additional interactions as suggested by Bandow et al. [3]. The results for the expected Raman shifts are listed in TAB. 1. Strong shifts toward higher wave numbers are found in the experiment for the second and especially for the third inner tube, where the mode is shifted by more than 23% with respect to the RBM position expected from the HR-TEM measurement.

tube no.	d_{T}(nm)	ω_{Raman} [cm^{-1}]	ω_{RBM} [cm^{-1}]	ω_{BLM} [cm^{-1}]
1	0.84	270	266.4	270.9
2	1.54	161	145.3	162.1
3	2.24	131	99.9	130.1
4	2.94		76.1	117.4
5	3.64		61.5	94.7
6	4.34		51.6	62.0

TAB. 1: Comparison of the measured Raman shifts and the simulated BLM-frequencies.

We have shown that the stiffening of the Raman modes can be explained by means of a coupling of the phonon modes due to van der Waals interactions between the walls of the MWCNT using a model of coupled harmonic oscillators [2].

In FIG. 1 the experimentally obtained spectra are compared with the position of the Raman modes obtained from the simulation. The best agreement between simulated and measured Raman shifts is found at a coupling frequency of Ω_{c} = 1.84 THz, which is a measure for the coupling strength. It will reach the inter-layer coupling of graphite Ω_{c} = 3.81 THz for d_{T} → ∞ and infinite number of shells. The values obtained for the Raman shifts ω_{BLM} of the BLMs reflect the experimental data very well (see TAB. 1). And therefore, coupled breathing-like modes (BLMs) as predicted by Popov et al. [4] are observed rather than individual RBMs.

We could unambiguously attribute the Raman mode at ω_{Raman} = 270 cm^{-1} to the counter-phase BLM, while the modes at ω_{Raman} = 161 cm^{-1} and at ω_{Raman} = 131 cm^{-1} are the first two BLMs of mixed modes. Three more modes are expected to be observed at ω_{BLM} = 117 cm^{-1}, at ω_{BLM} = 95 cm^{-1} and at ω_{BLM} = 62 cm^{-1} following the model. These modes do not show up in our measurements, because they are masked by the edge of the Rayleigh peak.

We conclude that the inter-layer coupling in MWCNTs cannot be neglected. The coupling strength we obtain from the model to be Ω_{c} = 1.84 THz is smaller than expected. Calculations for few-layer graphene [5] predict values which are smaller than for graphite but Ω_{c} > 3 THz. In order to understand this deviation and also possible influences of the curvature, a model would be needed that includes the Van der Waals interaction explicitly.

[1] A. Barreiro, R. Rurali, E. R. Hernández, J. Moser, T. Pichler, L. Forró, A. Bachtold, Science **320**, 775 (2008)

[2] C. Spudat, M. Müller, L. Houben, J. Maultzsch, K. Goß, C. Thomsen, C. M. Schneider, C. Meyer, Nano Lett. **10**, 4470 (2010)

[3] S. Bandow, S. Asaka, Y. Saito, A. M. Rao, L. Grigorian, E. Richter, P. C. Eklund, Phys. Rev. Lett. **80**, 3779 (1998)

[4] V. Popov, L. Henrard, Phys. Rev. B **65**, 235415 (2002)

[5] X. Q. He, S. Kitipornchai, K. M. Liew, Nanotechnology **16**, 2086 (2005)

High Temperature Conductance of LaAlO3 / SrTiO3 Heterostructures

F. Gunkel[1], S. Hoffmann-Eifert[1], R. Dittmann[1], S. Mi[2], C. Jia[2], P. Meuffels[1], R. Waser[1]

[1]PGI-7: Electronic Materials, Forschungszentrum Jülich, Germany
[2]PGI-5: Microstructure Research, Forschungszentrum Jülich, Germany

The interface conductance of LaAlO3 / SrTiO3 heterostructures was investigated under high temperature oxygen equilibrium, at a pO2 range from 10−22 to 1 bar and a temperature of 800 to 1100 K. It is compared to the characteristic of SrTiO3 single crystals, which is described in terms of a defect chemistry model. Up to 950 K the equilibrated heterostructures reveal an additional influence of a metallic-like conduct-ion path with a very slight dependence on the oxygen partial pressure. Donor-type interface states are discussed as a possible origin for the exceptional interface conduction of LaAlO3/SrTiO3 heterostructures.

The discovery of the highly conducting interface between $LaAlO_3$ (LAO) films and $SrTiO_3$ (STO) substrates[1] has led to miscellaneous studies on the fundamental properties of LAO/STO-hetero-structures grown by pulsed laser deposition (PLD) and has evoked extensive discussions about the physical mechanisms which underlie the high concentration of charge carriers in the interface region (10^{13} - 10^{17} cm^{-2}).[1,2]

In this context, a strong impact of the oxygen atmosphere during PLD growth on the low temperature conductivity of LAO/STO-hetero-structures with undefined defect configuration has been observed [3] but no studies of the interface conductivity under equilibrium conditions have been reported so far. Therefore, we performed *in situ* measurements of the high temperature conductance (HTC) of LAO/STO-heterostructures under controlled oxygen partial pressure in order to gain more detailed insight into the defect structure of the LAO/STO-interface.[4]

8 unit cells of LAO were grown on TiO_2-terminated (100) STO substrates by means of PLD at a temperature of 970 K and a deposition oxygen pressure of $4x10^{-5}$ mbar. Clear reflection high energy electron diffraction intensity oscillations were observed during the process indicating layer-by-layer growth mode. Those samples exhibited a sheet conductance of about 0.03 mS at 300 K as determined by four-point-probe measurements in a van der Pauw configuration.

The perfect crystallinity and the heteroepitaxial character of the thin films were verified by high-resolution scanning transmission electron microscopy. Figure 1 shows a high angle annular dark field (HAADF) image of an interface region of a representative, as grown sample. The brightness across the interface shows rather a gradual decrease than an abrupt, step-like change demonstrating A-site cation intermixing on a length scale of 2–3 unit cells at the interface in agreement with the findings of Nakagawa et al.[5]

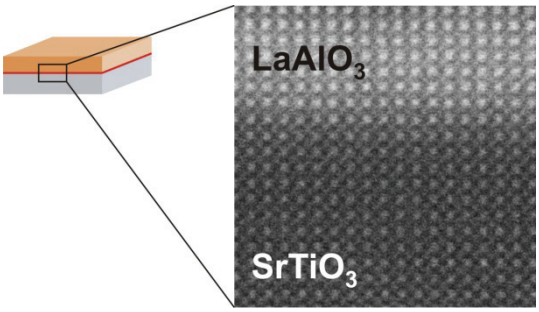

FIG. 1: HAADF image of the LAO/STO-interface region in an as-grown sample.

The HTC measurements were performed at temperatures between 820 and 1250 K in an YSZ-oxygen-pump system which allowed to continuously adjust the oxygen partial pressure between 1 and 10^{-22} bar (for details see ref. 6).

The results of HTC measurements of a LAO/STO heterostructure under controlled oxygen atmosphere are illustrated in Figure 2 in comparison to the bare STO single crystal. In a simple model the dc characteristic of the heterostructure can be described by the sum of three parallel conductance contributions G_{STO}, G_{IF}, and G_{LAO} corresponding to STO single crystal, metallic interface, and LAO layer, respectively. Since the STO-substrate exceeds the thickness of the LAO thin film by a factor of 10^4, one can deduce from reference measurements that the LAO film contribution is always small compared to the substrate contribution and can be neglected.[4] The total conductance of the heterostructure G_{tot} is then given by

$$G_{tot} = G_{IF} + G_{STO} + G_{LAO} \approx G_{IF} + G_{STO} \quad (1)$$

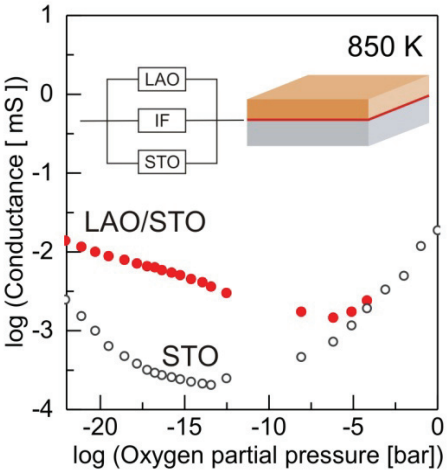

FIG. 2: HTC characteristics of a LAO/STO-heterostructure (red circles) and a STO single crystal (open circles) in equilibrium with the surrounding pO_2 measured at 850 K.

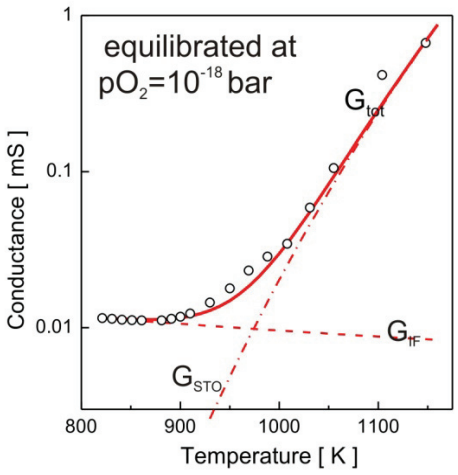

FIG. 3: Temperature dependence of the heterostructure's conductance equilibrated at $pO_2=10^{-18}$ bar. Expt. data (○); fits: metallic interface contribution $G_{IF}\sim 1/T$, substrate contribution $G_{STO}\sim\exp(-E_A/k_BT)$, and total conductance $G_{tot}=G_{STO}+G_{IF}$.

At temperatures lower than 1100 K clear deviations between the conductance characteristic of the heterostructure and the single crystal are observed in the range 10^{-18} bar ≤ pO_2 ≤ 10^{-5} bar. For the given temperature and pO_2 range it can be deduced that G_{IF} possesses a very weak pO_2-dependence far beyond the (-1/4)-dependence of the STO single crystal.

The temperature dependence of the heterostructure's conductance measured under a controlled pO_2 of 10^{-18} bar is analyzed in more detail in Figure 3. Two temperature regimes can be distinguished: from 820 to 900 K, G_{tot} (black circles) decreases with increasing temperature down to a value of about 0.01 mS possessing to a metallic-type behavior. Above 900 K, G_{tot} increases with increasing temperature due to the exponentially rising conductance of the STO substrate. Hence, the decrease in the total conductance below 900 K has to be attributed to the interface contribution according to Eq. (1). This remarkable result indicates that the interface still exhibits a metallic-like conductance at 900 K under equilibrium conditions. The metallic-like behavior of G_{IF} implies the electronic nature of the charge carriers at the interface since ionic conduction possesses thermal activation. For the in-situ measurements it can be excluded that a mere reduction in the STO substrate during the PLD process is the main reason for the high electron density at the LAO/STO interface. Reduction would result in mobile oxygen vacancies which would strive for equilibration with the surrounding pO_2 when heating up the samples.

Furthermore, it is known from the research on defects in perovskite-type titanates that lanthanum donor doped STO bulk ceramics show a constant conductivity over a broad range of pO_2 in which the charge carrier density is determined by the fixed concentration of ionized dopants.[7] Hence, the weak pO_2-dependence of the interface conductivity might give hints for localized, donator-type defects in the interface region such as provided by A-site cation intermixing. Assuming this scenario of La-doping the sheet carrier density n_S within the interface region can be estimated directly from the conductance measurements adopting the values for the known electron mobility μ_{STO} in the STO bulk.[7] Thereby, one obtains $n_S(850\ K) = G_{IF}/e\,\mu_{STO} \approx 10^{13}$–$10^{14}$ cm^{-2} in accordance with published values.[1,2]

In summary, the results of this study show that for a discussion on the nature of the interface conductivity in LAO/STO heterostructures one has to pay attention that the complex defect chemical state of the entire heterostructure is well defined.

[1] A. Ohtomo et al., *Nature* 427, 423 (2004).

[2] S. Thiel et al., *Science* 313, 1942 (2006).

[3] A. Brinkman et al., *Nature Materials* 6, 493 (2007).

[4] F. Gunkel et al., *Appl. Phys. Lett.* 97, 12103 (2010).

[5] N. Nakagawa et al., *Nature Materials* 5, 204 (2006).

[6] C. Ohly et al., *J. Am. Ceram. Soc.* 89, 2845 (2006).

[7] R. Moos et al., *J. Am. Ceram. Soc* 80, 2549 (1997).

Complementary resistive switches for future memory devices

R. Rosezin[1], E. Linn[2], C. Kügeler[1], R. Bruchhaus[1], R. Waser[1,2]

[1]PGI-7: Electronic Materials, Forschungszentrum Jülich, 52425 Jülich, Germany
[2]IWE II: Institute for Electronic Materials II, RWTH Aachen University

Charge based non-volatile memory (Flash) approaches its physical limits. Thus, alternative concepts for the realization of highly scalable and area efficient memory devices are in the focus of research. In this report, a memory element, which is based on the very promising resistive switching effect, is introduced. The complementary resistive switch (CRS) is an anti-serial connection of two bipolar resistive switching devices and can be integrated into passive crossbar arrays while mitigating the sneak path problem. This makes high density memories based on CRS cells possible.

Charge based non-volatile memory devices face serious scaling challenges. With shrinking features sizes, memory levels in Flash transistors are only separated by a few 10 electrons. Thus, it becomes increasingly difficult to ensure data retention over 10 years. As an alternative non-volatile memory concept, ReRAM based on the resistive switching effect is in the focus of investigations [1-5]. In ReRAM, information is stored by a non-volatile resistance change of a simple metal/insulator/metal structure. This resistance can be toggled between at least two different values (high resistance state – HRS and low resistance state – LRS) by the application of a voltage stimulus. The simple device structure promotes the integration of resistive switching materials into high density architectures like passive crossbar arrays. However so far, the feasibility of this architecture was limited by sneak paths, which constrain the size of such a memory (Fig. 1). In the pattern shown in Fig. 1, the state of the high resistance memristive element shown in red color cannot be detected correctly, because the read current is dominated by the sneak current flowing through the adjacent cells. In the Figure only one of the possible paths is shown for simplicity.

For bipolar memristive switches, we propose the CRS as a solution to the sneak path problem [6]. The schematic I-V-characteristic of such an element (here in form of an electrochemical metallization cell) is shown in Fig. 2. Important to note is that for switching to the HRS, a different voltage polarity is required than for the switching to the LRS.

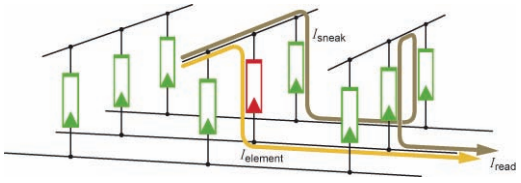

Fig. 1 Parasitic current paths
This figure shows a section of a crossbar array. In this example only the red element in the middle of the array is in HRS, the rest in LRS. In addition to the desired current path through the element in the middle, several other current paths (here is only marked one) occur and cause a large parasitic sneak current.

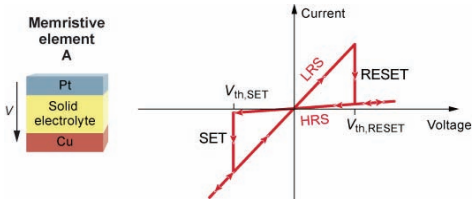

Fig. 2 Memristive element
Here the I-V-characteristic of a memristive element is shown. Initially, the memristive element is low resistive (LRS) and can be switch to the high resistive state (HRS) by applying a positive voltage V>VRESET. For negative voltages (V<VSET) the memristive element switches back to the LRS.

The complementary resistive switch (CRS) consists of two anti-serially (complementary) interconnected resistive switches, schematically shown in Fig. 3, together with a sketch of the resulting I-V-curve. A CRS cell is a two terminal device, just like a resistive switch, with four possible states (Table 1).

Tab. 1 CRS states

CRS	Memristive Element A	Memristive Element B	Overall resistance
0	HRS	LRS	≈ HRS
1	LRS	HRS	≈ HRS
ON	LRS	LRS	LRS + LRS
OFF	HRS	HRS	>> HRS

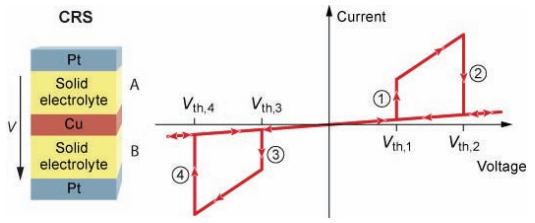

Fig. 3 I-V-characteristic of a CRS cell
A CRS consists of two memristive elements which are connected antiserially. If e.g. memristive element A is in the LRS and memristive element B in the HRS almost all voltage drops over memristive element B until Vth,1 is reached. At this point (①), element B switches to the LRS and element A remains in the LRS, because the potential drop at A is far below Vth,RESET. The CRS state is defined as 'ON' with now both memristive elements being low resistive and having an equal voltage drop. If the voltage reaches Vth,2 (②) memristive element A becomes high resistive, because this is equivalent to a voltage drop of Vth,RESET over element A. This state is defined as '0'. For all applied voltages larger than Vth,3, the memristive element A stays high resistive and element B low resistive. If a potential V comes into the range Vth,4 < V < Vth,3 (③), the high resistive element A switches to the low resistive state and both memristive elements in the CRS are in LRS (state 'ON'). If the negative potential exceeds Vth,4, element B switches back to HRS (④) and the resulting state is '1'.

The 'OFF' state is only found in uninitialized cells. It can be shown that the cells can be initialized into one of the operation states easily. The states '0 'and '1' are the storage states. It is noteworthy that the resistances of the internal memory states '0 'and '1' of a CRS cell are indistinguishable at low voltages because state '0' as well as state '1' exhibit a high resistance. Therefore, no parasitic current paths due to low resistance cells and no pattern dependencies can arise. Information is not stored by a resistance value but rather by a resistance combination of the two constituting elements. To determine the stored information of a single CRS cell the transient region of high current which can be seen in Fig. 3 is used. By choosing a read voltage $V_{th1} < V_{read} < V_{th2}$, the CRS cell will switch into the ON state only, if the cell originally stored a '1'. If the stored state was a '0', no change is induced and the current stays low. This difference can be detected easily, because it is not disturbed by the adjacent cells. The destructive readout makes it necessary, to write back the previous state after reading.

In principle, every bipolar resistive switching material can be integrated into a CRS configuration. However, for an application, only elements which do not require a complicated dedicated forming procedure come into question. This is why we chose Cu/SiO2/Pt bipolar resistive switches for a fully vertical integration [7]. A schematic cross section of the resulting CRS cell stack is depicted in Figure 4.

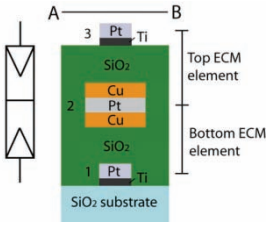

Fig. 4. Schematic cross section of the fabricated CRS stack. The constituting top and bottom ECM elements are marked. The final CRS device stack is (in order of deposition) 30 nm Pt/ 20 nm SiO2/ 20 nm Cu/ 20 nm Pt/ 20 nm Cu/ 20 nm SiO2/ 5 nm Ti/ 40 nm Pt.

The quasi-static electrical characterization, of these cells shows high resistance ratios (Roff/Ron > 1500), which allows for passive arrays of more than 106 elements, which is an improvement of more than 4 orders of magnitude compared to simple resistive switch based arrays. Furthermore, fast switching speed (< 120 µs) was proven (Figure 5). The results are one step further towards the realization of high-density passive nano-crossbar arrays based Gbit memory devices.

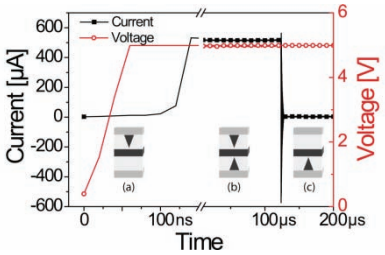

Fig. 5. High resolution pulse measurement of a CRS cell based on Cu/SiO2 memristive elements showing the dynamics of the change of states. The CRS is initially in LRS/HRS, schematically shown in (a). About 120 ns after pulse application, the CRS cell switches to the LRS/LRS state (b), and a significant current flow through the device can be detected. After 125 µs the CRS cell switches to the HRS/LRS state (c), completing the write operation.

In summary, the use of CRS cells as memory element makes high density crossbar arrays feasible paving the way towards next-generation non-volatile memories.

1. J. Borghetti et al., *Nature* 464, 873-876 (2010).
2. D. Strukov et al., *Nature* 453, 80-83 (2008).
3. J. Green et al., *Nature* 445, 14-17 (2007).
4. R. Waser et al., *Nat. Mater.* 6, 833-840 (2007).
5. K. Szot et al., *Nat. Mater.* 5, 312-20 (2006).
6. E. Linn et al., *Nat. Mater.* 9, 403-406 (2010).
7. R. Rosezin et al., *IEEE EDL* 32, 191-193 (2011).

Filament Detection in Resistively Switching $SrTiO_3$ by Grazing Incidence Small Angle X-ray Scattering

S. Krannich[1], S. Stille[1], R. Landrock[2], R. Dittmann[2], R. Waser[2,3], J. Perlich[4], S.V. Roth[4], U. Klemradt[1]

[1] II. Institute of Physics, RWTH Aachen University
[2] Peter-Grünberg-Institute, Forschungszentrum Jülich
[3] Institute of Materials in Electrical Engineering 2, RWTH Aachen University
[4] HASYLAB at DESY, Hamburg

The feasibility of filament detection in resistively switching $SrTiO_3$ thin films was demonstrated using grazing incidence small angle X-ray scattering (GISAXS). Small differences in the scattering patterns could be attributed to the formation of channels with an electron density contrast. The technique enables insight into the geometry of oxygen vacancy agglomerations and opens up new possibilities for in-situ observations.

Today, dynamic random access memories (DRAM) and Flash represent the dominant solid-state memory technologies. Although DRAMs are fast and show almost unlimited cycle times for read and write operations, their main drawback is that they are volatile memory devices. Moreover, they have limitations in scalability because they are charge-based and the cell capacitors cannot be reduced below a certain intrinsic value. On the contrary, Flash memories are non-volatile and show a better scaling behaviour than DRAMs. However, their writing speed is quite low and the number of writing cycles is limited. Promising candidates to overcome these limitations are resistively switching memory devices based on a valence change effect [1].

The bipolar resistance switching effect has been observed in many transition metal oxides like manganates, zirconates or titanates [2-5]. These materials consist of transition metals that can form different stable oxides because of different valence states. The valence state can be changed by introducing oxygen vacancies into the crystal that act as charged shallow donors. Typically, a forming step is needed to enable resistance switching within this class of materials, which is typically performed by applying an external voltage on a two-terminal cell. This leads to the field-induced migration of oxygen vacancies along extended defects, resulting in a change of the valence state of the cation sublattice and a decreasing resistance at the electrode interface [1, 6]. Because of the defect migration along extended defects, the forming process results in the formation of conducting filaments with a lateral size of up to some hundred nm [7]. Those filaments exhibit a contrast in electron density of about 10-20 % with respect to the surrounding matrix. However, so far filaments have only been observed indirectly at their intersections with surfaces and by means of electronic transport measurements.

The structural detection of filaments in thin films was in the focus of an interdisciplinary feasibility study carried out with synchrotron radiation [8]. GISAXS was employed to detect buried structures on the nm scale near surfaces (Fig. 1). Especially designed samples were prepared by pulsed laser deposition of Fe-doped $SrTiO_3$ thin films onto metallic Nb:$SrTiO_3$ substrates. Pt electrodes were evaporated on top and structured into arrays lithographically. The experimental focus was on film thicknesses of 20 and 50 nm.

The X-ray data for the 50 nm film exhibit a correlation maximum both for the formed and unformed state, which are located at $q_y = 0.11$ nm^{-1} and $q_y = 0.07$ nm^{-1} respectively. These values refer to a characteristic length of 60 nm for the formed and 90 nm for the unformed state.

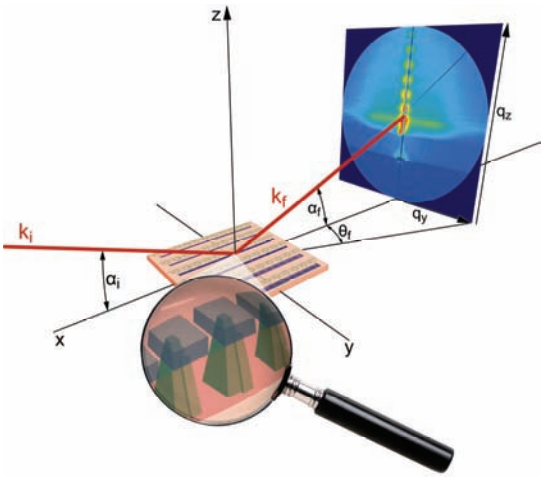

FIG. 1: Experimental setup for GISAXS measurements. On top of the sample, electrodes and structures for alignment are present. An area detector records the diffusely scattered X-ray intensity. The magnifying glass shows a cartoon of the filaments after the forming process. The GISAXS pattern in the sketch is the result of an actual measurement at Hasylab [8].

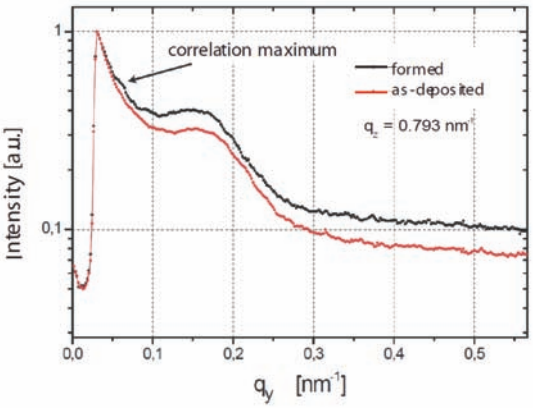

FIG. 2: Lateral cut of a GISAXS pattern for a 20 nm thick Fe:SrTiO₃ film. A correlation maximum appears after electroforming.

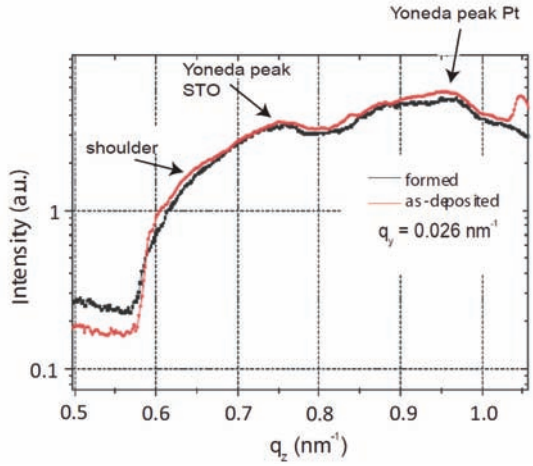

FIG. 3: Vertical cut of a GISAXS pattern for a 20 nm thick Fe:SrTiO₃ film. A small shoulder vanishes due to the forming step.

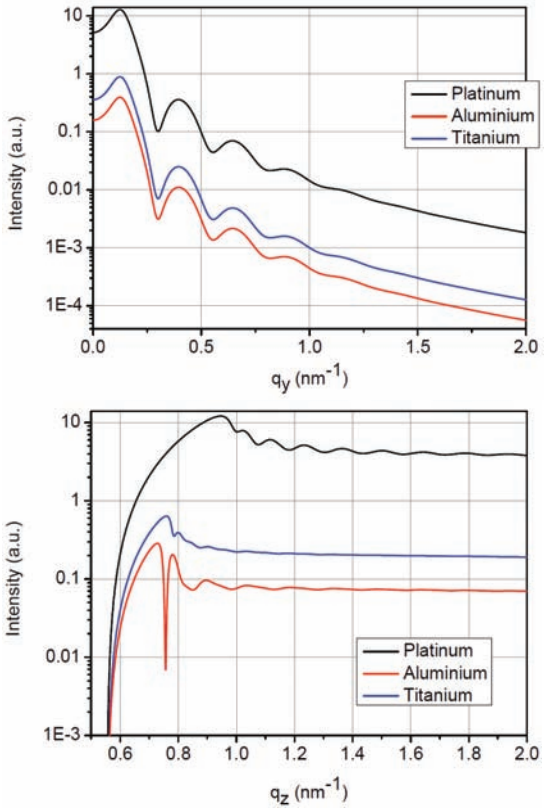

FIG. 4: Simulated scattering intensities in vertical and lateral directions for different electrode materials. The electrode signal is superimposed on the weak X-ray signature of filament formation.

For the 20 nm films, a correlation maximum is detected resulting from electroforming and can thus be considered as a signature of the conducting filaments. Hence, the electroforming process affects the lateral electron density profile and leads to a decreased characteristic length. This can be interpreted in terms of field-induced oxygen migration towards the top electrode.

Currently, the standard material for electrodes is Pt, which however generates a strong X-ray background. The filament formation in the active material then gives rise only to a small intensity modulation. To overcome this limitation, several techniques are under investigation. One route is the removal of the top electrodes, pioneered by Münstermann et al. [7] for conductive AFM measurements. Another promising approach for future GISAXS experiments is the replacement of Pt by Al or Ti. Simulations indicate a significantly reduced elastic scattering background (Fig. 4).

Further progress will also be achieved by using GIUSAXS techniques, where ultra small angles allow to access larger structures. In conjunction with strongly focused submicron beams, the X-ray measurement of structure formation beneath single electrodes is getting experimentally within reach.

[1] R. Waser, R. Dittmann, G. Staikov, and K. Szot, Adv. Mater. **21**, 2632 (2009).

[2] A. Asamitsu, Y. Tomioka, H. Kuwahara, and Y. Tokura, Nature **388**, 50 (1997).

[3] H. Oshima, K. Miyano, Y. Konishi, M. Kawasaki, and Y. Tokura, Appl. Phys. Lett. **75**, 1473 (1999).

[4] A. Beck, J.G. Bednorz, C. Gerber, C. Rossel, and D. Widmer, Appl. Phys. Lett. **77**, 139 (2000).

[5] Y. Watanabe, J.G. Bednorz, A. Bietsch, C. Gerber, D. Widmer, A. Beck, and S. J. Wind, Appl. Phys. Lett. **78**, 3738 (2001).

[6] K. Szot, W. Speier, G. Bihlmayer, and R. Waser, Nature Materials **5**, 312 (2006).

[7] R. Muenstermann, T. Menke, R. Dittmann, and R. Waser, Adv. Mater. **22**, 4819 (2010).

[8] S. Krannich, diploma thesis in physics, RWTH Aachen University (2010); Hasylab Annual Report 2010.

Coexistence of filamentary and homogeneous resistive switching in Fe-doped $SrTiO_3$ thin film memristive devices

R. Landrock[1], T. Menke[1], R. Dittmann[1], R. Waser[1,2]

[1] Peter-Grünberg-Institute, Forschungszentrum Jülich
[2] Institute of Materials in Electrical Engineering 2, RWTH Aachen University

We have demonstrated that resistive switching in Fe-doped $SrTiO_3$ thin films can be either confined to a single strong filament or distributed over larger areas beneath the electrode, in the ideal case the whole junction area. Both types of switching coexist in one and the same sample and exhibit the opposite switching polarity. We suggest allocating those two switching types to areas of different defect density beneath the same electrode.

In the search for promising resistive switching oxide materials for future non-volatile memories [1], special attention has to be paid to their scaling capabilities. The issue of scaling is strongly linked to the question of, whether the switching current is distributed homogeneously across the device area or localized to one or a few conducting filaments [2]. In this work we used conductive AFM (LC-AFM) combined with a delamination technique to remove the top electrode of Fe-doped $SrTiO_3$ devices to gain insights into the nanoscale current distribution at the active switching interface

Figure 1a depicts the current-voltage (I-V) characteristic of a 1 at% Fe doped $SrTiO_3$ metal-insulator-metal (MIM) structure performed after an initial electroforming procedure (+12V, 50s). In the low bias regime, a stable resistive switching state, shown in green, is reached ("counter eightwise"). At higher negative voltage amplitude, a stable second type of switching can be achieved, shown in orange ("eightwise polarity"). Both types of switching occur in the same pad [3].

Figure 1b shows the topography and local current distribution of a junction after electroforming and top electrode removal. The inset covers the whole junction area, while the main topography and current images are magnifications of the lower right part of the junction area. Most of the interface is smooth and has not been structurally altered by the electroforming step. Only a small region in the lower right part of the junction shows some deformation as a result of the electroforming. The conductivity of the formed junction is shown on the right hand side of Figure 1b and is confined to a section close to the crater. The crater itself is well conducting (marked in green) and a somewhat broadened area around the crater shows moderate conductivity (marked in orange).

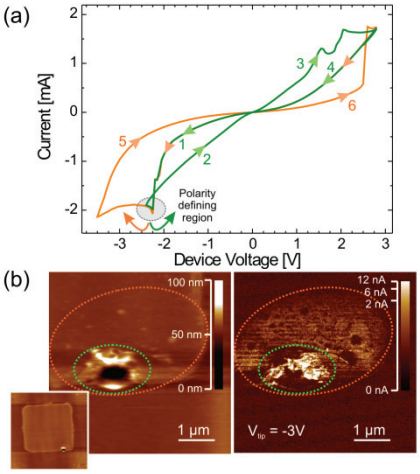

FIG. 1: (a) I-V-characteristics of a pulsed laser deposited 500nm thick 1at% Fe-doped $SrTiO_3$ thin film with 1 at% Nb-doped STO bottom ectrode and Pt top electrode. (b) LC- AFM topography and current image of a junction after electroforming and top electrode remova recorded at -3V [3].

Fig. 2(a) shows a series of LC-AFM scans performed on the same sample. Starting from the conductivity image of an as-formed interface as shown Figure 1b, the tip was biased with -5 V, scanned across the surface, and afterwards another readout image at -3 V was recorded. This treatment step results in a conductivity decrease of the area marked in orange (upper left part of Figure 2a). A second scan with a reversed tip bias of +5 V recovers the conductivity of that region (upper right part of Figure 2a, recorded at -3 V again). In fact, not only this initial region but the complete junction area within the scan range has been switched on. A scan with -5V causes the conductivity to vanish again (with exception of the central crater), while yet another scan with +5 V switches it on again (lower right and lower left part of Figure 2a). The polarity of this type of switching corresponds to the eightwise polarity (orange curve) in Figure 1a.

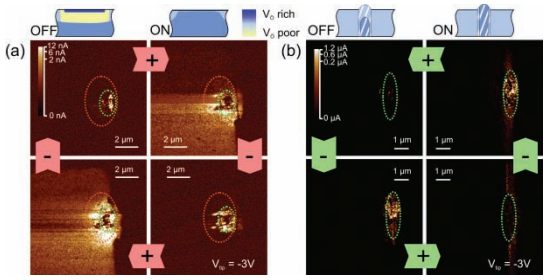

FIG. 2: Tip induced resistive switching of a delaminated MIM structure [3].

The crater region can be switched as well: a scanning voltage of +6 V decreases its conductivity (Figure 2b upper left to lower left), while a voltage of -6 V recovers it (Figure 2b lower left to lower right). The overall polarity of this type of switching corresponds to the green curve in Figure 1a (counter-eightwise). It is interesting to note that in this case only the crater region itself contributes to the switching, indicating a completely localized, filamentary process.

Supplementary to above experiments, two thin film MIM structures have been switched within the "eightwise" polarity and set to the LRS and HRS state before delamination. After delamination, the junction that has been left in the LRS state (Figure 3a) shows both a conducting crater region and a conducting surrounding region. The junction that has been switched to the HRS state, however, lacks the conducting surrounding region (Figure 3b). This experiment proofs that eightwise resistive switching of takes place within an extended region surrounding the forming crater.

Concerning the underlying mechanisms, a standard DC forming step as described above results in the formation of a conducting filament (in our case the crater region) that locally bypasses the Schottky-like interface barrier between oxide material and top electrode [4] and that is a prerequisite for subsequent filamentary switching. The formation of this initial forming filament is aided by Joule heating. Due to heat conduction and a built up chemical gradient even a broadened area around this filament is reduced (extended region marked in orange in Figure 1- 3).

Both regions are involved in subsequent resistive switching steps. The crater (and the underlying forming channel) is a very defect-rich and slightly non-stoichiometric region, judging from its good conductivity and massive topography changes. The mobility of oxygen vacancies along this channel is expected to be quite high. Resistive switching within this channel relies on the attraction of oxygen vacancies into the upper interface and a corresponding lowering of the Schottky-like interface barrier for negative voltages (LRS), and a repulsion of oxygen vacancies with a corresponding recovery of that barrier for positive voltages (HRS).

We suggest the following as one possible explanation for the eight-wise switching: due to slightly reducing deposition conditions, the overall film is n-conducting and contains a certain amount of distributed oxygen vacancies. If a negative voltage is applied to the upper interface, these vacancies migrate out of the lower regions and accumulate at the upper interface. Depending on the top electrode geometry (MIM electrode or AFM tip), this migration could ultimately result in an oxygen vacancy depleted region at the bottom electrode, where no further vacancies can be supplied from below (MIM structure), or in a depleted region at the penetration depth of the AFM tip's electric field (see yellow region in inset in Figure 2a, Off state). Because of the low chemical mobility of oxygen vacancies in this structurally unperturbed region of the film (as opposed to the high mobility forming channel) a subsequent relaxing due to a chemical gradient is subdued and the overall resistance increases. A reversed voltage at the upper interface drives the oxygen vacancies out of the interface again and restores the completely n-type, well conducting film.

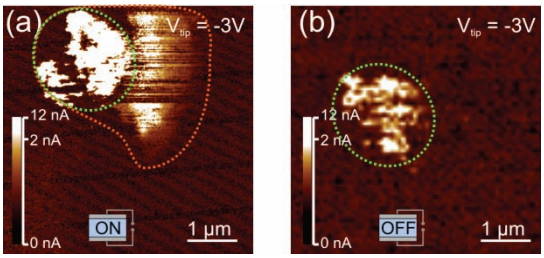

FIG. 3: Conductive AFM current images of a junction that has been set to On state (a) and a junction that has been set to the Off state before delamination. A vanishing of the broadened conducting area around the crater due to the Off switching can be seen [3].

Concerning device scaling, these results imply that resistive switching in $SrTiO_3$ thin films can in principle be extended over the whole junction area if the formation of thermally generated strong filaments is prevented during an appropriate electroforming process.

[1] R. Waser, R. Dittmann, G. Staikov, and K. Szot, Adv. Mater. **21**, 2632 (2009).

[2] A. Sawa, Mater. Today **11**, 28 (2008).

[3] R. Muenstermann, T. Menke, R. Dittmann, and R. Waser, Adv. Mater. **22**, 4819 (2010).

[4] T. Menke, P. Meuffels, R. Dittmann, K. Szot, and R. Waser, J. Appl. Phys.**105**, 066104 (2009).

Search for the permanent electric dipole moment of the electron: Multiferroics bring us a step closer

K. Z. Rushchanskii[1] , M. Ležaić [1], N. A. Spaldin[2]

[1]PGI-1: Quantum Theory of Materials, Forschungszentrum Jülich, 52425 Jülich
[2] Department of Materials, ETH Zurich, Switzerland

We describe the first-principles design of a new material with the specific functionalities required for a solid-state-based search for the permanent electric dipole moment of the electron. We show computationally that perovskite-structure $Eu_{0.5}Ba_{0.5}TiO_3$ should exhibit the required large and pressure-dependent ferroelectric polarization, local magnetic moments and absence of magnetic ordering at liquid-helium temperature.

The standard model of particle physics incorporates the breaking of the discrete symmetries of parity (P) and the combined charge conjugation and parity (CP). It is thought, however, that the CP violation within the framework of the standard model is insufficient to explain the observed matter-antimatter asymmetry of the Universe; therefore, a so far unknown source of CP violation probably exists in nature. The existence of a non-zero permanent electric dipole moment (EDM) of a particle, such as an electron, neutron or atom, would violate time reversal (T) symmetry (Fig. 1*a*) and therefore imply CP violation through the CPT theorem. The values of the EDMs predicted by the standard model are many orders of magnitude below the present experimental limits. However, many theories beyond the standard model predict EDM values within experimental reach. Searching for EDMs therefore constitutes a method of probing the CP-violating physics beyond the standard model.

A number of experimental EDM searches are currently under way or are being developed. One of the most promising new techniques rests on the fact that, as spin is the only intrinsic vector associated with the electron, a non-vanishing electron EDM is either parallel or antiparallel to its spin and hence its magnetic moment. Consequently, atoms with unpaired spins should also possess EDMs. When an electric field, which lifts the degeneracy between the atoms with EDMs parallel and antiparallel to it, is applied to a paramagnetic sample, the associated imbalance of atomic populations generates a magnetization (Fig. 1*b*). Switching the electric field direction reverses the magnetization orientation; in a proposed experiment [1], the change in magnetization is monitored using a SQUID magneto-meter.

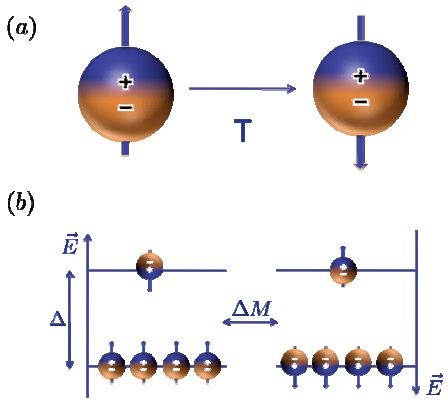

FIG. 1: (a) Time reversal, T, flips the direction of the spin of the electron (depicted by the arrow), but leaves the EDM of the electron (indicated by the +/-) intact. The existance of the EDM therefore violates T; (b) Schematic of the physics underlying the experiment to search for the electron EDM. The energy of electrons with EDMs parallel to the effective electric field E is lower than that for electrons with anti-parallel EDMs by an amount Δ . As a result, there is a population imbalance, creating the corresponding net magnetization, M. When the electric field is reversed there is a magnetization reversal, ΔM, which can be detected using a sensitive magnetometer.

As the experiment aims to detect the intrinsic magnetoelectric response associated with the tiny EDM of the electron, the design constraints on the material are stringent. First, the solid must contain magnetic ions with unpaired spins, because the equal and opposite spins of paired electrons have corresponding equal and opposite EDMs and contribute no effect. These ions must have large atomic number Z, as the response is roughly proportional to Z3. Second, it must be engineered such that the conventional linear magnetoelectric tensor is zero; our approach to achieving this is to use a paramagnet in which the conventional effect is forbidden by time-reversal symmetry. To reach the required sensitivity, a high atomic density of magnetic ions (n≈1022 cm-3) is needed, and these magnetic ions must reside at sites with broken inversion symmetry. The energy splitting Δ shown in Fig. 1b is proportional to the product of the effective electric field experienced by the atom and its EDM.

The effective electric field is in turn determined by the displacement of the magnetic ion from the centre of its coordination polyhedron. We choose a ferroelectric so that it is possible to reverse the direction of the ionic displacements, and hence of the effective electric field, with a moderate applied electric field. Finally, the experiment will be carried out inside liquid helium, so the materials properties described above must persist at low temperature. With these materials properties, and optimal SQUID noise levels, the projected experimental sensitivity is 10-28 e cm [1].

No known materials meet all these requirements. The multiferroic materials in which the magnetic and ferroelectric orders coexist are scarce [2]. Furthermore, avoiding any magnetic ordering at low temperature, while retaining a high concentration of magnetic ions, poses a demanding challenge. In addition, the problem of ferroelectric switchability at low temperature is challenging, as coercivities tend to increase as temperature is lowered.

We choose, as a trial compound, an alloy of EuTiO3 and BaTiO3, with motivation as follows: to incorporate magnetism we require unfilled orbital manifolds of localized electrons; to avoid magnetic ordering the exchange interactions should be small. Therefore, the tightly bound 4f electrons are likely to be the best choice. For conventional ferroelectricity we require transition-metal ions with empty d orbitals to allow for good hybridization with coordinating anions on off-centring. Both $EuTiO_3$ and $BaTiO_3$ form in the *ABO₃* perovskite structure, with divalent Eu^{2+} or Ba^{2+} on the A site, and formally d^0 Ti^{4+} on the *B* site. $BaTiO_3$ is a non-magnetic ferroelectric. In the cubic paraelectric phase its lattice constant is 3.996 Å. The lattice parameter of the paraelectric $EuTiO_3$ is 3.905 Å, notably smaller than that of $BaTiO_3$. It is an antiferromagnet, ordering at a low Néel temperature of ~5.3 K. Seven unpaired 4f electrons of Eu^{2+} ion result in a large spin magnetization of $7\mu_B$. Our hypothesis is that by alloying Ba on the *A* site of $EuTiO_3$ the magnetic ordering temperature will be suppressed through dilution, and the tendency to ferroelectricity will be increased through the expansion of the lattice constant.

We carried out first-principles density-functional calculations within the spin-polarized generalized gradient approximation (GGA). The strong on-site correlations of the Eu 4f electrons were treated using the GGA+U method with parameters U=5.7 eV and J=1.0 eV. For structural relaxation and lattice dynamics we used the Vienna ab initio simulation package (VASP) [3] with the default projector augmented-wave (PAW) potentials [4].

We began our study by calculating the phonon dispersion for the high symmetry, cubic perovskite reference structure at a lattice constant of 3.95 Å (chosen, somewhat arbitrarily, for this first step because it is the average of the experimental $BaTiO_3$ and $EuTiO_3$ lattice constants), with the magnetic spins aligned ferromagnetically. Importantly, we find only one, polar 0-point instability, indicative of a tendency to ferroelectricity. Interestingly, we find that the Eu ions have a significant amplitude in the soft-mode eigenvector, in contrast to the Ba ions both here and in the parent $BaTiO_3$. Next we carried out a structural optimization of both the unit-cell shape and the ionic positions of our $Eu_{0.5}Ba_{0.5}TiO_3$ alloy. Our main finding is that the compound is polar with large relative displacements of O and both Ti and Eu relative to the high-symmetry reference structure. Using the Berry phase method we obtain a ferroelectric polarization value of P=23 $\mu C\ cm^{-2}$. The calculated ground state is orthorhombic with the polarization oriented along a [011] direction and lattice parameters a=3.94 Å, b=5.6 Å and c=5.59 Å. Importantly, the large Eu amplitude in the soft mode manifests as a large off-centring of the Eu from the centre of its O coordination polyhedron in the ground-state structure. This Eu off-centring is desirable for the EDM experiment because the change in local environment at the magnetic ions on ferroelectric switching determines the sensitivity of the EDM measurement. We note that the magnitude of the polarization is strongly dependent on the volume used in the calculation, suggesting that the use of pressure to reduce the volume and suppress the ferroelectric polarization could be a viable tool for reducing the coercivity at low temperatures. Indeed our computations show that, at a pressure of ~2.8 GPa, the polarization (as well as the coercivity) is reduced to zero.

To investigate the likelihood of magnetic ordering, we calculated the relative energies of several collinear magnetic structures (ferromagnetic and antiferromagnetic), obtaining small energy differences between the different configurations, ~1 meV per 40-atom supercell, suggesting an absence of magnetic ordering down to low temperatures.

In summary, the properties of the $(Eu,Ba)TiO_3$ alloy predicted by our first-principles calculations meet the criteria for the search of electron EDM. The subsequent synthesis and characterization of the alloy in form of ceramics confirmed that the material is indeed ferroelectric up to ~213 K, with a ferroelectric polarization ~1 μC cm-2 and is paramagnetic down to the temperature of 1.9 K [5]. The experimental EDM search is now underway.

[1] A. O. Sushkov, S. Eckel, and S. K. Lamoreaux, Phys. Rev. A 81, 022104 (2010).

[2] N. A. Hill, J. Phys. Chem. B **104**, 6694 (2000).

[3] G. Kresse and J. Furthmüller, Phys. Rev. B **54**, 11169 (1996).

[4] P. E. Blöchl, Phys. Rev. B **50**, 17953(1994).

[5] K. Z. Rushchanskii, S. Kamba, V. Goian, P. Vaněk, M. Savinov, J. Prokleška, D. Nuzhnyy, K. Knížek, F. Laufek, S. Eckel, S. K. Lamoreaux, A. O. Sushkov, M. Ležaić and N. A. Spaldin, Nature Mater. **9**, 649 (2010).

Magnetron sputtering of large area epitaxial oxide heterostructures at high oxygen pressures

M. I. Faley and U. Poppe

Peter Grünberg Institut, Microstructure Research (PGI-5), Forschungszentrum Jülich, 52425 Jülich, Germany

We have developed a magnetron sputtering source for high oxygen pressure deposition of large area epitaxial oxide heterostructures. Special arrangement of magnets with iron yoke in the target holder provided improved stability of plasma during sputtering at oxygen pressures from 0.5 mbar up to about 5 mbar with more flat profile of deposited film thickness and/or more homogeneous target utilization compared to the previous deposition methods.

Large area epitaxial oxide heterostructures are required for ultrasensitive high-T_c superconducting magnetic field sensors [1,2], increase of complexity as well as for scale-up of production of the multilayered epitaxial electroceramic devices.

The technique of sputtering at high oxygen pressures allows a smart and homogeneous on-axis in-situ deposition of high-quality metal-oxide thin films from stoichiometric targets [3, 4]. For deposition of the epitaxial metal-oxide films it is necessary to heat the substrate to temperatures above 600 ^{o}C and introduce oxygen into the sputtering gas atmosphere. If conventional sputtering pressures of about 0.01 mbar are used for the on-axis deposition of cuprate superconductors, the negatively charged oxygen ions are accelerated towards the heated substrate by the bias potential and they thus resputter copper atoms from the deposited film leaving copper-deficient non-stoichiometric cuprate films. With the high oxygen pressure sputtering technique, this problem is solved by multiple scattering of the oxygen ions at background gas pressures above 1 mbar with subsequent reduction of their kinetic energy down to thermal energies before they reach the substrate. This results in negligible backsputtering of different components of the deposited films and, consequently, their good stoichiometry and electron transport properties. The typical superconducting transition temperature T_c of the $YBa_2Cu_3O_{7-x}$ (YBCO) films obtained by this method is about 93 K with a critical current density $J_c \approx 6$ MA/cm^2 at 77.4 K.

The high oxygen pressure sputtering technique presupposes deposition at 0.5 to 5 mbar of a pure oxygen (99.999%) sputtering gas atmosphere. The main feature of the sputtering apparatus for the high oxygen pressure sputtering is the presence of a solid insulator, typically made of MACOR, between the target holder and the ground shield. The solid insulator prevents short circuit discharge at these relatively high sputtering pressures and a short mean free path ~ 0.1 mm of the accelerated electrons. If necessary, the entire range of deposition conditions from high-energy impact to low-energy thermalized quasi-condensation is accessible by changing the sputtering gas pressure in this apparatus. During deposition, the substrate typically lies unrestrained on a stainless-steel heat-resistant metal plate and is heated mainly by radiation heat transfer from a metal resistive heater. The typical substrate temperature during deposition depends on the material to be deposited and for YBCO is about 800 ^{o}C while the heater temperature is about 920 ^{o}C.

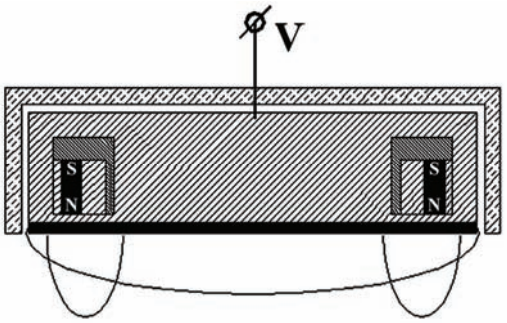

FIG. 1: High oxygen pressure magnetron sputtering: sketch of plasma and target holder with a YBCO target and a MACOR insulator [5].

Magnetron sputtering can be used at high oxygen pressure, but it has characteristic features in conditions of very short mean free path of electrons at pressures above 1 mbar. Large targets require magnetic fields in order to stabilise the sputtering plasma and the optimum distance between magnetic poles is typically in the range between 1 mm and 5 mm [5]. One of the magnetic poles can be replaced by a high-μ yoke made, for example, of iron (see Figure 1). The magnetic field of the Sm_2Co_{17} magnets in such modified target holders additionally excites the sputtering plasma at positions away from the middle and perimeter of the target where otherwise

the plasma tends to localize. This optimized arrangement of the Sm_2Co_{17} magnets in the magnetron target holder is mainly intended to stabilize the plasma. Figure 1b shows an example of magnetron sputtering from a 50-mm YBCO target demonstrating an approximately 3 mm wide ring of the most intensitive plasma region observed at 3 mbar pressure of the pure oxygen sputtering atmosphere (see Figure 2).

FIG. 2: Photograph of plasma and target holder with a YBCO target and a MACOR insulator during the high oxygen pressure magnetron sputtering.

In order to prepare multilayer heterostructures it is important that all layers should be of sufficiently homogeneous thickness. In the case of sputtering, the trivial rule is that the size of the target should significantly exceed the size of the substrate. Films deposited at an oxygen pressure about 3.5 mbar from 50-mm magnetron targets were only about 2.5 % thinner at the corners of square 10-mm substrates and only 15 % thinner at the perimeter of round wafers of diameter 30 mm compared to the film thickness in the middle of the substrates(see Figure 3).

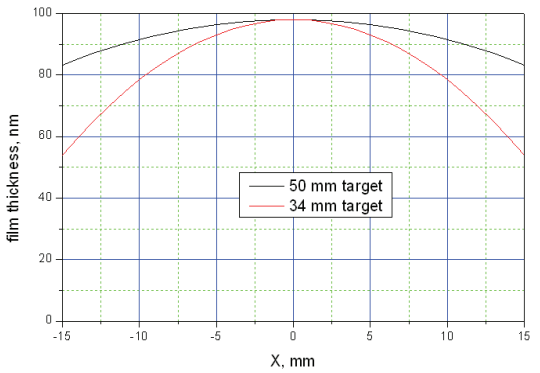

FIG. 3: Thickness homogeneity for YBCO films deposited with 50-mm magnetron target (top line) and for ones deposited with non-magnetron 34-mm targets (bottom line).

At the moment, the wafers up to 30 mm in diameter can be covered with heterostructures of such homogeneous thickness by the high oxygen pressure sputtering technique [6]. Larger area epitaxial metal-oxide heterostructures can be produced with a proper scanning apparatus or larger magnetron targets [5].

The high oxygen pressure sputtering technique is suitable for the deposition of high-quality epitaxial films of all metal-oxide materials required for the production of multilayer high-T_c DC SQUID sensors. No organic material is present in the vacuum chamber of the sputtering machine. We metallize the rear of the targets with an approximately 100 μm thick silver layer, which is partially diffused into the targets at 850 °C to a depth of about 30 μm, and we bond them to the Cu holder by soldering with AgSn solder. The diffusion coefficient of Ag into bulk YBCO ceramic samples is $D_{Ag} \approx 4.5 \times 10^{-9}$ cm²/s at 850 °C [7].

The base pressure in the deposition chamber for YBCO was about 2×10^{-7} mbar while sputtering of YBCO was performed at about 3.5 mbar pressure of pure (99.999%) oxygen. The DC sputtering technique is usually used for deposition from sufficiently conducting targets, while in the case of more insulating targets deposition is carried out by the RF sputtering technique. The typical deposition rate obtained with the DC sputtering technique was about 90 nm/hour while in the case of RF sputtering it was about 20 nm/hour.

[1] Faley M. I., "Cuprate high-T_c superconductors", Chapter in book "Electronic Oxides: Correlation Phenomena, Exotic Phases, and Novel Functionalities" S. Blügel, T. Brückel, R. Waser, and C.M.Schneider (Eds.), Schriften des Forschungszentrums Jülich, **13**, C4 ISSN 1866-1807; ISSN 978-3-89336-609-5. (2010)

[2] Faley M. I. "Epitaxial oxide heterostructures for ultimate high-T_c quantum interferometers", Chapter in book "Superconductivity - Theory and Applications", A. Luiz (Ed.), ISBN: 978-953-307-167-1, *InTech*, Rijeka, Croatia, in press (2011).

[3] Poppe U., Schubert J., and Evers W., Patent US4965248 (1990).

[4] Poppe U. et al., *Journal of Applied Physics*, **71**, pp.5572-5578 (1992).

[5] Faley M.I. and Poppe U. Patent pending, DE 102010049329 (2010).

[6] Faley M. I., Poppe, U., Urban, K., and Fagaly, R.L., *Journal of Physics: Conference Series*, **234**, 042009 (2010).

[7] Dogan O., *Journal of Quantitative Spectroscopy & Radiative Transfer*, **95**, 263 (2005).

Strain induced shift of the crystal-field splitting of $SrTiO_3$

M. Luysberg[1, 2], D. Avila[1, 2, 3], M. Boese[1, 4], L. Houben[1, 2], J. Schubert[5]

[1] Peter Grünberg Institut, Microstructure Research (PGI-5), Forschungszentrum Jülich, Germany
[2]ER-C: Ernst Ruska Centre, Forschungszentrum Jülich, Germany
[3]present address: Dep. de Química Inorgánica I, Fac. CC. Químicas, Universidad Complutense, Madrid
[4]present address: CRANN, Trinity College Dublin, Dublin, Ireland
[5] Peter Grünberg Institut, Semiconductor Nanoelectronics (PGI-9) Forschungszentrum Jülich, Germany

Strained $SrTiO_3$ layers have become of interest, since the paraelectric-to-ferroelectric transition temperature can be increased to room temperature. The effect of strain on the electron loss near edge structure of the Ti $L_{2,3}$ edge in comparison to unstrained samples is investigated by electron energy loss spectroscopy. $SrTiO_3$ grown on $DyScO_3$ and $GdScO_3$, which is tensilely strained, shows a smaller crystal field splitting as observed for the unstrained case. Ab initio calculations of the Ti $L_{2,3}$ and O K edge show a linear decrease of the crystal field splitting with increasing strain, i.e. the energy splitting of the fundamental transitions in the fine structure of Ti $L_{2,3}$ and O K edges become smaller as the strain is increased. Calculated and experimental values of the crystal field splitting show a very good agreement [1].

Thin films with a ferroelectric to paraelectric transition near room temperature are the object of an intense development for their use in different devices such as gate dielectrics for metal semiconductor field-effect transistors (MOSFETs) [2]. $SrTiO_3$ (STO) is an incipient ferroelectric material but in its pure form at room temperature it exhibits a cubic structure and only at very low temperature its ferroelectric properties are observed. However, the transition temperature T_c can be adjusted by strain, e.g. by epitaxial growth on substrates with different lattice parameters [2]. Here we report on tensilely strained STO grown onto $DyScO_3$ (DSO) and $GdScO_3$ (GSO) substrates. Electron energy loss spectroscopy (EELS) is employed to measure the crystal field splitting of the Ti L_3 edge. Ab-initio calculations reveal that the crystal field splitting depends linearly on the strain. Hence, the crystal field splitting provides a measure of the strain in STO.

Multilayers of $SrTiO_3/DyScO_3$ and $SrTiO_3/GdScO_3$ were deposited by pulsed laser deposition on $REScO_3$ (RE: Gd, Dy) (110) substrates [3]. Previous studies revealed perfect epitaxial growth, which implies the formation of a domain structure within the $REScO_3$ layers [4]. EEL spectra were recorded in a probe aberration-corrected FEI Titan 80-300 scanning transmission electron microscope, equipped with a Wien-type electron monochromator and a Gatan GIF Tridiem 866 ERS post column energy filter. The titanium L_3 and oxygen K-edges were calculated by means of real-space multiple scattering calculations, using the self-consistent version of this method implemented in the *ab initio* FEFF8.20 code [5].

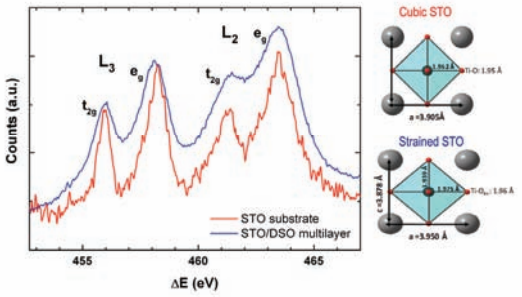

FIG. 1: EEL spectra showing the Ti $L_{2,3}$ edges from unstrained and strained STO, which have been measured on a STO reference sample and STO grown onto DSO substrate. Clearly, the splitting of the L edges is reduced for the strained material. The schematic models on the right hand side display the effect of strain on the Ti-O bond lengths within the octahedra.

Figure 1 illustrates the experimental EEL spectra recorded in the multilayer system STO/DSO. The graph displays the features of the Ti $L_{2,3}$ edge of strained STO grown onto a DSO substrate in blue and from a cubic STO reference sample in red. The two measurements were recorded with an energy resolution of 0.3 and 0.6 eV, respectively. The Ti $L_{2,3}$ edge is formed by four well split peaks attributed to excitations of $2P_{3/2}$ and $2P_{1/2}$ sub-shells to unoccupied t_{2g} and e_g states. In cubic STO the Ti is surrounded by six oxygen atoms forming a regular octahedron with six equivalent Ti-O distances of 1.95 Å (see Figure 1). Under tensile strain this octahedron is distorted, with the four equatorial Ti-O distances being larger than the two apical ones, yielding an average distance Ti-O of 1.96 Å. This enlargement of the average bond length produces a weaker crystal field, which is traduced in a smaller line splitting as it is observed in the blue spectrum.

In order to evaluate the bonding effect, these situations were modeled by means of real-space full multiple scattering (FMS) calculations using the self-

consistent version of this method implemented in the *ab-initio* FEFF8.20 code [5]. The FEFF calculations were done with the Hedin-Lungqvist self-energies to account for inelastic losses and it is found that a cluster of about 50 atoms was sufficient to obtain well converged self consistent field (SCF) potentials. For two cases, i.e. a strain values of 0% and of 1.25%, calculations with larger clusters containing 150 atoms have been performed, which result in the same splitting of the Ti L_3 edge as obtained for a cluster of 50 atoms. For the FMS calculations, a cluster size of 185 atoms was used for both the titanium $L_{2,3}$ and oxygen K edges (not shown here, see [1] for details). The presence of final-state effects in the observed edges resulting from the core-level excitation is also taken into account. The core-hole effect is considered in the present FMS calculations with a fully relaxed potential in the presence of a core hole. The broadening of the theoretical spectra was implemented by measuring the FWHM of the zero loss peaks in the experimental spectra which gives the experimental resolution.

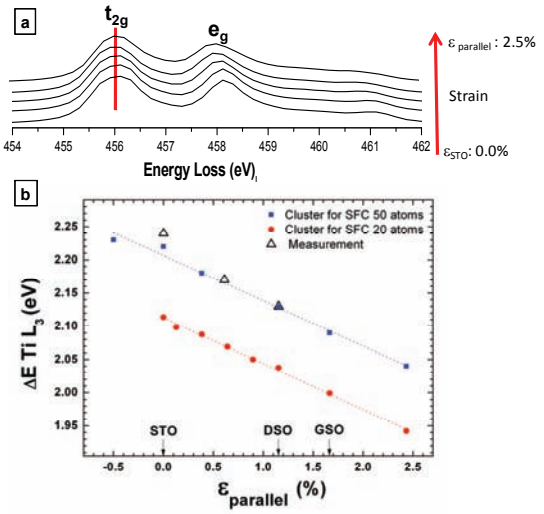

FIG. 2: : a) Calculated Ti L_3 edges for different strain values for a cluster of 50 atoms b) The splitting of the L_3 edge calculated for different strain values (ε) and different cluster sizes (20 and 50 atoms) shows a linear decrease with increasing strain. Experimental values (triangles) show excellent agreement with calculations when the size of the cluster is 50 atoms.

Figure 2a represents the calculated titanium L_3 edges for different strain situations ranging from pure STO, where ε = 0, to a large strain value of ε = 2.5 %. The larger the biaxial strain represented by ε the smaller is the splitting of the L_3 edge. The plot of energy splitting of the L_3 edge against strain reveals a linear relationship. A cluster of only 20 atoms (circles in Fig. 2b) used in SCF calculations already reproduces the linearity. However, only for cluster sizes larger than 50 atoms (triangles in Fig 2b) the theoretical shift converges yielding an almost perfect agreement of calculated and experimental values. Two of the data points were measured from the spectra shown in Figure 1, where EEL spectra have been recorded within unstrained STO substrate and STO grown onto a DSO substrate. The data agree very well with the splitting expected for a strain of 0% and 1.15%, respectively.

The ELNES of the O K edge gives also information about different coordination around the oxygen atom. It has been described that the first two peaks of the oxygen K edge are related to the hybridization of the titanium 3d orbitals with the oxygen 2p and their separation is related to the crystal field splitting. Therefore the calculated oxygen K edges should provide similar information as in the previously described case of Ti L edges. Indeed, a linear decrease of the separation between the two first peaks is observed upon increasing strain [1].

It is well known, that the Ti atom within a strained oxygen octahedron can be shifted with respect to central position, which causes ferroelectrical behavior of $SrTiO_3$. Hence, it is expected, that the Ti atoms within the biaxially strained STO layers investigated here, may not be located at the central position of the octahedra. However, such a shift of the Ti atom is not likely to affect the splitting of the fundamental transitions in the Ti L edges and O K edge, because the average bond length is maintained. Indeed, ab initio calculations of such asymmetric octahedra (not shown here), did not reveal any change in the crystal field splitting.

So far only biaxially dilatations of $SrTiO_3$ have been discussed, which match the experimental situation in scandate/STO multilayer systems. It is worth noticing, that also for compressive strain the linear relationship of crystal field splitting and strain is maintained, which can be deduced from the data point at a strain of -0.5% included into Figure 2. Hence, it is expected, that the crystal field splitting is a measure of biaxial compressive strain as well.

[1] D. Avila, M. Boese, L. Houben, J. Schubert, M. Luysberg, submitted to ACS Applied Materials & Interfaces (2011).

[2] J. H. Haeni, P. Irvin, W. Chang, R. Uecker, P. Reiche, Y. L. Li, S. Choudhury, W. Tian, M. E. Hawley, B. Craigo, A. K. Tagantsev,X. Q. Pan, S. K. Streiffer, L. Q. Chen, S. W. Kirchoefer, J. Levy, D. G. Schlom, *Nature* **430**, 758-761 (2004).

[3] T. Heeg, M. Wagner, J. Schubert, S. H. Buchal, M. Boese, M. Luysberg, E. Cicerrella, J. L. Freeouf, *Microelectron Eng*. **80**,150-153 (2005).

[4] M. Boese, T. Heeg, J. Schubert, M. Luysberg, *J. Mater Sci* **41**, 4434-4439 (2006).

[5] A. L. Ankudinov, C. E. Bouldin, J. J. Rehr, J. Sims, H. Hung, *Phys. Rev. B* **65**,104107/1-11 (2002).

Ab Initio Raman Spectra of Phase-Change Materials

R. Mazzarello[1], G. C. Sosso[2], S. Caravati[3], M. Bernasconi[2], M. Parrinello[3]

[1]Institute for Theoretical Solid State Physics, RWTH Aachen University
[2]Department of Materials Science, Milano-Bicocca University, Milan, Italy
[3]Department of Chemistry and Applied Biosciences, ETH Zurich, USI Campus, Lugano, Switzerland

Phase-change materials are attractive systems for storage applications due to their high crystallization speeds and the optical and electronic contrast between their amorphous and crystalline phases. In this work we have computed the Raman spectrum of amorphous GeTe and cubic and amorphous Ge2Sb2Te5 (GST) by ab initio phonons and an empirical bond polarizability model. The calculated spectra are in good agreement with experimental data: in particular, the spectra of the amorphous phases contain the signatures of the structural motifs revealed by recent ab initio simulations, namely tetrahedral sites for a fraction of Ge and defective octahedral sites for the other Ge atoms and for all Sb and Te atoms.

Phase-change materials (PCMs) based on chalcogenide alloys are of great technological importance due to their ability to undergo reversible and fast transitions between the amorphous and crystalline phases upon heating [1].

This property is exploited in rewritable optical media (CDs, DVDs and, recently, Blu-Ray Discs) and electronic nonvolatile memories of new concept, which are based on, respectively, the strong optical and electronic contrast between the two phases.

Ge2Sb2Te5 (GST) and the related binary GeTe are prototypical PCMs and have been thoroughly investigated. In particular, GST is the most widely studied PCM for applications in electronic memories. In spite of this, the structural properties of amorphous GeTe (a-GeTe), amorphous GST (a-GST) and the metastable cubic phase of GST (c-GST), which is obtained during fast crystallization in optical and electronic devices, are still debated.

Recent ab initio molecular dynamics (MD) simulations based on Density Functional Theory (DFT) of a-GST and a-GeTe [2,3] have contributed to elucidate the structural properties of the amorphous phase: more specifically, they have shown that Ge atoms are mostly fourfold coordinated and that approximately one third of Ge atoms have tetrahedral coordination. The majority of Ge atoms and all Sb and Te atoms are in defective octahedral environments, resembling the cubic phase. A compelling experimental evidence of these structural motifs has not been provided yet.

In this work we have calculated the Raman spectrum of a-GeTe, a-GST and c-GST [4,5]. The models of a-GeTe and a-GST (containing 216 and 270 atoms respectively) were generated by quenching from the melt within ab initio MD, as implemented in the CP2K package [6]. The model of c-GST was obtained by relaxing a 270 atoms supercell where Te atoms occupied one sublattice and Ge, Sb and vacancies were randomly placed in the second sublattice. Phonons at the Γ point were also calculated from first-principles by diagonalizing the dynamical matrix obtained from the variation of forces due to small atomic displacements.

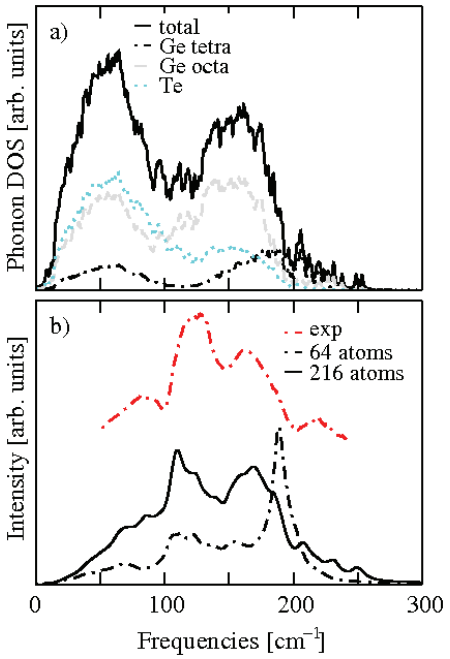

FIG. 1: a) Total phonon density of states (DOS) and phonon DOS projected onto tetrahedral Ge, octahedral Ge and Te of the 216 atoms model of a-GeTe. Tetrahedra dominate the DOS at frequencies above 190 cm-1. b) Reduced Raman spectrum of 64-atoms and 216-atoms models of amorphous GeTe computed within the BPM for unpolarized light in backscattering geometry, compared with the experimental spectrum from Andrikopoulos et al., J. Phys. Condens. Matter 18, 965 (2006). The small, 64-atoms model is in bad agreement with experimental data, whereas the 216-atoms system is able to reproduce the main features of the experimental spectrum.

Since the fully *ab initio* calculation of the Raman spectrum of our models is computationally demanding due to their size, we developed a bond polarizability model (BPM): within this model, the Raman tensor is expressed in terms of bond polarizabilities and their derivatives with respect to bond lengths. These quantities were computed by fitting the *ab initio* Raman tensors of a) a small model of a-GeTe containing 64 atoms and b) the following three crystalline systems: trigonal GeTe, hexagonal Sb_2Te_3 and hexagonal GST. Finally, these BPM parameters were used to compute the Raman spectra in non-resonant conditions of our realistic models of a-GeTe, a-GST and c-GST.

The computed phonon density of states (DOS) of the 216 atoms model of a-GeTe is shown in Fig.1a. Fig. 1b shows the calculated spectrum of the same model of a-GeTe, as well as the spectrum of the small, 64 atoms model and the experimental spectrum. The spectrum of the big model is in very good agreement with experiments and contains two large peaks at about 110 and 170 cm^{-1}, which are mainly due to vibrations of defective octahedral structures. The spectrum at frequencies above 190 cm^{-1}, on the other hand, is dominated by the modes of tetrahedral structures, as revealed by the phonon DOS projected onto Ge atoms in tetrahedral environment (Fig. 1a).

The Raman spectra of cubic GST and a-GST are presented and compared with experiments in Figs. 2a and 2b respectively.

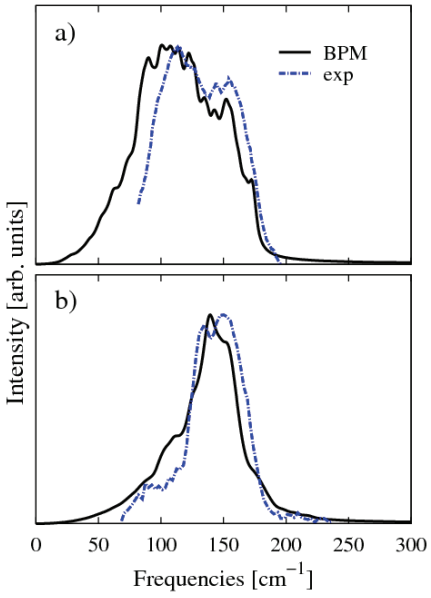

FIG. 2: a) Reduced Raman spectrum of a) crystalline c-GST and b) a-GST, computed within the BPM (continuous black line), for unpolarized light in backscattering geometry, compared with the analogous experimental spectra (dashed blue line) for as-deposited GST from De Bastiani et al., Appl. Phys. Lett. 92, 241925 (2008).

The agreement between theoretical and experimental spectra of GST is also good. The two peaks of the calculated spectrum of a-GST at about 130 and 150 cm^{-1} are due to defective octahedral structures. However, no peak is present at high frequencies, in spite of the fact that a) tetrahedral structures are present in a-GST as well and b) these very structures dominate its phonon DOS at high frequencies. The reason for the absence of high-frequency peaks is that the polarizabilities of GeTe and GeGe bonds are much lower than those of the SbTe bonds and the latter bonds are not present in tetrahedral structures: as a result, the signatures of tetrahedral motifs are hidden by the larger Raman cross section of the vibrations of defective octahedral structures.

As far as the crystalline phase is concerned, it had been shown experimentally (see Fig. 2) that the spectrum of this phase is broader than that of the amorphous phase, in contrast to the behaviour of most materials. This feature is well reproduced by the theoretical spectra. This unusual property is due to the presence of 20% vacancies in one sublattice of the cubic phase, which induce large relaxations of the atoms resulting in a broad distribution of GeTe and SbTe bonds. The spread of these bond lengths turns out to be larger in c-GST than in a-GST: this suggests that, as far as short-range order is concerned, the cubic phase is actually more disordered than the amorphous phase.

In conclusion, we have provided an assignment of the Raman spectra of amorphous GeTe and crystalline and amorphous GST to the vibrations of the peculiar structural motifs found in the structural models of these prototypical PCMs obtained by DFT simulations, which corroborates the validity of these very models.

The next step will be a microscopic investigation of the mechanisms driving the fast crystallization of PCMs (which can proceed on time scales of a few nanoseconds) by the same *ab initio* methods. This project will be carried out in close collaboration with the experimental group of Prof. Wuttig, who will be perfoming measurements of the crystal growth velocity over a wide range of temperatures and time scales.

[1] Wuttig M., Yamada N., Nature Mater. **6**, 824 (2007).

[2] Caravati S., Bernasconi M., Kühne T., Krack M., Parrinello M., Appl. Phys. Lett. **91**, 171906 (2007).

[3] Akola J., Jones R. O., Phys. Rev. B **76**, 235201 (2007).

[4] Mazzarello R., Caravati S., Angioletti-Uberti S., Bernasconi M., Parrinello M., Phys. Rev. Lett. **104**, 085503 (2010).

[5] Sosso G. C., Caravati S., Mazzarello R., Bernasconi M., Phys. Rev. B, **83** (2011), 134201

[6] VandeVondele J. *et al.*, Comput. Phys. Commun. **167**, 103 (2005); http://cp2k.berlios.de.

Disorder induced localization in crystalline phase-change materials

P. Jost[1], H. Volker[1], M. Woda[1], P. Merkelbach[1], C. Schlockermann[1], T. Siegrist[1,2], and M. Wuttig[1]

[1]I. Institute of Physics (IA), RWTH-Aachen University
[2]Department of Chemical and Biomedical Engineering, Florida State University

Mechanisms leading to metal–insulator transition include electron correlation [1] (Mott transition) or disorder [2] (Anderson localization). Although in most systems correlation seems to be dominant a clear distinction is difficult. In this report we discuss a metal–insulator transition (MIT) on increasing annealing temperature [3] for a group of crystalline phase-change materials [4], where the metal–insulator transition is due to strong disorder usually associated only with amorphous solids. With pronounced disorder but weak electron correlation, these phase-change materials form an unparalleled quantum state of matter.

Resistivity measurements of as-deposited amorphous thin films of $GeSb_2Te_4$ are depicted in FIG. 1. Starting at room temperature, the films are heated at a constant rate. With the onset of crystallization, the resistivity suddenly drops by almost 3 orders of magnitude. However, the resistivity in the crystalline state decreases by a factor of approximately 400 on increasing the annealing temperature from 150 to 350 °C.

As depicted in FIG. 2, this pronounced annealing dependence of the resistivity in the crystalline state is also observed for other alloys on the pseudo-binary line between GeTe and Sb_2Te_3. Only resistivity data points obtained on cooling (see the marked region in FIG. 1) are shown to separate the reversible temperature dependence from the irreversible changes due to relaxation. Remarkably, the qualitative and quantitative changes in the temperature coefficient of the resistivity (dρ/dT) as a function of step-annealing temperature follow a generic behavior. All four materials change the electronic transport mechanism from non-metallic (dρ/dT<0) to metallic (dρ/dT >0) behavior at the same critical resistivity value of 2–3 mΩ cm - strong evidence for an MIT at elevated temperatures for all four PCMs depicted in FIG. 2, and hinting at universal behavior. This universal electronic behavior seems to be at the origin of the remarkable reproducibility of the resistance switching that is crucial to the applications of phase-change materials in non-volatile-memory devices.

The existence of an MIT can also be verified in the low temperature limit as shown in FIG. 3. The 150-°C-annealed film exhibits the most pronounced increase of the resistivity at low temperatures, which can be fitted by a variable-range hopping

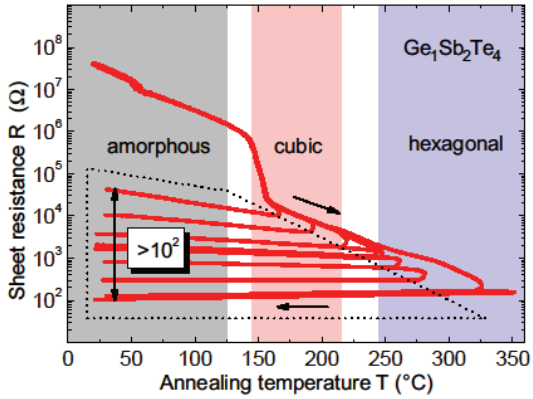

FIG. 1: Temperature dependence of the sheet resistance of a 100-nm-thick $GeSb_2Te_4$ film measured in van der Pauw geometry on heating and subsequent cooling to room temperature. The region marked with dotted lines is further discussed in FIG. 2.

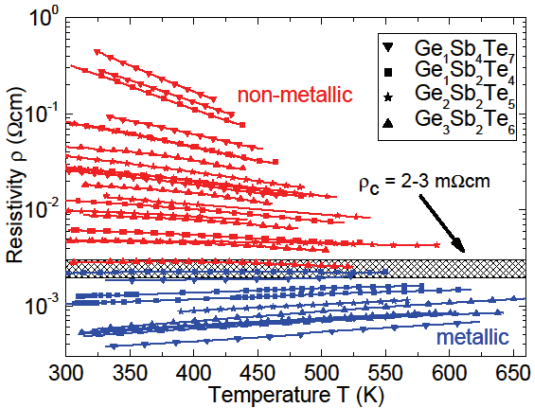

FIG. 2: With increasing annealing temperature a systematic change of the resistivity and dρ/dT is observed for four different GeSbTe alloys. At a critical resistivity of about 2–3 mΩ cm the behavior changes from non-metallic (dρ/dT<0) to metallic (dρ/dT>0) for all four alloys, indicative of a aeneric behavior on annealina.

model giving a conductivity of $\sigma=\sigma_0\exp[-(T_0/T)^{1/4}]$. Hence this sample acquires a vanishing conductivity (insulating behavior) in the limit of $T \rightarrow 0$ K. In contrast, the resistivity on extrapolation to 0 K is clearly finite when annealed to temperatures exceeding 275 °C. It is noteworthy that the critical boundary resistivity between metallic (dρ/dT>0) and insulating (dρ/dT<0) behavior observed in FIG. 2 is valid in the whole temperature range. Indeed, the maximum metallic

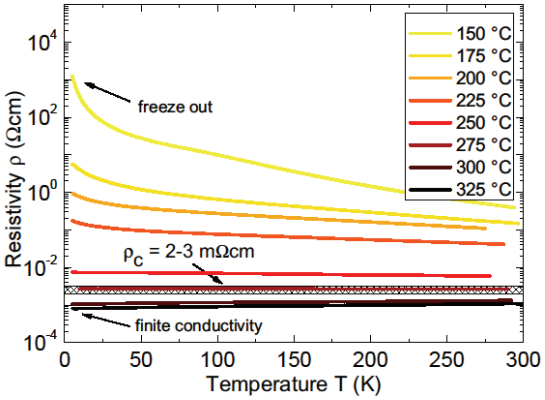

FIG. 3: The resistivity for eight $Ge_1Sb_2Te_4$ samples annealed in the range from 150 to 325 °C is shown. For annealing temperatures lower than 275 °C the non-metallic character of the TCR (compare FIG. 1&2) is preserved down to 5 K. The resistivity of the samples annealed to temperatures higher than 275 °C remains metallic in the whole range.

resisitivity predicted from the Ioffe-Regel criterion (2.7 mΩcm) is in excellent agreement with this number, clear evidence for a maximum metallic resistivity (minimum metallic conductivity) between 5 and 600 K in this family of systems.

Having validated the MIT in $GeSb_2Te_4$, questions about its microscopic origin arise. It is tempting to attribute the MIT to electron correlation effects similar to the Mott transition in doped semiconductors such as Si:P. However, in this case the Mott criterion $n_c^{1/3}a_H^*$=0.26 should forecast the correct carrier concentration at the transition. With an effective mass of 0.4 m_e and a static dielectric constant of at least 98, the Bohr radius a_H^* is determined to be 130 Å, giving a small charge-carrier concentration n_c of 8.0×10^{15} cm^{-3} required to create a metallic state. This estimate fails completely for $GeSb_2Te_4$, where the observed critical carrier concentration of 2.0×10^{20} cm^{-3} determined by Hall measurements is larger by a factor of 25,000. Edwards & Sienko have proven the Mott criterion to accurately reproduce the critical concentration in a vast number of doped semiconductors. Thus, in $GeSb_2Te_4$ correlation effects cannot drive the MIT and a different mechanism impeding metallic charge transport must be at play.

One pronounced difference between $GeSb_2Te_4$ and ordinary sp^3-bondedsemiconductors is the high degree of disorder in $GeSb_2Te_4$. In the rock-salt-like structure produced on initial crystallization tellurium atoms form an fcc sublattice. This fast process will produce a random arrangement of germanium, antimony and empty lattice positions in the octahedral sites provided by the tellurium lattice. This random arrangement on the cation sublattice creates pronounced disorder-induced localization effects. Owing to the strong directionality of the resonant p bonds, the orbitals' overlap is more sensitive to lattice distortions in $GeSb_2Te_4$ than in sp^3-bonded semiconductors.

Therefore, initially, the high degree of disorder leads to tremendous electron scattering, resulting in insulating behavior. This is in line with the observation of variable-range hopping for the sample annealed to 150 °C—evidence for a significant amount of disorder in the system. Consequently, $GeSb_2Te_4$ annealed to low temperatures can be regarded as an Anderson insulator. A very simplistic presentation of the MIT is given in FIG. 4: As long as the Fermi energy E_F lies within the localized states (shaded regions) the system is insulating (left). Annealing reduces the disorder and thus lifts the mobility edge E_μ. When the mobility edge passes the Fermi energy (centre) the 'Anderson-like' transition to metallic behavior (right) occurs. For simplicity the Fermi energy is kept constant.

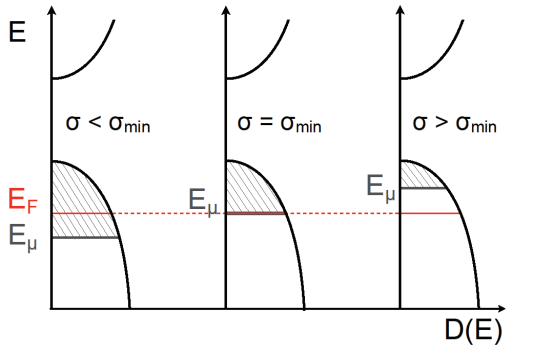

FIG. 4: Simplistic presentation of the MIT in $Ge_1Sb_2Te_4$: The reduction of disorder on annealing lifts the mobility edge E_μ with respect to the Fermi energy E_F triggering the transition to the metallic state.

In summary, we have shown that phase-change materials in the $GeTe\text{-}Sb_2Te_3$ system exhibit a disorder induced MIT on annealing the crystalline phase. This is in contrast to the well-studied correlation driven MITs in doped semiconductors. The small mean free path of the charge carriers in conjunction with the crystalline state provides a unique opportunity to explore disorder-induced localization both experimentally and theoretically.

We would like to thank F. Evers, A. Kapitulnik, S. Kievelson, T. Geballe, B. Shklovskii and B. Spivak for helpful discussions. Financial support by the DFG (Wu243/17), the Seed Funds of the Faculty for Mathematics, Informatics, and the Natural Sciences at RWTH Aachen and the Alexander von Humboldt Foundation (for T.S.) is acknowledged.

[1] Mott, N. F. Conduction in non-crystalline systems IV. Anderson localization in a disordered lattice. Phil. Mag. 22, 7–29 (1970).

[2] Anderson, P. W. Absence of diffusion in certain random lattices. Phys. Rev. 109, 1492–1505 (1958).

[3] Siegrist, T. et al. Disorder-induced localization in crystalline phase-change materials. Nature Mater. 10, 202-208 (2011).

[4] Wuttig, M. & Yamada, N. Phase-change materials for rewritable data storage. Nature Mater. 6, 824-832 (2007).

Chemical tuning of π-conjugated Molecules for Molecular Electronics

V. Caciuc[1,3], M. C. Lennartz[2,3], N. Atodiresei[1,3], R. Waser[2,3], S. Blügel[1,3,4] and S. Karthäuser[2,3]

[1]PGI-1/IAS-1: Peter Grünberg Institut and Institute for Advanced Simulation - Quantum Theory of Materials, Forschungszentrum Jülich, Germany
[2]PGI-7: Peter Grünberg Institut - Electronic Materials, Forschungszentrum Jülich, 52425 Jülich
[3]JARA-FIT, [4]JARA-HPC

We have performed a combined experimental and theoretical study of several carboxylate molecules chemisorbed on the Cu(110) surface to investigate how to intentionally tune the electronic properties of such possible molecular electronic systems. By using the density functional theory (DFT) we predicted the electronic structure of single carboxylate-Cu(110) systems obtained by a systematic chemical functionalization process. For several carboxylate-surface systems, we carefully checked the predicted electronic structure by performing scanning tunnelling microscopy (STM) and scanning tunnelling spectroscopy (STS) experiments. On the basis of the experimental and theoretical data, molecular properties like the character (σ or π) of the individual molecular orbitals and the HOMO-LUMO gap variations caused by different substituents can be identified.

The development of future molecular electronic devices relies on a clear picture of the complex structure-physical property relationships present in molecule-surface systems [1]. To rationally design molecular electronic devices, a basic prerequisite is to understand how to specifically modify the electronic properties of a molecule-surface system in order to reach the desired device functionality. In this context, the theoretical tool of choice to predict the electronic structure of a molecule-surface system is DFT while experimentally it can be probed by STM and STS experiments.

In a recent study [2] we have investigated how to change the electronic properties of a benzoate ($C_7H_5O_2$) molecule chemisorbed on the Cu(110) surface by a systematic chemical functionalization process. As depicted in Figure 1, the electronic structure of the benzoate-Cu(110) surface can be rationally modified by (1) including an N atom in the aromatic ring, (2) by replacing an H atom at the aromatic ring by the carboxylic (COOH) functional group or by combining (1) and (2). As in depth discussed in [2], each functionalization path leads to fingerprint features of the calculated density of states (DOS) at the molecular site. For instance, one of the main differences between the possible functionalization paths, i.e. (1), (2) and (1+2), is how the hybridized molecule-surface states with a π character at the molecular site are located with respect to the Fermi level of the whole system (see reference 2 for more details). This knowledge can be further used either (i) to identify which specific carboxylate molecules are chemisorbed on a metal surface or (ii) to outline a practical scheme to design molecule-metal systems with specific transport properties.

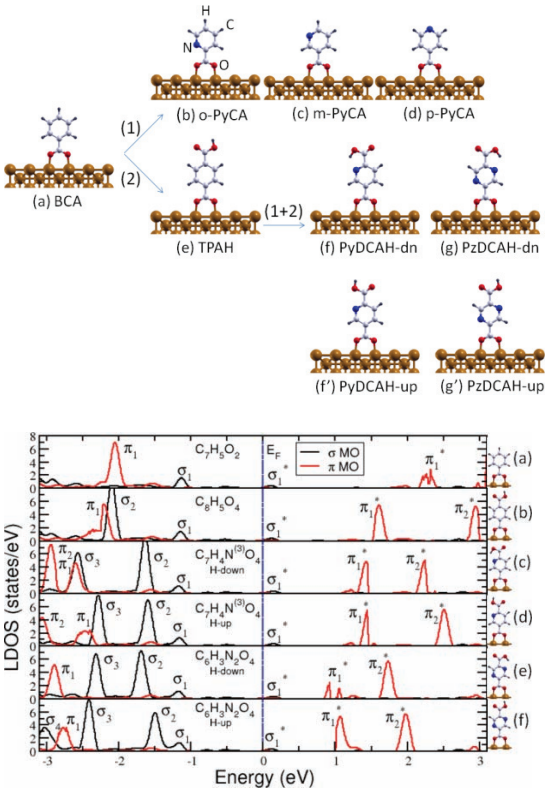

FIG. 1: (upper panel) Chemical functionalization process of (a) the benzoate (BCA) on the Cu(110) surface by (1) replacing a CH group in the aromatic ring through an N atom to obtain (b) ortho- ($C_6H_4N^{(2)}O_2$), (c) meta- ($C_6H_4N^{(3)}O_2$) and (d) para- ($C_6H_4N^{(4)}O_2$) pyridine carboxylate (PyCA) or by (2) replacing an H atom at the aromatic ring through a carboxylic group (COOH) resulting in (e) terephthalate ($C_8H_5O_4$). Starting from (e) and further replacing a CH group by one N atom one obtains dehydrogenated pyridine-2,5-dicarboxylic acid ($C_7H_4N^{(3)}O_4$) with (f) or without an hydrogen bond (f'). A similar substitution in the latter system leads to dehydrogenated pyrazine-2,5-dicarboxylic acid ($C_6H_4N_2O_4$) also with (g) or without an hydrogen bond (g'). (lower panel) A characteristic feature of the density of states (DOS) calculated for the paths (2) and (1+2) is the shift of the unoccupied molecule-surface states with a π character at the molecular site closer to Fermi level.

The accuracy of the electronic structure predicted by the DFT calculations for the carboxylate-Cu(110) surface systems investigated in [2] can be experimentally verified via STS measurements. More specifically, the *dI/dV* spectra measured in STS experiments can be compared with the theoretical molecular density of states in order to identify for example the nature (σ or π) of the molecule-surface states at the molecular site. As an example, the molecule-surface states corresponding to the *dI/dV* peaks measured for the benzoate-Cu(110) surface system have a π character at the molecular site (see Figure 2). It is also interesting to note that the states with a σ character close to Fermi level like the bonding σ_1 state does not appear as a clear feature in the *dI/dV* spectra. This fact is related to a lack of the charge density of this σ_1 state at the molecule-vacuum interface.

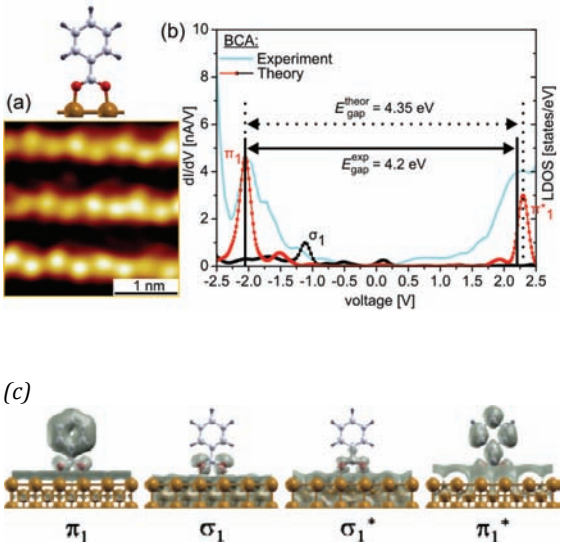

FIG. 2: (a) High-resolution STM image of the BCA on Cu(110) surface. (b) The comparison between the experimental dI/dV spectrum recorded at a current set point of 0.5 nA and the theoretical DOS reveals that at the molecular site these peaks have a π character. Note that the molecule-surface states close to Fermi level with a σ character at the BCA site do not appear as a clear feature in the dI/dV curve. (c) Charge density plots of the molecule-surface states in an energy range corresponding to σ and π depicted in (b).

Furthermore, we have shown in a recent publication [3] that a careful analysis of the experimentally measured *dI/dV* curves in terms of the calculated DOS can reveal also the molecular structural changes that can occur during an STM/STS experiment performed for a molecule-surface system.

As shown in Figure 3, in the case of the pyridine-2,5-dicarboxylic acid on Cu(110) the height-dependent *dI/dV* curves measured for different values of the tunnelling current set points exhibit a peak structure characteristic for each STM-tip height. Interestingly, for this molecule on the Cu(110) substrate, several different conformers are possible controlled by the specific position of the H atom in the carboxylic group (COOH) at the vacuum interface. From theoretical point of view, for each of these possible conformers a fingerprint DOS can be calculated which unambiguously indentifies it. Then a careful comparison between the STS measurements and the theoretical DOS reveals that a different peak structure of the height-dependent *dI/dV* spectra can be assigned to different positions of the H atom in the carboxylic group. Besides this structural information our combined experimental and theoretical work also reveals, as already shown in the previous example, the character (σ or π) of the hybridized molecule-surface states at the molecular site as a function of the tip position.

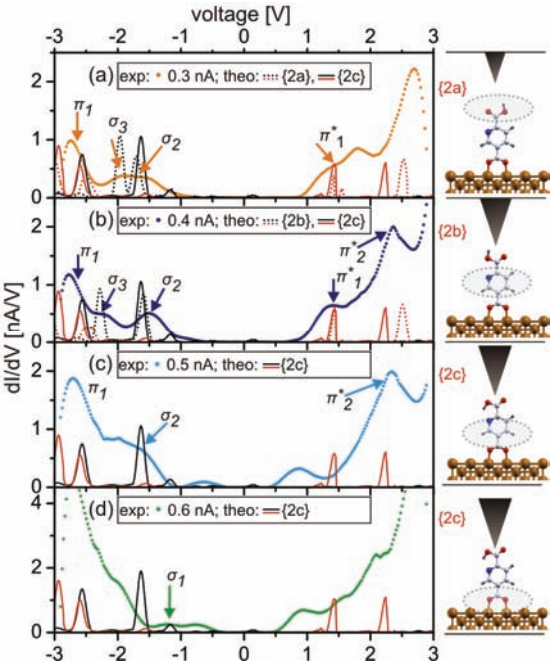

FIG. 3: Experimental dI/dV spectra vs calculated DOS for (dehydrogenated) pyridine-2,5-dicarboxylic acid on the Cu(110) surface. By increasing the tunneling current set point, some occupied molecule-surface states with a σ character at the molecular site like σ_3 modify their energetic position relative to σ_2 and π_1 suggesting a molecular structural change. Depending on the STM tip height, the molecule-surface states spatially localized at different molecular parts can be also detected.

The theoretical calculations have been performed on the JUROPA and JUGENE supercomputers at the Jülich Supercomputing Center, Forschungszentrum Jülich (Germany).

[1] S. Karthäuser, J. Phys.: Condens. Matter. **23**, 013001 (2010).

[2] V. Caciuc, M. C. Lennartz, N. Atodiresei, S. Karthäuser and S. Blügel, Nanotechnology **22**, 145701 (2011).

[3] M. C. Lennartz, V. Caciuc, N. Atodiresei, S. Karthäuser and S. Blügel, Phys. Rev. Lett. 105, 066801 (2010).

Electronic transport properties of individual 4,4'-bis(mercaptoalkyl)-biphenyl derivatives measured in STM-based break junctions

Adam Busiakiewicz[1,2], Silvia Karthäuser[2], Melanie Homberger[1], Peter Kowalzik[2], Rainer Waser[2], Ulrich Simon[1]

[1] Institute of Inorganic Chemistry (IAC), RWTH Aachen University
[2] Peter Grünberg Institut (PGI-7), Forschungszentrum Jülich, 52425 Jülich

Electronic transport measurements of individual systematically varied 4,4'-bis(mercaptoalkyl)-biphenyl derivatives deposited on Au (111) substrates are performed using STM-based break junctions. From these measurements it is concluded that the molecular conductance depends upon the relative position of the biphenyl-unit within the molecule and thus upon the "distance" of the biphenyl-unit to a gold contact. Furthermore we address the role of the specific contact situation (-S-Au) which altogether allows us to achieve a deeper understanding of the electronic transport properties of respective molecules.

The design and production of molecular species with defined electronic properties are fundamental prerequisites of molecular electronics. If a complex molecular electronic device based on individual molecular units shall be realized, a detailed knowledge of how the respective molecular subunits contribute to the overall electrical characteristics is vital.

We focus on electronic transport measurements of organic molecules composed of a central biphenyl unit (BP) carrying two mercaptoalkyl substituents with different chain lengths (m = n = 5, m = 3/n = 7, m = 1/n = 9, m, n = number of CH_2-units), in para-position of the BP unit.[1] The two mercaptoalkyl substituents enable chemical contact to an Au-surface and an Au-STM tip. The tailor-made molecules are synthesized via a six step reaction pathway utilizing Pd-catalyzed Suzuki cross-coupling reaction of phenylboronic acids with haloarenes. Following this preparation scheme the MABPs are obtained as thioacetyl protected moieties, purified by column chromatography or crystallization. Immersion of freshly prepared Au(111) substrates into a 0.1 mM ethanolic solution of the acetyl protected MABPs and addition of ammonium hydroxide yields self-assembled monolayers of MABP. The samples are heated up to 70°C in solution, rinsed with hot ethanol and directly transferred into the UHV-STM chamber.

For the electronic transport measurements we utilized an STM-based break junction setup. Thereby the STM tip is approached to the sample until a contact with the molecules is formed. Subsequently the tip is retracted while recording the current-distance (I(s)) characteristics. The observed steps on the I(s)-traces (see Figure 1a) correspond to the breaking of bonds between the tip or Au-substrate and the molecule.

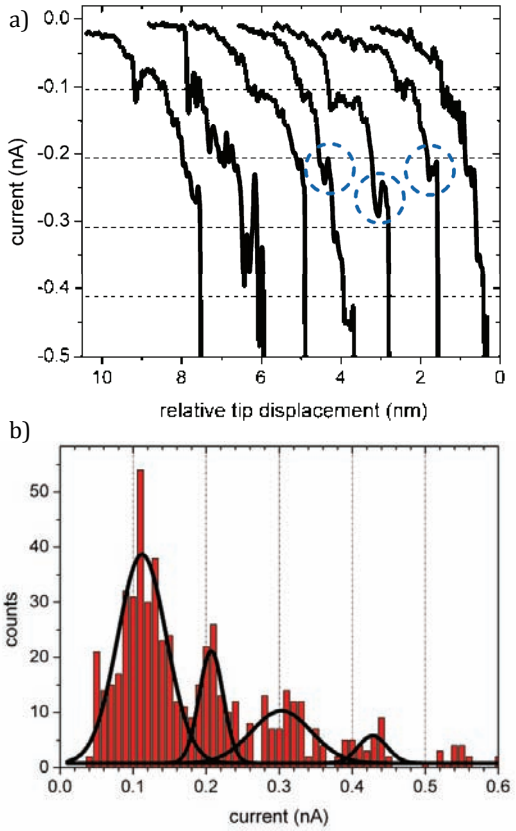

FIG. 1: a) Representative current-distance (I(s)) traces obtained from STM-BJ experiments in UHV with the 5BP5 derivative. b) Representative current histogram constructed from plateau values of about 300 I(s) traces for 5BP5.

From the last step and the difference between the steps on the I(s) traces the conductance of the individual MABPs (5BP5, 3BP7, 1BP9) can be estimated. Figure 1b shows the obtained histogram in case of 5BP5, constructed from values of the current plateaus of about 300 current-distance traces (I(s)). Taking into account the applied sample bias voltage of 1.5 V the values for the molecular conductance derived from the histograms are: $G_{(5BP5)}$ = 0.07 ± 0.01 nS, $G_{(3BP7)}$ = 0.08 ± 0.02 nS and $G_{(1BP9)}$ = 0.17 ± 0.03 nS, respectively. For each individual MABP we obtain clearly one series of peaks which we relate to one contact geometry of the molecules. Generally, for thiols there are at least two different pronounced contact configurations possible: a) the sulfur end group is coupled to a bridge/hollow site (high-conductance state, H) and b) an atop site (low-conductance state, L) on the Au(111) surface. Following, for dithiols three possible conductance peak series should be expected: H-H, H-L/L-H, L-L. In the case of 1BP9 we also observe current plateaus in the lower conductance range of the I(s) traces. Statistical analysis yields a considerably lower value for the molecular conductance which can be attributed to the H-L contact situation ($G_{(1BP9\ -\ HL)}$ = 0.04 ± 0.01 nS). [1]

Additionally, we observed in the case of 1BP9 relative to 3BP7 and 5BP5 an increased molecular conductance. This phenomenon can be subscribed to a lowering of the effective tunneling barrier (under the experimental conditions) due to an enlarged delocalization of the molecular orbital located at the BP-group towards the Au-S contact.

For further analysis we separate the contact contributions from the molecular conduction properties. The total conductance of the Au/nBPm/Au junction can be calculated by the following expression[2]:

$$G_{Au/nBPm/Au} = G_{con}\ exp\{-(\beta_N d_n + \beta_N d_m + \beta_{BP} d_{BP})\} \quad (1)$$

Here β_N is the decay constant of the alkane chain, d_m and d_n correspond to the lengths of the alkane chains ($d_m + d_n$ = 1.28 nm), β_{BP} is the decay constant of the biphenyl unit (β_{BP} = 4.7 ± 0.8 nm^{-1}) and d_{BP} its length (~0.7 nm). [2] G_{con} represents an effective contact conductance of the molecule. For the decay constant β_N different values exist in literature. We therefore performed a refined statistical analysis of the single alkanedithiol conductivities based on the recently available data in literature obtained in STM-BJ approaches. [1] The result is shown in Fig. 2. For each of the three possible contact situations a specific trend line can be given with the following β_N and G_{con} values: H-H: 0.97 ± 0.05, 33 ± 5 µS, H-L/L-H: 0.91 ± 0.03, 5.5 ± 0.9 µS, and L-L: 0.86 ± 0.03, 0.96 ± 0.16 µS. Thus β_N, the decay constant for an alkane chain, is in first approximation independent from the contact situation (one chemical contact, two chemical contacts H-H, H-L/L-H, or L-L) and can be given by β_N = 0.91 ± 0.05 (per methylene group).

Following, we state that the decay constants can be obtained independently from the contact conductance in the respective testbed. The variations in β_N presumably refer to conformational changes (*(multiple) gauche* to *all trans*).

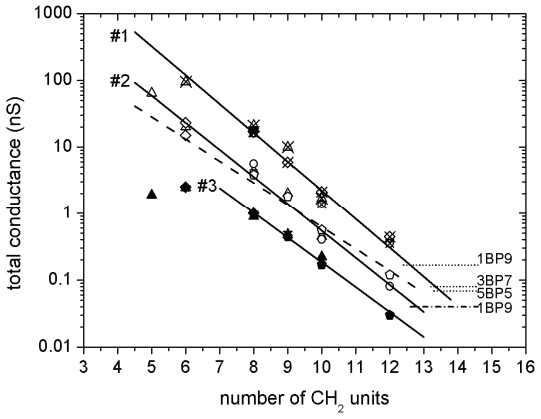

FIG. 2: Single molecular conductance of alkanedithiols estimated with STM-BJ as a function of the number of CH_2 units in the alkane chain from [1]. Crossed symbols: high conducting H-H situation (#1: β_N = 0.97±0.05, G_{con} = 33±5 µS), open symbols: H-L/L-H contacts (#2: β_N = 0.91±0.03, G_{con} = 5.5±0.9 µS), and filled symbols: low conducting L-L contacts (#3: β_N = 0.86±0.03, G_{con} = 0.96±0.16 µS). Dashed trendline taken over from Akkerman [3] corresponds to the mean of all single molecular conductances of alkanedithiols. Dotted horizontal lines: single molecular conductivities of 5BP5, 3BP7 and 1BP9[1].

Applying β_N (H-H) = 0.97 (per methylene group) = 7.6 nm^{-1}, and β_{BP} = 4.7 nm^{-1} in Equation 1, we calculated the effective contact conductance G_{con}(5BP5) = 34 µS and G_{con}(3BP7) = 39µS, and deduce G_{con}= 31 µS for 1BP9, which clearly indicate that the values for the molecular conductance obtained in this work correspond to the H-H contact situation.

In conclusion, it was demonstrated that the charge transport through the molecular backbone can be treated independently from the contact situation between the molecule and the electrodes. Moreover, the charge transport characteristics of the whole molecule can be described by simply combining the individual transport properties of each subunit, *i.e.* β_N and β_{BP}, meaning combination of the individual subunits leads to an adequate description of molecular conductivity.

[1] A. Busiakiewicz, S. Karthäuser, M. Homberger, P. Kowalzik, R. Waser and U. Simon, Phys. Chem. Chem. Phys. 2010, 12, 10518-10524

[2] B. Lüssem, L. Müller-Meskamp, S. Karthäuser, M. Homberger, U. Simon and R. Waser, J. Phys. Chem. C, 2007, 111, 6392.

[3] H. B. Akkerman, B. de Boer, J. Phys.: Condens. Matter, 2008, 20, 013001.

Going beyond the Surface with 3D Scanning Force Microscopy

Alexandra Sperschneider[1], M. Hund[2], Axel H.E. Müller[1], Larisa Tsarkova[3], Alexander Böker[3,4]

[1]Lehrstuhl für Makromolekulare Chemie II, Universität Bayreuth
[2]Lehrstuhl für Physikalische Chemie II, Universität Bayreuth
[3]DWI an der RWTH Aachen University
[4]IPC, RWTH Aachen University

We report on the quasi *in-situ* scanning force microscopy (SFM) study of complex self-assembled block copolymer structures and demonstrate the efficiency of the SFM nanotomography method to resolve the microdomain structure of ABC triblock copolymers in 3-dimensions. We performed a controlled erosion of the material by using low-pressure plasma etching coupled to the SFM. The 3D SFM reconstruction provides insights into the structural behaviour in very thin volume elements and reveals important morphological details not accessible with other methods.

In recent years, nanotomography turned out to be a promising method to image three-dimensional (3D) soft and hybrid nanostructures. With the technical advances in the field of microscopy and image processing, nowadays a reliable 3D reconstruction of soft structured materials with a resolution down to 10 nm becomes feasible.

The quasi in-situ scanning force microscope (QIS-SFM) is a novel SFM design which eliminates experimental limitations of state-of-the-art SFMs. It enables virtually all kind of harsh treatments such as low plasma, aggressive solvent or electric field treatment which may require a hermetically closed sample cell and/or which can not be applied in the presence of the tip while scanning inside the SFM [1]. The procedure includes controlled delicate erosion with a constant height-depth resolution in the range of ~1.0 nm by using approved low pressure plasma treatments inside the QIS-SFM. With this set-up and a commercial 3D imaging software, a nanotomographic examination of a 3D sample structure is performed on routine basis with an excellent reliability and high sample throughput.

Earlier, the QIS-SFM working principle has been successfully used to follow the details of the structural evolution of lamellar block copolymers under solvent vapor treatment in the presence of high electric fields [2]. Here we report on further applications of the QIS-SFM for scanning-probe-microscopy based on nanotomography [3]. Our approach provides insights into the structural behavior of polymer material in confined geometry on a 3-dimensional nano-scale and thus overcomes the basic limitation of SPMs where typically only the surface layer of a sample can be visualized.

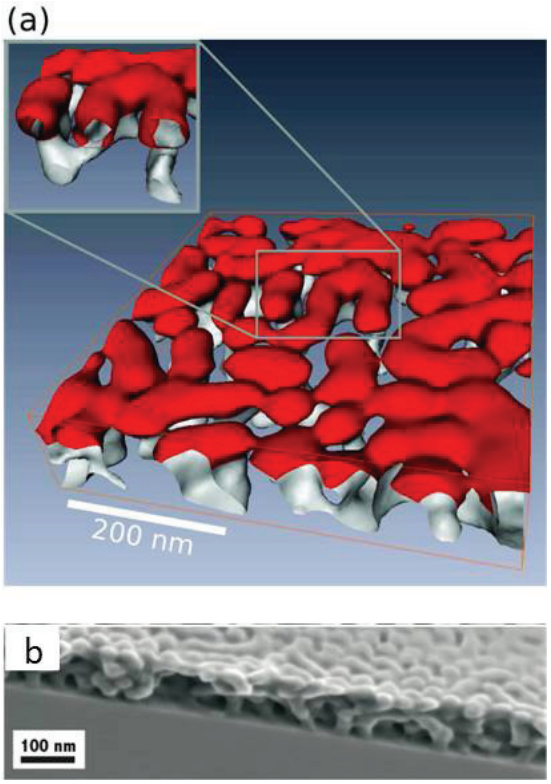

FIG. 1: (a) 3D reconstruction of a HO-BVT triblock terpolymer thin film. The nanotomographic volume image is displayed as isosurface. The 3D image was reconstructed from a series of 14 process steps. The HO-PB and P2VP compartments represent the rigid polymer blocks. The matrix material PtBMA is transparent. The inset shows a cylinder network with the structures oriented predominantly parallel to the film plane at the free surface and a perpendicular to the film plane next to the substrate.(b) Cross-sectional SEM image of the same film.

The interest in nanopatterned block copolymer films lies in their versatile phase behavior and tailor-made microphase separated structures both with respect to their functionality and to the morphology. In linear ABC terblock copolymers, an intricate diversity of structures becomes possible due to considerable increase in the number of involved

polymer-polymer and polymer-surface interaction parameters. Earlier studies on ABC block copolymers demonstrated that confined structures are very sensitive to the changes in the energetic interactions.

Using the QIS-SFM technique we were able to gain a detailed understanding of the morphological reconstructions and microdomain orientation in the interior of thin films of a polybutadiene-block-poly(2-vinyl pyridine)-block-poly(tert-butyl meth-acrylate) (BVT) triblock terpolymer and of its hydrogenated derivative HO-BVT. By oxidative hydroboration in solution, the polarity of PB can be selectively adjusted to increase its surface tension and, in that way, to balance interactions of the constituting blocks with both confining surfaces. This strategy allowed for the successful stabilization of complex 3D morphologies under confinement, i.e. in thin film geometry [4].

In the 3D reconstructed image of HO-BVT (FIG. 1a) the PtBMA matrix in which the objects are embedded is transparent. For the calculation of the 3D reconstruction, the nonlinear etching behavior was taken into account [3]. Inset in FIG. 1a displays short interconnected cylindrical domains which are predominantly oriented parallel to the film at the free surface and partially penetrate the film toward the substrate.

The cross-section scanning electron microscopy (SEM) image in FIG. 1 b highlights a complex cylindrical structure where only two phases can be distinguished.

The described observations were enabled by a quasi in situ (QIS) SFM nanotomography procedure that solves the major limitation of conventional SFM imaging techniques, making it possible to deduce the nature of the underlying structure.

In our experiments, we show with unprecedented high depth resolution that thin polymer films can be investigated tomographically by a combination of topography and phase imaging after successive surface erosion via low-pressure plasma treatment. In addition, our setup circumvents the well-known problems of the state-of-the-art ex situ LP plasma treatments (reliability, practicability, and manageability). In general, the plasma technique is extremely flexible with respect to the sample treatment.

Thus, in the future, this technique can be expanded by using various plasma gases attuned to the specimens' properties. Moreover, the fast growing SPM capabilities realize an improved sensing of material features. Besides, instead of ablating material during the etching treatment, the reverse progression (e.g., plasma deposition process) can be easily achieved with the QIS SFM setup leading to new insights into the growth of 3D structures. Thus, the QIS SFM used in our experiments has a large potential, which goes significantly beyond the problem studied here.

[1] Hund, M.; Herold, H. Review of Scientific Instruments 2007, 78, 063703.

[2] Olszowka et al, ACS Nano 2009, 3, 1091-1096.

[3] Sperschneider et al, ACS Nano 2010, 4, 5609-5616.

[4] Sperschneider et al, Macromolecules 2010, 43, 10213-10215.

Transition from direct tunnelling to field emission in molecular junctions

X. Dong[1], Y. Zhang[1], F. Pyatkov[1], A. Offenhäusser[1], D. Mayer[1]

[1] PGI-8: Bioelectronics, Forschungszentrum Jülich, 52425 Jülich

I-V characteristics recorded in mechanically controllable break junctions revealed that field emission transport is enhanced in single molecule junctions as the gap size between two nanolectrodes is reduced. This observation indicates that Folwer-Nordheim tunneling occurs not only for intermolecular but also intramolecular electron transport driven by enhanced fields at short tunneling distances.

Over the past decade, fundamentals of charge transport through (bio-)molecules have been extensively investigated. Beebe *et al*. demonstrated that metal-molecule-metal junctions can exhibit current-voltage characteristics that correspond to a transition from direct tunneling to field emission as the applied bias exceeds a threshold voltage [1]. The voltage at which this transition occurs (transition voltage V_T) is proportional to the energy offset between the metal Fermi level at zero bias and e.g. the highest occupied molecular orbital (HOMO). This feature allows probing of the effective energy barrier of charge transport by measuring V_T. Later, Wang *et al*. revealed that the transition voltage (V_T) is not fixed for a definite molecule. Using atomic force microscopy (AFM), they demonstrated that V_T shifts to lower voltages when the metal-molecules-metal junction was compressed [2]. Wang attributed the shifting of V_T to the enhanced interaction between parallel molecules (intermolecular electron transport) as the sandwiched molecules within the self assembled monolayer were compressed. However, the relation between intermolecular interaction and charge transport mechanism is still under debate.

In this work, the charge transport characteristics of single molecule junctions instead of molecule layer junctions were investigated to evaluate the influence of neighboring molecules on the charge transport mechanism. For this purpose, a mechanically controllable break junction (MCBJ) setup was used, Fig. 1. An attenuation factor of $r = \Delta x / \Delta z \approx 5 \times 10^{-6}$ (Δx is the gap distance change, Δz is the push rod displacement) was determined for the used setup, which implies that the distance between the nanoelectrodes was tunable with sub Angstrom accuracy. 1,8-octanedithiol (ODT) molecules were self-assembled on the gold wire from solution, dried and mounted into the MCBJ setup [3]. The whole breaking process of the wire can be followed by monitoring the junction conductance, Fig. 2. One can observe the formation of point contact with discreet conductance values of multiples of G_0. Further elongation of the junction will result in a breaking of the gold-gold contact and a sharp drop of the conductance can be observed.

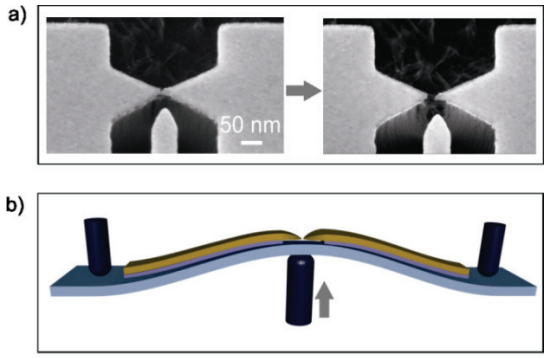

FIG. 1: Working principle of the mechanically controllable break junction (MCBJ). a) Scanning electron microscopy images of micro-fabricated MCBJ consisting of a freestanding metal bridge with a central constriction. Left) before and right) after breaking of the constriction. b) Schematic of the MCBJ mounted into a three-point bending configuration. The push rod (piezo actuated) exerts a bending force to the substrate. The bending force breaks the metal bridge at the smallest constriction creating two separate nanoelectrodes.

After breaking the metal wire, two separated nanoelectrodes are generated. Due to the two thiol termini of ODT, the molecule is able to bind covalently to both generated nanoelectrodes and a metal-molecules-metal junction is formed. Several hundred metal-molecule-metal junctions were analyzed and the single molecule conductance determined statistically to $2.5 \times 10^{-4}\ G_0$, which is consistent with earlier reports. In contrast, the typical plateaus at values below $1 G_0$ are absent for molecule free junctions. To establish single molecule junctions, we stopped the push rod right before the conductance reached the value of $2.5 \times 10^{-4}\ G_0$ and waited until a stable junction was formed. Under these conditions, the gap size effect on the transport properties of a single molecule junction was investigated. Three sets of I/V curves were acquired at varied gap size, Fig. 2 bottom. Curves B, and curves C were obtain after the gap size was reduced by 0.2 nm and 0.4 nm respectively based on curves A (conductance plateau at $2.5 \times 10^{-4}\ G_0$). $ln(I/V^2)$ versus

$1/V$ curves of three different gap sizes are shown in the insert of Fig.2. At the initial gap size (red curve), the $ln(I/V^2)$ versus $1/V$ plot exhibits no significant voltage dependence. The curve reveals that only direct tunneling was present within the bias range between -1 V and 1 V.

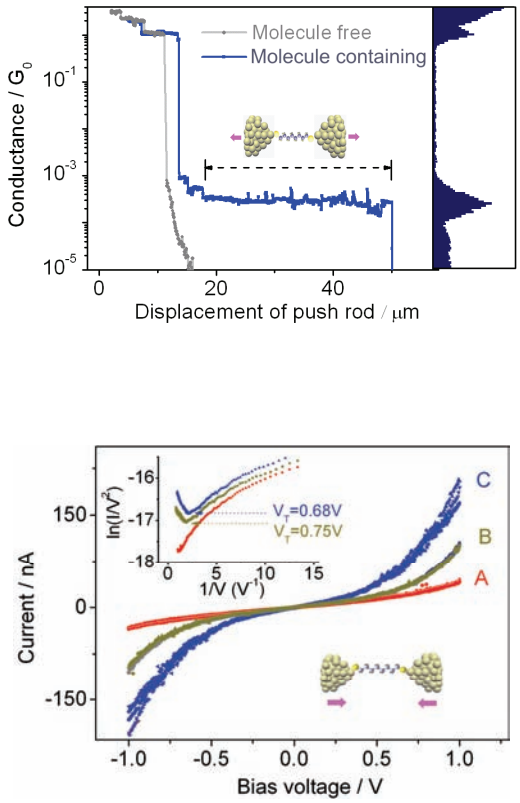

FIG. 2 Top: The conductance of a molecule free junction and a molecule containing junction as a function of push rod displacement. The conductance histogram shows a typical peak at 2.5x10⁻⁴ G₀. Bottom: I/V curves of single molecule junctions with three different gap sizes. Curves B and C were recorded after the gap size was decreased by approximately 0.2 and 0.4 nm based on curves A. The insert shows corresponding ln(I/V²) versus 1/V characteristics. An inflection point can be observed, which shifts to lower biases as the gap size decreases.

After the junction was compressed by approximately 0.2 nm, a transition from direct tunneling to field emission occurred at a transition voltage of 0.75 V. An additional decrease of the gap size by 0.2 nm leads to a further shift of the transition point towards lower voltages, now 0.68 V. The insert picture explicitly demonstrates that the energy barrier of the junction decreases as the gap size decreases. In other words, field emission is enhanced as the gap size is reduced in the single molecule junction, too. It should be noted that intermolecular tunneling between parallel molecules was improbable since the junction was bridged by only a single molecule, and adjacent molecules were linked to only one of the two facing nanoelectrodes. Thus, an explanation that attributes the enhanced field emission only to changed transport pathways including intermolecular electron transport (chain-to-chain tunneling) seems to be inappropriate. Also directly tunneling between the electrodes is leading to a rather linear increase of the tunneling current within the investigated bias regime (0V to 1V) [4] and cannot explain the observed strong nonlinear current response. In order to further evaluate the role of intermolecular charge transport, an additional experiment was performed where the number of trapped molecules was altered, but the final gap size was kept mainly unchanged [3]. We found that 90% of the I/V characteristics fall into three distinct sets of curves, representing multiples of each other and can be deduced from the (fundamental) characteristics of a single molecule junction. Each set of curves corresponds to nanoelectrodes bridged by 1, 2, or 3 molecules. No field emission was observed for all three sets of I/V characteristics within the bias window between -1V and +1V. A correlation between transition voltage and number of molecules in the junction was not found for this type of molecule.

Several aspects have to be considered for the explanation of the enhancement of field emission in single molecule junctions if intermolecular transport can be neglected. At first, according to the full Simmons model, V_T will decrease as the tunneling distance decreases for narrow gaps, if one takes the image potential into account. Furthermore, one can assume that a decreasing gap size leads to an enhancement of the electric field, resulting in a decrease of the tunneling barrier height. A smaller barrier height causes a shift of the transition voltage to lower bias voltages, which can be observed as an enhancement of field emission.

In summary, charge transport at the single molecule level was investigated by means of high stability mechanically controllable break junction experiments. Although the transport between parallel molecules was improbable in the single molecular junction, a shifting of V_T was observed as the molecular junction was compressed. I/V measurements with different numbers of molecules in the junction at a given gap size revealed that intermolecular electron transport between adjacent molecules was of minor importance and alkanedithiols molecules can be considered as individual transport channels. The presented observations lead to the conclusion that the distance change between the electrodes and associated alternations of the molecular electronic structure rather than inter-molecular tunneling result in the enhancement of field emission for alkanedithiols.

[1] J.M. Beebe et al. Phys. Rev. Lett., 2006, **97**, 026801.

[2] G. Wang et al. Am. Chem. Soc., 2009, **131**, 5980.

[3] X. Dong et al. Chem. Commun., 2011, **47**, 4760.

[4] M.L. Trouwborst et al. Nano Lett., 2011, **11**, 614.

Gold micro-spine structures for enhanced cell/device adhesion

G. Panaitov, S. Thiery, B. Hofmann, A. Offenhäusser

PGI-8: Bioelectronics, Forschungszentrum Jülich, 52425 Jülich, Germany

Improvement of the adhesion contact between biological cells and electronic devices can significantly enhance the quality of electronic signal transfer. We report on results of fabrication of submicron golden spines by means of e-beam lithography and electroplating. The structures with different spine profiles and spacing have been fabricated for optimization of cell growth conditions. We present the results of growth of rat cortical neurons on the surface of spine modified samples. Well defined cell guidance was established at the spine arrays. Furthermore the results of transmission electron microscope and focused ion beam technique confirm the good adhesion between the spines and cell structures.

Modification of surface topography in micrometer to nanometer scale is the commonly used technique for improvement of cell adhesion [1-4]. Our approach is based on particle phagocytosis – the phenomenon naturally occurring in living cells [2].

Schematically, the fabrication process consists of five technological steps. Initially, a gold thin film is deposited onto the substrate and covered with electron-beam resist. Next, the circular openings are patterned in the resist by means of e-beam lithography. In the following step, the samples are thermally treated in order to achieve appropriate round shaped edges. The openings are then filled with gold by galvanic electroplating. As the last step, the resist is removed releasing free standing gold spines.

We used PMMA resist of 600 kD molecular weight solved with concentration 7% in ethyllactat. At spin speed 2000 r.p.m. for 60s. it results in about 1µm resist thickness. After exposition and development the holes of 500 and 250nm in radius were opened in the resist. A post-exposure backing was used for further formation of the holes profiles, which are determinant for the shape of final spine steams. We treated the samples for 2 min at 180°C on the hot plate. The treatment at higher temperatures leads to over backing of the sample resulting in a strongly deformed positive wall slope.

A potassium-gold-cyanide solution (K[Au(CN)2]) was used for electroplating of gold into the holes. An optimal plating regime with moderate deposition rate (~150 nm/min at 0.4 A/dm2) we achieved by reduction of bath temperature down to 35-40°C. A slightly increased surface roughness at this plating regime contributes additionally to an effective enlarging of spine heads surface area. By variation of the deposition time we could control the size of spine caps.

After plating, the resist was removed by acetone releasing the free standing spines on the gold surface. Fig.1 demonstrates an example of fabricated spine array and spines of different shape and cap size (insert). The radius of single spine stalks is about 250 nm and the height ranges from 1 µm to 1.2 µm. For experiments with cell growth we fabricated arrays with interspacing varying from 3 µm to 10 µm.

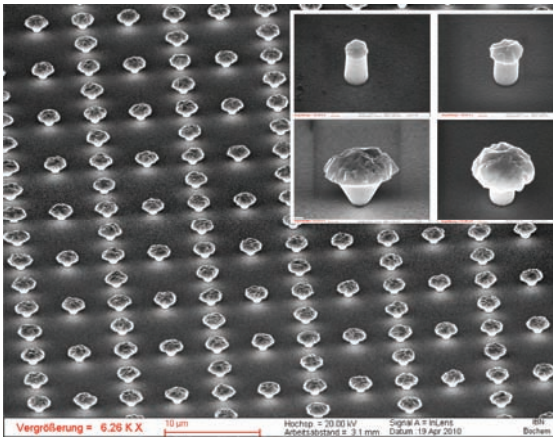

FIG. 1: Spine array and examples of single gold spines of different shape and head size (insert).

In order to analyze the cell response to the gold spines the rat cortical neurons were grown on previously functionalized spine surfaces. A surface-functionalization consisting of amino terminated PEG-Thiols ($SH(CH)_{11}(EG)_6NH_2$) was applied. The samples were incubated for 24 hours in a solution of 1 mmol/l PEG-Thiols in Ethanol, after that rinsed with Ethanol and DI-H_2O and finally dried with N_2. Thus, resulting in a positive charged surface due to the amino-groups, now located at the top border of the monolayer.

Neurons were prepared as described by Brewer et.al [5]. After separation and cleaning steps the cells were centrifuged, counted and plated onto the substrates at a density of 30 k-75k cells per sample in a volume of

500 µl. After one hour adhesion the medium was exchanged completely to remove unadhered and dead cells.

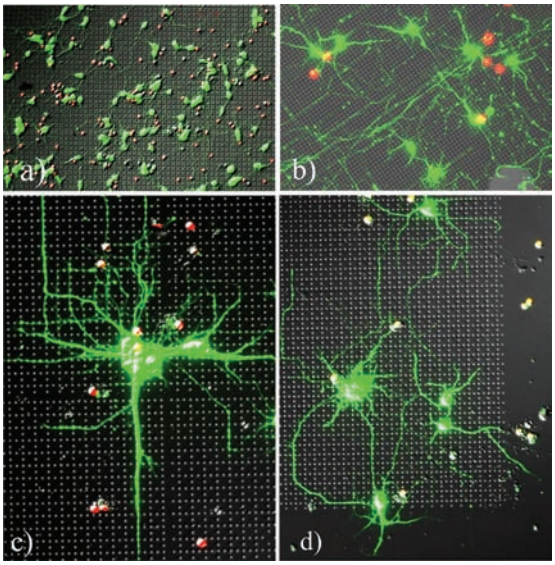

FIG. 2: Live (green) and dead (red) neuron cells after DIV3 (a) and DIV7 (b). Pictures (c, d) illustrate the guiding of neuronal growth.

First analysis of the cell culture was performed with a live-dead-staining after DIV3 and DIV7. Therefore, life and dead cells were stained using Calcein-AM and Ethidium Homodimer-1, respectively. Fluorescence-images showed a healthy and stable culture on the gold spines (Fig.2). The pictures illustrate that neurites are establishing well, forming a dense network. After DIV3 the live-dead-ratio of the cells on the gold-spines with different spacing did not differ significantly. The 3 µm inter-spine distance led to a live-dead yield of 38% and 62%, while 4 µm distance - to 39% and 61%, and the 5 µm - to 37% and 63%. Next to a healthy cell culture, the fluorescence pictures illustrated a guiding effect of the spines for cell growth (Fig.2c). The neurites grow from one spine to another obviously preferring the shortest distance between the spines in a square-shaped array. Analysis of dendrite growth in Fig.2 shows that around 70% of dendrites prefer the shortest distance to the next spine.

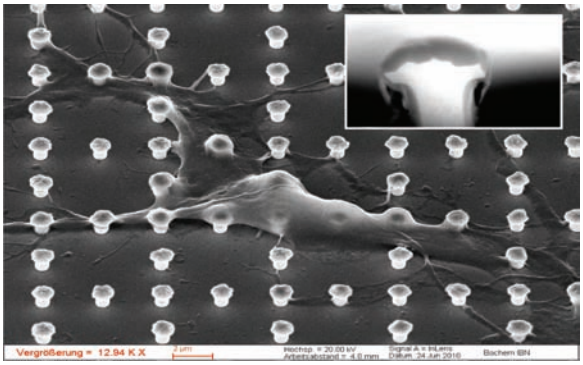

FIG. 3: SEM picture of a cortical rat neuron engulfing the gold spines and a FIB-cut (insert) through the fragment of cell engulfing a gold-spine.

For more detailed analysis of attachment of cells and dendrites to the substrates the scanning electron microscope was applied. The cells were fixated with 3.1% glutaraldehyd in 20 mM Hepes over night followed by dehydration in increasing concentrations of isopropanol. Finally, the samples were dried in a Critical Point Dryer to avoid artefacts caused by evaporating isopropanol. Images revealed that the cells are completely engulfing the spines (Fig.3).

Most of neurites are too small in diameter to engulf the spines completely. They rather seem to enclose the caps of gold-spines or merely follow them as growth guides fitting tightly to the stem of the spines. A focused ion beam sectioning was performed in order to get a more detailed picture of the cell/spine interface (insert in Fig.3). The membrane fits very tight to the cap of the spine and exactly follows the outer border.

In conclusion, we fabricated the gold spine arrays, which improve the adhesion of neurone cells and reveal well defined cell growth guiding effect.

[1] G. Panaitov, S. Thiery, B. Hofmann, and A. Offenhäusser, Microelectronics Engeneering (2011), doi:10.1016/j.mee.2010.12.074.

[2] A.Hai, A.Dormann, J.Shappir, S.Yitzchaik, C.Bartic, G.Borghs, J.Langedijk and M.E.Spira, J. R. Soc. Interface 6, (2009), 1153-1165.

[3] M.Matsuzaki, G.C.Ellis-Davies, T.Nemoto, Nat Neurosci 4 (2001), 1086–1092.

[4] A.K.Vogt, L.Lauer, W.Knoll and A.Offenaeusser, Biotechnol Prog, v.19, (2003), 1562-1568M.

[5] G.J.Brewer, J.R.Torricelli, E.K.Evege and P.J.Price J.Neurosci Res, v.35, (1993), 567-576.

Formation of complex intermetallics in the Al-Pd-Cr alloy system

B. Grushko[1], W. Kowalski[2], D. Pavlyuchkov[1,3], M. Surowiec[2]

1 Peter Grünberg Institut, Microstructure Research (PGI-5), Forschungszentrum Jülich, Germany
[2] Institute of Materials Science, University of Silesia, Katowice, Poland
[3] I.N. Frantsevich Institute for Problems of Materials Science, Kiev, Ukraine

The Al-Pd-Cr constitutional diagram was determined in the compositional range above 50 at.% Al and temperature range of 930 to 1020 °C. The study was carried out by a combination of powder XRD, DTA, SEM/EDX and TEM. The system exhibits the formation of five complex ternary intermetallics.

The work continues the investigation of Al-based alloys containing Cr and other transition metals [1], interesting because of formation their structurally complex intermetallics. The title phase diagram was studied for the first time. The isothermal section at 930 °C containing five ternary intermetallic phases is shown in Fig. 1. The crystallographic data for the ternary phases are included in Table 1. In more detail this study is published in Ref. [2].

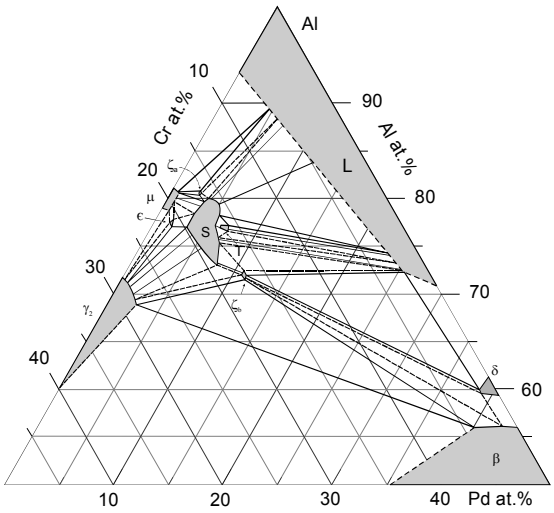

FIG.1: Al-rich part of the Al-Pd-Cr phase diagram at 930 °C.

The study revealed low solubility of the third element in the binary Al-Cr and Al-Pd phases, apart from the Al-Pd β-phase dissolving up to at least 10 at.% Cr. Two ternary phases are formed very close to the binary Al-Cr terminal at somewhat higher or lower Al concentrations than that of the μ-phase. That forming around the $Al_{77.5}Pd_{1.5}Cr_{21}$ composition only exists in a small temperature range between ~1010 and at 900 °C. Electron diffraction examinations revealed an orthorhombic structure associated with the ε-phase (see Fig. 2) also forming in Al-Ni(Fe)-Cr [1].

	S.G. or symmetry	Lattice parameters, nm		
		a	*b*	*c*
ε	*Cmcm*	1.244	3.462	2.038
ζ_a	*hexag.*	1.767	-	1.251
ζ_b	*hexag.*	1.801	-	1.277
S	orthor.	2.48	3.87	2.04
T	*Pnma*	1.47	1.24	1.25

TAB. 1 Crystallographic data of the ternary phases in Al-Pd-Cr.

Another ternary structure forming around $Al_{81.5}Pd_{1.5}Cr_{17}$ is similar to the ζ-phase observed in Al-Ni(Cu)-Cr [1]. Surprisingly, a similar hexagonal structure with very close lattice parameters was also revealed around $Al_{73}Pd_{11}Cr_{16}$. In order to stress their mutual similarity and similarity to the ζ-phase in Al-Ni(Cu)-Cr the lower-Pd phase is designated ζ_a and the higher-Pd phase ζ_b (see Table 1). Both structures exhibit some differences in the distribution of the reflection intensities (see Figs 2d-f vs.2g-i). Their compositional regions are separated by a quite wide gap, inside which other structures (T and S, see Fig. 1) are formed. There is also a visible difference in their existence temperatures: the ζ_a-phase melts at ~980 °C and might be unstable at 780 °C and below this temperature, while the ζ_b-phase exists from 937 °C down to at least 680 °C.

The T-phase (see Table 1) resembling the Al-Mn T-phase (see [3] and references therein) is formed around $Al_{77}Pd_7Cr_{16}$ below 940 °C Its typical electron diffraction patterns are shown in Fig. 3a-c. The structure of the T-phase was assumed to be closely related to the structure of the stable Al-Pd-Mn decagonal quasicrystal.

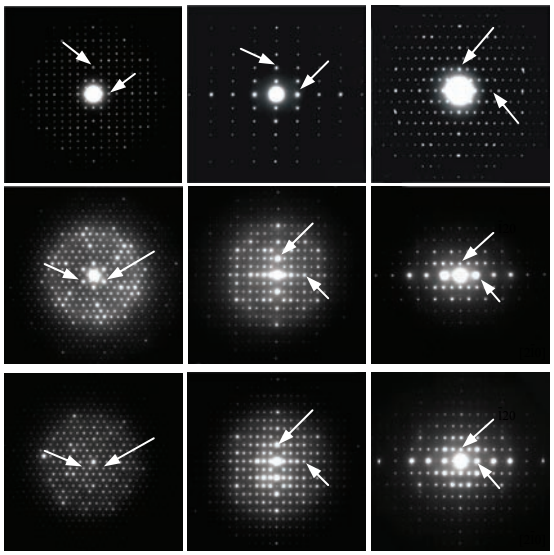

FIG.2: Electron diffraction patterns of the Al-Pd-Cr phases: a-c) ϵ-phase, d-f) ζ_a-phase, g-i) ζ_b-phase.

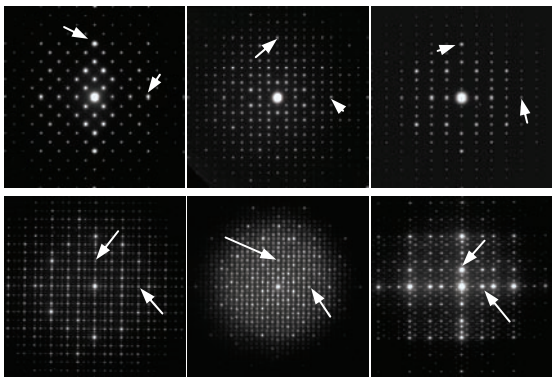

FIG.3: Electron diffraction patterns of the Al-Pd-Cr phases: a-c) T-phase, d-f) S-phase

Another orthorhombic structure designated S-phase (see Table 1), whose electron diffraction patterns are presented in Fig. 3d-f was found in a compositional region between $Al_{80}Pd_4Cr_{16}$, $Al_{73}Pd_8Cr_{19}$, $Al_{77}Pd_4Cr_{19}$ and $Al_{77}Pd_6Cr_{17}$, i.e. very close to that of the T-phase. The S-phase is also in equilibrium with μ and ζ_a, ϵ and ζ_b (see Fig.1). Its upper melting temperature is 1000 ºC.

The S-phase has even more pronounced than the T-phase pseudodecagonal symmetry. Other electron diffraction patterns, more closely resembling decagonal structure were also revealed in the present work. They were observed in the same samples as the S-phase but annealed at lower temperatures. In as-cast materials those patterns were not observed. The nature of this decagonal-like structure is unclear and no specific compositional region is associated with this substance.

While the stability of quasicrystals in Al-Pd-Cr was not yet clarified, stable quasicrystals were indeed observed in other ternary Al-based alloy systems with Pd, Ni or Cu and a second transition element [4]. So far no stable quasicrystals have been confirmed in Al-Cu(Ni)-Cr, but a stable decagonal (D_3) phase was revealed in Al-Fe-Cr [5].

[1] B. Grushko, W. Kowalski, B. Przepiórzyński, D. Pavlyuchkov, S. Balanetskyy and M. Surowiec, IFF Report (2008), p.. 94-95.

[2] W. Kowalski, B. Grushko, D. Pavlyuchkov, and M. Surowiec, J. Alloys Comp. 496, 129-134 (2010).

[3] B. Grushko, S. Balanetskyy, Intern. J. Mater. Res. 99, 1319-1323 (2008).

[4] B. Grushko and T. Velikanova, CALPHAD, 31, 217-232 (2007).

[5] D. Pavlyuchkov, S. Balanetskyy, W. Kowalski, M. Surowiec and B. Grushko, J. Alloys Comp. 477, L41-L44 (2009).

Structure analysis of $Cs_{0.5}[Nb_{2.5}W_{2.5}O_{14}]$ with advanced HRTEM techniques

J. Barthel[1,2], Th. E. Weirich[3], G. Cox[4], H. Hibst[5],A. Thust[1,2]

[1]PGI-5: Microstructure Research, Forschungszentrum Jülich, Germany
[2]ER-C: Ernst Ruska-Centre for Microscopy and Spectroscopy with Electrons
[3]Central Facility for Electron Microscopy, RWTH Aachen University
[4]BASF SE, Polymer Physics Department, Ludwigshafen
[5]BASF SE, Chemicals Research and Engineering, Ludwigshafen

The structure of the oxygen sub-lattice in $Cs_{0.5}[Nb_{2.5}W_{2.5}O_{14}]$ has been investigated for the first time by advanced electron-optical methods. Since the material resembles the crystal structure of the so-called M1 phase of Mo-V-Nb-Te-O, which is the best catalyst for the selective oxidation of propane to acrylic acid, the structure analysis of the oxygen sub-lattice can contribute substantially to a better understanding of this catalytic process.

The crystal structure of $Cs_{0.5}[Nb_{2.5}W_{2.5}O_{14}]$ resembles strongly the M1 phase of $Mo_{10}V_2^{4+}Nb_2TeO_{42-x}$, which is the active mass of the hitherto best heterogeneous catalyst for the partial and selective gas-phase oxidation of propane with molecular oxygen to acrylic acid [1]. The main difference between the crystal structures of $Mo_{10}V_2^{4+}Nb_2TeO_{42-x}$ and $Cs_{0.5}[Nb_{2.5}W_{2.5}O_{14}]$ is that the channels in the former compound contain Te-ions, while the channels in the latter compound are occupied by Cs-ions.

The crystal structure of $Cs_{0.5}[Nb_{2.5}W_{2.5}O_{14}]$ was first discovered and characterised by Lundberg and Sundberg in 1993 [2]. According to the latter study, the structure crystallises with a primitive orthorhombic cell with the approximate lattice parameters a = 2.71 nm, b = 2.16 nm, and c = 0.394 nm. The analysis of conventional high-resolution transmission electron micrographs recorded along the [001] direction allowed the previous authors to determine the positions of the heavy atoms within the projected unit cell. Later attempts to measure the so far only estimated oxygen positions by using precession electron diffraction and X-ray powder diffraction failed due to the difficulties to detect the light oxygen atoms in the vicinity of the heavier niobium and tungsten atoms.

Because of the strong interaction of electrons with matter, high-resolution transmission electron microscopy (HRTEM) offers the possibility to investigate the projected atomic structure in objects of extremely small volumes down to the length scale of a few nanometres. HRTEM is therefore a highly beneficial method for the structural analysis of very small crystals present in powder samples. In previous HRTEM studies oxygen columns could be resolved and quantitatively analysed in the proximity of heavier atom columns within perovskite ceramics by employing spherical aberration correction, which is a hardware technique [3], together with focal-series reconstruction, which is mainly a software technique [4]. Using the reconstruction technique, the systematic errors in the quantification of atom positions, which are frequently caused by unavoidable residual lens aberrations persisting even after hardware correction, can be eliminated effectively by an a-posteriori numerical aberration correction of a reconstructed wave function. The combination of these two electron microscopy techniques is applied in the present investigation in order to determine the oxygen positions in the structure projection of $Cs_{0.5}[Nb_{2.5}W_{2.5}O_{14}]$ along the short c-axis. The phase of the finally resulting electron wave function at the exit plane of the object is displayed in Fig. 1.

In addition to these electron microscopy techniques two further techniques for the data evaluation are employed: In order to determine the average atom positions in the c-axis projection, the phase of the reconstructed and aberration-corrected electron wave function is subsequently used as input for the crystallographic image processing (CIP) procedure [5]. Within the CIP procedure the best fitting space-group symmetry is determined and finally imposed on a periodic part of the reconstructed wave function, as is shown in Fig. 2. In a further step, first-principles calculations [6] are used to check the consistency of the experimentally determined atom positions with theoretical values and to rule out the influence of surface relaxation effects, which might occur for the very small crystal thickness required by HRTEM in the 1 Ångström resolution regime.

By the application of the aforementioned techniques it is possible to determine the position of atomic columns with high accuracy. The average root-mean-square deviations of the x- and y- atom co-ordinates between experiment and the first-principles calculations amount to less than 9 pm for the nine heavy atoms, and to less than 13 pm for the 27 oxygen atoms of the unit cell [7]. In particular, the positions of the oxygen atoms in the vicinity of the strongly scattering metal atoms can be experimentally quantified, which has not been accomplished before. Additionally, it turns out that the phase of the reconstructed exit-plane wave function reveals remarkable deviations from the periodic structure, including a possible splitting of oxygen columns [7]. Examples for different types of

such deviations from the periodic crystal structure are highlighted in the phase image of Fig. 3.

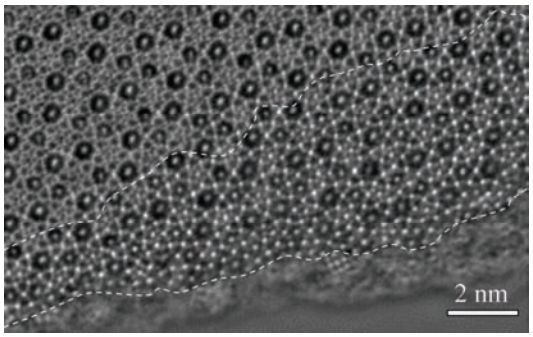

FIG. 1: Phase of the reconstructed and aberration-corrected wave function belonging to a thin region near the crystal edge. The average structure of $Cs_{0.5}[Nb_{2.5}W_{2.5}O_{14}]$ was determined from the area enclosed by the dashed curves. The area is 54.5 nm² large and contains approximately nine projected unit cells.

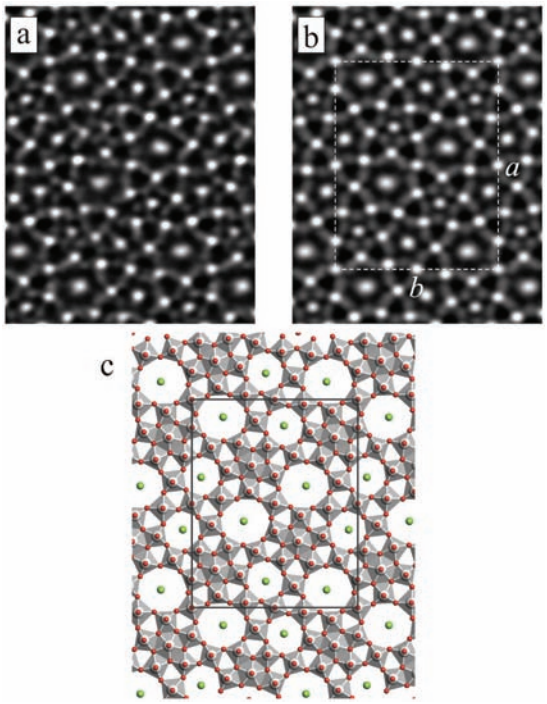

FIG. 2: Crystallographic image processing for $Cs_{0.5}[Nb_{2.5}W_{2.5}O_{14}]$. (a) Phase image obtained by averaging the unit cells within the area displayed in Figure 1. (b) Phase image obtained after imposing additionally p2gg symmetry. The prominent sharp maxima in the map show columns composed of niobium and tungsten atoms, whereas the broader and more diffuse maxima inside the 6- and 7-fold tunnels belong to columns of caesium atoms. The weakest peaks in the map indicate positions of oxygen columns. (c) Structure model as derived from the experimentally determined atom positions in projection along the [001] zone axis. Cs = green; Nb, W = light grey; O = red.

The present study describes a straightforward procedure for the acquisition of quantitative structural information by high-resolution transmission electron microscopy, which yields close-to-picometre accuracy for the determination of atom positions. The chosen combination of HRTEM techniques and data evaluation techniques constitutes a feasible alternative in experimental scenarios where traditional methods like XRD or neutron diffraction cannot be applied for structure analysis.

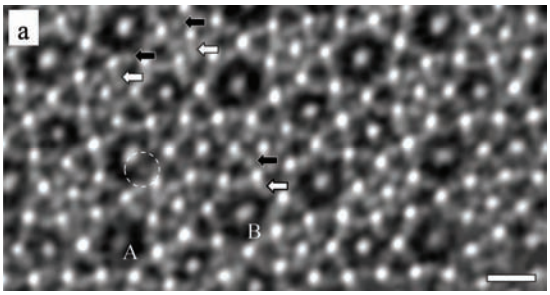

FIG. 3: Enlarged part of the reconstructed phase of Fig. 1 showing the defect structure of $Cs_{0.5}[Nb_{2.5}W_{2.5}O_{14}]$. Whereas the dark arrows point out symmetric and well-separated peaks belonging to oxygen columns, the white arrows highlight elongated peaks which are most likely caused by a splitting of the related oxygen columns. Further structural defects are additional or misplaced atoms in the tunnels, as can be seen in the encircled region. The lower peak height at the caesium position A indicates a site occupancy which is lower than the occupancy at the position B. The scale bar at the lower right corner corresponds to a length of 1 nm.

[1] H. Hibst, F. Rosowski, G. Cox, Catalysis Today (2006), 117, 234 – 241.

[2] M. Lundberg, M. Sundberg, Ultramicroscopy (1993), 52, 429 – 435.

[3] M. Lentzen, B. Jahnen, C.L. Jia, A. Thust, K. Tillmann, K. Urban, Ultramicroscopy (2002), 92, 233 – 242.

[4] A. Thust, W.M.J. Coene, M. Op de Beek, D. van Dyck, Ultramicroscopy (1996), 64, 211 – 230.

[5] S. Hovmöller, A. Sjögren, G. Farrants, M. Sundberg, B.O. Marinder, Nature (1984), 311, 238 – 241.

[6] M. Payne, M. Teter, D. Allen, T. Arias, J. Joannopoulos, Rev. Mod. Phys. (1992), 64, 1045 – 1097.

[7] J. Barthel, Th. E. Weirich, G. Cox, H. Hibst, A. Thust, Acta Materialia (2010), 58, 3764 – 3772.

Enhanced infrared spectroscopy with optical antennas

J. M. Hoffmann[1], J. Richter[1], A. Hartung[1], X. Yin[2] and T. Taubner [1, 2]

[1] I. Institute of Physics (IA), RWTH Aachen University
[2] Fraunhofer Institute for Laser Technology (ILT), Aachen

"Optical antennas" are nanostructures that concentrate light into nanoscale dimensions. They can be understood in analogy to conventional radio antennas, e.g. the well-known λ/2 dipole antenna that converts radiation into currents. Due to their much smaller sizes these optical antennas have resonance frequencies not at radio frequencies, but in the visible or infrared spectral range. If such an optical antenna is driven in resonance, the scattering, the absorption and the local field around the antenna can be dramatically enhanced. We exploit this enhancement of electromagnetic fields around such nanostructures for enhancing the sensitivity of infrared spectroscopy in two configurations: in far-field Fourier-Transform-Infrared spectroscopy (FTIR) and in spatially resolved near-field spectroscopy with a scattering-type Scanning Near-field Optical Microscope (s-SNOM).

Infrared vibrational spectroscopy is sensitive to characteristic molecule absorption bands, yielding a "fingerprint" spectrum of the molecules involved. In order to exploit the local field enhancement of optical antennas, the antenna resonance has to be tuned to the vibrational absorption band of interest. We fabricated IR antennas of triangular shape using nanosphere lithography (NSL). Spherical particles with diameters of a few micrometers served as shadowing masks during the evaporation of a thin gold film. After removal of the spheres, arrays of triangular shaped IR antennas of a well-defined size are available for further investigation. For the characterization of these structures we use diffraction-limited FTIR microscopy. Our specially equipped FTIR microscope (BRUKER Hyperion) enables us to measure reflection and transmission spectra from very small areas, e.g. *20 μm* x *20 μm*. Thus we are able to determine the resonance wavelengths of the antennas while averaging only over <100 nanostructures, reducing the errors associated with slight fabrication deviations. We can tailor the resonance wavelength of the antennas by changing the length of the antenna structure, the refractive index of the substrate below the gold triangles and the gold layer thickness. Overall, we can cover the whole mid-IR spectral range with NSL-created antennas by properly choosing the fabrication parameters [1].

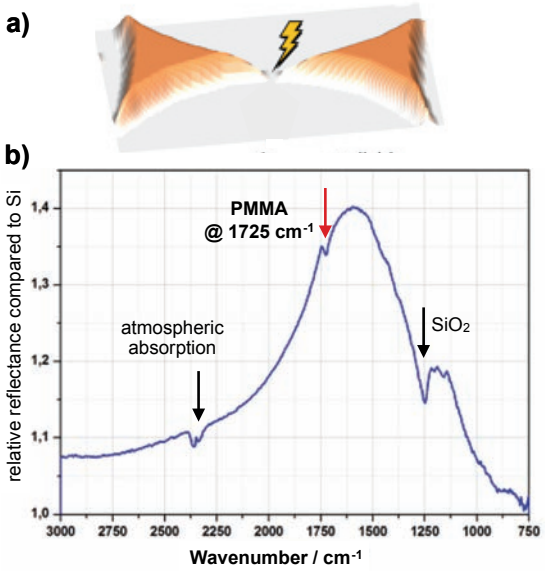

FIG. 1: a) Sketch of a gold antenna consisting of two triangles. The local electric field in the gap (indicated by yellow arrow) is expected to be strongly enhanced. b) FTIR reflection spectrum of an array of gold antennas shows a broad resonance peak at about 1600 cm^{-1}. The vibrational absorption band of a thin layer of PMMA covering the antennas is also visible in the spectrum at 1725 cm^{-1} (red arrow), proving the enhancement. Other peaks (black arrows) arise from atmospheric absorption and the (also enhanced) native SiO_2 layer on top of the silicon substrate.

In order to use these IR antennas for surface enhanced infrared absorption (SEIRA), we prepared a *40 nm* thin layer of a polymer on top of the IR antennas by spin-coating. The polymer we used was polymetamethylacrylat (PMMA) and has a characteristic IR absorption band at a frequency of 1725 cm^{-1}. With the aid of the resonant enhancement by the IR antennas, the absorption band of PMMA is clearly visible (Fig 1b). With a similar integration time, the absorption signal of the PMMA on Silicon would be barely visible in the IR spectra (not shown). We observe an averaged enhancement of about 10 times. The local field enhancement however, e.g. at the tips of the IR antennas is expected to be even higher. Estimated enhancement factors of more than 4 orders of magnitude for linear antennas have been reported [2]. These factors might even be improved by an order of magnitude when employing two nanostructures separated by a small gap. Such a configuration is expected to exhibit an even higher local field enhancement due to coupling of the two neighboring structures.

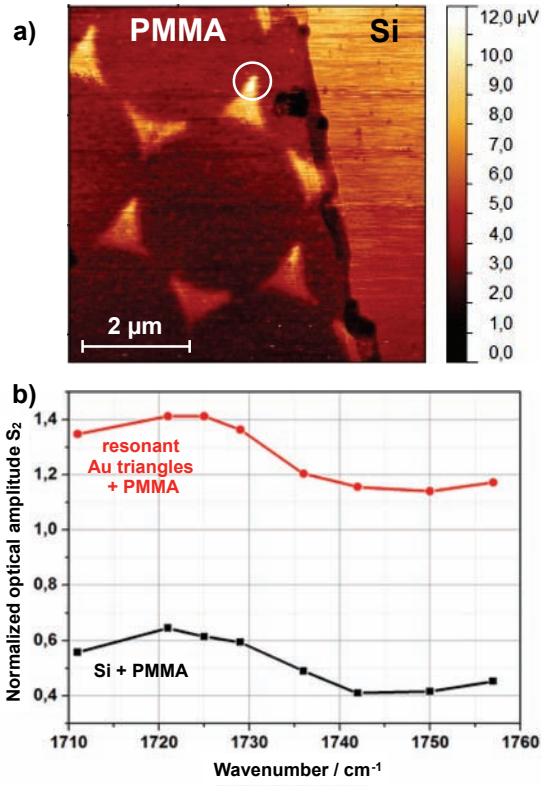

FIG. 2:
a) Infrared s-SNOM image of resonant gold antennas (triangular shapes) covered with PMMA. The infrared amplitude is enhanced on the gold island compared to the bare PMMA on Si, especially on the tips of the islands, (e.g. marked with a with circle) indicating a resonant enhancement.
b) Infrared s-SNOM spectra of the 40 nm thin PMMA film taken on Silicon (black) and on the bright spot of the gold triangles (red curve). The amplitude signal is enhanced by more than two times on the gold triangle.

In order to acquire information on the local field enhancement we employ high-resolution scattering-type scanning near-field optical microscopy (s-SNOM). In s-SNOM, a sharp probing tip is illuminated with infrared laser light. The electric field at the tip apex is strongly enhanced within an area of about the tips radius, which is usually in the order of 20-30 nm. The localized field interacts with the sample and allows for high-resolution probing of the samples optical properties. The spatial resolution is only limited by the tips radius of curvature and is independent of the illumination wavelength [3] Therefore, material specific imaging and chemical characterization at nanoscale resolution become possible when using infrared light for illumination. We use our infrared s-SNOM with a CO-laser as tunable mid-IR light source and illuminate the tip while scanning the sample. The backscattered light by the tip is detected interferometrically, and a demodulation procedure enables to suppress the background light scattered by other parts of the sample.

Fig 2a shows an infrared s-SNOM image of gold triangles covered with PMMA. The infrared amplitude on PMMA is higher on gold compared to the amplitude on PMMA on the silicon surface, which is due to a substrate enhancement effect discovered already earlier [4]. Additionally, at the upper right tips of three triangles, a higher infrared signal can be observed. This is a signature of resonantly enhanced near-field spectroscopy. We evaluated the spectral response by tuning our CO-laser over the PMMA vibrational band at 1725 cm^{-1} and compared the spectra of PMMA on silicon with those obtained on the tip of the gold triangle (Fig 2b). In both spectra the vibrational absorption band is observable, and the signals on the gold triangles are enhanced more than two-fold. This is remarkable, even though we are disturbing the near-fields of the IR antenna with our metallic probing tip.

In order to minimize the disturbance of the probing tip, we plan the use of dielectric tips as well as polarization-sensitive measurements. We also envision to further increase the local field enhancement by creating structures with small gap sizes. This might allow to unambiguously measure - and not estimate- the local absorption enhancement of different kinds of IR antennas.

In summary, we have shown that infrared antennas can be used to enhance the sensitivity of vibrational spectroscopy with in conventional far-field FTIR measurements as well as in spatially resolved near-field spectroscopy (s-SNOM). One limitation of s-SNOM has been the restricted spectral range of operation due to the lack of powerful, tuneable IR laser sources. Our shown sensitivity enhancement together with the development of new broadband mid-IR laser sources at the Fraunhofer Institute of Laser Technology will push infrared spectroscopy to the level of single nanostructures, such as nanowires and particles and thus will open up exciting new possibilities for the characterization of functional nanocomposites.

[1] A. Hartung, Bachelorarbeit, RWTH Aachen 2010

[2] F. Neubrech et al.: „Resonant Plasmonic and Vibrational Coupling in a Tailored Nanoantenna for Infrared Detection“, Physical Review Letters 101, 157403 (2008).

[3] T. Taubner, R. Hillenbrand and F. Keilmann: "Performance of visible and mid-infrared scattering-type near-field optical microscopes." *Journal of Microscopy* **210**(3), 311-314 (2003).

[4] J. Aizpurua, T. Taubner, F.J. Garcia de Abajo, M. Brehm, R. Hillenbrand: “Substrate-enhanced infrared near-field spectroscopy.” Optics Express 16, 1529 (2008).

The benefit of negative-C_S imaging technique for quantitative HRTEM

C.L. Jia, L. Houben, A. Thust, and J. Barthel

PGI-5: Microstructure Research, Forschungszentrum Jülich, 52425 Jülich
Ernst Ruska Centre for Microscopy and Spectroscopy with Electrons

Employing an aberration corrector in a transmission electron microscope, the spherical aberration C_S can be tuned to negative values, resulting in a novel imaging technique: the negative C_S imaging (NCSI) technique. The image contrast obtained with the NCSI technique is compared quantitatively with the image contrast formed with the traditional positive C_S imaging (PCSI) technique. For the case of thin objects negative C_S images are superior to positive C_S images concerning the magnitude of the obtained contrast. As a consequence, the image signal obtained with a negative C_S is significantly more robust against noise caused by amorphous surface layers, resulting in a measurement precision of atomic positions which is by a factor of 2 to 3 better at an identical noise level. The quantitative comparison of the two imaging modes shows that the NCSI mode yields significantly more precise results than the traditional PCSI mode in quantitative high-resolution transmission electron microscopy of thin objects.

The availability of spherical aberration (C_S) correction has opened up a large field of applied materials research for high-resolution transmission electron microscopy (HRTEM). Based on the tunability of C_S, optimum imaging conditions were derived, which provide minimum contrast delocalization and maximum phase contrast at the same time [1]. Under such optimized conditions the point resolution is extended up to the information limit of the instrument. It was found that a high image contrast is obtained when employing a negative value of C_S in conjunction with an overfocus [2]. The related negative C_S imaging (NCSI) mode yields a bright atom contrast for thin objects, and leads to a substantially higher contrast compared to the dark atom images formed under the traditional positive C_S imaging (PCSI) mode.

For quantitative HRTEM it is mandatory to have on the one hand an adequate resolution in order to separate closely spaced atom columns, and to obtain on the other hand a sufficiently strong signal from these columns in order to achieve a high precision for the quantification of the atomic positions. Important conclusions on the selection of the appropriate imaging conditions for quantitative HRTEM can therefore be drawn from a quantitative comparison of the NCSI and the PCSI mode with respect to the obtained contrast and with respect to the resulting measurement precision of atomic column positions.

In the present study [3] we report on the benefit of the NCSI mode for quantitative HRTEM by a direct comparison with the traditional PCSI mode. The influence of the two imaging modes on the strength of the obtained image contrast is investigated quantitatively by means of image calculations. In addition, the precision obtained for the measurement of atom column positions is quantified including the effect of image noise caused by amorphous surface layers. Considering the technological relevance of perovskite materials, we select $SrTiO_3$ as an exemplary reference material for the image calculations.

Figure 1 shows a thickness series of images calculated for the two alternative imaging modes. The displayed atom symbols clarify that the NCSI mode leads to a bright atom contrast under a darker background. This bright atom contrast is preserved up to an object thickness of $t = 7.7$ nm. In contrast, the traditional PCSI mode results in a dark atom contrast for relatively thin objects ($t < 4.4$ nm), while bright peaks appear at the atom positions for an object thickness larger than 4.4 nm.

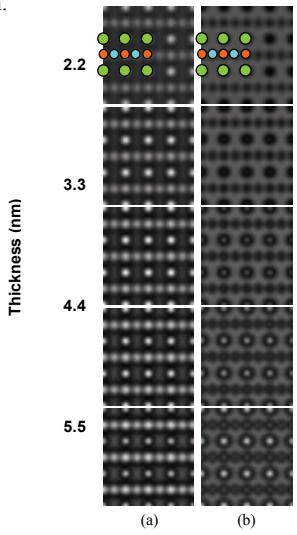

Fig. 1. Thickness series of [110] images of $SrTiO_3$ calculated for (a) the NCSI mode with C_S = –15 µm, defocus of +6 nm, and for (b) the PCSI mode with C_S = +15 µm, defocus of –6 nm, assuming a microscope information limit of 0.08 nm and an accelerating voltage of 300 kV.

The difference in image contrast between the NCSI and the PCSI mode is already evident from the visual inspection of the two image series of Fig. 1. A key requirement in quantitative HRTEM is the achievement of a good signal-to-noise ratio. The obtainable signal-to-noise ratio depends directly on the image intensity recorded at an atomic column and determines finally the precision of position and

occupancy determinations. The image intensity values for the three types of columns, SrO, Ti, and O are plotted in Fig. 2 for the images with a thickness of 3.3 nm. The solid-line profiles are taken from the images calculated for the NCSI mode and the dashed-line profiles are taken from the images calculated for the PCSI mode. The mean intensity is denoted by a dotted line.

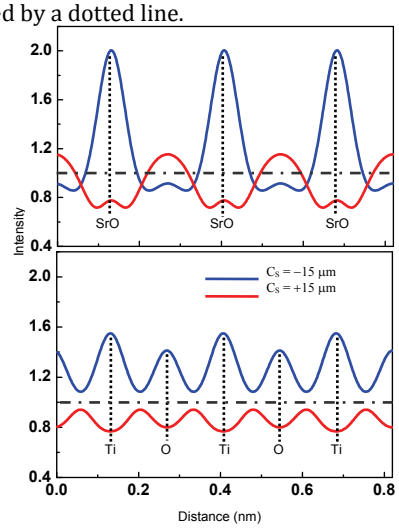

Fig. 2. Image intensity profiles belonging to SrO, Ti and O columns with a thickness of 3.3 nm resulting from the NCSI mode (blue lines) and from the PCSI mode (red lines). Images are normalized to a mean value of 1.

The $SrTiO_3$ images of Fig. 2 for a crystal thickness of 3.3 nm were selected for investigating the effect of an amorphous layer on the measurement precision. In order to evaluate the effect of different amorphous layer thicknesses, one up to five random phase object images were added to the selected images of the $SrTiO_3$ crystal as is illustrated in Fig. 3. The resulting precision of the column position determination is shown in Fig. 4 as a function of the number of amorphous layers. The displayed precision values represent twice the standard deviation of the scatter in the peak position of a Gaussian peak profile after a non-linear least squares fit. Overall, the precision obtained for the NCSI mode is by a factor of 2 to 3 better than the results of the PCSI mode.

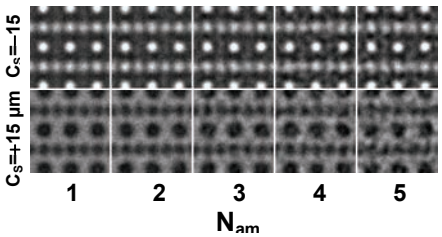

Fig. 3. Modelling of amorphous cover layers. The figure shows various thicknesses of fluctuating amorphous cover layers. The thickness of the amorphous cover layers is given as the number Nam of random phase object images added to the crystal image.

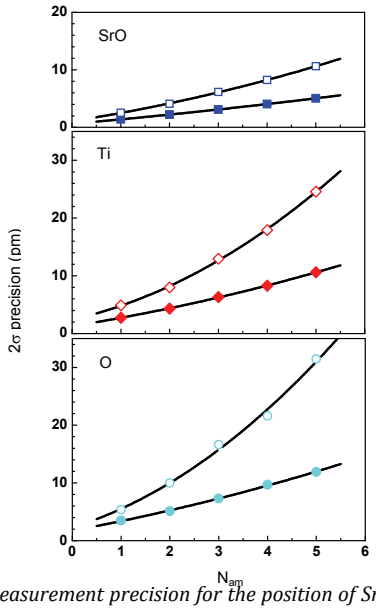

Fig. 4. Measurement precision for the position of SrO, Ti, and O atomic columns obtained with the NCSI mode (solid symbols) and the PCSI mode (open symbols). Each data point corresponds to the repeated measurement on a set of images of 3.3 nm thick $SrTiO_3$ [110] with stochastically modelled amorphous cover layers. The number Nam of random phase object images used to simulate the effect of amorphous cover layers is proportional to the thickness of these layers.

The images obtained by applying the NCSI mode exhibit extraordinary advantages with respect to the overall image contrast and the atom column intensity. In addition, for the NCSI mode the image intensity of all columns follows essentially a linear dependence on the total atomic number accumulated up to a thickness of at least 3.3 nm. Beyond this thickness the linear relation is still valid for the lighter Ti- and O-columns, whereas the linearity is lost for the heavier SrO columns due to the shorter extinction length of the latter column type. In the case of the PCSI mode, the linearity between column intensity and the accumulated atomic number is already lost for all column types at a thickness of 3.3 nm.

The NCSI mode in aberration-corrected electron microscopy offers unique advantages for direct atomic imaging in HRTEM. Furthermore, the strong contrast offered by the NCSI mode provides also an excellent basis for quantitative measurements of various local structure properties at lattice defects such as grain boundaries, domain walls, interfaces, and dislocations in electroceramic materials [4,5].

1. M. Lentzen *et al.*, Ultramicroscopy **92**, 233 (2002).
2. C.L. Jia, M. Lentzen, K. Urban, Science **299**, 870 (2003).
3. C.L. Jia *et al.*, Ultramicroscopy **110**, 500 (2010).
4. C.L. Jia *et al.*, Phys. Rev. Lett. **102**, 117601 (2009).
5. A.H. Heuer, C. L. Jia, and K.P.D. Lagerlöf, Science **330**, 1227 (2010).

POWTEX – Past and Future

A. Houben[1], W. Schweika[2], R. Engels[3], G. Kemmerling[3], M. Klein[4], Chr. Schmidt[5], U. Schmidt[4], Th. Brückel[2,6], R. Dronskowski[1]

[1]Institute of Inorganic Chemistry, RWTH Aachen University
[2]JCNS-2: Scattering Methods, Jülich Centre for Neutron Science
[3]ZEL: Central Institute for Electronics, Forschungszentrum Jülich, 52425 Jülich
[4]Physikalisches Institut der Universität Heidelberg
[5]Detector Laboratory, GSI
[6]PGI-4: Scattering Methods, Peter Grünberg Institut, Forschungszentrum Jülich, 52425 Jülich

The POWTEX instrumentation project for time-of-flight neutron POWder diffraction and TEXture studies at the FRM II research reactor in Munich has met important milestones at the end of the first funding period. The main parts of the primary instrument, neutron guide and chopper system, have been designed, include significant new developments and are under construction. An enormous challenge has materialized by the recently and abruptly depleted ^{3}He world market, affecting the heart of the secondary instrument, i.e., the large area-detector system. We have promptly initiated a prototype development using two alternative detector systems, both offering promising solutions adjusted to the particular needs of POWTEX. Because of these successes, the BMBF has rewarded the project POWTEX with continued full funding.

Since the origins of the ^{3}He crisis have already been elaborately discussed in the scientific literature and in the regular press [1, 2], we want to address herein how the POWTEX group has dealt with that unfortunate situation. As it is seemingly impossible (i.e., unaffordable) to buy ^{3}He in large quantities (3700 liter×bar for POWTEX), it is very well understandable that the BMBF would bring all ^{3}He-based detector proposals to a full stop. Nonetheless, the as-proposed funding of the POWTEX project was recently granted to RWTH Aachen University by the German Federal Ministry of Education and Research (BMBF).

At present, many new detector concepts are under investigation by different groups throughout the world. Since we became aware of the beginning ^{3}He crisis in 2008 already, we initiated the search for alternative concepts at this earliest possible moment. In order to search for a future detector perspective for POWTEX, two cooperation projects to develop ^{3}He-free detector prototypes were immediately started.

Because POWTEX uses a thermal neutron source with wavelengths down to λ = 1.0 Å and even lower, achieving a high detection efficiency is the most challenging task. While ^{3}He-PSD-tubes are still the most efficient detector type (70–80% for 1.0 Å), a minimum requirement for the efficiency of the new prototypes was formulated as >50% for 1.0 Å. Second, the detectors need to cover a huge solid angle and must have a large detector surface area. Because of their small size and their formerly low price per area, the ^{3}He-PSDs would have been an ideal choice in this respect, too. Although the alternative concepts are not expected to be as compact, they generally have to meet the same conditions. Both prototypes will allow for a *better* spatial resolution of 5×5 mm² pixel size (instead of 20x25 mm²).

Due to these requirements, gas-based BF_3 detectors can be neglected because of their low efficiency at small wavelengths. Semiconducting detectors are still in very early design states and do not match our urgent need for finding a proper solution. Alternative concepts are solid-state detectors using ^{6}Li or ^{10}B. Two such detector concepts are in the prototype state as described in the following. While being designed to fit the needs of POWTEX, at the time being, both prototypes are under assembly. After thorough testing of these prototypes, we intend to decide for the best performing detector system in 2011.

FIG. 1: WSF concept (top) and its prototype (bottom).

The Wavelength-Shifting-Fiber (WSF) detector is a ^{6}Li based scintillation detector (FIG. 1). In the first step, the scintillator converts the energy released by neutron absorption into a pulse of blue light. When the blue light hits the two layers of perpendicular

wavelength-shifting fibers, it is converted to green light. After this second step, the light is transported inside the fiber using total reflection. Finally, the light pulse is detected using a multi-channel photomultiplier (red square in the picture). By a coincidence mapping of the perpendicular grid of fibers, the neutron position can be extracted. The basic concept of WSF detectors is already used in large scale at the SNS instruments POWGEN and VULCAN. In order to meet POWTEX's requirements, the detector development group (ZEL) of the Forschungszentrum Jülich is currently investigating various possibilities to improve the resolution and, most importantly, the overall detection efficiency.

The grazing incidence ^{10}B-Jalousie detector uses ^{10}B as solid absorption material in an ionization gas chamber for detection. The concept is pictured in FIG. 2. The detector is assembled from single blinds of which each has a small angle of grazing incidence (≈10°) to neutrons scattered from the sample position. Thus, the cylindrical detector geometry of POWTEX is perfectly matched. In addition, the neutron's path through the canted ^{10}B layer is much longer than the thickness of the coating such that the near surface absorption probability is raised. Vice versa, a thin coating is crucial to ensure that the reaction products leave the coating and reach the anode wires. Similar to the WSF concept, the neutron position is extracted by coincident signals on the segmented cathode (^{10}B layers) and the anode wires. As indicated by the orange circles in FIG. 2, each neutron might be absorbed by one of several layers such that the overall detection efficiency is tunable and improved to the desired value. The additional flight-path will be corrected for a proper TOF determination of every neutron.

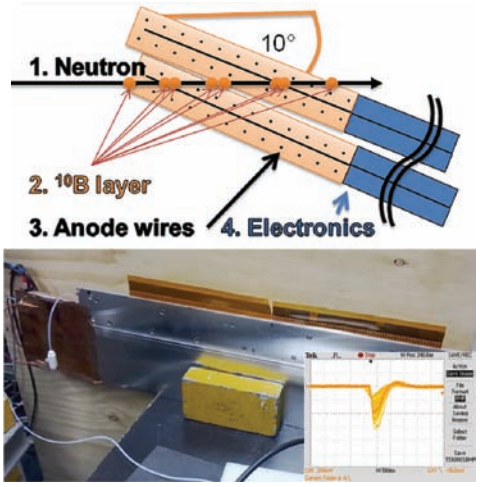

FIG. 2: Jalousie concept (top) and its pre-prototype (bottom). The pre-prototype is irradiated with a lab neutron source.

So far, we have summarized our activities with respect to POWTEX's detector part. In the following, we will concentrate on the primary part of the instrument.

The chopper system is certainly the most essential part of a time-of-flight diffractometer. The chopper system will be built by the chopper group of the ZAT at the Forschungszentrum Jülich [3]. Apart from well-established techniques such as the magnetic bearing, new concepts will be realized as well. These are, for example, the use of disks made from carbon reinforced plastics and, furthermore, the very small distance of the disks (5 mm) in the pulse double-chopper. Together with the small slit size (1×1 cm^2) the latter allows for a sharp pulse structure. Consequently, the λ-2θ-diffractograms will profit from good resolution and high intensity regimes that are functionally connected by Bragg's law. Furthermore, the system is flexible in the pulse frequency (100–**200**–2000 Hz) as well as in the wavelength range (<1.0–2.4 Å) allowing for many different kinds of experiments.

We have completed the design of the elliptic neutron guide system. It has been recently committed to SwissNeutronics and is under construction. The system consists of two double-elliptic neutron guides focusing at the source, the pulse disk-chopper as a needle's eye and the small sample spot, which leads to a low background and small sample sizes (1×1 cm^2). Next to that, the divergence profile can be optimized to be of Gaussian shape by changing the super-mirror coating along the guide ($1.75 \leq m \leq 5.00$). In contrast to 2009's report, one may homogenize the divergence profile while keeping the perfect elliptic focusing geometry which is favorable by means of a low background. This can be nicely achieved with Monte-Carlo instrument simulations using the VITESS software [4] on the RWTH Aachen cluster. By further developing the guide module, it is possible to define the desired "good neutrons" and trace their way through the guide by the innovative "back-tracing" mechanism. Thus, the coating can be perfectly matched to an optimal transport of the "good neutrons". A homogeneous profile of the beam divergence is crucial for a straightforward data analysis which, however, turned out to be challenging. The solution found is an improved "quadrature of the circle" using an octagonal guide cross section instead of the commonly used rectangular cross section. For this purpose, the guide module of the VITESS simulation software has been extended. The technical realization of an octagonal guide, never done before on a large scale, will be challenging as well.

Both chopper and neutron guide system will be delivered in 2012.

We thank the BMBF for funding the POWTEX project and especially for the short-term support for developing two new detector prototypes.

[1] T. Feder, *Phys. Today* **2009**, October, 21–23.

[2] M.L. Wald, *The New York Times* **2009**, November, 22.

[3] S. Polachowski, H. Stelzer, ZAT, Forschungszentrum Jülich.

[4] VITESS 2.9, G. Zsigmond, K. Lieutenant, S. Manoshin, M. Fromme, P. Bentley, A. Houben, D. Champion, October 2009 and VITESS 2.10 α.

Publications

Abouzar, M. H.; Pedraza, A.; Schöning, M. J.; Poghossian, A.
Label-free DNA hybridization and denaturation detection by means of field-effect nanoplate SOI capacitors functionalized with gold nanoparticles
Procedia Engineering, 5 (2010), 918 -921

Abouzar, M. H.; Poghossian, A.; Siqueira, J.R.; Oliveira, N.O.; Moritz, W.; Schöning, M. J.
Capacitive electrolyte-insulator-semiconductor structures functionalised with a polyelectrolyte/enzyme multilayer:New strategy for enhanced field-effect biosensing
Physica Status Solidi A, 207 (2010) 4, 884 - 890

Akabori, M.; Trinh, T.Q.; Kudo, M.; Hardtdegen, H.; Schäpers, T.; Suzuki, T.
Strain-enhanced electron mobility anisotropy in InxGa1-xAs/InP two-dimensional electron gases
Physica E, 42 (2010) 4, 1130 - 1133

Akrap, A.; Angst, M.; Khalifah, P.; Mandrus, D.; Sales, B.C.; Forro, L.
Electrical transport in charge-ordered Fe2BO4: Resistive switching and pressure effects
Physical Review B, 82 (2010) 16, 165106

Akola J.,Jones R. O.
Comment on "Formation of Large Voids in the Amorphous Phase-Change Memory Ge2Sb2Te5 Alloy"
Physical Review Letters 104, 1, 019603 (2010)

Akola J., Jones R. O., Kohara S., Usuki T., Bychkov E.
Density variations in liquid tellurium: Roles of rings, chains and cavities
Physical Review B 81, 9, 094202 (2010)

Alagha, S.; Estévez Hernández, S.; Blömers, C.; Stoica, T.; Calarco, R.; Schäpers, Th.
Universal conductance fluctuations and localization effects in InN nanowires connected in parallel
Journal of Applied Physics, 108 (2010), 113704

Amekura, H.; Tanaka, M.; Katsuya, Y.; Yoshikawa, H.; Shinotsuka, H.; Tanuma, S.; Ohnuma, M.; Matsushita, Y.; Kobayashi,K.; Buchal, Ch.; Mantl, S.; Kishimoto, N.
Melting of Zn nanoparticles embedded in SiO2 at high temperatures: Effects on surface plasmon resonances
Applied Physics Letters, 96 (2010), 023110

Andergassen S., D. Feinberg, S. Florens, M. Lavagna, S. Shiau, P. Simon, and R. Van Roermund
New trends for the Kondo effect in nanostructures
Int. J. Nanotechnology 7, 438 (2010)

Andergassen S., V. Meden, H. Schoeller, J. Splettstoesser, and M.R. Wegewijs
Charge transport through single molecules, quantum dots, and quantum wires
Nanotechnology 21, 272001 (2010)

Armstrong, C. L.; Sandqvist, E.; Schmalzl, K.; Rheinstädter, M. C.
Membrane mediated protein-protein interactions
Physics in Canada, 66 (2010) 3, 189 - 191

Atodiresei, N.; Brede, J.; Lazic, P.; Caciuc, V.; Hoffmann, G.; Wiesendanger, R.; Blügel, S.
Design of the Local Spin Polarization at the Organic-Ferromagnetic Interface
Physical Review Letters, 105 (2010), 066601

Avila-Paredes H. J., Zhao J., Wang S., Pietrowski M., De Souza R. A., Reinholdt A., Munir Z. A., Martin M., Kim S.
Protonic conductivity of nano-structured yttria-stabilized zirconia: dependence on grain size
J. Mater. Chem. 20, 990 (2010)

Avila-Paredes H. J., Barrera-Calva E., Anderson H. U., De Souza R. A., Martin M., Munir Z. A., Kim S.
Room-temperature protonic conduction in nanocrystalline films of yttria-stabilized zirconia
J. Mater. Chem. 20, 6235 (2010)

Avila-Paredes H. J., Chen C.-T., Wang S., De Souza R. A., Martin M., Munir, Z. A., Kim S.
Grain boundaries in dense nanocrystalline ceria ceramics: exclusive pathways for proton conduction at room temperature
J. Mater. Chem. 20, 10110 (2010)

Barannik, A.; Bunyaev, S.; Cherpak, N.; Prokopenko, Y.; Kharchenko, A.; Vitusevich, S.
Whispering gallery mode hemisphere dielectric resonators with impedance plane.
IEEE Transactions on Microwave Theory and Techniques, 58 (2010) 10, 2682 - 2691

Bedanta, S.; Petracic, O.; Chen, X.; Rhensius, J.; Kentzinger, E.; Rücker, U.; Brückel, T.; Doran, A.; Scholl, A.; Cardoso, S.; Freitas, S.S.; Kleemann, W.
Single-particle blocking and collective magnetic states in discontinuous CoFe/Al2O3 multilayers
Journal of Physics D - Applied Physics, 43 (2010) 47, 474002

Beekman, M.; Hermann, R.; Möchel, A.; Juranyi, F.; Nolas, G. S.
A study of low-energy guest phonon modes in clathrate-II NaxSi136 (x = 3, 23, and 24)
Journal of Physics: Condensed Matter, 22 (2010) 35, 355401

Beging, S.; Mlynek, D.; Hataihumakul, S.; Poghossian, A.; Baldsiefen, G.; Busch, H.; Laube, N.; Kleinen, L.; Schöning, M. J.
Field-effect calcium sensor for the determination of the risk of urinary stone formation
Sensors and Actuators B, 144 (2010) 2, 374 - 379

Behmenburg H., L. Rahimzadeh Khoshroo, C. Mauder, N. Ketteniss, K. H. Lee, M. Eickelkamp, M. Brast, D. Fahle, J. F. Woitok, A. Vescan, H. Kalisch, M. Heuken, R. H. Jansen
In-situ SiN passivation of AlInN/GaN heterostructures by MOVPE
physica status solidi (c), 7: 2104-2106 (2010)

Belyaev, A.E.; Boltovets, N.S.; Vitusevich, S. A.; Ivanov, V.N.; Konakova, R.V.; Kudryk, Y.Ya.; Lebedev, A.A.; Milenin, V.V.; Svechnikov, Yu.N.; Sheremet, V.N.
Effect of microwave treatment on the current transport mechnisms in Au-TiBx-Al-Ti-n+ -n- n+-GaN-Al2O3 Ohmic contacts
Semiconductors, 44 (2010) 6, 745 - 751

Bettaieb, L.; Kokabi, H.; Poloujadoff, M.; Krause, H.-J.; Coillot, C.
Comparison of the use of SQUID and Hall Effect sensors in NDE
Materials Evaluation, 68 (2010), 535 - 541

Betzinger, M.; Friedrich, C.; Blügel, S.
Hybrid functionals within the all-electron FLAPW method: Implementation and applications of PBE0
Physical Review B, 81 (2010) 19, 195117

Bihlmayer, G.; Koroteev, Y. M.; Chulkov, E. V.; Blügel, S.
Surface- and edge-states in ultrathin Bi-Sb films
New Journal of Physics, 12 (2010) 065006

Bland, S.R.; Angst, M.; Adiga, S.; Scagnoli, V.; Johnson, R.D.; Herrero-Martin, J.; Hatton, P.D.
Symmetry and charge order in Fe2OBO3 studied through polarized resonant x-ray diffraction
Physical Review B, 82 (2010) 11, 115110

Blech K., M. Homberger, U. Simon,
Electrical Properties of Metal Nanoparticles
in G. Schmid: Nanoparticles (2nd Edition), Wiley-VCH (2010).

Bohrn, U.; Stütz, E.; Fleischer, M.; Schöning, M. J.; Wagner, P.
Real-time detection of CO by Eukaryotic cells
Procedia Engineering, 5 (2010), 17 - 20

Brede, J.; Atodiresei, N.; Kuck, S.; Lazic, P.; Caciuc, V.; Morikawa, Y.; Hoffmann, G.; Blügel, S.; Wiesendanger, R.
Spin- and Energy-Dependent Tunneling through a Single Molecule with Intramolecular Spatial Resolution
Physical Review Letters, 105 (2010) 4, 047204

Brako R., Sokcevic D., Lazic P., Atodiresei N.
Graphene on the Ir(111) surface: from van der Waals to strong bonding
New Journal of Physics, 12, 11, 113016 (2010)

Bretos, I.; Schneller, T.; Waser, R.; Hennings, D.F.; Halder, S.; Thomas, F.
Compositional substitutions and aliovalent doping of BaTiO3-based thin films on Nickel foils prepared by chemical solutiion deposition
Journal of American Chemical Society, 93 (2010) 2, 506 - 515

Brezinova I., L. Wirtz, S. Rotter, C. Stampfer, and J. Burgdörfer,
Transport through open quantum dots: making semiclassics quantitative
Phys. Rev. B 81 125308 (2010)

Brona, J.; Cherepanov, V.; Romanyuk, K.; Voigtländer, B.
Formation of pits during growth of Si/Ge nanostructures
Surface Science, 604 (2010) 3/4, 424 - 427

Brückel, T.; Schweika, W.; Tonnerre, J.-M.
PNSXM 2009; 2nd Workshop on Polarized Neutrons and Synchrotron X-Rays for Magnetism
Journal of Physics : Conference Series, 211 (2010) 1, 011001

Buniatyan, V.V.; Abouzar, M. H.; Martirosyan, N.W.; Schubert, J.; Gevorgian, S.; Schöning, M. J.; Poghossian, A.
pH-sensitive properties of barium strontium titanate (BST) thin films prepared by pulsed laser deposition technique
Physica Status Solidi A, 207 (2010) 4, 824 - 830

Busiakiewicz, A.; Karthäuser, S.; Homberger, M.; Kowalzik, P.; Waser, R.; Simon, U.
Electronic transport properties of individual 4,4'-bis(mercaptoalkyl)-biphenyl derivatives measured in STM-based break junctions
Physical Chemistry Chemical Physics, 12 (2010) 35, 10518 - 10524

Cao J.-L., Ren Y.-B., Peng L., Qiao L., Gu H.-W., Li T., Yue Z., Klemradt U.
Evidences for Interfacial Phase Decomposition in Ferroelectric Thin Films during Fatigue
Electrochem. Solid-State Lett. 13, G102 (2010)

Cavaliere F., E. Mariani, R. Leturcq, C. Stampfer, M. Sassetti
Asymmetric Franck-Condon factors in suspended carbon nanotube quantum dots
Phys. Rev. B 81 201303(R) (2010)

Chang, L. J.; Su, Y.; Kao, Y.-J.; Chou, Y. Z.; Mittal, R.; Schneider, H.; Brückel, T.; Balakrishnan, G.; Lees, M. R.
Magnetic correlations in the spin ice Ho2-xYxTi2O7 as revealed by neutron polarization analysis
Physical Review B, 82 (2010), 172403

Chatterji, T.; Wuttke, J.; Sazonov, A.P.
Hyperfine interaction in Co2SiO4 investigated by high resolution neutron spectroscopy
Journal of Magnetism and Magnetic Materials, 322 (2010) 20, 3148 - 3152

Cheng, X.; Xu, D.; Sun, Q.-Q.; He, D.; Wang, Z.; Yu, Y.; Zhang, D.W.; Zhao, Q.
Al2O3/NbAlO/Al2O3 sandwich gate dielectric film on InP
Applied Physics Letters, 96 (2010) 2, 022904

Clavero, C.; Bode, M.; Bihlmayer, G.; Blügel, S.; Lukaszew, R. A.
Island-assisted interface alloying and magnetic polarization at submonolayer V/Cr(001) interfaces
Physical Review B, 82 (2010) 8, 085445

Deiter, C.; Bierkandt, M.; Klust, A.; Kumpf, C.; Su, Y.; Bunk, O.; Feidenhans'l, R.; Wollschläger, J.
Structural transitions and relaxation processes during the epitaxial growth of ultrathin CaF2 films on Si(111)
Physical Review B, 82 (2010) 8, 085449

De Souza R. A., Martin M.
Secondary ion Mass Spectrometry – SIMS
In: The encyclopedia of mass spectrometry, D. Beauchemin, D. E. Matthews (Volume Eds.) Elsevier Ltd. 5 (2010) pp 381-397

Dippel, A.C.; Schneller, T.; Waser, R.; Park, D.; Mayer, J.
Formation sequence of lead platinum interfacial phases in chemical solution deposition derived Pb(Zr1-xTix)O-3 thin films
Chemistry of Materials, 22 (2010) 23, 6209 - 6211

Dong, H.; Zhang, Y.; Krause, H.-J.; Xie, X.; Braginski, A.I.; Offenhäusser, A.
Comparison of different detectors in low field NMR measurements
Journal of Physics : Conference Series, 234 (2010) 4, 042008

Dong, H.; Zhang, Y.; Krause, H.-J.; Xie, X.; Braginski, A.I.; Offenhäusser, A.
Effect of HTS Superconductors on the Homogeneity of Measurement Field in Low Field NMR Detection
Chinese Physics Letters, 27 (2010) 8, 088502

Durgun Özben, E.; Nichau, A.; Lopes, J. M. J.; Lenk, S.; Besmehn, A.; Bourdelle, K.K.; Zhao, Q. T.; Schubert, J.; Mantl, S.
Electrical characterization of TbScO3/TiN gate stacks in MOS capacitors and MOSFETs on strained and unstrained SOI
ECS Transactions, 33 (2010) 3, 195 - 202

Eickelkamp M., D. Fahle, J. Lindner, M. Heuken, C. Lautensack, H. Kalisch, R. H. Jansen, A. Vescan
Impact of Gate Dielectric Thickness on the Electrical Properties of AlGaN/GaN MISHFETs on Si(111) Substrate
physica status solidi (a), 207: 1342-1344 (2010)

Eliasen A., Paaske J., Flensberg K., Smerat S., Leijnse M., Wegewijs M. R., Jørgensen H. I., Monthioux M., Nygård J.
Transport via coupled states in a c60 peapod quantum dot.
Phys. Rev. B (2010), 81:155431.

Ellersiek D., Fassbender H., Bruners P., Pfeffer J. G., Penzkofer T., Mahnken A. H., Schmitz-Rode T., Mokwa W. and Schnakenberg U.
A monolithically fabricated flexible resonant circuit for catheter tracking in magnetic resonance imaging
Sensors and Actuators B: Chemical, B144, pp. 432-436 (2010)

Estévez Hernández, S.; Akabori, M.; Sladek, K.; Volk, C.; Alagha, S.; Hardtdegen, H.; Pala, M.G.; Demarina, N.; Grützmacher, D.; Schäpers, T.
Spin-orbit coupling and phase coherence in InAs nanowires
Physical Review B, 82 (2010) 23, 235303

Fassbender H., Thiel W. and Mokwa W.
Pressure propagation in encapsulated pressure sensor systems
Procedia Engineering, pp. 601-604 (2010)

Feygenson, M.; Schweika, W.; Ioffe, A.; Vakhrushev, S. B.; Brückel, T.
Magnetic phase transition in confined MnO nanoparticles studied by polarized neutron scattering
Physical Review B, 81 (2010) 6, 064423

Finger, T.; Senff, D.; Schmalzl, K.; Schmidt, W.; Regnault, L. P.; Becker, P.; Bohaty, L.; Braden, M.
Electric-field control of the chiral magnetism of multiferroic MnWO4 as seen via polarized neutron diffraction
Physical Review B, 81 (2010) 5, 054430

Finger, T.; Senff, D.; Schmalzl, K.; Schmidt, W.; Regnault, L.-P.; Becker, P.; Bohaty, L.; Braden, M.
Polarized-neutron-scattering studies on the chiral magnetism in multiferroic MnWO4
Journal of Physics : Conference Series, 211 (2010) 1, 012001

Freimuth F., Blügel S., Mokrousov Y.
Anisotropic Spin Hall Effect From First Principles
Physical Review Letters 105, 24, 246602 (2010)

Friedrich, C.; Blügel, S.; Schindlmayr, A.
Efficient implementation of the GW approximation within the all-electron FLAPW method
Physical Review B, 81 (2010) 12, 125102

Frielinghaus, R.; Batov, I. E.; Weides, M.; Kohlstedt, H.; Calarco, R.; Schäpers, T.
Josephson supercurrent in Nb/Inn-nanowire/Nb junctions
Applied Physics Letters, 96 (2010) 13, 132504

Fu, Z.; Kögerler, P.; Rücker, U.; Su, Y.; Mittal, R.; Brückel, T.
An approach to the magnetic ground state of the molecular magnet {Mo72Fe30}
New Journal of Physics, 12 (2010), 083044

Funke M., Buchenauer A., Schnakenberg U., Mokwa W., Diederichs S., Mertens A., Muller C., Kensy F. and Buchs J.
Microfluidic BioLector-Microfluidic Bioprocess Control in Microtiter Plates
Biotechnology and Bioengineering, 107, 3, pp. 497-505 (2010)

Funke M., Buchenauer A., Mokwa W., Kluge S., Hein L., Müller C., Kensy F. and Büchs J.
Bioprocess Control in Microscale: Scalable Fermentations in Disposable and User-Friendly Microfluidic Systems
Microbial Cell Factories, 9, 86, (2010)

Gerber, A.; Fitsilis, M.; Waser, R.; Rece, T.J.; Rije, E.; Ducharme, S.; Kohlstedt, H.
Ferroelectric field effect transistors using very thin ferroelectric polyvinylidene fluoride copolymer films as gate dielectrics
Journal of Applied Physics, 107 (2010) 12, 124119,

Gilles, S.; Diez, M.; Offenhäusser, A.; Lensen, M.C.; Mayer, D.
Deformation of nanostructures on polymer molds during soft UV nanoimprint lithography
Nanotechnology, 21 (2010) 245307

Göbbels K., Kuenzel T., van Ooyen A., Baumgartner W., Schnakenberg U. and Bräunig P.
Neuronal cell growth on iridium oxide
Biomaterials, 31, 6, pp. 1055-1067 (2010)

Gobbels K., Thiebes A. L., van Ooyen A., Schnakenberg U. and Braunig P.
Low density cell culture of locust neurons in closed-channel microfluidic devices
Journal of Insect Physiology, 56, 8, pp. 1003-1009 (2010)

Gomeniuk, Y.Y.; Gomeniuk, Y.V.; Nazarova, A.N.; Hurley, P.K.; Cherkaoui, K.; Monaghan, S.; Gottlob, H.D.B.; Schmidt, M.; Schubert, J.; Lopes, J. M. J.; Engström, O.
Electrical Properties of LaLuO3/Si(100) Structures Prepared by Molecular Beam Deposition
ECS Transactions, 33 (2010) 3, 221 - 227

Gossuin, Y.; Disch, S.; Vuong, Q. L.; Gillis, P.; Hermann, R.; Park, J.-H.; Sailor, M. J.
NMR relaxation and magnetic properties of superparamagnetic nanoworms
Contrast Media & Molecular Imaging, 5 (2010) 6, 318 - 322

Grabowski M., Buchenauer A., El Hasni A., Klockenbring T., Barth S., Mokwa W. and Schnakenberg U.
Microfluidic system for cell fusion
Procedia Engineering, 5, pp. 1332-1335 (2010)

Gräfe M., Göttsche T., Osypka P., Görtz M., Trieu K., Fassbender H., Mokwa W., Urban U., Schmitz-Rode T., Bender B., Glocker R., Fähnle M.
HYPER-IMS: A Fully Implantable Blood Pressure Sensor for Hypertensive Patients
Proc. Sensor&Test (2010)

Gregusova, D.; Gazi, S.; Sofer, Z.; Stoklas, R.; Dobrocka, E.; Mikulics, M.; Gregus, J.; Novak, J.; Kordos, P.
Oxidized Al Film as an Insulation Layer in AlGaN/GaN Metal-Oxide-Semiconductor Heterostructure Field Effect Transistors
Japanese Journal of Applied Physics Part 1: Regular Papers, Short Notes and Review Papers, 49 (2010), 046504

Grünwald, A. T. D.; Wildes, A. R.; Schmidt, W.; Tartakovskaya, E. V.; Kwo, J.; Majkrzak, C.; Ward, R. C. C.; Schreyer, A.
Magnetic excitations in Dy/Y superlattices as seen via inelastic neutron scattering
Physical Review B, 82 (2010) 1, 014426

Grünwald, A. T. D.; Wildes, A. R.; Schmidt, W.; Tartakovskaya, E. V.; Nowak, G.; Theis-Bröhl, K.; Schreyer, A.
Neutron scattering measurements of magnetic excitations in Gd/Y superlattices
Applied Physics Letters, 96 (2010) 19, 192505

Gunkel, F.; Hoffmann-Eifert, S.; Dittmann, R.; Mi, S.B.; Jia, C.-L.; Meuffels, P.; Waser, R.
High temperature conductance characteristics of LaAlO3/SrTiO3-heterostructures under equilibrium oxygen atmospheres
Applied Physics Letters, 97 (2010) 1, 012103

Gürlich, C.; Scharinger, S.; Weides, M.; Kohlstedt, H.; Mints, R.G.; Goldobin, E.; Koelle, D.; Kleiner, R.
Visualizing supercurrents in ferromagnetic Josephson junctions with various arrangements of 0 and pi segments
Physical Review B, 81 (2010) 9, 094502

Habicht, S.; Zhao, Q. T.; Feste, S. F.; Knoll, L.; Trellenkamp, S.; Ghyselen, B.; Mantl, S.
Electrical characterization of strained and unstrained silicon nanowires with nickel silicide contacts
Nanotechnology, 21 (2010) 10, 105701

Harikrishnan, S.; Rößler, S.; Kumar, C. M. N.; Xiao, Y.; Bhat, H. L.; Rößler, U. K.; Steglich, F.; Wirth, S.; Elizabeth, S.
Memory effect in Dy0.5Sr0.5MnO3 single crystals
Journal of Physics: Condensed Matter, 22 (2010) 34, 346002

Hauschild, A.; Temirov, R.; Soubatch, S.; Bauer, O.; Schöll, A.; Cowie, B.C.C.; Lee, T.-L.; Tautz, F. S.; Sokolowski, M.
Normal-incidence x-ray standing-wave determination of the adsorption geometry
of PTCDA on Ag(111): Comparison of the ordered room-temperature
and disordered low-temperature phases
Physical Review B, 81 (2010) 12, 1254321

Hermann, R.; Nielsch, K.; Böttner, H.
Nanostructured Thermoelectric Materials: 451. WE-Heraeus-Seminar
Physik Journal, 9 (2010) 5, 54 - 55

Hermann, R.; Rücker, U.; Angst, M.
PNSXM 2009: Workshop on Polarized Neutrons and Synchrotron X-rays for Magnetism
Synchrotron Radiation News, 23 (2010) 2, 16 - 17

Hermann, R.; Rücker, U.; Angst, M.
Workshop on Polarized Neutrons and Synchrotron X-rays for Magnetism - PNSXM 2009
Neutron News, 21 (2010) 3, 3 - 7

Herzog S., Wegewijs M. R.
Dzyaloshinskii-moriya interaction in transport through single molecule transistors.
Nanotechnology(2010) 21: 274010,.

Hirschfeld J. A., Lustfeld H., Reißel M., Steffen B.
A novel scheme for precise diagnostics and effective stabilization of currents in a fuel cell stack
International Journal of Energy Research 34, 3, 293 - 302 (2010)

Hirschfeld J. A., Lustfeld H., Reißel M., Steffen B.
Tomographic diagnostics of current distributions in a fuel cell stack
International Journal of Energy Research 34, 3, 284 - 292 (2010)

Hofmann, B.; Maybeck, V.; Eick, S.; Meffert, S.; Ingebrandt, S.; Wood, P.; Bamberg, E.; Offenhäusser, A.
Light induced stimulation and delay of cardiac activity
Lab on a Chip, 10 (2010), 2588 - 2596

Hofmann M. C., Funke M., Buchs J., Mokwa W. and Schnakenberg U.
Development of a four electrode sensor array for impedance spectroscopy in high content screenings of fermentation processes
Sensors and Actuators B-Chemical, 147, 1, pp. 93-99 (2010)

Holländer, B.; Buca, D.; Mantl, S.; Hartmann, J.M.
Wet Chemical Etching of Si, Si1-xGex, and Ge in HF:H2O2:CH3COOH
Journal of the Electrochemical Society, 157 (2010) 6, H643 - H646

Homberger M., U Simon,
On the Application Potential of AuNPs in Nanoelectronics and Medicine
Phil. Trans. A 368, 1405-1453 (2010).

Hsieh D., Wray L., Qian D., Xia Y., Dil J. H., Meier F., Osterwalder J., Bihlmayer G., Hor Y. S., Cava R. J., Hasan M. Z.
Direct observation of spin-polarized surface states in the parent compound of a topological insulator using spin- and angle-resolved photoemission spectroscopy in a Mott-polarimetry mode
New Journal of Physics 12, 12, 125001 (2010)

Ishida H., Liebsch A.
Cluster dynamical mean-field study of strongly correlated heterostructures: Correlation-induced reduction of proximity effect
Physical Review B 82, 4, 045107 (2010)

Ishida H., Liebsch A.
Fermi-liquid, non-Fermi-liquid, and Mott phases in iron pnictides and cuprates
Physical Review B 81, 5, 054513 (2010)

Jin, B.B.; Zhu, B.Y.; Wördenweber, R.; de Souza Silva, C.C.; Wu, P.H.; Moshchalkov, V.V.
High-frequency vortex ratchet effect in a superconducting film with a nanoengineered array of asymmetric pinning sites
Physical Review B, 81 (2010) 17, 174505

Josten, E.; Rücker, U.; Mattauch, S.; Korolkov, D.; Glavic, A.; Brückel, T.
Magnetization Flop in Fe/Cr GMR Multilayers
Journal of Physics : Conference Series, 211 (2010), 012023

Jovanovic, V.; Biasotto, C.; Nanver, L.K.; Moers, J.; Grützmacher, D.; Gerharz, J.; Mussler, G.; van der Cingel, J.; Zhang, J.J.; Bauer, G.; Schmidt, O.G.; Miglio, L.
n-Channel MOSFETs Fabricated on SiGe Dots for Strain-Enhanced Mobility
IEEE Electron Device Letters, 31 (2010) 10, 1083 - 1085

Karrasch C., M. Pletyukhov, L. Borda, and V. Meden
A functional renormalization group study of the interacting resonant level model in and out of equilibrium
Phys. Rev. B 81, 125122 (2010)

Karrasch C., S. Andergassen, M. Pletyukhov, D. Schuricht, L. Borda, V. Meden, and H. Schoeller
Non-equilibrium current and relaxation dynamics of a charge-fluctuating quantum dot
Europhys. Lett. 90, 30003 (2010)

Karrasch C., V. Meden, and K. Schönhammer
Finite-temperature linear conductance from the Matsubara Green function without analytic continuation to the real axis
Phys. Rev. B 82, 125114 (2010)

Kätelhön, E.; Hofmann, B.; Lemay, S.G.; Zevenberge, M.A.G.; Offenhäusser, A.; Wolfrum, B.
Nanocavity Redox Cycling Sensors for the Detection of Dopamine Fluctuations in Microfluidic Gradients
Analytical Chemistry, 82 (2010) 20, 8502 - 8509

Keeble, D.J.; Wicklein, S.; Dittmann, R.; Ravelli, L.; Mackie, R.A.; Egger, W.
Identification of A- and B-site cation vacancy defects in perovskite oxide thin films
Physical Review Letters, 105 (2010) 22, 226102

Kemmler, M.; Weides, M.; Weiler, M.; Opel, M.; Goennenwein, S.T.B.; Vasenko, A.S.; Golubov, A.A.; Kohlstedt, H.; Koelle, D.; Kleiner, R.; Goldobin, E.
Magnetic interference patterns in 0-pi superconductor/insulator/ferromagnet/superconductor Josephson junctions: Effects of asymmetry between 0 and pi regions
Physical Review B, 81 (2010) 5, 054522

Kennes D.M.,and V. Meden
Relaxation dynamics of an exactly solvable electron-phonon model
Phys. Rev. B 82, 085109 (2010)

Kessel M., De Souza R. A., Yoo H.-I., Martin M.
Strongly enhanced incorporation of oxygen into barium titanate based multilayer ceramic capacitors using water vapor
Appl. Phys. Lett. 97, 021910 (2010).

Ketteniss N., L. Rahimzadeh Khoshroo, M. Eickelkamp, M. Heuken, H. Kalisch, R. H. Jansen, A. Vescan
Study on quaternary AlInGaN/GaN HFETs grown on sapphire substrates
Semicond. Sci. Technol. 25 075013 (2010)

Kinza M., J. Ortloff, C. Honerkamp
Effective low-energy Hamiltonians for interacting nanostructures
Phys. Rev. B 82, 155430 (2010)

Kimura, A.; Krasovskii, E. E.; Nishimura, R.; Miyamoto, K.; Kadono, T.; Kanomaru, K.; Chulkov, E. V.; Bihlmayer, G.; Shimada, K.; Namatame, H.; Taniguchi, M.
Strong Rashba-Type Spin Polarization of the Photocurrent from Bulk Continuum States: Experiment and Theory for Bi(111)
Physical Review Letters, 105 (2010) 7, 076804

Kirchner, P.; Ng, Y.A.; Spelthahn, H.; Schneider, A.; Henkel, H.; Friedrich, P.; Kolstad, J.; Berger, J.; Keusgen, M.; Schöning, M. J.
Gas sensor investigation based on a catalytically activated thin-film thermopile for H2O2 detection
Physica Status Solidi A, 207 (2010) 4, 787 - 792

Kirchner, P.; Oberländer, J.; Friedrich, P.; Berger, J.; Rysstad, G.; Keusgen, M.; Schöning, M. J.
Realization of a calorimetric gas sensor on polyimide foil for applications in aseptic food industry
Procedia Engineering, 5 (2010), 264 - 267

Kiselov, V.S.; Lytvyn, P.M.; Yukhymchuk, V.O.; Belyaev, A.E.; Vitusevich, S. A.
Synthesis and properties of porous SiC ceramics
Journal of Applied Physics, 107 (2010) 9, 093510

Klingschat G., C. Honerkamp
Exact diagonalization study of trionic crossover and trion liquid in the attractive three-component Hubbard model
Phys. Rev. B 82, 094521 (2010)

Knackstedt C., Schimpf T., Napp A., Wessling B., Rothe C., Mischke K., Schnakenberg U. and Schauerte P.
Super-selective electrical stimulation of the left ventricle via a miniaturized magnetized stimulation wire: proof of concept study
Biomed.Tech.(Berl), 55, 5, pp. 285-290 (2010)

Knoll, L.; Zhao, Q. T.; Habicht, S.; Urban, C.; Ghyselen, B.; Mantl, S.
Ultrathin Ni Silicides with low contact resistance on Strained and Unstrained Silicon
IEEE Electron Device Letters, 31 (2010) 4, 350 - 352

Koehler F.M., A. Jacobsen, K. Ensslin, C. Stampfer, and W. J. Stark
Selective Chemical Modification of Graphene surfaces: Distinction between Single and Bilayer Graphene
Small 6 1125 (2010)

KollerS., Grifoni M., Leijnse M., Wegewijs M. R.
Density-operator approaches to transport through interacting quantum dots: Simplifications in fourth-order perturbation theory.
Phys. Rev. B (2010) 82:235307

Kordos, P.; Mikulics, M.; Fox, A.; Gregusová, D.; Cico, K.; Carlin, J-F.; Grandjean, N.; Novák, J.; Fröhlich, K.
RF Performance of InAlN/GaN HFETs and MOSHFETs with fTxLG up to 21GHzum
IEEE Electron Device Letters, 31 (2010) 3, 180 - 182

Kröger, I.; Stadtmüller, B.; Stadler, C.; Ziroff, J.; Kochler, M.; Stahl, A.; Pollinger, F.; Lee, T.-L.; Zegenhagen, J.; Reinert, F.; Kumpf, C.
Submonolayer growth of copper-phthalocyanine on Ag(111)
New Journal of Physics, 12 (2010), 083038

Krug I., Barrett N., Petraru, A., Locatelli, A., Mentes, T. O., Niño, M. A., Rahmanizadeh, K., Bihlmayer, G., Schneider, C. M.
Extrinsic screening of ferroelectric domains in Pb(Zr0.48Ti0.52)O3
Applied Physics Letters 97, 22, 222903 (2010)

Kügeler, C.; Weng, R.; Schroeder, H.; Symanczyk, R.; Majewski, P.; Ufert, K.-D.; Waser, R.
Study on the dynamic resistance switching properties of NiO thin films
Thin Solid Films, 518 (2010) Issue 8, 2258 - 2260

Laviano, F.; Ghigo, G.; Mezzetti, E.; Hollmann, E.; Wördenweber, R.
Control of the vortex flow in microchannel arrays produced in YBCO films by heavy-ion lithography Physica C, 470 (2010) 19, 844 - 847

Lazic, P.; Alaei, M.; Atodiresei, N.; Caciuc, V.; Brako, R.; Blügel, S.
Density functional theory with nonlocal correlation: A key to the solution of the CO adsorption puzzle
Physical Review B, 81 (2010) 4, 045401

Lazic P., Atodiresei N., Alaei M., Caciuc V., Blügel S., Brako R.
JuNoLo – Jülich nonlocal code for parallel post-processing evaluation of vdW-DF correlation energy
Computer Physics Communications 181, 2, 371 - 379 (2010)

Lee, J.H.; Fang, L.; Vlahos, E.; Ke, X.; Jung, Y.W.; Fitting Kourkoutis, L.; Kim, J.W.; Ryan, P.; Heeg, T.; Roeckerath, M.; Goian, V.; Bernhagen, M.; Uecker, R.; Hammel, C.; Rabe, K.M.; Kamba, S.; Schubert, J.; Freeland, J.W.; Muller, D.A.; Fennie, C.J.; Schiffer, P.; Gopalan, V.; Johnston-Halperin, E.; Schlom, D.G.
A strong ferroelectric ferromagnet created by means of spin-hhonon coupling
Nature, 499 (2010), 954 - 958

Lee, J.H.; Ke, X.; Misra, R.; Ihlefeld, J.F.; Xu, X.S.; Mei, Z.G.; Heeg, T.; Roeckerath, M.; Schubert, J.; Liu, Z.K.; Musfeldt, J.L.; Schiffer, P.; Schlom, D.G.
Adsorption-controlled growth of BiMnO3 thin films by molecular-beam epitaxy
Applied Physics Letters, 96 (2010) , 262905

Leijnse M., Wegewijs M.R., FlensbergK.
Nonlinear thermoelectric properties of molecular junctions with vibrational coupling.
Phys. Rev. B (2010), 82:045412

Lennartz, M.C.; Caciuc, V.; Atodiresei, N.; Karthäuser, S.; Blügel, S.
Electronic Mapping of Molecular Orbitals at the Molecule-Metal Interface
Physical Review Letters, 105 (2010) 6, 066801

Li, H.-F.; Su, Y.; Chatterji, T.; Nefedov, A.; Persson, J.; Meuffels, P.; Xiao, Y.; Vaknin, D.; Brückel, T.
Soft x-ray resonant scattering study of single-crystal LaSr2Mn2O7
European Physical Journal B, 74 (2010) 4, 457 - 461

Li, J.-B.; Rao, G.H.; Xiao, Y.; Liang, J. K.; Luo, J.; Liu, G. Y.; Chen, J. R.
Structural evolution and physical properties of Bi1-xGdxFeO3 ceramics
Acta Materialia, 58 (2010) 10, 3701 - 3708

Libisch F., S. Rotter, J. Güttinger, C. Stampfer, and J. Burgdörfer
Transition to Landau Levels in Graphene Quantum Dots
Phys. Rev. B 81 245411 (2010)

Liebsch A.
Spectral weight of doping-induced states in the two-dimensional Hubbard model
Physical Review B 81, 235133 (2010)

Liebsch A., Ishida H.
Correlation-induced spin freezing transition in FeSe: A dynamical mean field study
Physical Review B 82, 15, 155106 (2010)

Linn, E.; Rosezin, R.; Kügeler, C.; Waser, R.
Complementary resistive switches for passive nanocrossbar memories Published online: 18 April 2010
Nature Materials, 9 (2010), 403 - 406

Liu, Y.; Offenhäusser, A.; Mayer, D.
An Electrochemically Transduced XOR Logic Gate at the Molecular Level
Angewandte Chemie-International Edition, 49 (2010) 14, 2595 - 2598

Liu, Y.; Offenhäusser, A.; Mayer, D.
Electrochemical current rectification at bio-functonalized electrodes
Bioelectrochemistry, 77 (2010) 2, 89 - 93

Liu, Y.; Offenhäusser, A.; Mayer, D.
Molecular rectification in metal-bridge molecule-metal junctions
Physica Status Solidi A, 207(2010) 4, 891 - 897

Liu, Y.; Offenhäusser, A.; Mayer, D.
Rectified tunneling current response of bio-functionalized metal-bridge-metal junctions
Biosensors and Bioelectronics, 25 (2010) 5, 1173 - 1178

Lizzit, S.; Zampieri, G.; Petaccia, L.; Larciprete, R.; Lacovig, P.; Rienks, E. D. L.; Bihlmayer, G.; Baraldi, A.; Hofmann, Ph.
Band dispersion in the deep 1s core level of graphene
Nature Physics, 6 (2010), 345 . 349

Lorenz B., Carbone G., Schulze C.
Average separation between a rough surface and a rubber block: Comparison between theories and experiments
Wear 268, 7-8, 984 - 990 (2010)

Lounis S., Dederichs P. H.
Mapping the magnetic exchange interactions from first principles: Anisotropy anomaly and application to Fe, Ni, and Co
Physical Review B 82, 18, 180404(R) (2010)

Mader W., Prangenberg T., Eichhorn S., De Souza R. A., Martin M.
Iron Diffusion and Compound Formation in Zinc Oxide
Diffusion Fundamentals 12, 57 (2010)

Mairoser, T.; Schmehl, A.; Melville, A.; Heeg, T.; Canella, L.; Böni, P.; Zander, W.; Schubert, J.; Shai, D.E.; Monkman, E.J.; Shen, K.M.; Schlom, D.G.; Mannhart, J.
Charge Carrier Induced Increase of the Curie Temperature of EuO - Is there an Instrinsic Limit?
Physical Review Letters, 105 (2010) , 257206

Mairoser, T.; Schmehl, A.; Melville, A.; Heeg, T.; Canella, L.; Böni, P.; Zander, W.; Schubert, J.; Shai, D.E.; Monkman, E.J.; Shen, K.M.; Schlom, D.G.; Mannhart, J.
Charge Carrier Induced Increase of the Curie Temperature of EuO - Is There an Intrinsic Limit?
Physical Review Letters, 105 (2010) , 257206

Malleo D., Nevill J. T., van Ooyen A., Schnakenberg U., Lee L. P. and Morgan H.
Note: Characterization of electrode materials for dielectric spectroscopy
Review of Scientific Instruments, 81, 1 (2010)

Mathias, S.; Ruffing, A.; Deicke, F.; Wiesenmayer, M.; Sakar, I.; Bihlmayer, G.; Chulkov, E. V.; Koroteev, Yu. M.; Echenique, P. M.; Bauer, M.; Aeschlimann, M.
Quantum-well induced giant spin-orbit splitting
Physical Review Letters, 104 (2010) 6, 066802

Mavropoulos, P.; Lounis, S.; Blügel, S.
Exchange coupling in transition-metal
nanoclusters on Cu(001) and Cu(111) surfaces
Physica Status Solidi B, 247, (2010) 5, 1187 - 1196

McNellis, E.R.; Mercurio, G.; Hagen, S.; Leyssner, F.; Meyer, J.; Soubatch, S.; Wolf, M.; Reuter, K.; Tegeder, P.; Tautz, F. S.
Bulky spacer groups - A valid strategy to control the coupling of functional molecules to surfaces?
Chemical Physics Letters, 499 (2010) 4/6, 247 - 249

Mercurio, G.; McNellis, E.R.; Martin, I.; Hagen, S.; Leyssner, F.; Soubatch, S.; Meyer, J.; Wolf, M.; Tegeder, P.; Tautz, F. S.; Reuter, K.
Structure and Energetics of Azobene on Ag(111): Benchmarking Semiempirical Dispersion Correction Approaches
Physical Review Letters, 104 (2010), 036102

Mikulics, M.; Adam, R.; Sofer, Z.; Hardtdegen, H.; Stancek, S.; Knobbe, J.; Kocan, M.; Stejskal, J.; Sedmidubsky, D.; Pavlovic, M.; Necas, V.; Grützmacher, D.; Marso, M.
Femtosecond and highly sensitive GaAs metal-semiconductor-metal photodetectors grown on aluminum mirrors/pseudo-substrates
Semiconductor Science and Technology, 25 (2010) 7, 075001

Mikulics, M.; Stoklas, R.; Dadgar, A.; Gregusová, D.; Novák, J.; Grützmacher, D.; Krost, A.; Kordos, P.
InAIM/GaN/Si heterostructures and field-effect transistors with lattice matched and tensely or compressively strained InAIN
Applied Physics Letters, 97 (2010) 17, 173505

Minamisawa, R.A.; Habicht, S.; Buca, D.; Carius, S.; Trellenkamp, S.; Bourdelle, K.K.; Mantl, S.
Elastic strain and dopant activation in ion implanted strained Si nanowires
Journal of Applied Physics, 108 (2010) 12, 124908

Miyamoto, K.; Kaneko, K.; Matsuo, A.; Wagner, T.; Kanoh, S.; Schöning, M. J.; Yoshinobu, T.
Miniaturized chemical imaging sensor system using an OLED display panel
Procedia Engineering, 5 (2010), 516 - 519

Miyamoto, K.; Sugawara, Y.; Shin'ichiro, K.; Yoshinobu, T.; Wagner, T.; Schöning, M. J.
Image correction method for the chemical imaging sensor
Sensors and Actuators B, 144 (2010) 2, 344 - 348

Mokwa W.
Mems Technologies for Artificial Retinas
Proc. SPIE, 7594, p. 759402, doi:10.1117/12.848218 (2010)

Moras, P.; Wortmann, D.; Bihlmayer, G.; Ferrari, L.; Alejandro, G.; Zhou, P. H.; Topwal, D.; Sheverdyaeva, P. M.; Blügel, S.; Carbone, C.
Probing the electronic transmission across a buried metal/metal interface
Physical Review B, 82 (2010) 15, 155427

Morawski, I.; Voigtländer, B.
Simultaneously measured signals in scanning probe microscopy with a needle sensor: Frequency shift and tunneling current
Review of Scientific Instruments, 81 (2010) 3, 033703

Morgenstern M.
STM ready for the time domain.
Science (Perspective) 329, 1609 (2010)

Mueller D. N., De Souza R. A., Weirich T. E., Roehrens D., Mayer J., Martin M.
A kinetic Study of the decomposition of the cubic perovskite-type oxide BaxSr1-xCo0.8Fe0.2O3-δ (BSCF) (x=0.1 and 0.5)
Phys. Chem. Chem. Phys. 12, 10320 (2010)

Müller S. Y., V. Koerting, D. Schuricht, and S. Andergassen
Spin and orbital fluctuations in non-equilibrium transport through quantum dots: A renormalization-group analysis
Europhys. Lett. 92, 10002 (2010) (cond-mat/1007.3605)

Müller-Meskamp, L.; Karthäuser, S.; Zandvliet, H.J.W.; Homberger, M.; Simon, U.; Waser, R.
Field emission resonances at tip/Mercaptoalkyl-ferrocene/Au interfaces
E Nano Newsletters, 19 (2010), 28 - 29

Münstermann, R.; Menke, T.; Dittmann, R.; Waser, R.
Coexistence of filamentary and homogeneous switching in Fe-doped SrTiO3 thin film memristive devices
Advanced Materials, 22 (2010) 43, 4819 - 4822

Münstermann, R.; Yang, J.J.; Strachan, J.P.; Medeiros-Ribeiro, G.; Dittmann, R.; Waser, R.
Morphological and electical changes in TiO2 memristive devices induced by elecroforming and switching
Physica Status Solidi - Rapid Research Letters, 4 (2010) 1/2, 16 - 18

Muentjes J., Meine S., Flach E., Goertz M., Hartmann R., Schmitz-Rode T., Trieu H.-K. and Mokwa W.
Monitoring intravascular pressure with a pulmonary artery pressure sensor system - assembly aspects
Proc.Smart Systems Integration 2010, pp. 81 (2010)

Myllymäki, P.; Roeckerath, M.; Lopes, J. M. J.; Schubert, J.; Mizohata, K.; Putkonen, M.; Niinistö, L.
Rare earth scandate thin films by atomic layer deposition: effect of the rare earth cation size
Journal of Materials Chemistry, 20 (2010), 4207 - 4212

Myslivecek, J.; Dvorak, F.; Strozecka, A.; Voigtländer, B.
Scanning tunneling microscopy contrast in lateral Ge-Si nanostructures on Si(111)-3x3-Bi
Physical Review B, 81 (2010) 84, 245427

Nauenheim, C.; Kügeler, C.; Rüdiger, A.; Waser, R.
Investigation of the electroforming process in resistively switching TiO_2 nanocrosspoint junctions
Applied Physics Letters, 96 (2010) 12, 122902

Nelles J., D. Sendor, F.-M. Petrat, U. Simon,
Electrical Properties of Surface Functionalized Silicon Nanoparticles
J. Nanopart. Res. 12(4), 1367-1375 (2010).

Niggemeyer M., Nolten U., Heger S., Radermacher K. and Mokwa W.
Sterilizability evaluation of strain gauges for the use in an intraoperative environment
Proceedings of the 10th Annual Meeting of CAOS International (2010)

Nolten U., Kempf H., Mattes U. and Mokwa W.
Force Sensor Clip for Orthopedic Applications
Procedia Engineering, 5, pp. 730-733 (2010)

Ono, T.; Heide, M.; Atodiresei, N.; Baumeister, P.; Tsukamoto, S.; Blügel, S.
Real-space electronic structure calculations with full-potential all-electron precision for transition metals
Physical Review B, 82 (2010) 20, 205115

Pfuhl, E.; Voigt, J.; Mattauch, S.; Korolkov, D.; Brückel, T.
Interlayer exchange coupling in ErjTb superlattices mediated by short range incommensurate Er order
Journal of Physics : Conference Series, 211 (2010), 012019

Phan, M.H.; Frey, N.A.; Angst, M.; de Groot, J.; Sales, B.C.; Mandrus, D.G.; Srikanth, H.
Complex magnetic phases in LuFe2O4
Solid State Communications, 150 (2010) 7/8, 341 - 345

Quach D.-V., Avila-Paredes H. J., Kim S., Martin M., Munir Z. A.
Pressure effects and grain growth kinetics in the consolidation of nanostructured fully stabilized zirconia by pulsed electric current sintering
Acta Materialia 58, 5022 (2010)

Quach D. V., Kim S., Martin M., Munir Z. A.
Sintering and properties of nanometric functional oxides
Ceramic Transactions 212, 55 (2010)

Radev I., Topalov G., Slavcheva E., Lefterova E., Tsotridis G. and Schnakenberg U.
Experimental validation of the "EasyTest Cell" operational principle for autonomous MEA characterization
International Journal of Hydrogen Energy, 35, 6, pp. 2428-2435 (2010)

Radtke, C.; Krug, C.; Soares, G.V.; Baumvol, I.J.R.; Lopes, J. M. J.; Durgun Özben, E.; Nichau, A.; Schubert, J.; Mantl, S.
Physicochemical and Electrical Properties of LaLuO3/Ge(100) Structures Submitted to Postdeposition Annealings
Electrochemical and Solid State Letters, 13 (2010) 5, G37 - G39

Rahimzadeh Khoshroo L., N. Ketteniss, C. Mauder, H. Behmenburg, J. F. Woitok, I. Booker, J. Gruis, M. Heuken, A. Vescan, H. Kalisch, R. H. Jansen
Quaternary nitride heterostructure field effect transistors
physica status solidi (c), 7: 2001-2003 (2010)

Reckermann F., Splettstoesser J., Wegewijs M.R.,
Interaction-induced adiabatic non-linear transport
Phys. Rev. Lett. 104 (2010), 226803

Reiche, M.; Kittler, M.; Buca, D.; Haehnel, A.; Zhao, Q. T.; Mantl, S.; Gösele, U.
Self-Organized Si-Nanotransistors
Japanese Journal of Applied Physics Part 1: Regular Papers, Short Notes and Review Papers, 49 (2010), 04DJ02

Riwar R.-P., Splettstoesser J.,
Charge and spin pumping through a double quantum dot,
Phys. Rev. B 82 (2010), 205308

Roeckerath, M.; Lopes, J. M. J.; Durgun Özben, E.; Urban, C.; Schubert, J.; Mantl, S.; Jia, Y.; Schlom, D.G.
Investigation of terbium scandate as an alternative gate dielectric in fully depleted transistors
Applied Physics Letters, 96 (2010) 1, 013513

Roehrens D., Brendt J., Samuelis D., Martin M.
On the ammonolysis of Ga2O3: An XRD, neutron diffraction and XAS investigation of the oxygen-rich part of the system Ga2O3-GaN
Journal of Solid State Chemistry 183, 532 (2010)

Roescher, M.; Schneller, T.; Waser, R.
Comments on the processing of the niobium omponent for chemical solution derived niobium oxide-based thin films
Journal of Sol-Gel Science and Technology, 56 (2010) 3, 236 – 243

Rodriguez-Gonzalez L., U. Simon,
NH3-TPD Measurements Using a Zeolite-based Sensor,
Measurement Science and Technology 21, 027003 (7pp) (2010).

Rosezin, R.; Meier, M.; Trellenkamp, S.; Kügeler, C.; Waser, R.
Observation of unipolar resistance switching in silver doped methyl-silsesquioxane
Microelectronic Engineering, 87 (2010) 5/8, 1531 - 1533

Ruh, E.; Mueller, E.; Mussler, G.; Sigg, H.C.; Gruetzmacher, D.
Investigation of the local Ge concentration in Si/SiGe nanostructures by convergent-beam electron diffraction
Ultramicroscopy, 110 (2010) 10, 1255 - 1266

Rushchanskii K., Kamba S., Goian V., Vanek P., Savinov M., Prokleska J., Nuzhnyy D., Knizek K., Laufek F., Eckel S., Lamoreaux S.K., Sushkov A.O., Lezaic M., Spaldin N.A.
A multiferroic material to search for the permanent electric dipole moment of the electron
Nature Materials 9, 8, 649 - 654 (2010)

Sarreshtedari, F.; Jahed, NMS.; Hosseni, N.; Pourhashemi, A.; Banzet, M.; Schubert, J.; Fardmanesh, M.
FEM enhanced signal processing approach for pattern recognition in the SQUID based NDE system
Journal of Physics : Conference Series, 234 (2010) 4, 042030

Sarreshtedari, F.; Pourhashemi, A.; Asad, N.; Schubert, J.; Banzet, M.; Fardmanesh, M.
An Efficient Finite-Element Approach for the Modeling of Planar Double-D Excitation Coils and Flaws in SQUID NDE Systems
IEEE Transactions on Applied Superconductivity, 20 (2010) 2, 76 - 81

Sasioglu, E.; Schindlmayr, A.; Friedrich, C.; Freimuth, F.; Blügel, S.
Wannier-function approach to spin excitations in solids
Physical Review B, 81 (2010) 5, 054434

Sawade, G.; Krause, H.-J.
Prüfung von Spannbetonbauteilen mit magnetischen Methoden
Beton- und Stahlbetonbau, 105 (2010) 3, 154 - 164

Sayers R, De Souza R. A., Kilner J. A., Skinner S. J.
Low temperature diffusion and oxygen stoichiometry in lanthanum nickelate
Solid State Ionics 181, 386 (2010)

Scharinger, S.; Gürlich, C.; Mints, R.G.; Weides, M.; Kohlstedt, H.; Goldobin, E.; Koelle, D.; Kleiner, R.
Interference patterns of multfacet 20x (0-pi) Josephson junctions with ferromagnetic barrier
Physical Review B, 81 (2010) 174535,

Schindlmayr, A.; Friedrich, C.; Sasioglu, E.; Blügel, S.
First-Principles Calculation of Electronic Excitations in Solids with SPEX
Zeitschrift für physikalische Chemie, 224 (2010) 3/4, 357 - 368

Schmelzer, S.; Bräuhaus, D.; Hoffmann-Eifert, S.; Meuffels, P.; Böttger, U.; Oberbeck, L.; Reinig, P.; Schröder, U.; Waser, R.
SrTiO3 ultra thin film capacitors on silicon substrates with significant interfacial passive layers
Applied Physics Letters, 97 (2010) 13, 132907

Schoofs A., Niederegger S., van O. A., Heinzel H. G. and Spiess R.
The brain can eat: establishing the existence of a central pattern generator for feeding in third instar larvae of Drosophila virilis and Drosophila melanogaster
J.Insect Physiol, 56, 7, pp. 695-705 (2010)

Schroeder, H.; Zhirnov, V.V.; Cavin, R.K.; Waser, R.
Voltage-time dilemma of pure electronic mechanisms in resistive switching memory cells
Journal of Applied Physics, 107 (2010) 5, 054517

Schröper, F.; Offenhäusser, A.; Mayer, D.; Baumann, A.
Bidirectional immobilization of affinity-tagged cytochrome c on electrode surfaces
Chemical Communications, 46 (2010) 29, 5295 - 5297

Schumacher, D.; Mattauch, S.; Rücker, U.; Brückel, T.
Preparation and analysis of epitaxial Fe monolayers buried in Pd
Journal of Physics : Conference Series, 211 (2010) 1, 012021

Schweika, W.
XYZ-polarisation analysis of diffuse magnetic neutron scattering from single crystals
Journal of Physics : Conference Series, 211 (2010), 012026

Seemann K.M., Mokrousov Y., Azis A., Miguel J., Kronast F., Kuch W., Blamire M.G., Hindmarch A.T, Hickey B.J., Souza I., Marrows C.H.
Spin-orbit strength driven crossover between intrinsic and extrinsic mechanisms of the anomalous Hall effect in the epitaxial L1o-ordered ferromagnets FePd and FePt
Physical Review Letters 104, 7, 076402 (2010)

Semenov, A.; Cojocari, O.; Hübers, H.-W.; Song, F.; Klushin, A. M.; Müller, A.-S.
Application of zero-bias quasi-optical Schottky-diode detectors for monitoring short-pulse and weak terahertz radiation
IEEE Electron Device Letters, 31 (2010) 7, 674 - 676

Shen, Wan.; Dittmann, R.; Waser, R.
Reversible altenation between bipolar and unipolar resistive switching in polycrystalline barium strontium titanate thin films
Journal of Applied Physics, 107 (2010) 9, 094506

Shibuya, K.; Dittmann, R.; Mi, S.; Waser, R.
Impact of defect distribution on resistive switching characteristics of Sr2tiO4 thin Films
Advanced Materials, 22 (2010) 411 - 414

Siqueira, J.R.; Bäcker, M.; Poghossian, A.; Zucolotto, V.; Oliveira, N.O.; Schöning, M. J.
Associating biosensing properties with the morphological structure of multilayers containing carbon nanotubes
Physica Status Solidi A, 207 (2010) 4, 781 - 786

Skorb, E.V.; Grützmacher, D.; Dais, C.; Guzenko, V.A.; Sokolov, V.G.; Gaevskaya, T.V.; Sviridov, D.V.
Titania-assisted electron-beam and synchrotron lithography
Nanotechnology, 21 (2010) 31, 315301

Skoromets, V.; Kadlec, C.; Kuzel, K.; Kamba, S.; Schubert, J.
Electric field tuning of hard polar phonons in strained SrTiO3 films
Journal of Applied Physics, 107 (2010) 12, 124116

Sladek, K.; Klinger, V.; Wensorra, J.; Akabori, M.; Hardtdegen, H.; Grützmacher, D.
MOVPE of n-doped GaAs and modulation doped GaAs/AlGaAs nanowires
Journal of Crystal Growth, 312 (2010) , 635 - 640

Slavcheva E., Topalov G., Ganske G., Radev I., Lefterova E. and Schnakenberg U.
Influence of sputtering pressure on surface structure and oxygen reduction reaction catalytic activity of thin platinum films
Electrochimica Acta, 55, 28, pp. 8992-8997 (2010)

Song, F.; Levitchev, M.Y.; Markelov, V.A.; Kurin, V.V.; Fang, L.; Klushin, A. M.
Millimeter-wavelength radiation from arrays of discrete high-temperature superconductor Josephson junctions
Superconductor Science and Technology, 23 (2010) 3, 034026

Song, F.; Müller, F.; Behr, R.; Klushin, A. M.
Self-radiation from arrays of niobium Josephson junction embedded in the open resonator
Physica C, 470 (2010) 19, 750 - 753

Soni, R.; Meuffels, P.; Petraru, A.; Weides, M.; Kügeler, C.; Waser, R.; Kohlstedt, H.
Probing Cu doped Ge_0.3Se_0.7 based resistance switching memory devices with random telegraph noise
Journal of Applied Physics, 107 (2010) 2, 024517 - 024527

Spelthahn, H.; Schaffrath, S.; Coppe, T.; Rufi, F.; Schöning, M. J.
Development of an elctrolyte-insulator-semiconductor (EIS) based capacitive heavy metal sensor for the detection of Pb2+ und Cd2+ ions
Physica Status Solidi A, 207 (2010) 4, 930 - 934

Splettstoesser J., Samuelsson P., Moskalets M., Büttiker M.,
Two-particle Aharonov-Bohm effect in electronic interferometers,
J. Phys. A: Math. Theor. 43 (2010), 354027

Splettstoesser J., Governale M., König J., Büttiker M.,
Charge and spin dynamics in interacting quantum dots,
Phys. Rev. B 81 (2010), 165318.

Sprungmann, D.; Westerholdt, K.; Zabel, H.; Weides, M.; Kohlstedt, H.
Evidence for triplet superconductivity in Josephson junctions with ferromagnetic Cu2MnAl-Heusler barriers
Physical Review B, 82 (2010) 6, 060505

Stepina, N.P.; Koptev, E.S.; Dvurechenskii, A.V.; Osinnyukh, I.V.; Nikiforov, A.I.; Gruetzmacher, D.; Moers, J.; Gerharz, J.
Photo-induced conductance fluctuations in mesoscopic Ge/Si systems with quantum dots
Journal of Physics: Conference Series
245 (2010) 1, 012034

Sun, J.; Wang, J.; Wells, J.; Koroteev, Y. M.; Bihlmayer, G.; Chulkov, E. V.; Hofmann, Ph.; Pohl, K.
Structure and oscillatory multilayer relaxation of the bismuth (100) surface
New Journal of Physics, 12 (2010) 063016

Temirov, R.; Tautz, F. S.
Blick ins Molekül
Physik in unserer Zeit, 41 (2010) 6, 266 - 267

Tenne, D.A.; Farrar, A.K.; Brooks, C.M.; Heeg, T.; Schubert, J.; Jang, H.W.; Bark, C.W.; Folkman, C.M.; Eom, C.B.; Schlom, D.G.

Ferroelectricity in nonstoichiometric SrTiO3 films studied by ultraviolet Raman spectroscopy
Applied Physics Letters, 97 (2010) 14, 142901

Thiess A., Mokrousov Y., Heinze S.
Competing magnetic anisotropies in atomic-scale junctions
Physical Review B 81, 5, 054433 (2010)

Thomas, R.; Ehrhart, P.; Waser, R.; Schubert, J.; Devi, A.; Katiyar, R.S.
Liquid injection MOCVD grown binary oxides and ternary rare-earth oxide as alternate gate-oxides for logic devices
ECS Transactions, 33 (2010) 3, 211 - 219

Trinkaus, H.; Buca, D.; Holländer, B.; Minamisawa, R. A.; Hartmann, J.M.; Mantl, S.
Strain tensors in layer systems by precision ion channeling measurements
Journal of Applied Physics, 107 (2010) 12, 124906

Turek, M.; Heiden, W.; Guo, S.; Riesen, A.; Schubert, J.; Zander, W.; Krüger, P.; Keusgen, M.; Schöning, M. J.
Simultaneous detection of cyanide and heavy metals for environmental analysis by means of µISEs
Physica Status Solidi A, 207 (2010) 4, 817 - 823

Urban, C.; Emam, M.; Sandow, C.; Knoch, J.; Zhao, Q. T.; Raskin, J.-P.; Mantl, S.
Radio-Frequency Study of Dopant-Segregated n-Type SB-MOSFETs on Thin-Body SOI
IEEE Electron Device Letters, 31 (2010) 6, 537 - 539

Urban, C.; Sandow, C.; Zhao, Q. T.; Knoch, J.; Lenk, S.; Mantl, S.
Systematic study of Schottky barrier MOSFETs with dopant segregation on thin-body SOI
Solid-State Electronics, 54 (2010) 2, 185 - 190

Urbaszek A., Trieu H.-K., Traulsen T., Mokwa W., Schmitz-Rode T.
Entwicklung eines implantierbaren Drucksensors zum kontinuierlichen Monitoring des pulmonalarteriellen Drucks bei Herzinsuffizienzpatienten
Proc. IGBMT Tagung, Biomed Tech 2010; 55 (Suppl. 1), doi: 10.1515/BMT.2010.135 (2010)

van Ooyen A., Ulrich C. and Schnakenberg U.
Pulse-clamp method applied to SIROF stimulation electrodes
Sensors and Actuators B, in press (2010)

Vieweg, N.; Jansen, C.; Shakfa, M.K.; Scheller, M.; Krumbholz, N.; Wilk, R.; Mikulics, M.; Koch, M.
Molecular properties of liquid crystals in the terahertz frequency range
Optics Express, 18 (2010) 6, 6097 - 6107

Vitusevich, S. A.; Sydoruk, V. A.; Petrychuk, M. V.; Danilchenko, B. A.; Klein, N.; Offenhäusser, A.; Ural, A.; Bosman, G.
Transport properties of single-walled carbon nanotube transistors after gamma radiation treatment
Journal of Applied Physics, 107 (2010), 063701

Volk, C.; Schubert, J.; Schnee, M.; Weiss, K.; Akabori, M.; Sladek, K.; Hardtdegen, H.; Schäpers, T.
LaLuO3 as high-k gate dielectric for InAs nanowire structures
Semiconductor Science and Technology, 25 (2010) 8, 085001

Volk, C.; Schubert, J.; Weis, K.; Estévez Hernández, S.; Akabori, M.; Sladek, K.; Hardtdegen, H.; Schäpers, T.
Improved gate-control in InAs nanowire structures by the use of GdScO3 as a gate dielectric
Applied Physics A, 100 (2010) 1, 305 - 308

Vu, X. T.; Ghosh Moulick, R.; Eschermann, J. F.; Stockmann, R.; Offenhäusser, A.; Ingebrandt, S.
Fabrication and application of silicon nanowire transistor arrays for biomolecular detection
Sensors and Actuators B, 144 (2010) 2, 354 - 360

Vu, X. T.; Stockmann, R.; Wolfrum, B.; Offenhäusser, A.; Ingebrandt, S.
Fabrication and application of a microfluidic-embedded silicon nanowire biosensor chip
Physica Status Solidi A, 207 (2010) 4, 850 - 857

Wagner, C.; Kasemann, D.; Golnik, C.; Forker, R.; Esselinger, M.; Müllen, K.; Fritz, T.
Repulsion between molecules on a metal: Monolayers and submonolayers of hexa-peri-hexabenzocoronene on Au(111)
Physical Review B, 81 (2010) 3, 035423

Wagner, T.; Miyamoto, K.; Schöning, M. J.; Yoshinobu, T.
Novel combination of digital light processing (DLP) and light-addressable potentiometric sensors (LAPS) for flexible chemical imaging
Procedia Engineering, 5 (2010), 520 - 523

Wagner, T.; Werner, C.F.; Miyamoto, K.; Ackermann, H.-J.; Yoshinobu, T.; Schöning, M. J.
FPGA-based LAPS device for the flexible design of sensing sites on functional interfaces
Physica Status Solidi A, 207 (2010) 4, 844 - 849

Wang S., Chen C.-T., Navrotsky A., Martin M., Kim S., Munir Z. A.
Modified polyol-mediated synthesis and consolidation of Gd-doped ceria nanoparticles
Solid State Ionics 181, 372 (2010)

Wang, Zh.; Zhao, X.J.; Yue, H.W.; Song, F.-B.; He, M.; You, F.; Yan, S.L.; Klushin, A. M.; Xie, Q.L.
A method for self-radiation of Josephson junction arrays
Superconductor Science and Technology, 23 (2010) 6, 065013

Waser, R.; Dittmann, R.; Salinga, M.; Wuttig, M.
Function by defects at the atomic scale - New concepts for non-volatile memories
Solid-State Electronics, 54 (2010) 9, 830 - 840

Waser, R.; Dittmann, R.; Salinga, M.; Wuttig, M.
The role of defects in resistively switching chalcogenides
International Journal of Materials Research = Zeitschrift für Metallkunde, 101 (2010) 2, 182 - 198

Weides, M.; Peralagu, U.; Kohlstedt, H.; Pfeifer, J.; Kemmler, M.; Gürlich, C.; Goldobin, E.; Koelle, D.; Kleiner , R.
Critical current difraction pattern of SIFS Josephson junctions with step-type F-layer
Superconductor Science and Technology, 23 (2010) 9, 095007

Weiss, C.; Wagner, C.; Kleimann, C.; Rohlfing, M.; Tautz, F. S.; Temirov, R.
Imaging Pauli Repulsion in Scanning Tunneling Microscopy
Physical Review Letters, 105 (2010) 8, 086103

Weiss, C.; Wagner, C.; Temirov, R.; Tautz, F. S.
Direct Imaging of Intermolecular Bonds in Scanning Tunneling Microscopy
Journal of the American Chemical Society, 132 (2010) 34, 11864 - 11865

Wille, H.-C.; Hermann, R.; Sergueev, I.; Pelzer, U.; Möchel, A.; Claudio Weber, T.; Persson, J.; Rüffer, R.; Said, A.; Shvydko, Yu.
Nuclear forward and inelastic spectroscopy on 125Te and Sb2 125 Te3
Europhysics Letters, 91 (2010) 6, 62001

Wolff, S.; Lägel, B.; Trellenkamp, S.
Incident angle dependent damage of PMMA during Ar+-ion beam etching
Microelectronic Engineering, 87 (2010) , 1444 - 1446

Wördenweber, R.; Hollmann, E.; Schubert, J.; Kutzner, R.; Ghosh, A.K.
Vortex motion in high-Tc films and a micropattern-induced phase transition
Physica C, 470 (2010) 19, 835 - 839

Xiao, Y.; Su, Y.; Li, H.-F.; Kumar, C. M. N.; Mittal, R.; Persson, J.; Senyshyn, A.; Gross, K.; Brückel, T.
Neutron diffraction investigation of the crystal and magnetic structures in KCrF3 perovskite
Physical Review B, 82 (2010) , 094437

Xiao, Y.; Su, Y.; Mittal, R.; Chatterji, T.; Hansen, T.; Price, S.; Kumar, C. M. N.; Persson, J.; Matsuishi, S.; Inoue, Y.; Hosono, H.; Brückel, T.
Neutron diffraction study of phase transitions and thermal expansion of SrFeAsF
Physical Review B, 81 (2010) 9, 094523

Xiao, Y.; Su, Y.; Schmidt, W.; Schmalzl, K.; Kumar, C. M. N.; Price, S.; Chatterji, T.; Mittal, R.; Chang, L. J.; Nandi, S.; Kumar, C. M. N.; Dhar, S. K.; Thamizhavel, A.; Brückel, T.
Field-induced spin reorientation and giant spin-lattice coupling in EuFe2As2
Physical Review B, 81 (2010), 220406®

Xie, X.; Zhang, Y.; Wang, H.; Wang, Y.; Mück, M.; Dong, H.; Krause, H.-J.; Braginski, A. I.; Offenhäusser, A.; Jiang, M.
A Voltage biased superconducting quantum device bootstrap circuit
Superconductor Science and Technology, 23 (2010), 065016

Xu, X.S.; de Groot, J.; Sun, Q.-C.; Sales, B.C.; Mandrus, D.; Angst, M.; Litvinchuk, A.P.; Musfeldt, J.L.
Lattice dynamical probe of charge order and antipolar bilayer stacking in LuFe2O4
Physical Review B, 82 (2010) 1, 014304

Yi, Z.; Banzet, M.; Offenhäusser, A.; Mayer, D.
Fabrication of nanogaps with modified morphology by potential-controlled gold deposition
Physica Status Solidi (RRL), 4 (2010) , 73

Yi, Z.; Trellenkamp, S.; Offenhäusser, A.; Mayer, D.
Molecular junctions based on intermolecular electrostatic coupling
Chemical Communications, 46 (2010) 42, 8014 - 8016

Yoo H.-I., Martin M.
On the path-dependence of the open-cell voltage of a galvanic cell involving a ternary or multinary compound with multiple mobile ionic species under multiple chemical potential gradients
Phys. Chem. Chem. Phys. 12, 14699 (2010)

Yoon, S.; Dornseiffer, J.; Schneller, T.; Henning, D.; Iwaya, S.; Pithan, C.; Waser, R.

Percolative BaTiO3-Ni composite nanopowders from alkoxide-mediated synthesis
Journal of the European Ceramic Society, 30 (2010) 2, 561 - 567

Yoon, S.; Pithan, C.; Waser, R.; Dornseiffer, J.; Xiong, Y.; Gruner, D.; Shen, Z.; Iwaya, S.
Electronic conduction mechanisms in BaTiO3-Ni composites with ultrafine microstructure
Journal of the American Ceramic Society, 93 (2010) 12, 4075 - 4080

Zhirnov, V.V.; Cavin, R.K.; Menzel, S.; Linn, E.; Schmelzer, S.; Braeuhaus, D.; Schindler, C.; Waser, R.
Memory devices: Energy-space-time tradeoffs
Proceedings of the IEEE, 98 (2010) 12, 2185 - 2200

Zhong Z., Xu P. X., Kelly P. J.
Polarity-induced oxygen vacancies at LaAlO3/SrTiO3 interfaces
Physical Review B 82, 16, 165127 (2010)

Zhou L., Wiebe J., Lounis S., Vedmedenko E., Meier F., Blügel S., Dederichs P. H., Wiesendanger R.
Strength and directionality of surface Ruderman-Kittel-Kasuya-Yosida interaction mapped on the atomic scale
Nature Physics 6, 187 - 191 (2010)

Zhou, L.; Wiebe, J.; Lounis, S.; Vedmedenko, E.; Meier, F.; Blügel, S.; Dederichs, P. H.; Wiesendanger, R.
Strength and directionality of surface Ruderman-Kittel-Kasuya-Yosida interaction mapped on the atomic scale
Nature Physics, 6 (2010) 187 - 191

Zurbuchen, M.A.; Sherman, V.O.; Tagantsev, A.K.; Schubert, J.; Fong, D.; Streiffer, S.K.; Jia, Y.; Comstock, D.J.; Tian, W.; Schlom, D.G.
Synthesis, structure, and electrical behavior of Sr4Bi4Ti7O24
Journal of Applied Physics, 107 (2010) 2, 024106

Zyazin A. S., van den Berg J. W.G., Osorio E. A., van der Zant H. S.J., Konstantinidis N. P.,
May F., Leijnse M., Hofstetter W., Wegewijs M. R., Danieli C., Cornia A.
Electric field controlled magnetic anisotropy in a single molecule.
Nano Lett. (2010) 10:3307

JARA|FIT

JARA-FIT

Jülich Aachen Research Alliance
for Fundamentals of
Future Information Technology

Office:

Forschungszentrum Jülich GmbH
52425 Jülich
Germany

Phone: ++49-2461-613107
Email: w.speier@fz-juelich.de

AN INITIATIVE OF

RWTH AACHEN UNIVERSITY

JÜLICH FORSCHUNGSZENTRUM